Title

CHARACTERIZATION OF DISCONTINUITIES IN THE STRIPA GRANITE - FULL-SCALE HEATER EXPERIMENTS

Author

Paulsson, B.N.P.

Publication Date

1980-11-01

LBL-9063
SAC-38
UC-70

SWEDISH-AMERICAN COOPERATIVE PROGRAM ON RADIOACTIVE WASTE STORAGE IN MINED CAVERNS IN CRYSTALLINE ROCK

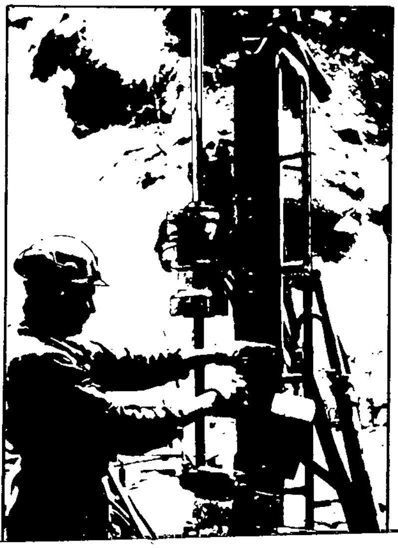

Technical Information Report No. 38

CHARACTERIZATION OF DISCONTINUITIES IN THE STRIPA GRANITE — FULL-SCALE HEATER EXPERIMENTS

B. N. P. Paulsson and P. H. Nelson
Lawrence Berkeley Laboratory
and
P. J. Kurfurst
Geological Survey of Canada

November 1980

A Joint Project of

Swedish Nuclear Fuel Supply Co.
Fack 10240 Stockholm, Sweden

Operated for the Swedish
Nuclear Power Utility Industry

Lawrence Berkeley Laboratory
Earth Sciences Division
University of California
Berkeley, California 94720, USA

Operated for the U.S. Department of
Energy under Contract DE-AC03-76SF00098

DISCLAIMER

LBL-9063
SAC-38
UC-70

CHARACTERIZATION OF DISCONTINUITIES IN THE STRIPA GRANITE--FULL-SCALE HEATER EXPERIMENTS

Björn N.P. Paulsson and Philip H. Nelson
Lawrence Berkeley Laboratory
University of California
Berkeley, California

Pavel J. Kurfurst
Geological Survey of Canada
Ottawa, Ontario, Canada

November 1980

This work was supported by the Assistant Secretary for Nuclear Energy, Office of Civilian Waste Management of the U.S. Department of Energy under Contract DE-AC03-76SF00098. Funding for this project was administered by the Office of Crystalline Repository Development at Battelle Memorial Institute.

PREFACE

This report is one of a series documenting the results of the Swedish-American cooperative research program in which the cooperating scientists explore the geological, geophysical, hydrological, geochemical, and structural effects anticipated from the use of a large crystalline rock mass as a geologic repository for nuclear waste. This program has been sponsored by the Swedish Nuclear Power Utilities through the Swedish Nuclear Fuel Supply Company (SKBF), and the U.S. Department of Energy (DOE) through the Lawrence Berkeley Laboratory.

The principal investigators are L.B. Nilsson and O. Degerman for SKBF, and N.G.W. Cook, P.A. Witherspoon, and J.E. Gale for LBL. Other participants will appear as authors of the individual reports.

Previous technical reports in this series are listed below.

1. Swedish-American Cooperative Program on Radioactive Waste Storage in Mined Caverns by P.A. Witherspoon and O. Degerman. (LBL-7049, SAC-01).
2. Large Scale Permeability Test of the Granite in the Stripa Mine and Thermal Conductivity Test by Lars Lundstrom and Haken Stille. (LBL-7052, SAC-02).
3. The Mechanical Properties of the Stripa Granite by Graham Swan. (LBL-7074, SAC-03).
4. Stress Measurements in the Stripa Granite by Hans Carlsson. (LBL-7078, SAC-04).
5. Borehole Drilling and Related Activities at the Stripa Mine by P.J. Kurfurst, T. Hugo-Persson, and G. Rudolph. (LBL-7080, SAC-05).
6. A Pilot Heater Test in the Stripa Granite by Hans Carlsson. (LBL-7086, SAC-06).
7. An Analysis of Measured Values for the State of Stress in the Earth's Crust by Dennis B. Jamison and Neville G.W. Cook. (LBL-7071, SAC-07).
8. Mining Methods Used in the Underground Tunnels and Test Rooms at Stripa by B. Andersson and P.A. Halen. (LBL-7081, SAC-08).
9. Theoretical Temperature Fields for the Stripa Heater Project by T. Chan, Neville G.W. Cook, and C.F. Tsang. (LBL-7082, SAC-09).
10. Mechanical and Thermal Design Considerations for Radioactive Waste Repositories in Hard Rock. Part I: An Appraisal of Hard Rock for Potential Underground Repositories of Radioactive Waste by N.G.W. Cook; Part II: In Situ Heating Experiments in Hard Rock: Their Objectives and Design by N.G.W. Cook and P.A. Witherspoon. (LBL-7073, SAC-10).
11. Full-Scale and Time-Scale Heating Experiments at Stripa: Preliminary Results by N.G.W. Cook and M. Hood. (LBL-7072, SAC-11).
12. Geochemistry and Isotope Hydrology of Groundwaters in the Stripa Granite: Results and Preliminary Interpretation by P. Fritz, J.F. Barker, and J.E. Gale. (LBL-8285, SAC-12).
13. Electrical Heaters for Thermo-Mechanical Tests at the Stripa Mine by R.H. Burleigh, E.P. Binnall, A.O. DuBois, D.O. Norgren, and A.R. Ortiz. (LBL-7063, SAC-13).
14. Data Acquisition, Handling, and Display for the Heater Experiments at Stripa by Maurice B. McEvoy. (LBL-7063, SAC-14).
15. An Approach to the Fracture Hydrology at Stripa: Preliminary Results by J.E. Gale and P.A. Witherspoon. (LBL-7079, SAC-15).
16. Preliminary Report on Geophysical and Mechanical Borehole Measurements at Stripa by P. Nelson, B. Paulsson, R. Rachiele, L. Andersson, T. Schrauf, W. Hustrulid, O. Duran, and K.A. Magnussen. (LBL-8280, SAC-16).
17. Observations of a Potential Size-Effect in Experimental Determination of the Hydraulic Properties of Fractures by P.A. Witherspoon, C.H. Amick, J.E. Gale, and K. Iwai. (LBL-8571, SAC-17).
18. Rock Mass Characterization for Storage in Nucler Waste in Granite by P.A. Witherspoon, P. Nelson, T. Doe, R. Thorpe, B. Paulsson, J.E. Gale, and C. Forster. (LBL-8570, SAC-18).
19. Fracture Detection in Crystalline Rock Using Ultrasonic Shear Waves by K.H. Waters, S.P. Palmer, and W.F. Farrell. (LBL-7051, SAC-19).

20. Characterization of Discontinuities in the Stripa Granite--Time Scale Heater Experiment by R. Thorpe. (LBL-7083, SAC-20).

21. Geology and Fracture System at Stripa by A. Okliewicz, J.E. Gale, R. Thorpe, and B. Paulsson. (LBL-8907, SAC-21).

22. Calculated Thermally Induced Displacements and Stresses for Heater Experiements at Stripa by T. Chan and N.G.W. Cook. (LBL-7061, SAC-22).

23. Validity of Cubic Law for Fluid Flow in a Deformable Rock Fracture by P.A. Witherspoon, J. Wang, K. Iwai, and J.E. Gale. (LBL-9557, SAC-23).

24. Determination of In-Situ Thermal Properties of Stripa Granite from Temperature Measurements in the Full-Scale Heater Experiments: Methods and Primary Results by J. Jeffry, T. Chan, N.G.W. Cook and P.A. Witherspoon. (LBL-8424, SAC-24).

25. Instrumentation Evaluation, Calibration, and Installation for Heater Tests Simulating Nuclear Waste in Crystalline Rock, Sweden by T. Schrauf, H. Pratt, E. Simonson, W. Hustrulid, P. Nelson, A. DuBois, E. Binnall, and R. Haught. (LBL-8313, SAC-25)

26. Part I: Some Results From a Field Investigation of Thermo-Mechanical Loading of a Rock Mass When Heater Canisters are Emplaced in the Rock by M. Hood. Part II: The Application of Field Data from Heater Experiments Conducted at Stripa, Sweden for Repository Design by M. Hood, H. Carlsson, and P.H. Nelson. (LBL-9392, SAC-26).

27. Progress with Field Investigations at Stripa by P.A. Witherspoon, N.G.W. Cook, and J.E. Gale (LBL-10559, SAC-27).

28. A Laboratory Assessment of the Use of Borehole Pressure Transients to Measure the Permeability of Fractured Rock Masses by C.B. Forster and J.E. Gale. (LBL-8674, SAC-28).

29. Thermal and Thermomechanical Data for In Situ Heater Experiments at Stripa, Sweden by T. Chan, E. Binnall, P. Nelson, O. Wan, C. Weaver, K. Ang, J. Braley, and M. McEvoy. (LBL-11477, SAC-29).

30. The Effect of Radon Transport in Groundwater Upon Gamma Ray Borehole Logs by P.H. Nelson, R. Rachiele, and A. Smith. (LBL-11180, SAC-30).

31. Strength and Permeability Tests on Ultra-Large Stripa Granite Core by R. Thorpe, D.J. Watkins, W.E. Ralph, R. Hsu, and S. Flexser. (LBL-11203, SAC-31).

32. Ultrasonic and Acoustic Emission Results from the Stripa Heater Experiments. Part I: A Cross-Hole Investigation of a Rock Mass Subjected to Heating by B.N.P. Paulsson and M.S. King. Part II: Acoustic Emission Monitoring During Cool-Down of the Stripa Heater Experiment by R. Rachiele. (LBL-10975, SAC-32).

33. Numerical Modeling to Assess Possible Influence of the Mine Openings on Far-Field In Situ Stress Measurements at Stripa by T. Chan, V. Guvanasen, and N. Littlestone (LBL-12469, SAC-33).

34. A Field Assessment of the Use of Borehole Pressure Transients to Measure the Permeability of Fractured Rock Masses by C.B. Forster and J.E. Gale. (LBL-11829, SAC-34).

35. Water Inflow into Boreholes During the Stripa Experiments by P.H. Nelson, R. Rachiele, J.S. Remer and H.S. Carlsson (LBL-12547, SAC-35).

36. Petrology and Radiogeology of the Stripa Pluton by H. Wollenberg, S. Flexser, and L. Andersson. (LBL-11654, SAC-36).

37. Geohydrological Data from the Macopermeability Experiment at Stripa, Sweden by C.R. Wilson, J.C.S. Long, R.M. Galbraith, K. Karasaki, H.K. Endo, A.O. DuBois, M.J. McPherson, and G. Ramqvist. (LBL-12520, SAC-37).

TABLE OF CONTENTS

LIST OF FIGURES

LIST OF TABLES

ABSTRACT

Fractures, faults, and dikes have been mapped in great detail on drift surfaces and in core to characterize the quartz monzonite rock mass surrounding the two full-scale heater experiments at Stripa. From the presence of pegmatite and quartz dikes in the full-scale drift, several well-defined N-S faults were determined to have produced offsets of 1 to 6 meters, and an inferred E-W fault is assigned a comparable throw. Several of the N-S faults and several dikes cut through the H9 experimental area, but none are present in the immediate H10 area.

Chlorite, epidote, and calcite were commonly identified on fracture surfaces, with chlorite present in 60 to 70% of all fractures and calcite being the least common. Because all closed as well as open fractures in retrieved core were recorded, the observed ratios of open/closed fractures permit a crude assessment of relative fracture strength among the three mineralization types. Only 10% of epidote-coated fractures were found open, whereas some 70% of the calcite-coated fractures were open. Hence the core data rank epidote, chlorite, and calcite in order of descending relative strength. The open-to-closed ratios also permit some limited observations on the effects of drilling and coring techniques upon core breakage.

The degree of fracturing in the full-scale drift is intense. Average fracture spacing is 11 cm, with considerable local variation. Zones of intense fracturing on a one-meter scale are common in the H10 area, but there is no evidence for structural control. In the H9 area, however, zones of intense fracturing close to the heater hole may be related to the north-south faults present.

The data base resulting from fracture mapping and core logging in the full-scale drift is available in several forms: as a computer-based listing of individual fractures, taken from the original field logging forms; on maps of the drift floor and walls; on eight vertical radial cross-sections through each of the main heater boreholes; on 59 stereoplots of fracture plane poles, categorized by hole orientation, hole location, fracture mineral type, and open or closed status; and in simplified form on a 1:20 scale plexiglass model. This compilation of detailed fracture data is available for interpreting results from several experiments conducted in and near the full-scale drift, including the in situ determination of state-of-stress, cross-hole measurements of ultrasonic velocity and attenuation, and rock displacement induced by the full-scale heater experiments.

I. INTRODUCTION

The Swedish-U.S. Cooperative Program to investigate radioactive waste storage in mined caverns has been conducted at the Stripa mine in central Sweden (Fig. 1.1) since June 1977. The Stripa mine is situated in the Bergslagen mining district, and the mining history of the area and of the Stripa mine is centuries old. Iron ore production at the mine ceased in early 1977. Since then the mine has been operated as an underground experimental site by the Swedish Nuclear Fuel Safety Program (Kärnbränslesäkerhet--KBS) under the auspices of its parent organization, the Swedish Nuclear Fuel Supply Company (Svensk Kärnbränsleförsörjning--SKBF). The program has several experimental tasks, which are described by Witherspoon, Cook, and Gale (1980).

To achieve a better understanding of the behavior of the rock mass under severe thermal stress and of groundwater flow through the fractured mass, a comprehensive study of the geology and geological discontinuities has been carried out in the underground test facilities at Stripa (Fig. 1.2). The general geological and hydrogeological studies of the Stripa quartz monzonite were done by the Swedish Geological Survey (SGU) and were published by Olkiewicz et al. (1978). A more detailed investigation of the geology and fracture systems of the Stripa granite was jointly conducted by Swedish, U.S., and Canadian scientists and is documented by Olkiewicz et al. (1979). A very detailed study of the rock discontinuities in the time-scaled, full-scale and extensometer drifts (Fig. 1.2) was carried out by scientists from Lawrence Berkeley Laboratory (LBL). The results from the time-scaled drift were published by Thorpe (1979), and the results of the study in the full-scale and extensometer drifts are presented in this report.

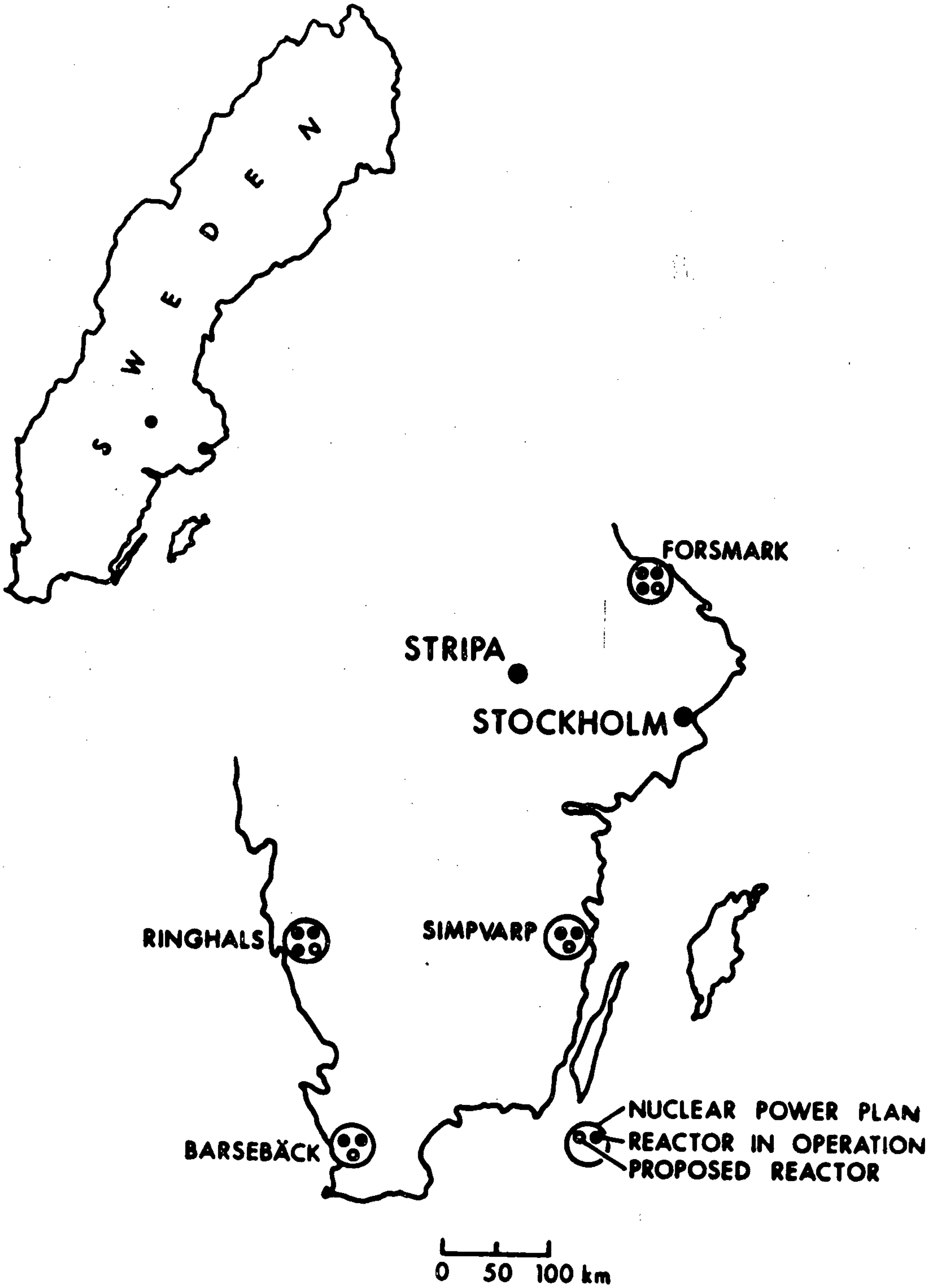

XBL 785-8717

Fig. 1.1. Location of the Stripa mine, Sweden.

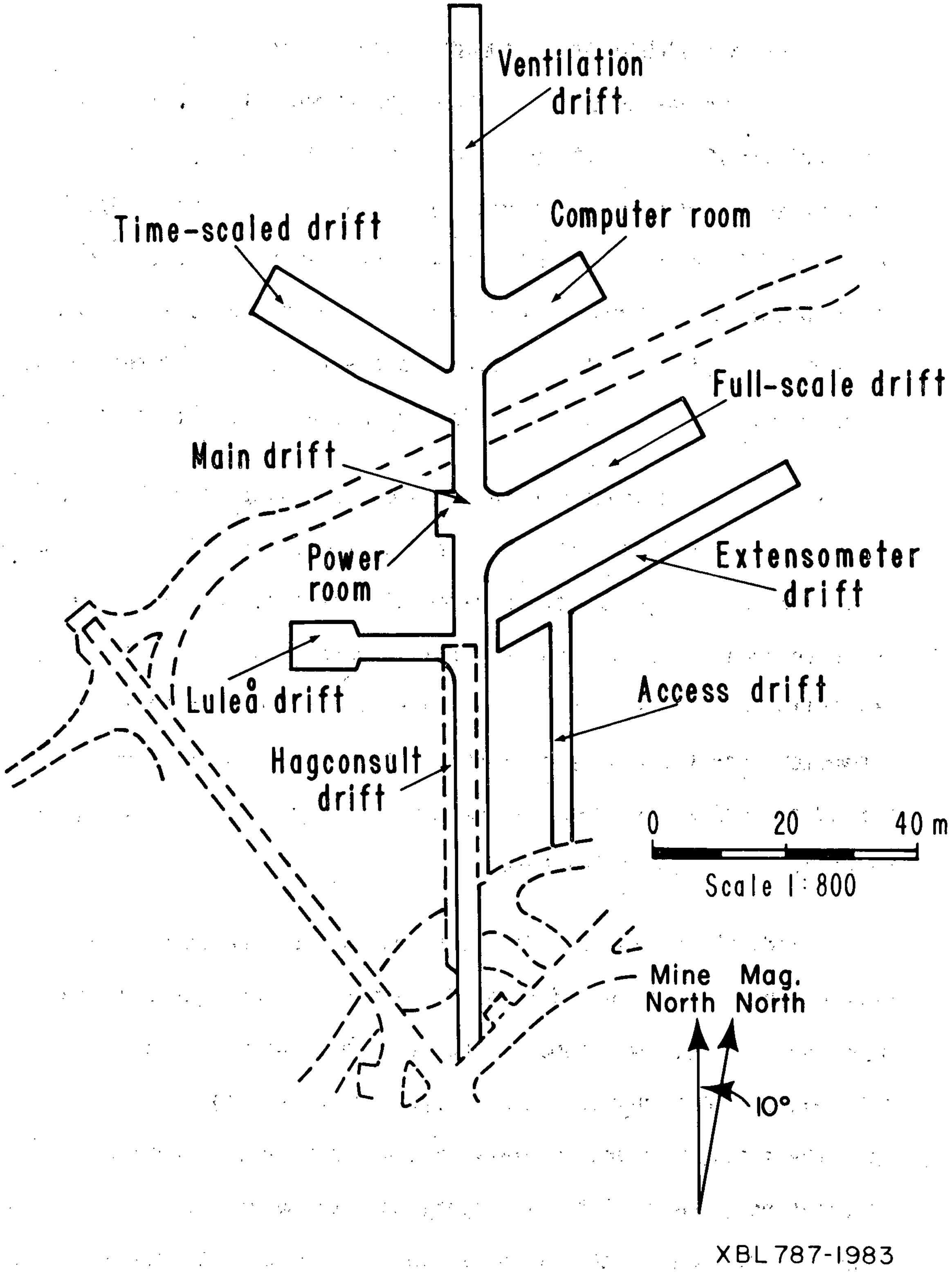

Fig. 1.2. Plan map of the underground site.

The common objective of the dual studies in the full-scale and time-scaled drifts was to define and characterize the location, orientation, and mineralogy of major and minor discontinuities in the granitic rock around the heater experiment areas. The data base for the full-scale drift differs from that for the time-scaled drift in several respects. First, the amount of information is greater; while 32 vertical boreholes were drilled in the time-scaled drift, a total of 102 boreholes were drilled for the full-scale experiments. Kurfurst et al. (1978) describe the drilling in detail.

Second, as indicated in the plan map and section of Figs. 1.3 and 1.4, horizontal as well as vertical holes penetrate the full-scale experimental areas: 38 horizontal or sub-horizontal boreholes, drilled from the wall of the extensometer drift, and 64 vertical boreholes drilled from the floor of the full-scale drift. The higher density of boreholes in the full-scale experiment ensures a larger amount of fracture data, and the use of data from horizontal holes also reduces the inherent tendency of vertical boreholes to oversample horizontal fractures.

Third, the full-scale data base was greatly enhanced by "relogging" much of the core to include closed fractures as well as fractures that were open when the core was removed from the core barrel. The closed fracture information, when summed with the open fracture logs, makes it possible to plot the total fracture population as a function of borehole size, borehole orientation, mineral infilling type, core diameter, etc. In addition, the degree of "openness" of fractures can be examined with respect to these same parameters.

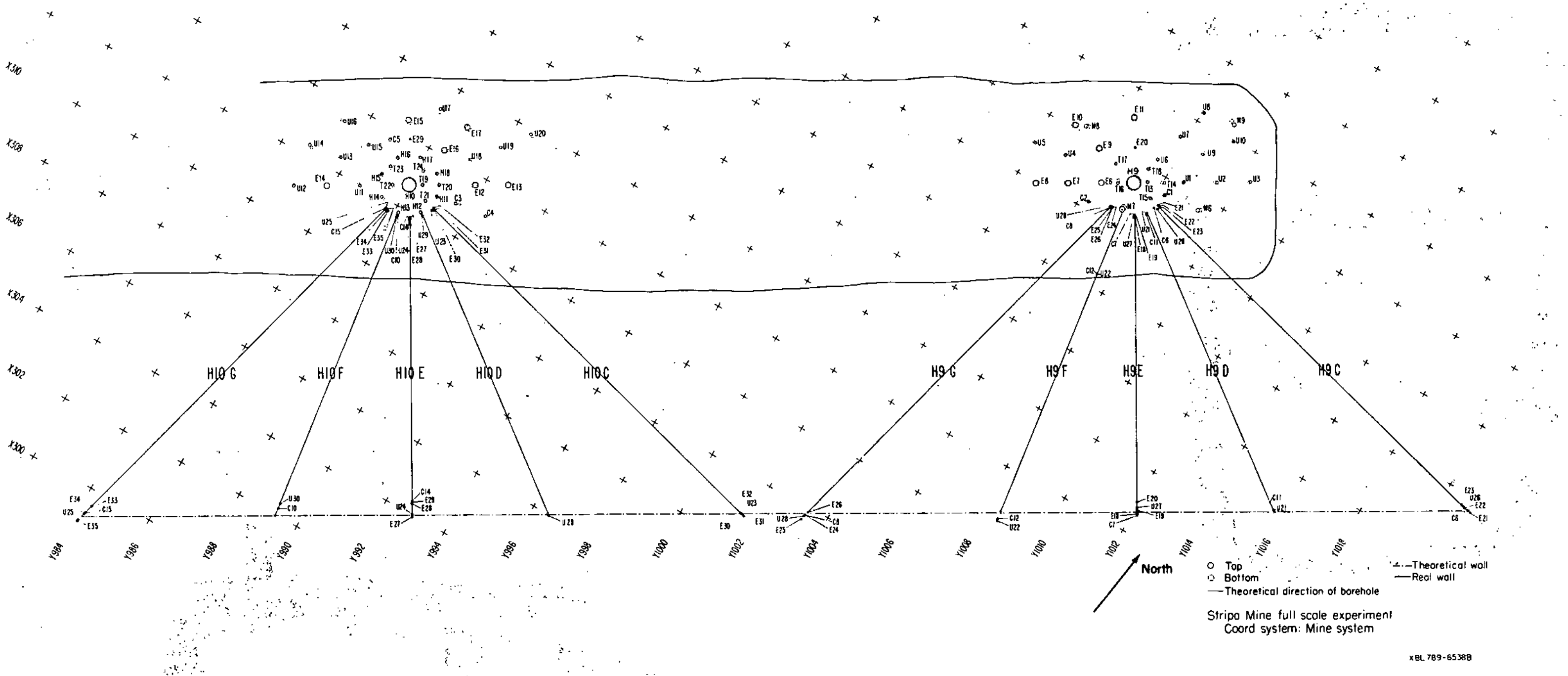

Fig. 1.3. Borehole layout from full scale and extensometer drifts. Also shown is mine coordinate system and labelling of vertical sections.

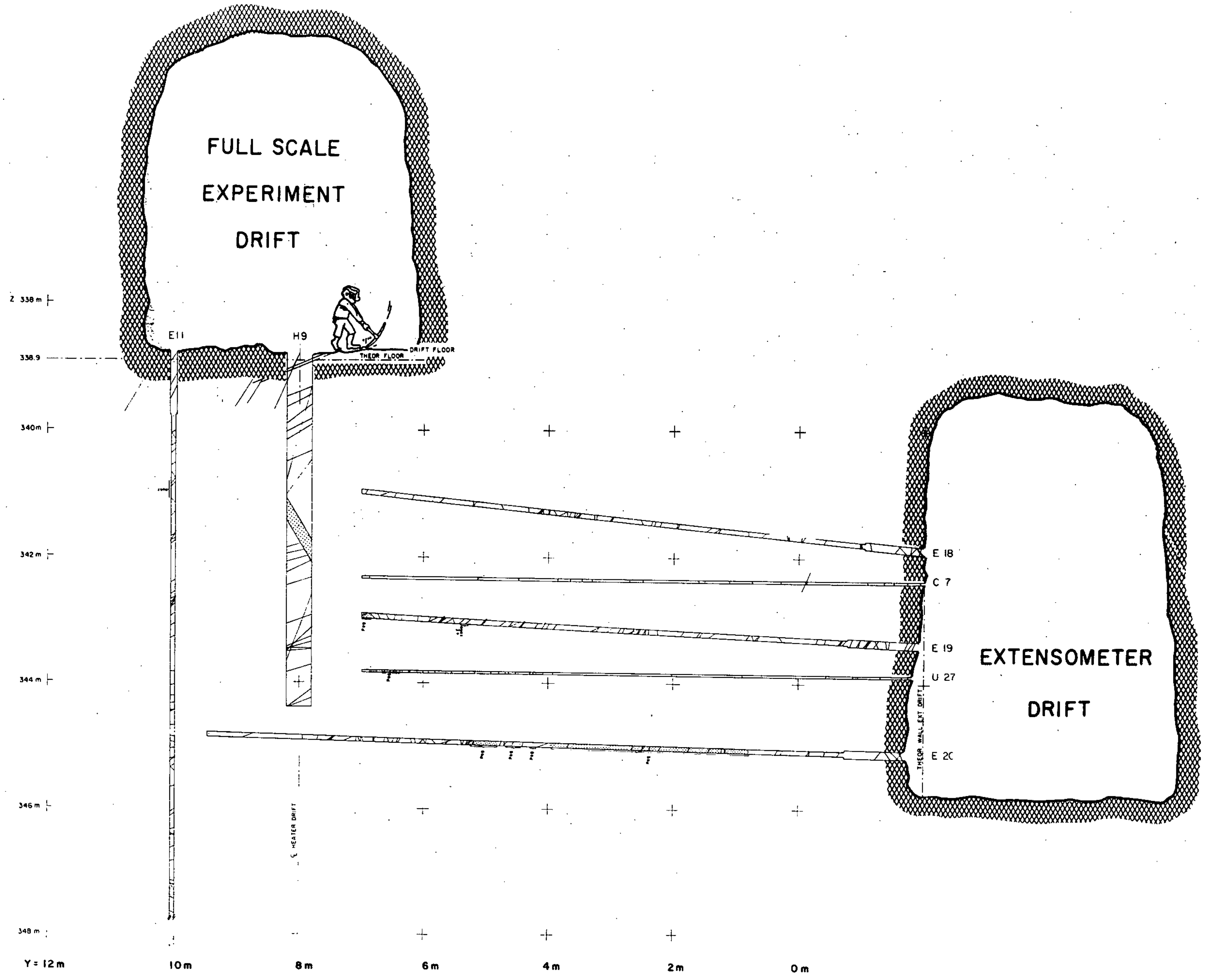

XBL 793-851

Fig. 1.4. Cross-section of full scale and extensometer drifts at the H9 heater experiment.

All planar discontinuities that could be mapped or recognized in core, including dikes, faults, shear zones, and fractures with no evidence of displacement are discussed in this report. The only dikes described in this report are the pegmatite and quartz veins which intersect the heater experiment areas, although others have been recognized within the quartz monzonite.

The H9 and H10 experimental areas* in the full-scale drift are almost identical as far as the geological data base is concerned, but the H9 fracture system has been interpreted in far more detail. The presence of quartz and pegmatite dike "markers" in the H9 area greatly facilitated tracing the offsets caused by several epidote-coated faults that cut through the area, and the potential influence of such through-going features on the thermomechanical experiments required detailed documentation.

Another reason the H9 area received such close attention is that one of the authors is conducting cross-hole ultrasonic experiments in four of the H9 boreholes (Paulsson and King, 1980). One ultrasonic experiment was carried out simultaneously with the heater experiment to map time-dependent changes; other experiments have been carried out to detect and map fractures between boreholes using ultrasonic techniques. To evaluate the feasibility of fracture characterization with ultrasonic methods, the geology had to be examined in the greatest detail possible.

---

*Throughout this report, the expressions "H9 area" and "H10 area" refer to the volume of rock intersected by boreholes for each experiment and the corresponding drift walls and floors which have been mapped. The plane separating the two areas is the plane normal to the centerline in the full-scale drift at a point halfway between the H9 and H10 heater holes.

The field stage of this study, described in Section 3, involved mainly the collection of fracture maps and photomosaics of the drift walls and floors, along with the logs of fractures observed in core. After calculation of true fracture orientation, two approaches were used to interpret the data. Using cross sections and a three-dimensional model, the fracture system is reconstructed as fully as possible and presented in a series of cross sections and plan maps in Section 4. To complete the analysis, an extensive set of stereograms were compiled for the various borehole and mineral infilling subsets. The resulting statistics and pole plots form the basis for the comparisons and conclusions given in Section 5. A final summary and a comparison with the results of the time-scaled drift fracture study are presented in Section 6.

2. GEOLOGY OF THE STRIPA MINE

2.1 Surface Geology

A number of reports have been written on the surface geology in the area of the Stripa mine. The most pertinent to date is that by Geijer and Magnusson (1973). Koark and Lundström (1979) have published a geologic map of and area called the Lindesberg southwest quadrangle, that includes Stripa. The surface geology around the mine is shown in Fig. 2.1. A recent report by Wollenberg et al. (1980) describes the results of petrological and radioelement studies on rock from the Stripa pluton and adjoining areas.

All bedrock units of the region are of late Precambrian age, the oldest being leptite. Leptite is a general term for predominantly high-grade metamorphic volcanic rock, high in SiO_2 and grain size of 0.5 - 0.05 mm. Some of the leptite has a sedimentary origin, as evidenced by rippled marks in the roof of the main drift leading to the experiment area. The strongly banded iron ore, predominantly interbedded quartz and hematite, is situated in the leptite. The distinct banding, together with its association with the leptite, suggests that the ore is of sedimentary origin. The leptite is in contact with apparently younger intrusive rocks. Both the supra-crustal and the intrusive rocks show signs of at least two folding phases. Stripa is situated within the NNE-trending Vikern syncline that was formed by an E-W compression during the first main folding phase. The second phase was a N-S compression that refolded the older one. The granitic rock at Stripa, predominantly quartz monzonite, intruded the leptite near the end of this folding period. The age of the quartz monzonite is reported as 1.69×10^9 years (Wollenberg et al., 1980). The Stripa quartz monzonite is classified as serogenic. It differs from the pre- or synorogenic granitic rocks because

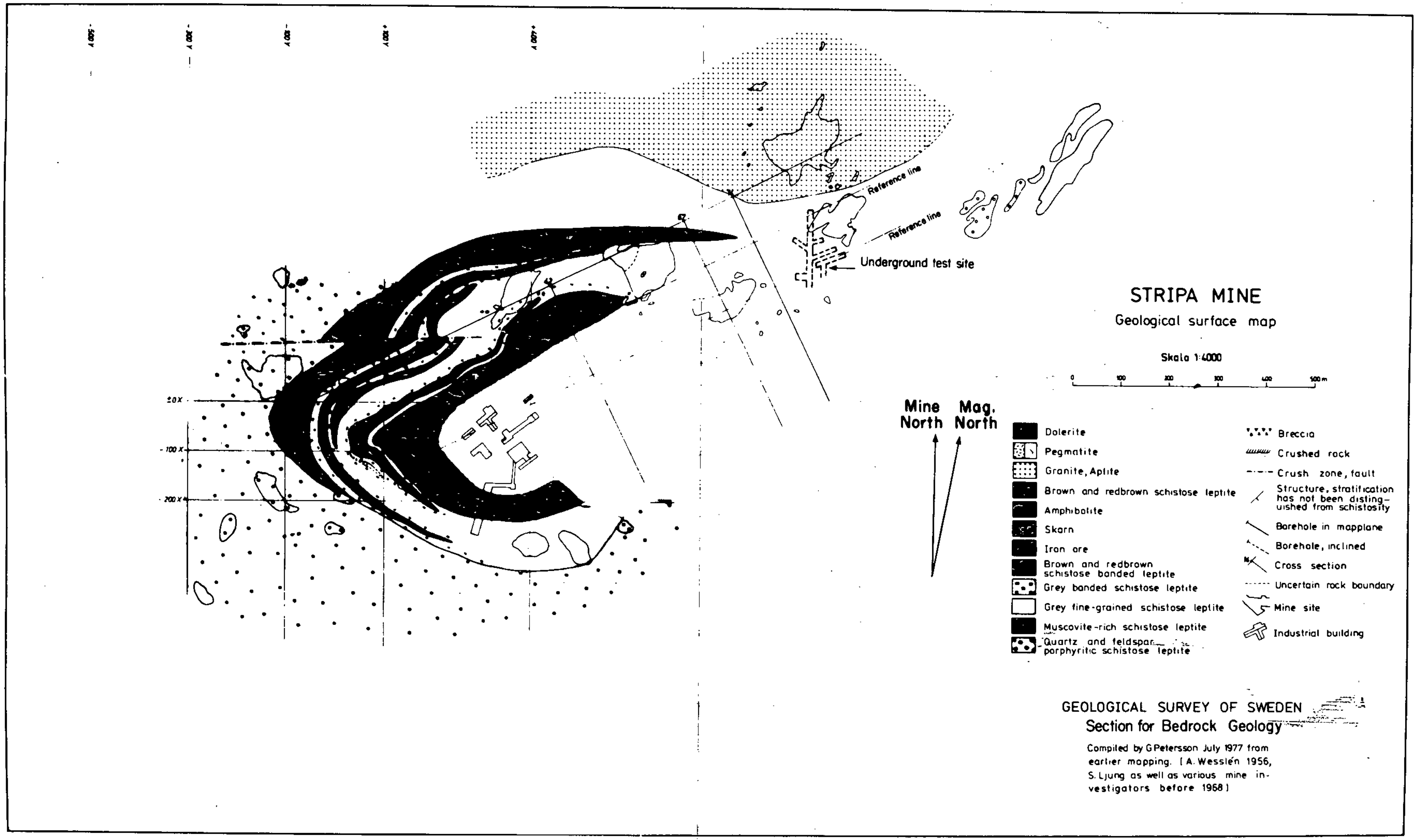

XBL 799-11293

Fig. 2.1. Geological surface map around the Stripa mine.

of its apparent homogeneity and relative lack of foliation. The rock mass at Stripa also contains pegmatites and aplites; the former occurs on many cross sections of the full-scale drift.

2.2 Mine Geology

The geology at the Stripa mine was described by Olkiewicz et al. (1978) and is based on material in the mine archives, including P. Geijer's monograph on Stripa (1938), A. Wesslen's mapping of the mine area (1956) and S. Ljung's mapping of the mine workings (1966). The ore in Stripa is mainly a quartz banded hematite with occasional occurrences of magnetic, iron-bearing chert. The ore, which has an iron content of 51% (there is also some phosphorus), is stratiform with the leptite. The oldest rock type is the series of grey leptites, which is approximately 2,000 million years old. The leptite above the main ore is layered, while the leptite below is not. Many diabase dikes in the mine are older than the quartz monzonite in the test area. The quartz monzonite is associated with a series of pegmatite and aplite dikes. The youngest dikes are the steeply dipping diabase dikes with a NNE strike. The test area is dominated by a reddish, medium-grained massive quartz monzonite. The grain size varies but averages 3 mm. The composition of one sample of the reddish quartz monzonite, determined by point counting (Wollenberg et al., 1980) is:

Mineral	Volume %
Quartz	37.1
Partly sericitised plagioclase	32.0
Microcline	22.2
Muscovite	7.4
Chlorite	1.3

Accessory minerals: opaques, carbonate, zircon

The quartz monzonite in the experiment area is less deformed than that near the ventilation shaft or in the northern part of the lower drift. In places, the rock is strongly fractured and brecciated. Wollenberg et al. (1980) emphasize that the high abundance of fractures extends down to the grain-size scale, stating that "fractures ranging from well under a millimeter to several centimeters or more in width, as well as wider ones of brecciation, are readily visible in hand sample, but only in thin section does the full extent of fracturing and brecciation become apparent. The great majority of fractures have been completely sealed, but in some cases fine openings can be seen in thin section....Even in relatively unfractured samples, fine discontinuous cracks within primary grains or along grain boundaries are very common."

Although the Stripa quartz monzonite has been severely disrupted mechanically, displaying abundant fracturing and occasional faulting, it is evident that most, if not all, of the discontinuities have been filled with secondary minerals. Evidence for this is also plentiful on all observational scales; in fact, the fractures described in this report and that by Thorpe (1979) are distinguished by the type of mineral infilling, as identified in mapping or inspection of core. Wollenberg et al. (1980) describe fracture mineralogy based on thin section observations and note that stringers of sericite and chlorite, quartz, and occasionally feldspars occur on the finest scale, even filling cracks in primary grains and along grain boundaries.

The majority of the fractures mapped are steeply dipping towards the north except in the northern part of the drift leading up to the experiment area, where many south-dipping fractures have been found. Two strike directions have been discovered: one evenly distributed from north to east, and one more tightly confined between NW and W (Olkiewicz et al., 1979). Most of the fractures are filled with chlorite. Epidote also occurs as a fracture-filling mineral, and is especially abundant in the end of the full-scale drift. Quartz and calcite are common fracture minerals in the experiment area.

Despite the pervasive fracturing, laboratory and field measurements have shown that in many respects the rock does not differ much from other competent igneous rocks. Laboratory determinations of porosity are around 0.5% (Paulsson and King, 1980; Nelson et al., 1979). Both field and laboratory measurements of compressional wave velocity at ultrasonic frequencies yield values of about 5,500 m/s. And at ambient pressure, laboratory determinations of static mechanical moduli also are comparable to values obtained on competent samples (Swan, 1978).

3. SOURCES OF DATA

To characterize a complicated fracture system in three dimensions, a comprehensive data set is required. Data were collected in two ways: first, by photographing the drift walls and floors to get a permanent record of the clean rock surfaces, followed by mapping the floors and walls in detail; and second by logging core recovered from the 64 horizontal and 38 vertical holes to record rock type, fracture location and orientation, condition and characteristics of the fracture surface, mineral infilling, and percent core recovery.

3.1 Floor and Wall Maps

The procedures used for mapping floors, walls, and roofs in the full-scale (FM) and extensometer (EX) drifts were those described by Knill and Jones (1965) and Kendorski and Mahtab (1976). Mapping was undertaken immediately after the drifts were excavated. The first step was a thorough cleaning and washing of the walls and floors of both drifts. A 1 x 1 m square base grid was painted on the floor in the full-scale drift, with the centerline of the drift as one axis of the grid. This made it possible to tie the local coordinate system in the FS drift with the mine's coordinate system.

The next step was to take a series of black-and-white overlapping photographs. The prints were sized to match a 1:20 scale and glued together to form a photomosaic of the drift floor. Practically all fractures longer than 0.3 m on the floor were mapped. With the help of a 1 x 1 m wooden frame, the tracings of floor fractures were transferred to a preliminary map. The traces of the fractures represent the average strike of the fractures found on the drift floor. Pegmatites were mapped, with special attention given to their faulting. While the type of fracture-filling minerals and the dip and the strike were recorded for all prominent fractures, only the dip direction was recorded for minor fractures. The topography of the floor was also surveyed at the grid intersection points and at every 0.5 m along all lines in the H9 and H10 areas.

The actual mapping of the drift floor was done for each square of the base grid, starting at the face of the drift and progressing toward its entrance. The location of each fracture was visually estimated within each square with an accuracy of ± 5.0 cm. All features were then sketched onto a 1:20 base map, which showed the intersections of the fractures, veins, and dikes with the drift surface. Changes in topography of the drift floor tended to be reflected in the traces of gently dipping fractures. However, nearly horizontal fractures proved to be difficult to map because of the extent of their exposed surfaces. This was especially evident in the H10 heater area, which has an apparent low fracture density at the surface. This is caused by the sub-horizontal, chlorite-filled fractures that are exposed in this part of the full-scale drift.

The side walls of the full-scale drift were mapped, and the fractures that were continuous across the width of the drift were projected onto a vertical plane through the centerline of the drift. The projections from the H9 and H10 areas are shown at the top of Figs. 4.4A, and 4.5A respectively. The fractures and the dikes found on the walls were assumed to be planar, so they were projected directly onto the centerline plot. The obvious features, such as pegmatites and quartz veins, were located and a line drawn to connect two points of a fracture at equal elevations on opposite drift walls. The intersection point with the centerline of the drift was then surveyed and plotted onto a field map. The success of this method was proved by very good correlation of these features above and below the drift floor. The pegmatite dikes, the quartz veins, and the wall fractures were also projected onto the centerline of the map because these features were continuous and considered important for fracture reconstruction.

The northwestern wall of the extensometer drift, which was nearest the experiment in the FS drift, was mapped by both visual inspection and photomosaic. This combination proved to be fast and convenient, as the surface was large and close inspection difficult because much of the wall surface was above eye level. The criteria for mapping fractures on the EX-drift wall were that they be continuous and well-defined over several meters. The mapped features, together with information on fracture-filling minerals, matrix grain size, color strike, and dip, were then drawn on a 1:20 scale field map.

The resulting floor maps, wall maps, and wall projections are presented and discussed in Section 4.

3.2 Drilling Techniques

For the H9 (3.5 kW) heater experiment, 49 horizontal and vertical boreholes of various diameters were drilled from the full-scale and extensometer drifts, yielding a total of 479 m of core. For the H10 (5.0 kW) experiment, 53 horizontal and vertical boreholes were drilled, yielding 471 m of core. The total meterage is tabulated by hole diameter and experiment location in Table 3.1. Borehole nomenclature is likewise summarized in Table 3.2. Kurfurst et al. (1978) describe the drilling procedures and survey results in detail.

Table 3.1. Summary of drilling meterage for the full-scale drift heater experiments.

Borehole Diameter (mm)	H9 Vertical	H9 Horizontal	H10 Vertical	H10 Horizontal
406	5.5	-	5.5	-
76	75.48	108.01	74.84	107.32
56	40.58	-	-	-
46	-	11.22	-	11.04
38	132.35	105.84	187.42	85.71
All	253.91	225.07	267.76	204.07

Table 3.2. Boreholes listed by diameter and location. Holes C9 and C13 were not drilled. A total of 102 boreholes were drilled and cored for the full-scale heater experiments.

Borehole Diameter (mm)	H9 Vert.	H9 Hor.	H10 Vert.	H10 Hor.	Total number
406	H9	-	H10	-	2
76	E6-E11	E18-E26	E12-E17, M10	E27-E35	31
56	M6-M9	-	-	-	4
46	-	N3	-	N4	2
38	C1-C2 U1-U10 T13-T18	C6-C8 C11-C12 U21-U22 U26-U28	C3-C5 U11-U20 T19-T24 H11-H18	C10 C14-C15 U23-U25 U29-U30	63
Total number	29	20	35	18	102

During initial logging of the recovered core, it was noted that the frequency of open fractures tended to vary with core size, drilling method, and drill rig used. For this reason, the drilling techniques are summarized in Table 3.3, which shows the drill rig and core barrel types used for each hole size and location. The Toram rig was used for the 76 mm and 406 mm holes, while the Diamec rig was used for holes of 56 mm diameter and less. The small diameter holes were cored with a double tube core barrel, whereas a triple tube was used in coring most of the 76 mm holes. The vertical 76 mm holes in the H10 area were drilled with a double tube core barrel and hence those open fracture statistics will differ from other 76 mm borehole results.

3.3 Core Logs

Continuous core samples were recovered from 64 vertical and 38 horizontal instrumentation, monitoring, and heater boreholes in the full-scale and extensometer drifts. The length of the boreholes varied from 5 to 15 m with an average length of about 10 m. All core from boreholes 56 mm or greater in diameter (E, M, and H boreholes) was oriented with respect to the drift centerline, but core samples from the 38 and 46 mm boreholes (T, U, C, H11-H18, and N boreholes) were not oriented.

3.3.1 Core Orientation Procedure

All oriented core from the larger diameter holes (56 mm and greater) was reassembled and logged immediately after drilling to ensure proper reconstruction of the orientation. Hence, the first task upon recovery of the core barrel was to check the orientation mark to ensure that it matched the mark on the previous uptake. Next, a line was drawn along the length of the core, matching the position of the orientation mark ($\beta = 0$). For the

Table 3.3. Summary of drilling techniques used for different boreholes in full-scale and extensometer drifts. The core diameter in the second column is nominal, no better than ± 1 mm. Core from the 76 mm holes depended on core barrel type, the triple tube barrel yielding 52 mm core.

Borehole Diameter (mm)	Core Diameter (mm)	H9 Vert.	H9 Hor.	H10 Vert.	H10 Hor.
406	--	sT *	-	sT	-
76	52, 62	tT	tT	dT	tT
56	45	dD	-	-	-
46	32	-	dD	-	dD
38	22	dD	dD	dD	dD

sT = Single tube core barrel, Toram drill rig
dT = Double tube core barrel, Toram drill rig
tT = Triple tube core barrel, Toram drill rig
dD = Double tube core barrel, Diamec 250 drill rig

*The first 3 m (out of 5.5) was drilled with the XF 60/90 H drill rig.

vertical holes, this line corresponds to an imaginary line on the side of the borehole wall closest to the opening of the full-scale drift (see Fig. 3.1). The orientation for $\beta = 0$ was surveyed before the drilling of the borehole started, and an orientation mark was cut with a grinder into the rock surface. After each uptake, an orientation device was lowered into the borehole, and the stub on the bottom, which would be the upper end of the next core run, was marked in the same direction as the mark on the floor surface. For the horizontal and sub-horizontal holes in the extensometer drift, the reference line $\beta = 0$ was chosen to be downward; marking of the core was done simply by inserting a rod with a hard metal tip in the borehole and marking the core stub before the drilling started again. This method was generally quite accurate, as indicated by the excellent matching of orientation marks for successive uptakes.

With the reference line established, two angles suffice to define the orientation of a fracture plane with respect to the borehole. The angle α, which ranges between 0 and 90 degrees, is the acute angle between the fracture plane and the central axis of the core or borehole. The angle β is the azimuth of the apparent dip as measured clockwise from the reference line while looking in the drilling direction. The angle β ranges from 0 to 360 degrees because it is measured from the reference line to the lowermost intercept of the fracture plane and the borehole wall.

3.3.2 Core Logging Procedures

After orientation was established, the core was logged at the drill site, as soon as possible after drilling and in accordance with procedures described by Kurfurst et al. (1978) and Thorpe (1979). The geologist took

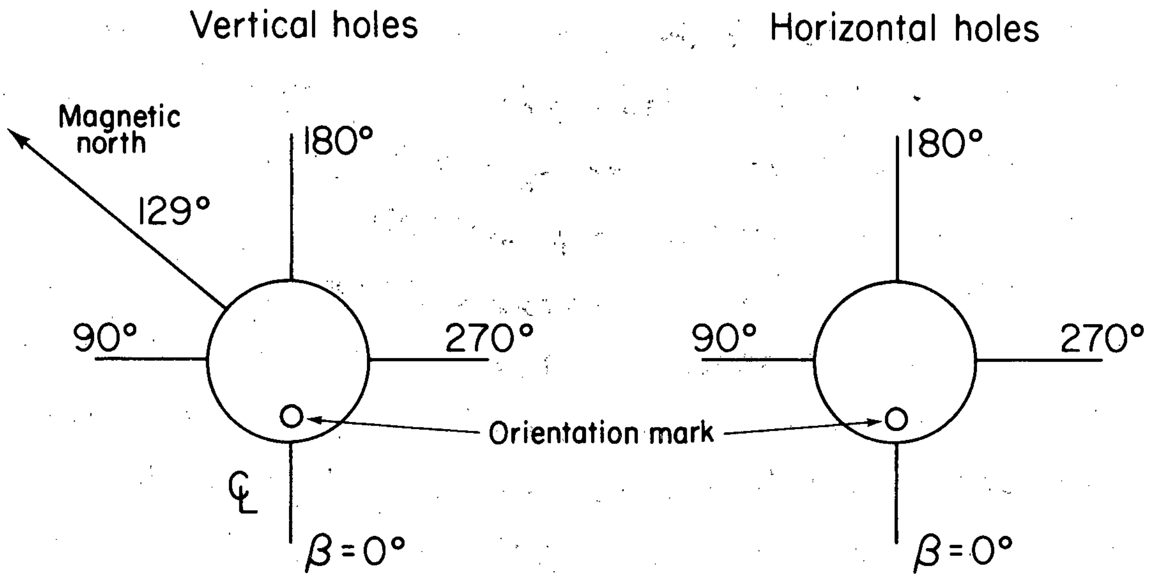

XBL 811-2556

Fig. 3.1. Orientation conventions for vertical and horizontal holes in full scale drift. For vertical holes, the zero angle is on drift centerline and nearest the drift opening. For horizontal holes, the zero angle is on the downward edge of the perimeter. In both cases the view is from the drift looking towards the collar.

core directly from the barrel for examination, to avoid disturbing the core by excess handling and transportation to the surface. For ready reference, the logging specifications and a sample logging form used in the field are included in Appendix A. These field logs of fracture location and characteristics formed an important part of the data base presented in this report.

Only open fractures were logged at the drill site, and, as already mentioned, it was soon noticed that the frequency of open fractures varied with drilling procedures. To correct this sampling problem and to obtain a more complete record of the total population of planar and sub-planar features intersected by the borehole, the core was brought up to the surface and relogged. This time, closed fractures were recorded, following the procedures used for open fracture logging. The second logging increased the number of fractures recorded in the H9 area from 1,055 to 3,385, markedly changing some of the fracture population statistics, as will be discussed in Section 5.

Table 3.4 summarizes the logging procedures used in the full-scale drift. As can be seen, all of the H9 core was relogged. For the H10 area, only the 76 mm core was relogged, and as the table indicates, only the vertical holes were entirely relogged. To save time, only the lowermost 3 m of the horizontal 76 mm holes in the H10 area were relogged; that is, the 3 m from each hole lying closest to the H10 heater hole.

In this report, the term "open fracture" simply refers to that class of fractures which were open when the core was retrieved and first logged; "closed fractures" refers to a fracture intersected in a core interval which was intact when retrieved from the core barrel.

Table 3.4. Summary of fracture logging procedures in the full-scale drift and extensometer drift boreholes. Core was logged in two passes. Open fractures were logged at the drill site while closed fractures were recorded during relogging.

Borehole Diameter (mm)	Oriented core	H9 Vert.	H9 Hor.	H10 Vert.	H10 Hor.
406	Y	OC	-	OC	-
76	Y	OC	OC	OC	OC, C
56	Y	OC	-	-	-
46	N	-	O	-	O
38	N	OC	O	O	O

O = Open fractures logged
C = Closed fractures logged
Y = Core oriented
N = Core not oriented

3.3.3 Mineral identification

When the core was logged, a number of different fracture infilling minerals could be distinguished visually. Chlorite, epidote, and calcite (one of these three was always present) were distinguished as the three dominant minerals coating the fracture surfaces. Calcite can be identified visually, but epidote and chlorite are more reliably distinguished by a scratch test with hardened steel; it scratches chlorite but not epidote. Although identification in hand specimen is always subject to error, the petrological study by Wollenberg et al. (1980) has in general confirmed the field identification of these minerals:

> "In megascopic appearance, the following generalizations are useful, though not foolproof: dark green or black fractures are usually dominated by chlorite; white or near-white fractures by quartz and/or carbonate. Light green fractures are more ambiguous, as they may be a mixture of the above types, or they may be filled mainly with sericite (fine fractures, particularly), or with epidote, or, in wide brecciated zones, with a clay-rich fault gouge."

Throughout this report the terms chlorite, epidote, and calcite refer to the visual identification of these minerals in core.

3.3.4 Core Log Availability

The core log data, an example of which is included in Appendix A of this report, have been entered into two computer files at LBL. The format and coding are similar to that given in Appendix A of Thorpe (1979). To access the files, use the control commands

```
GETTAPE,TAPE1=FULLSCALE/CLOSEFRAC/DATA,11883
```

and

```
GETTAPE,TAPE1=FULLSCALE/OPENFRAC/DATA,11883.
```

4. CHARACTERIZATION OF DISCONTINUITIES

4.1 Introduction

The field observations and the resulting interpreted fracture network are presented in this section in a series of maps and sections. The detailed floor map of the full-scale drift (upper portion of Fig. 4.1), the extensometer drift wall map (Fig. 4.2) and the map of the full-scale drift wall (upper portion of Fig. 4.4A) are all based directly on field mapping, described in Section 3.1. In addition to these three maps, two interpretive maps are also shown. From the detailed floor map, floor photomosaic, and direct observation, the major prominent continuous fractures and fracture zones were identified and plotted on the simplified floor map shown in the lower part of Fig. 4.1. A plan map through the H9 heater midplane, shown in Fig. 4.3, was constructed by projecting fractures and dikes encountered in vertical and horizontal boreholes onto the horizontal surface at the midplane elevation. No comparable map was completed for the H10 midplane, although some data necessary for its construction have been compiled.

Eight vertical cross sections displaying fracture intercepts and interpreted continuous fractures are shown in Fig. 4.4 for the H9 area. A complementary set of eight sections around the H10 area is shown in Fig. 4.5. To intersect the largest possible number of boreholes, the cross sections (originally drawn at a 1:20 scale) were drawn along the planes of symmetry in the H9 and H10 areas, as shown on the floor map of Fig. 4.1. Table 4.1 gives the strike direction and orientation of the cross sections.

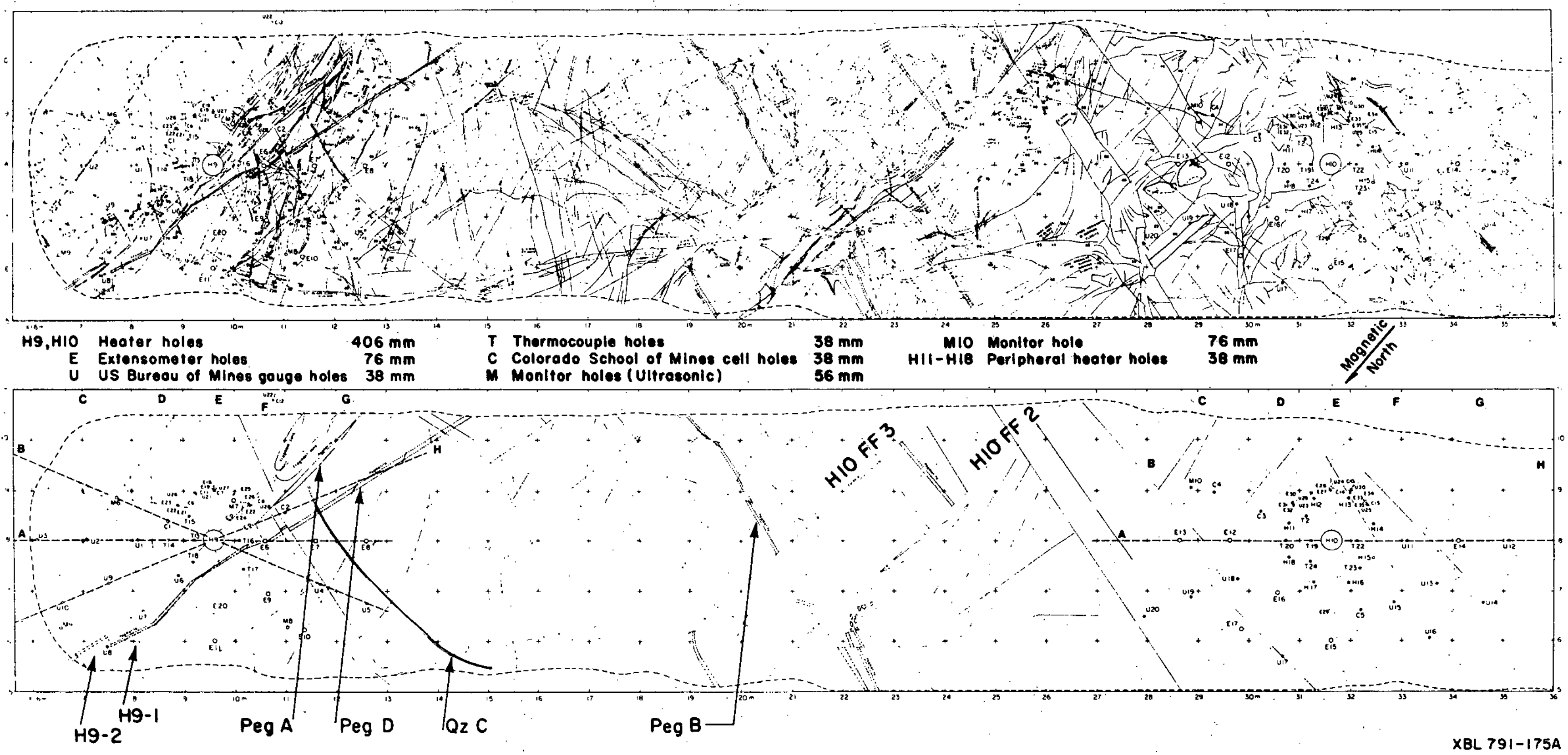

XBL 791-175A

Fig. 4.1. Detailed and simplified fracture maps of the floor in full scale drift. Entries on the detailed map (upper) include dip angle of fractures and notes on mineralogy and unusual features. Hachured areas represent exposures of horizontal fracture surfaces. Simplified map (lower) shows major dikes, faults, and fractures, some with identification labels. Large letters A through H are labels for vertical cross-sections. The one-meter grid used for mapping is shown on both maps.

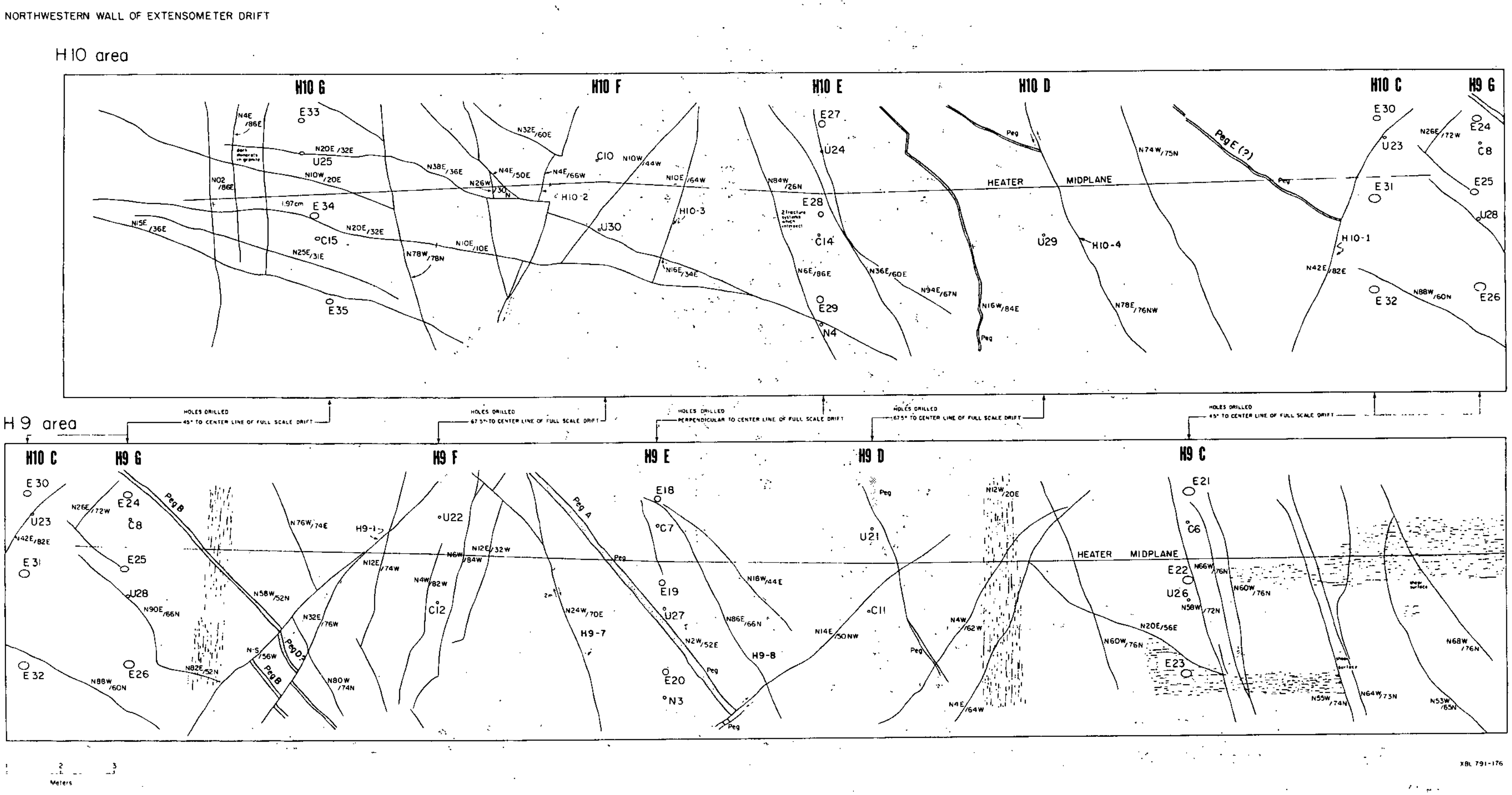

Fig. 4.2. Simplified fracture map of the northwest wall of the extensometer drift. Strike/dip are true measured values, not apparent. Large letters C through F designate intersection of vertical cross-sections coincident with horizontal boreholes, with the wall of the drift. Some dikes and faults are labeled for discussion purposes. The four areas with fine dashed lines represent areas where the fracture intensity is unusually high.

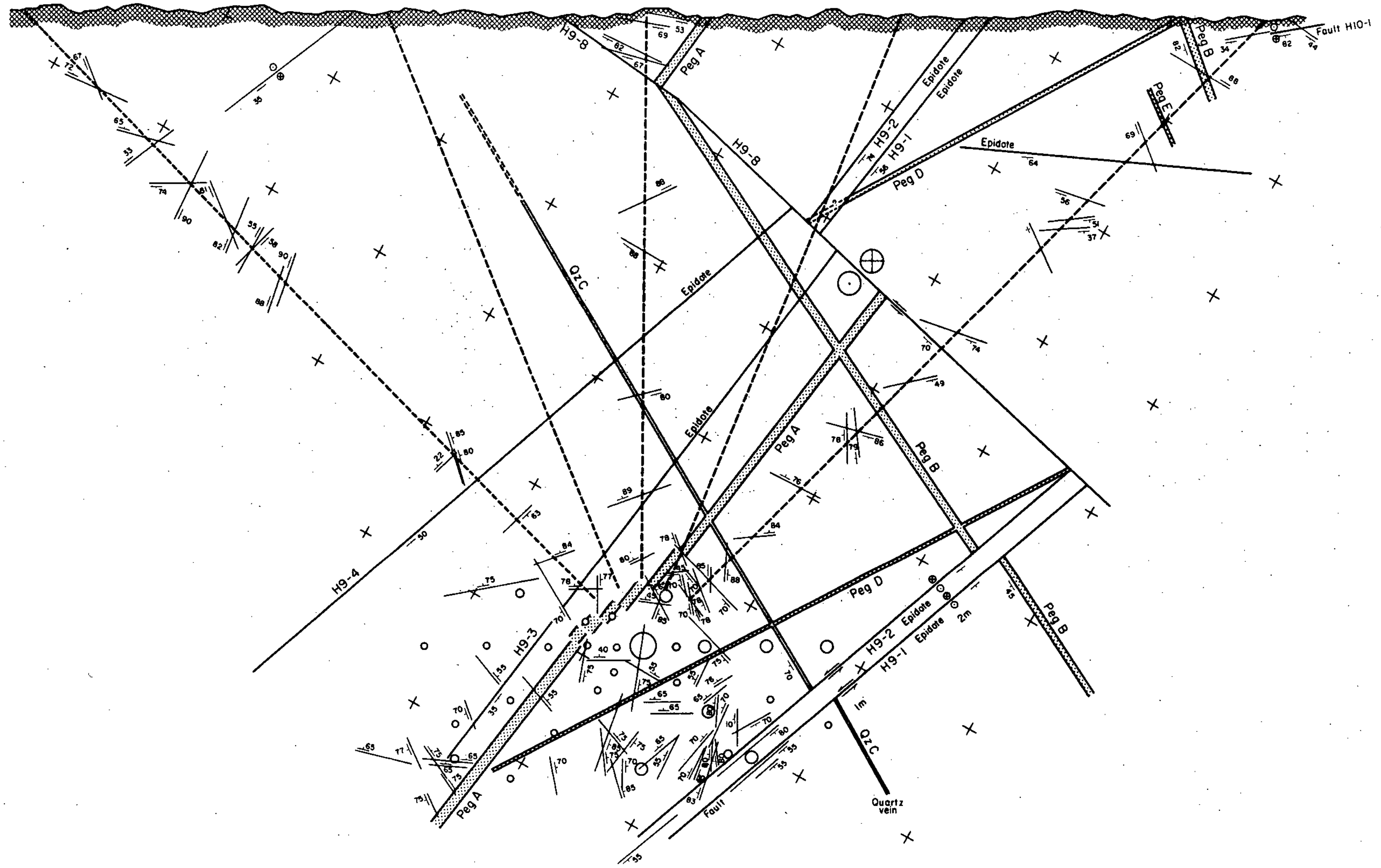

XBL 811-2570

Fig. 4.3. Major dikes and faults at elevation of H9 heater mid-plane, based on extrapolation from nearby surfaces and core data. Short lines with dip symbols show projected intercepts of calcite-bearing fractures. Upthrown (downthrown) sides of faults are designated by head (tail) of arrows. Part of mine coordinate system

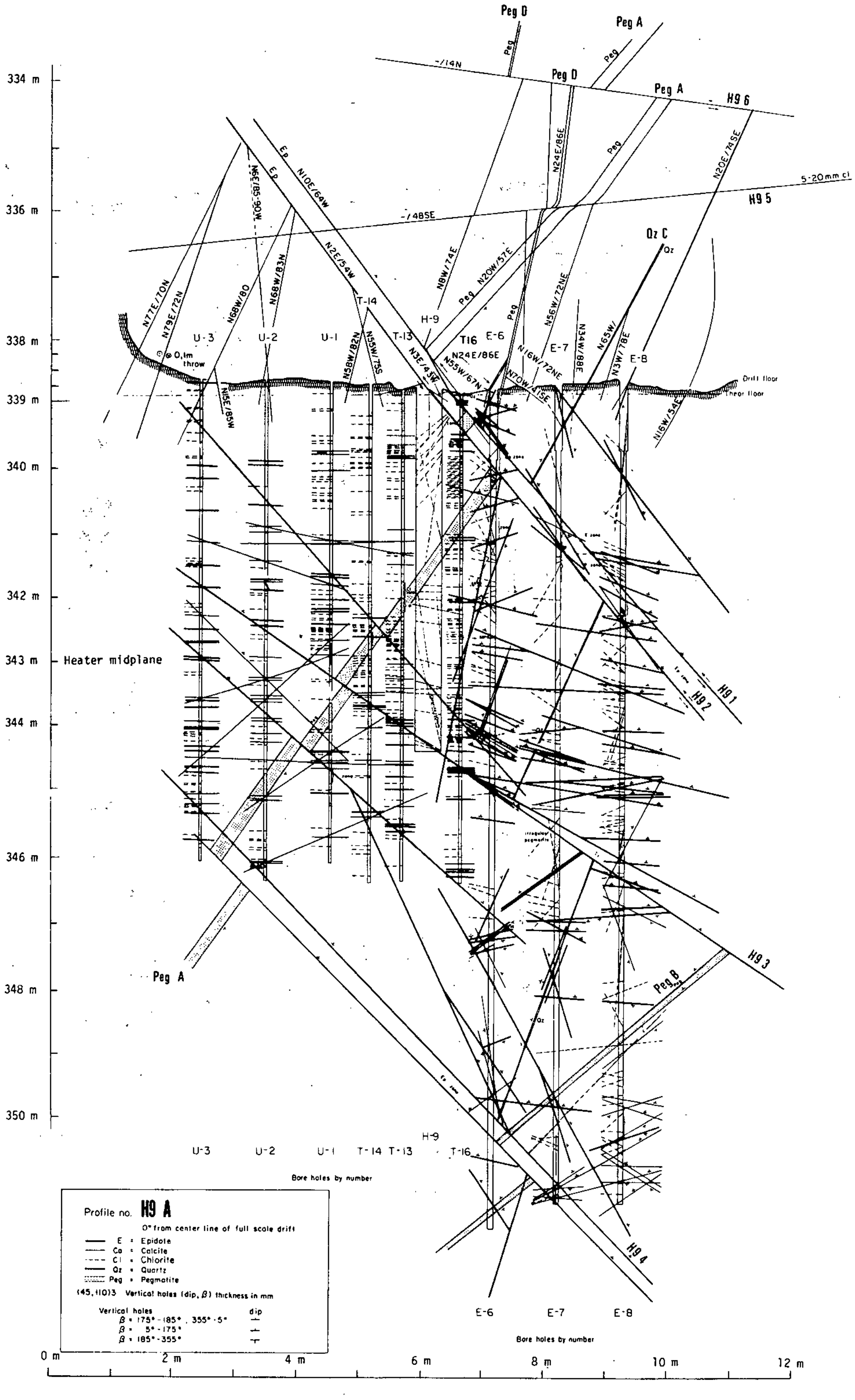

XBL 791-253A

Fig. 4.4. Interpreted fracture maps on vertical cross-sections around the H9 heater area. See Fig. 4.1 and Table 4.1 for orientation and position of cross-sections. Fracture reconstruction above drift floor is based on projection from walls. Strike/dip entries are true mapped values, not apparent. The left-to-right convention reverses between cross-sections B and C; the view is generally to the southeast.

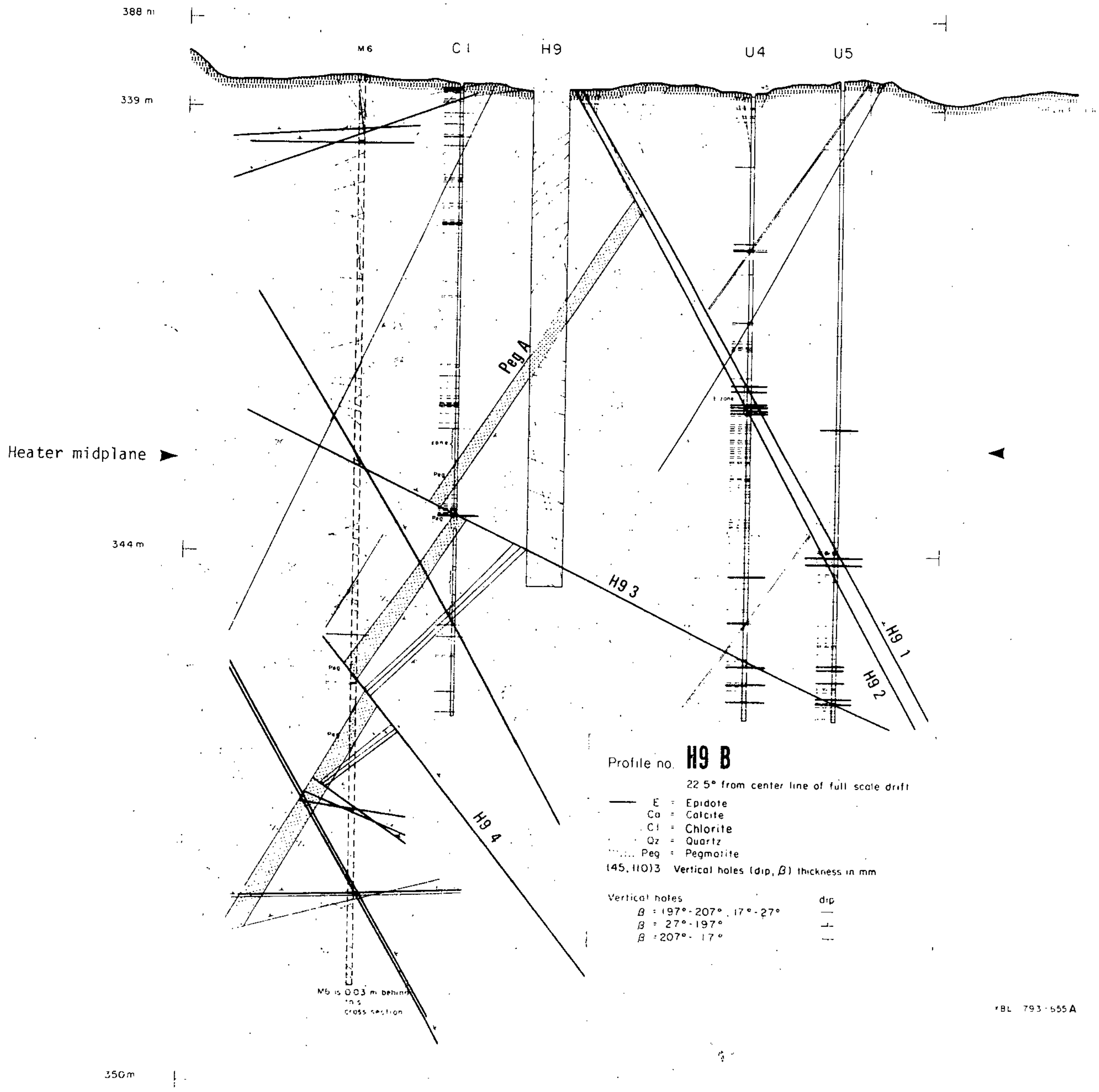
388 m
339 m
344 m
350m
M6
C1
H9
U4
U5
Heater midplane
Peg A
H9 3
H9 1
H9 2
H9 4
Peg
zone
M6 is 0.03 m behind this cross section
Profile no. H9 B
22.5° from center line of full scale drift
E = Epidote
Ca = Calcite
Cl = Chlorite
Qz = Quartz
Peg = Pegmatite
(45, 110)3 Vertical holes (dip, β) thickness in mm
Vertical holes
dip
β = 197°-207°, 17°-27°
β = 27°-197°
β = 207°-17°
XBL 793-555 A

Fig. 4.4 B

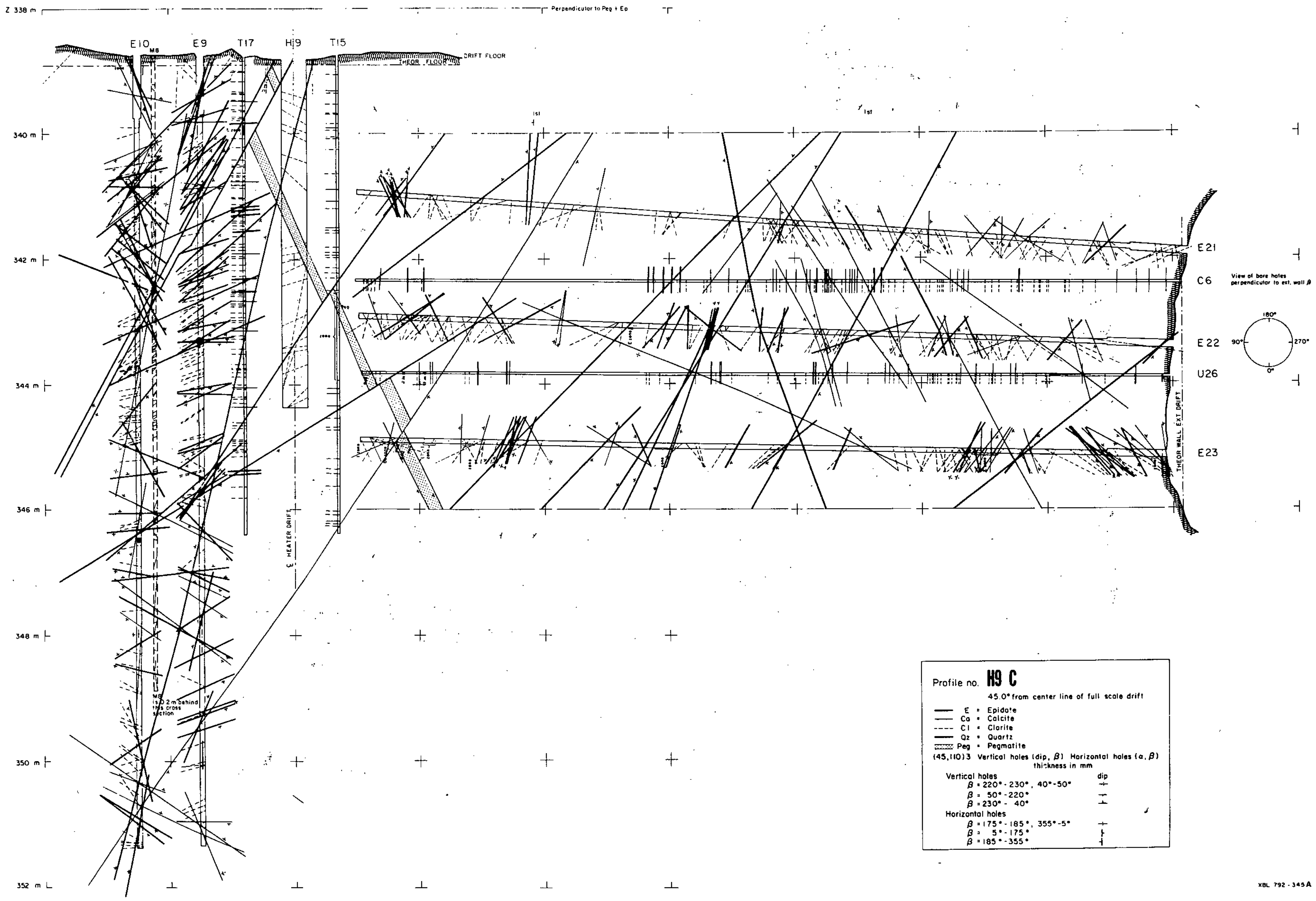
Z 338 m
340 m
342 m
344 m
346 m
348 m
350 m
352 m
Perpendicular to Peg + Ep
E10
M8
E9
T17
H9
T15
DRIFT FLOOR
THEOR. FLOOR
℄ HEATER DRIFT
M8 is 0.2 m behind this cross section
1st
E21
C6
E22
U26
E23
THEOR WALL EXT DRIFT
View of bore holes perpendicular to ext. wall β
180°
90°
270°
0°
Profile no. H9 C
45.0° from center line of full scale drift
E = Epidote
Ca = Calcite
Cl = Clarite
Qz = Quartz
Peg = Pegmatite
(45,110)3 Vertical holes (dip, β) Horizontal holes (α, β) thickness in mm
Vertical holes
dip
β = 220° - 230°, 40°-50°
β = 50° - 220°
β = 230° - 40°
Horizontal holes
β = 175° - 185°, 355°-5°
β = 5° - 175°
β = 185° - 355°
XBL 792-345A

Fig. 4.4 C

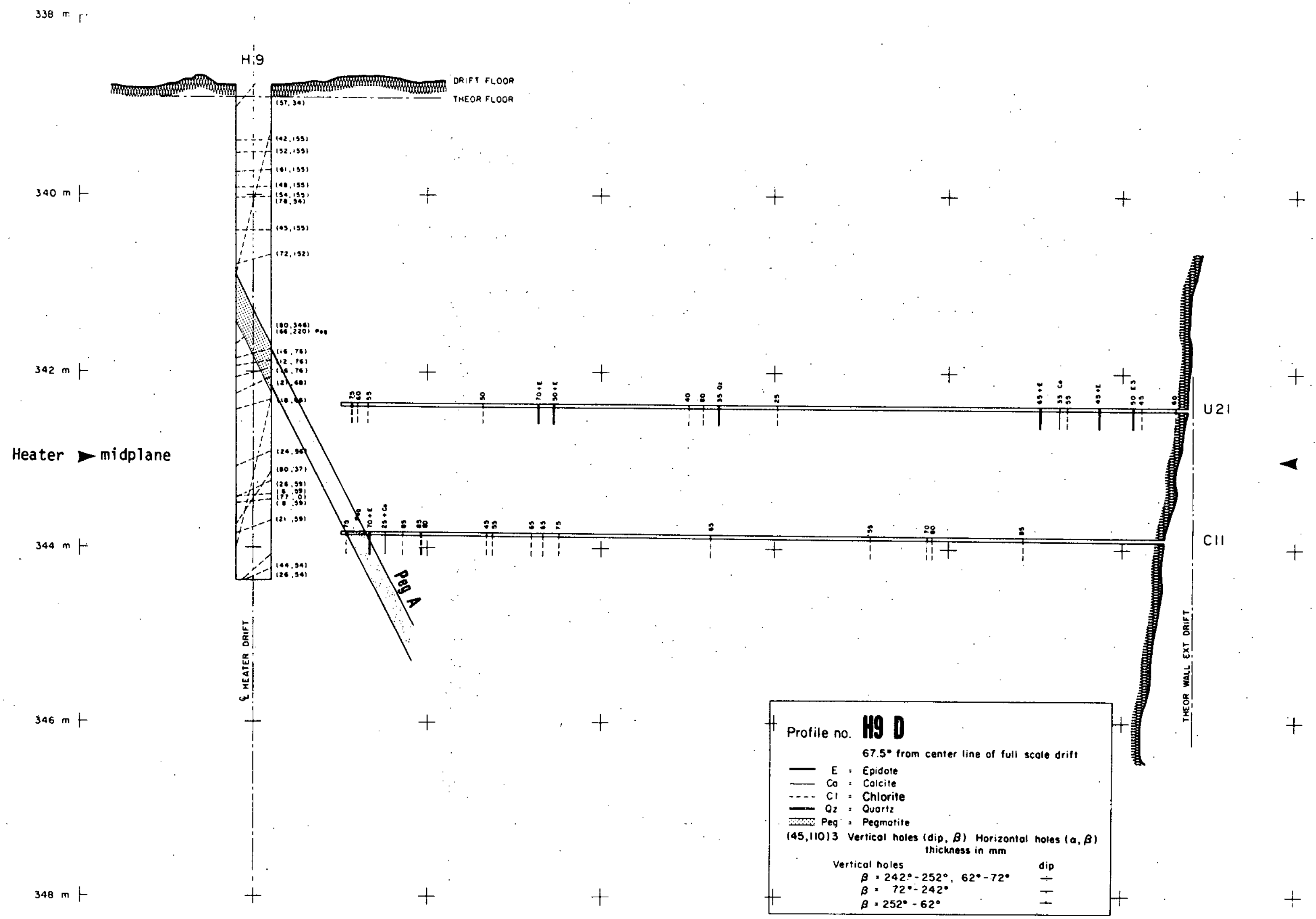

XBL 796-10326

Fig. 4.4 D

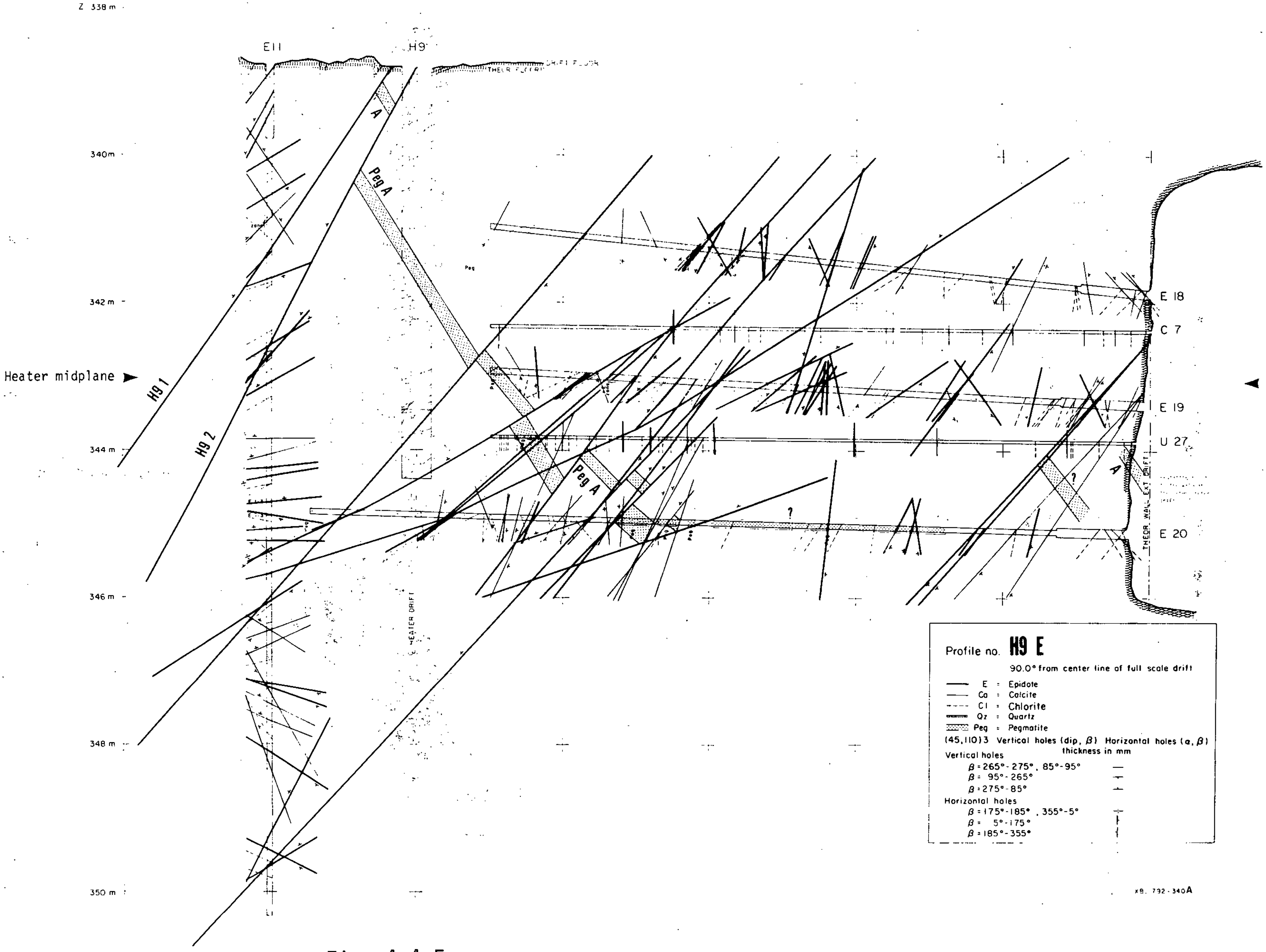
Z 338 m
340m
342 m
344 m
346 m
348 m
350 m
Heater midplane
E11
H9
THEOR FLOOR
DRIFT FLOOR
E 18
C 7
E 19
U 27
E 20
THEOR WALL EXT DRIFT
HEATER DRIFT
H9 1
H9 2
A
Peg A
Peg
?
Profile no. H9 E
90.0° from center line of full scale drift
E : Epidote
Ca : Calcite
Cl : Chlorite
Qz : Quartz
Peg : Pegmatite
(45,110)3 Vertical holes (dip, β) Horizontal holes (α, β) thickness in mm
Vertical holes
β = 265°-275°, 85°-95°
β = 95°-265°
β = 275°-85°
Horizontal holes
β = 175°-185°, 355°-5°
β = 5°-175°
β = 185°-355°
XBL 792-340A

Fig. 4.4 E

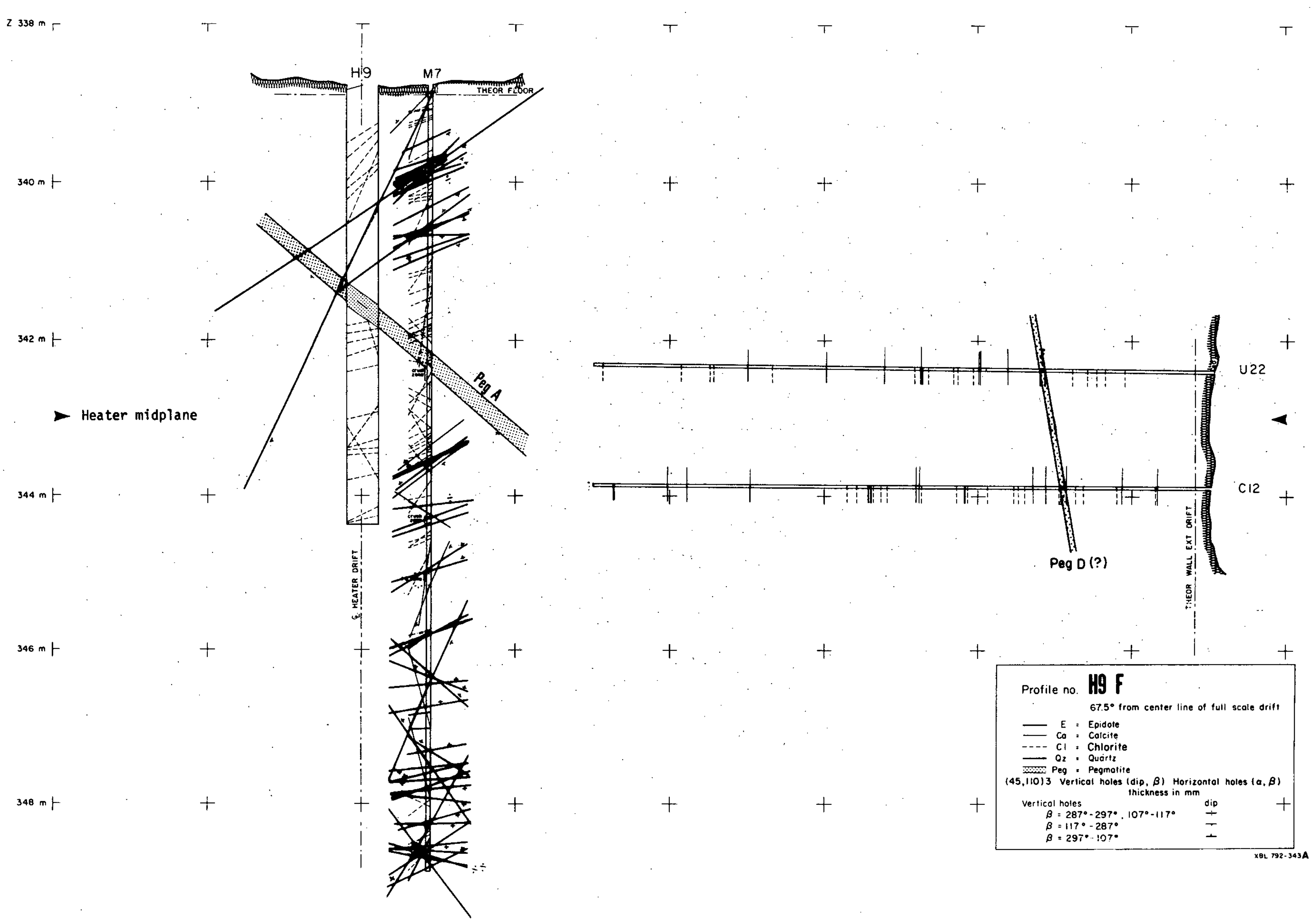
Z 338 m
340 m
342 m
344 m
346 m
348 m
Heater midplane
H9
M7
THEOR FLOOR
Peg A
℄ HEATER DRIFT
U22
C12
Peg D (?)
THEOR WALL EXT DRIFT
Profile no. H9 F
67.5° from center line of full scale drift
E = Epidote
Ca = Calcite
Cl = Chlorite
Qz = Quartz
Peg = Pegmatite
(45,110)3 Vertical holes (dip, β) Horizontal holes (α, β) thickness in mm
Vertical holes
dip
β = 287°-297°, 107°-117°
β = 117°-287°
β = 297°-107°
XBL 792-343A

Fig. 4.4 F

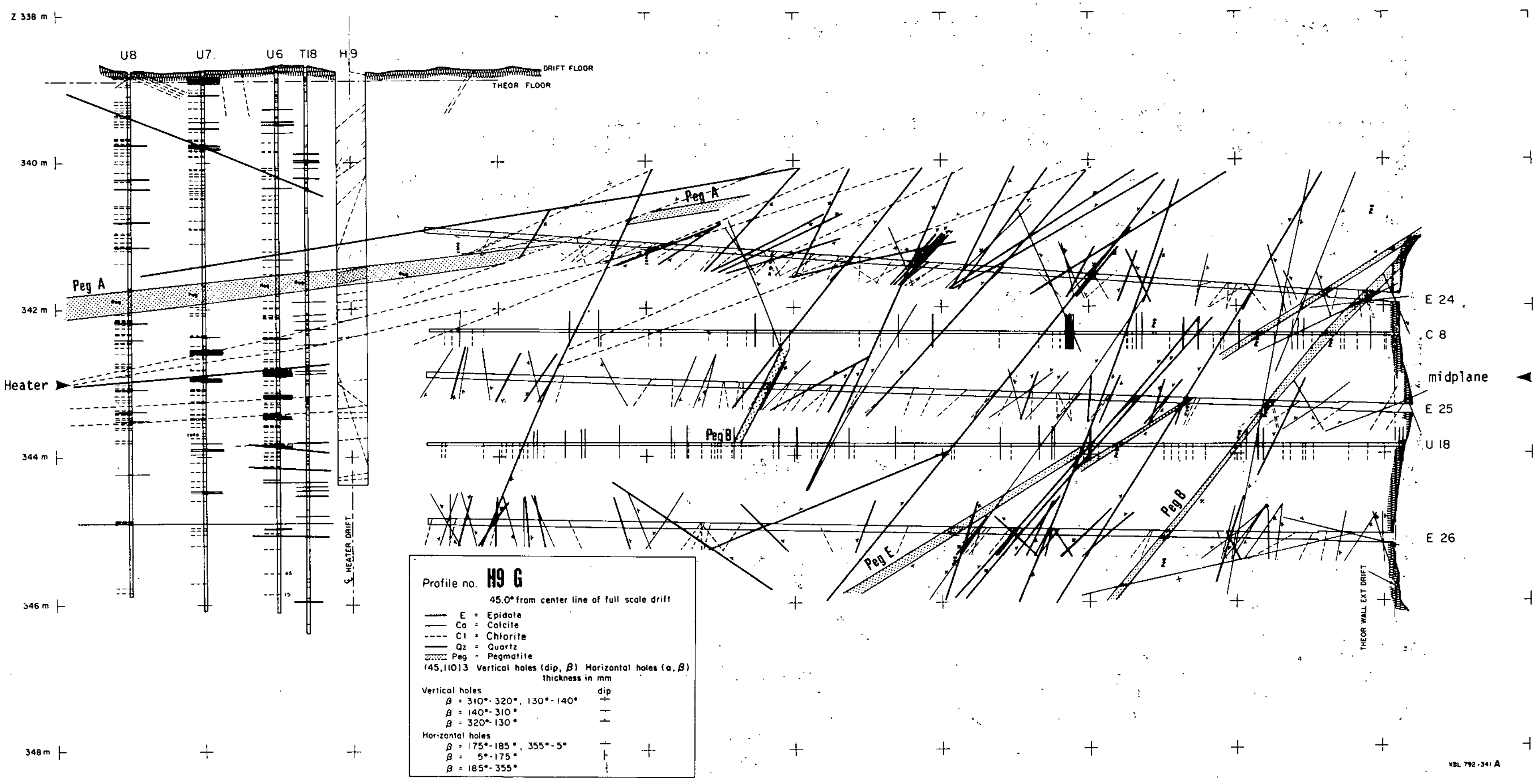
Z 338 m
340 m
342 m
Heater
344 m
346 m
348 m
U8
U7
U6
T18
H9
DRIFT FLOOR
THEOR FLOOR
℄ HEATER DRIFT
Peg A
Peg A
Peg B
Peg B
Peg E
E 24
C 8
midplane
E 25
U 18
E 26
THEOR WALL EXT DRIFT
Profile no. H9 G
45.0° from center line of full scale drift
E = Epidote
Ca = Calcite
Cl = Chlorite
Qz = Quartz
Peg = Pegmatite
(45,110)3 Vertical holes (dip, β) Horizontal holes (α, β) thickness in mm
Vertical holes
dip
β = 310°-320°, 130°-140°
β = 140°-310°
β = 320°-130°
Horizontal holes
β = 175°-185°, 355°-5°
β = 5°-175°
β = 185°-355°
XBL 792-341 A

Fig. 4.4 G

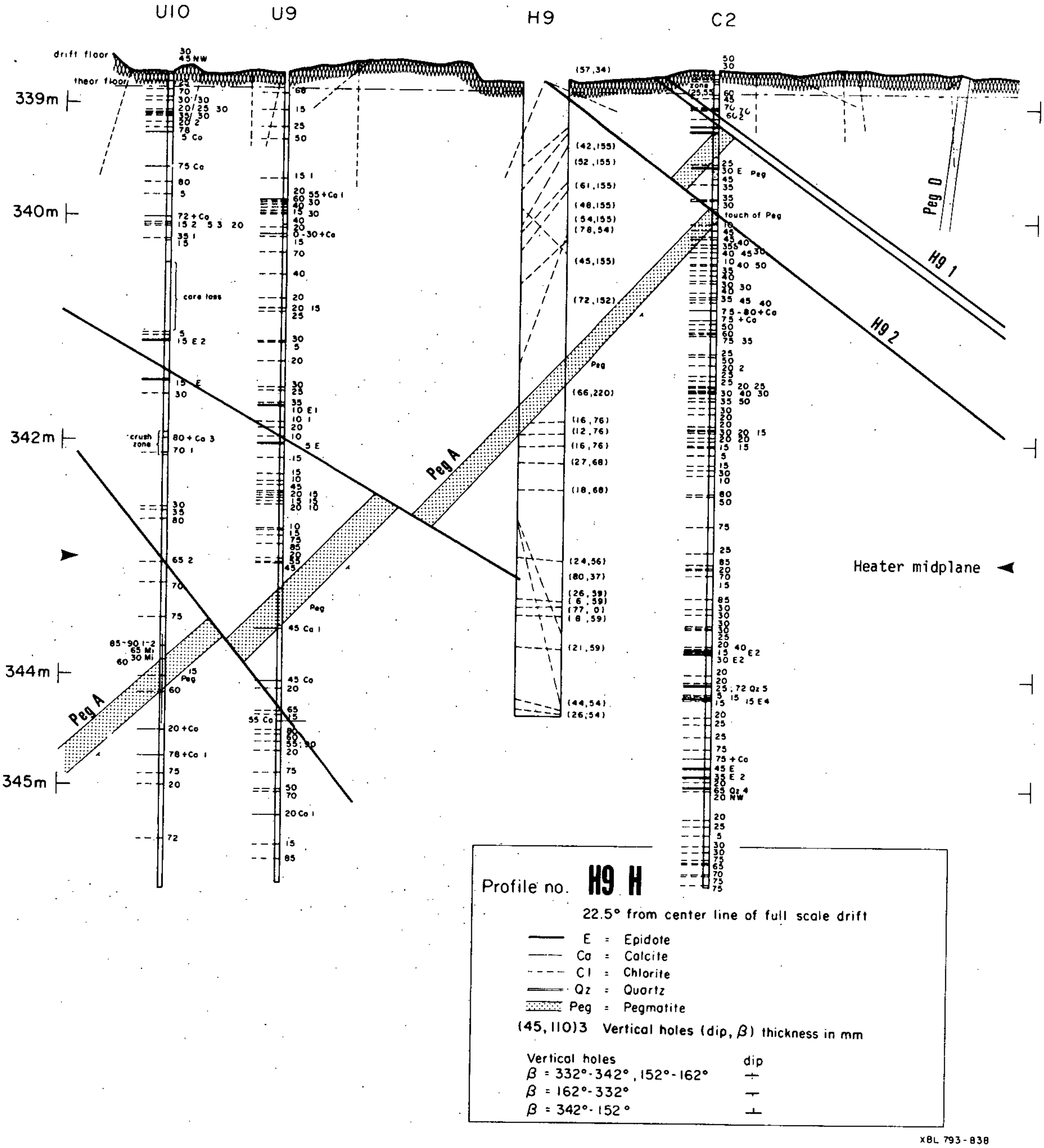
U10
U9
H9
C2
drift floor
theor floor
339m
340m
342m
344m
345m
core loss
crush zone
touch of Peg
Peg A
Peg A
Peg
Peg D
H9 1
H9 2
Heater midplane
Profile no. H9 H
22.5° from center line of full scale drift
E = Epidote
Ca = Calcite
Cl = Chlorite
Qz = Quartz
Peg = Pegmatite
(45, 110)3 Vertical holes (dip, β) thickness in mm
Vertical holes
dip
β = 332°-342°, 152°-162°
β = 162°-332°
β = 342°-152°
XBL 793-838

Fig. 4.4 H

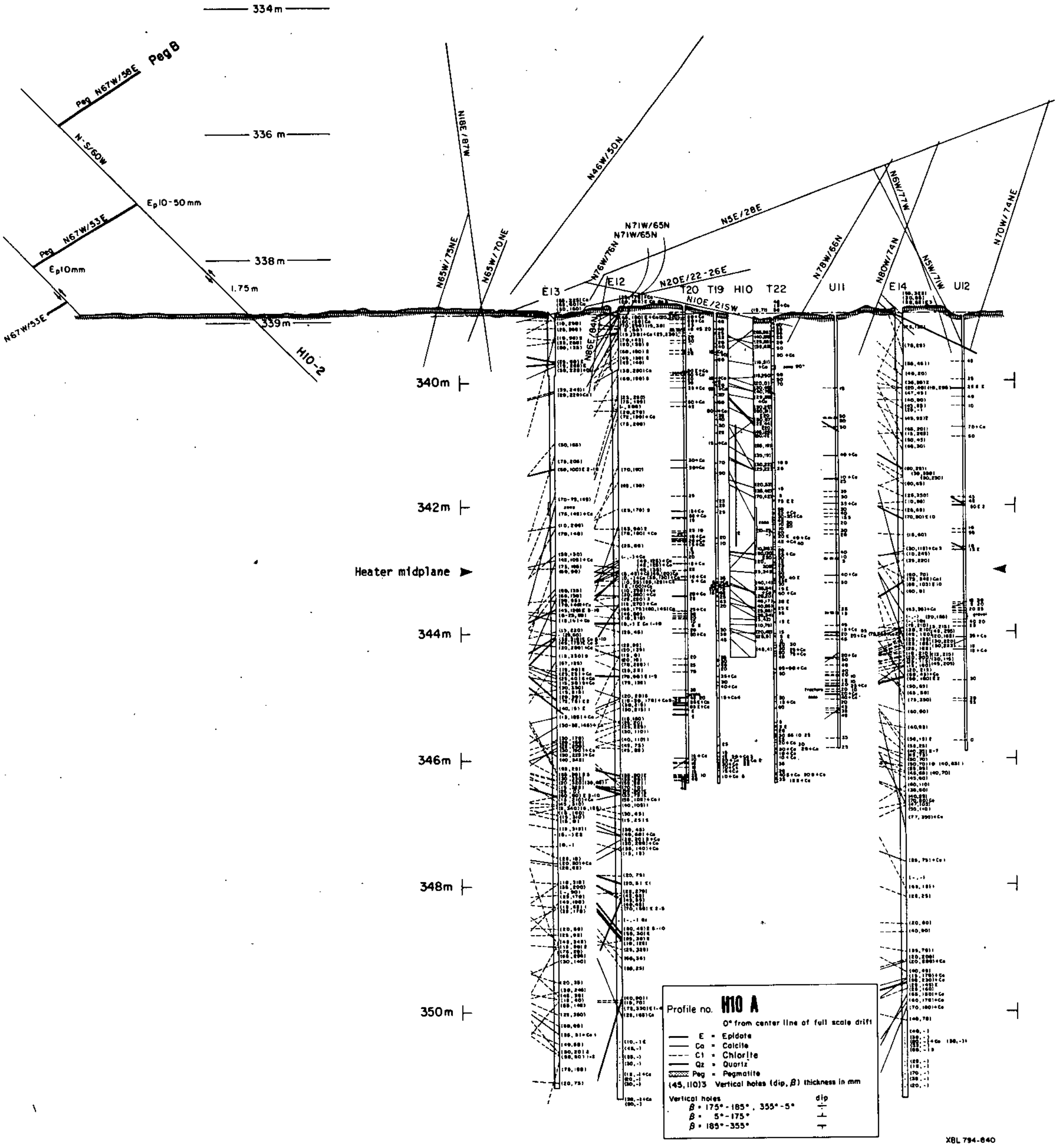

Fig. 4.5. Interpreted fracture maps on vertical sections A through H around H10 heater areas. See appendix A for explanation of data entries and Fig. 4.4 for general explanation.

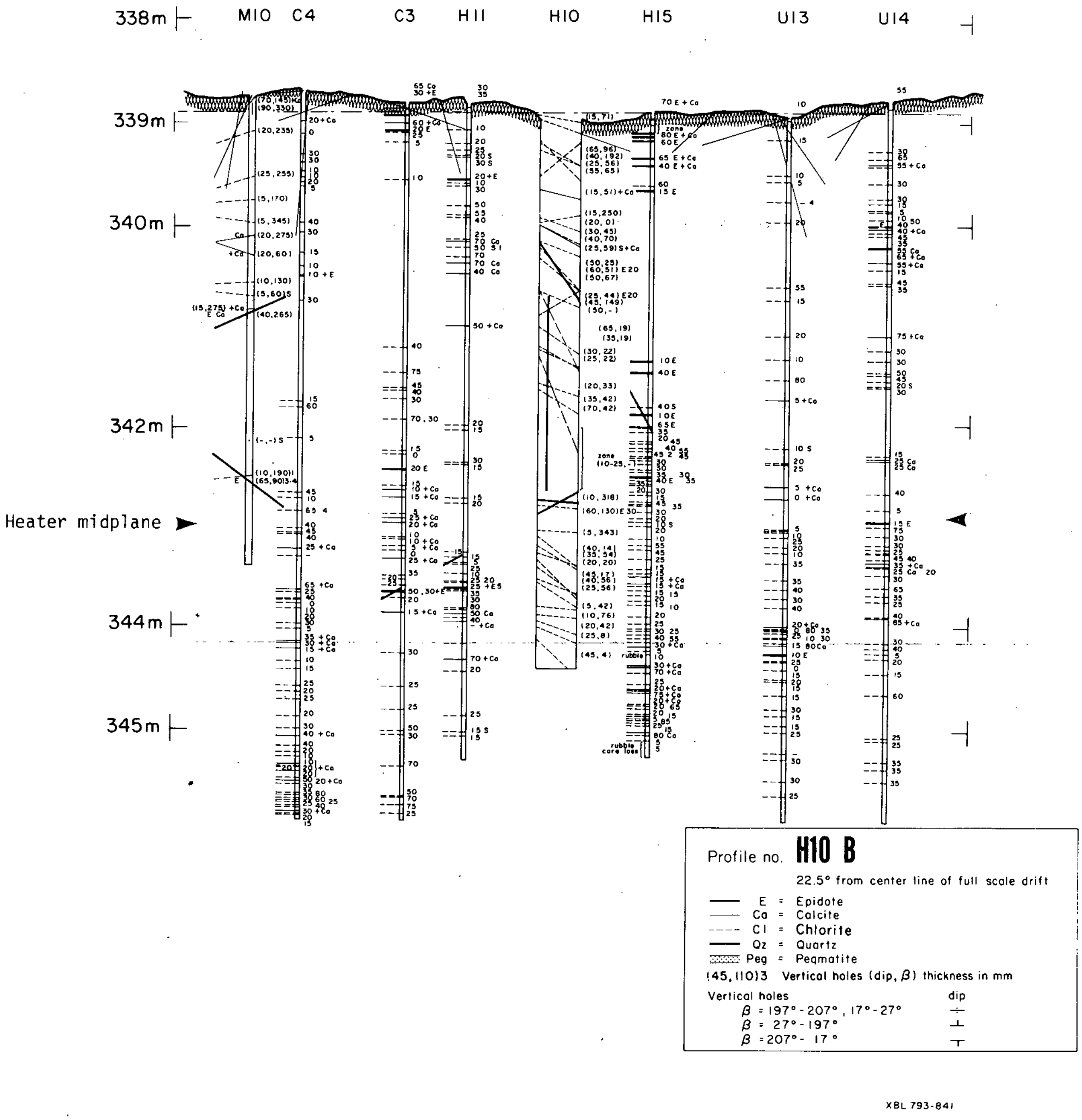
338m
339m
340m
342m
344m
345m
M10
C4
C3
H11
H10
H15
U13
U14
Heater midplane
zone
rubble
rubble core loss
Profile no. H10 B
22.5° from center line of full scale drift
E = Epidote
Ca = Calcite
Cl = Chlorite
Qz = Quartz
Peg = Pegmatite
(45, 110)3 Vertical holes (dip, β) thickness in mm
Vertical holes
dip
β = 197° - 207°, 17° - 27°
β = 27° - 197°
β = 207° - 17°
XBL 793-841

Fig. 4.5 B

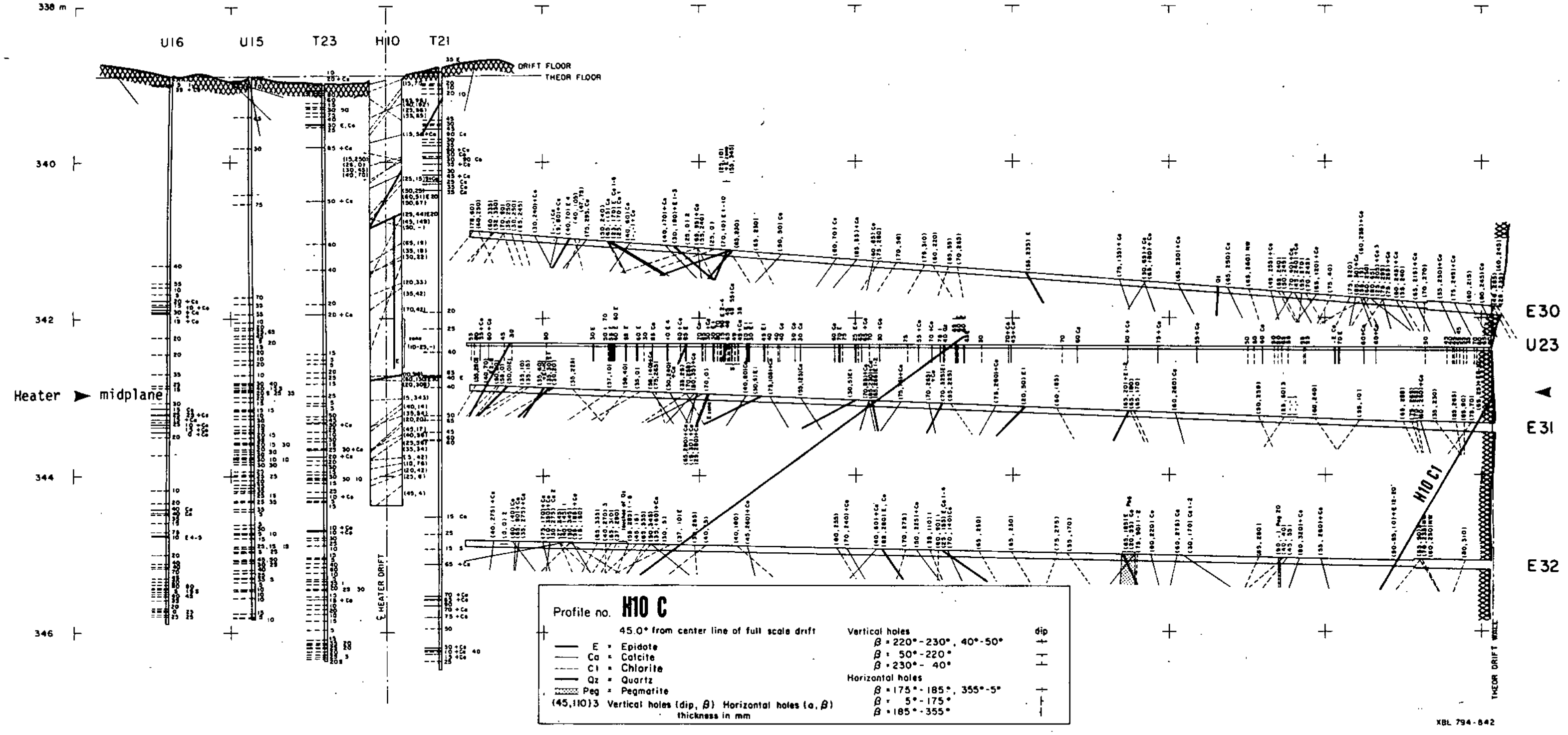
338 m
340
342
344
346
Heater ➤ midplane
U16
U15
T23
H10
T21
DRIFT FLOOR
THEOR FLOOR
℄ HEATER DRIFT
E30
U23
E31
E32
H10 C1
THEOR DRIFT WALL
XBL 794-842
Profile no. H10 C
45.0° from center line of full scale drift
E = Epidote
Ca = Calcite
Cl = Chlorite
Qz = Quartz
Peg = Pegmatite
(45,110)3 Vertical holes (dip, β) Horizontal holes (a, β) thickness in mm
Vertical holes
β = 220°-230°, 40°-50°
β = 50°-220°
β = 230°- 40°
Horizontal holes
β = 175°-185°, 355°-5°
β = 5°-175°
β = 185°-355°
dip

Fig. 4.5 C

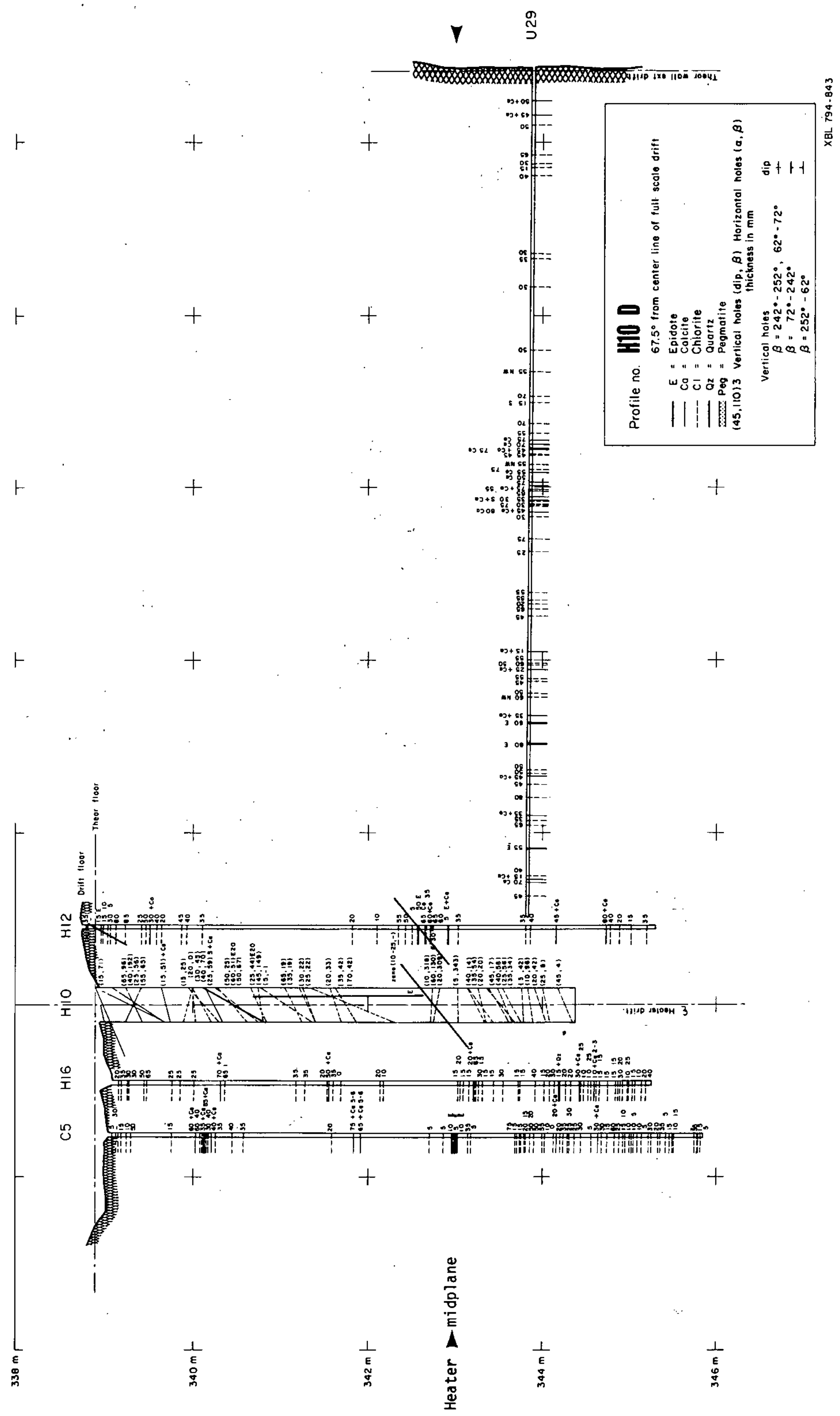
Profile no. H10 D
67.5° from center line of full scale drift
E = Epidote
Ca = Calcite
Cl = Chlorite
Qz = Quartz
Peg = Pegmatite
(45,110)3 Vertical holes (dip, β) Horizontal holes (α, β) thickness in mm
Vertical holes
β = 242°-252°, 62°-72°
β = 72°-242°
β = 252°-62°
dip
XBL 794-843
U29
Theor wall ext drift
Drift floor
Theor floor
H12
H10
H16
C5
℄ Heater drift
338 m
340 m
342 m
344 m
346 m
Heater ➤ midplane

Fig. 4.5 D

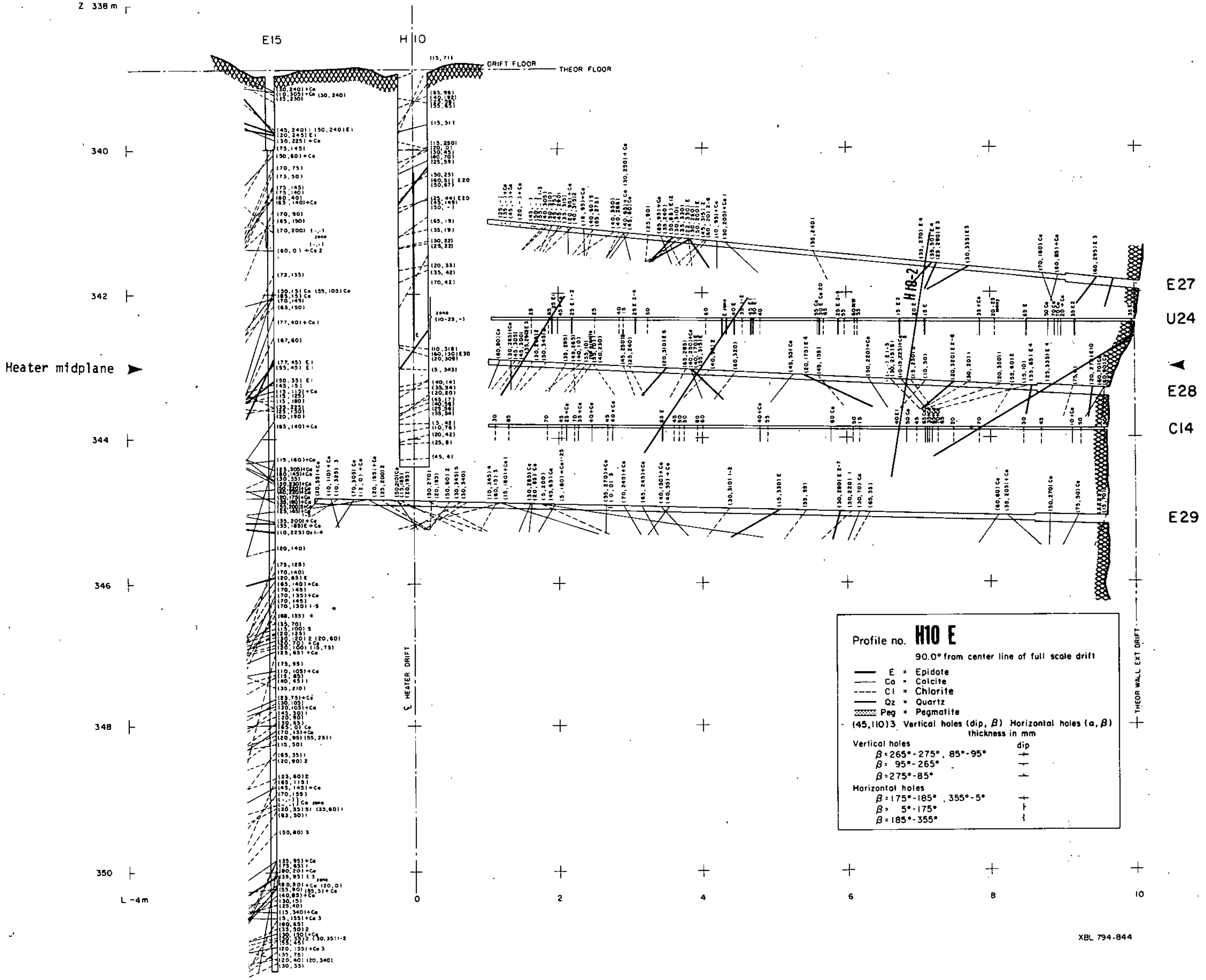
Z 338 m
340
342
Heater midplane
344
346
348
350
L -4m
E15
H10
DRIFT FLOOR
THEOR FLOOR
℄ HEATER DRIFT
THEOR WALL EXT DRIFT
0
2
4
6
8
10
E27
U24
E28
C14
E29
H18-2
Profile no. H10 E
90.0° from center line of full scale drift
E = Epidote
Ca = Calcite
Cl = Chlorite
Qz = Quartz
Peg = Pegmatite
(45,110)3 Vertical holes (dip, β) Horizontal holes (a, β) thickness in mm
Vertical holes
dip
β = 265°-275°, 85°-95°
β = 95°-265°
β = 275°-85°
Horizontal holes
β = 175°-185°, 355°-5°
β = 5°-175°
β = 185°-355°
XBL 794-844

Fig. 4.5 E

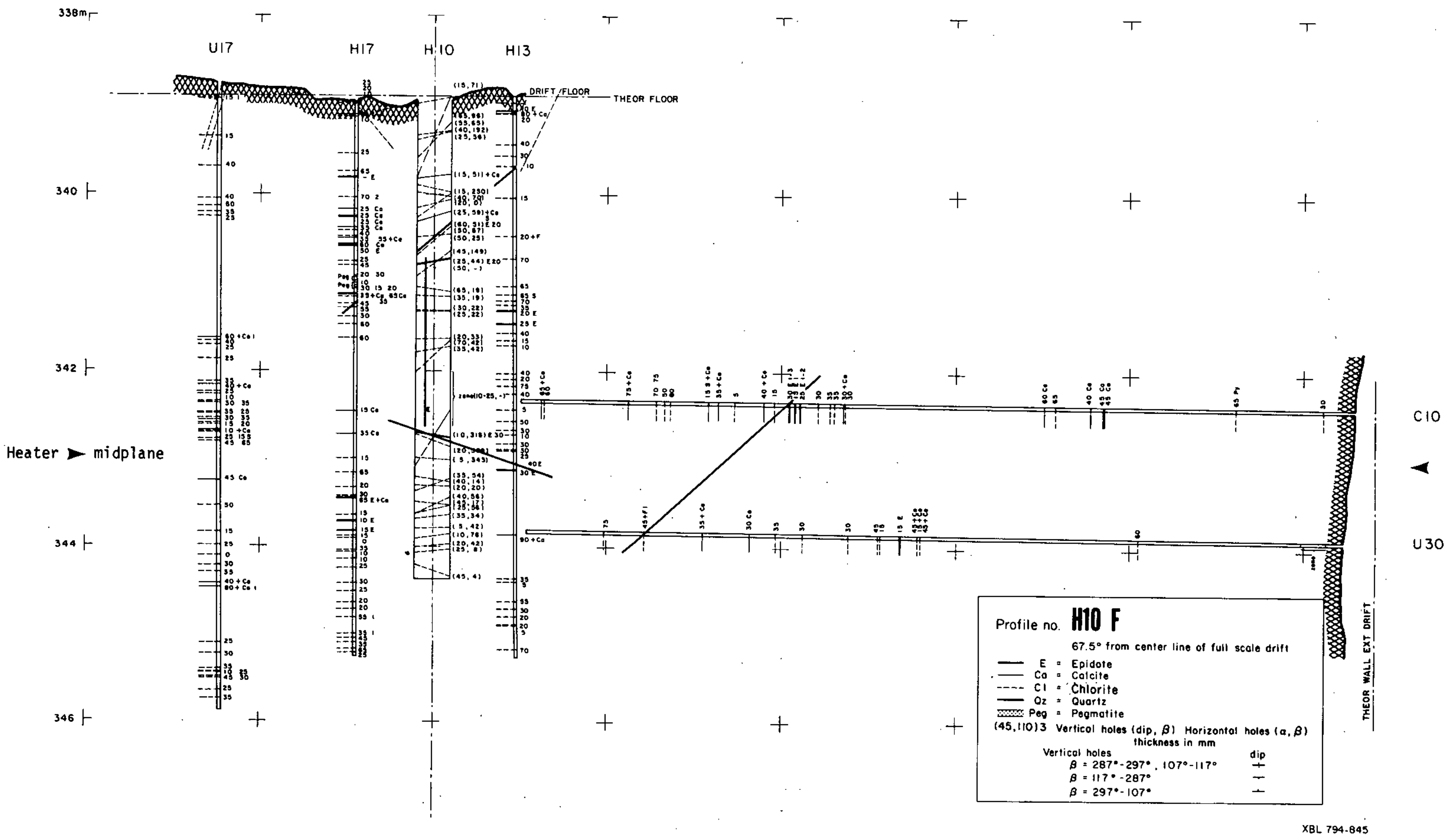
338m
340
342
344
346
Heater ➤ midplane
U17
H17
H10
H13
DRIFT FLOOR
THEOR FLOOR
C10
U30
THEOR WALL EXT DRIFT
Profile no. H10 F
67.5° from center line of full scale drift
E = Epidote
Ca = Calcite
Cl = Chlorite
Qz = Quartz
Peg = Pegmatite
(45,110)3 Vertical holes (dip, β) Horizontal holes (α, β) thickness in mm
Vertical holes
β = 287°-297°, 107°-117°
β = 117°-287°
β = 297°-107°
dip
XBL 794-845

Fig. 4.5 F

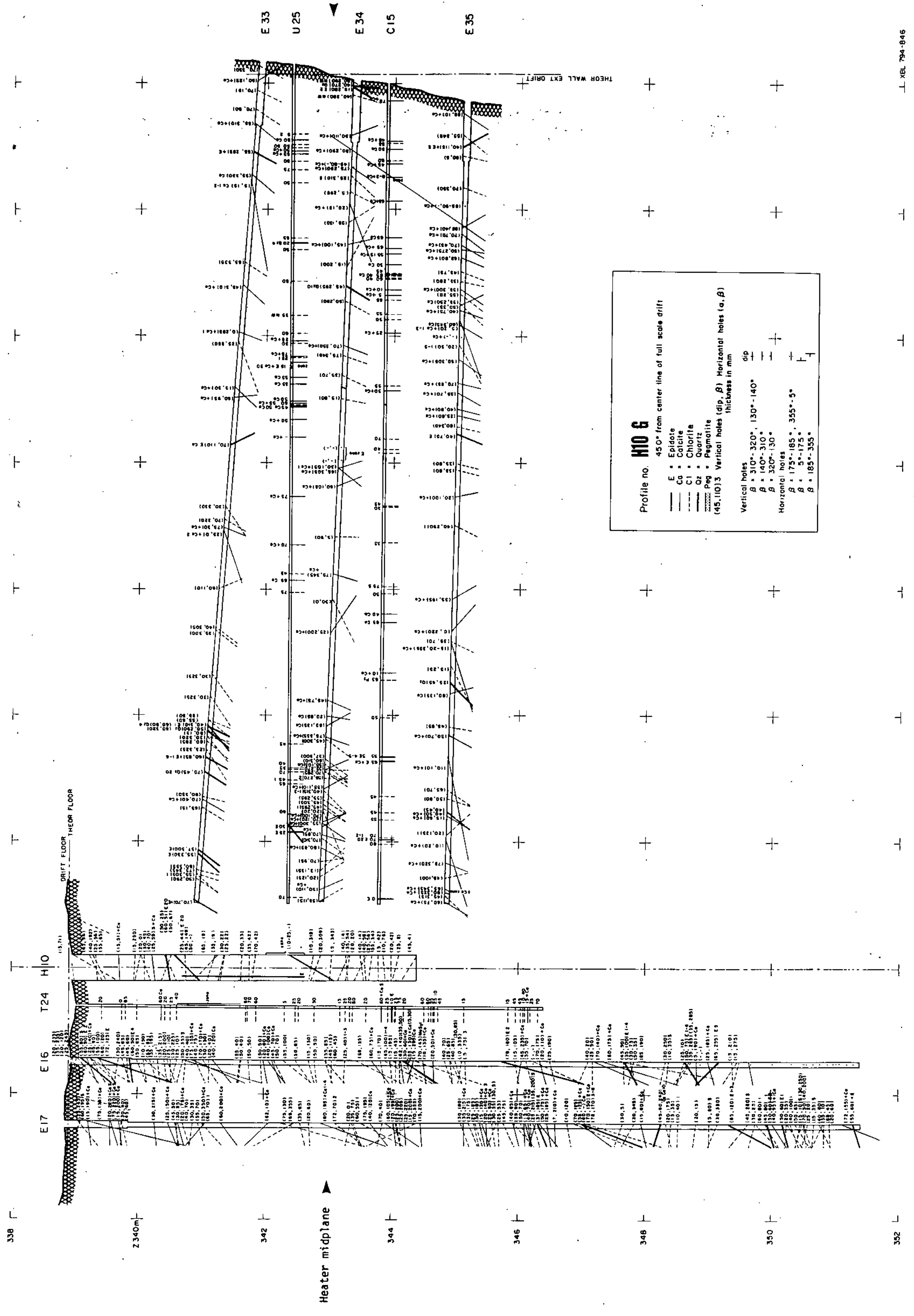
E 33
U 25
E 34
C 15
E 35
THEOR WALL EXT DRIFT
H10
T24
E16
E17
DRIFT FLOOR
THEOR FLOOR
338
Z 340m
342
344
346
348
350
352
Heater midplane
Profile no. H10 G
45.0° from center line of full scale drift
E = Epidote
Ca = Calcite
Cl = Chlorite
Qz = Quartz
Peg = Pegmatite
(45,110)3 Vertical holes (dip, β) Horizontal holes (α, β) thickness in mm
Vertical holes
β = 310°-320°, 130°-140°
β = 140°-310°
β = 320°-130°
Horizontal holes
β = 175°-185°, 355°-5°
β = 5°-175°
β = 185°-355°
dip
XBL 794-846

Fig. 4.5 G

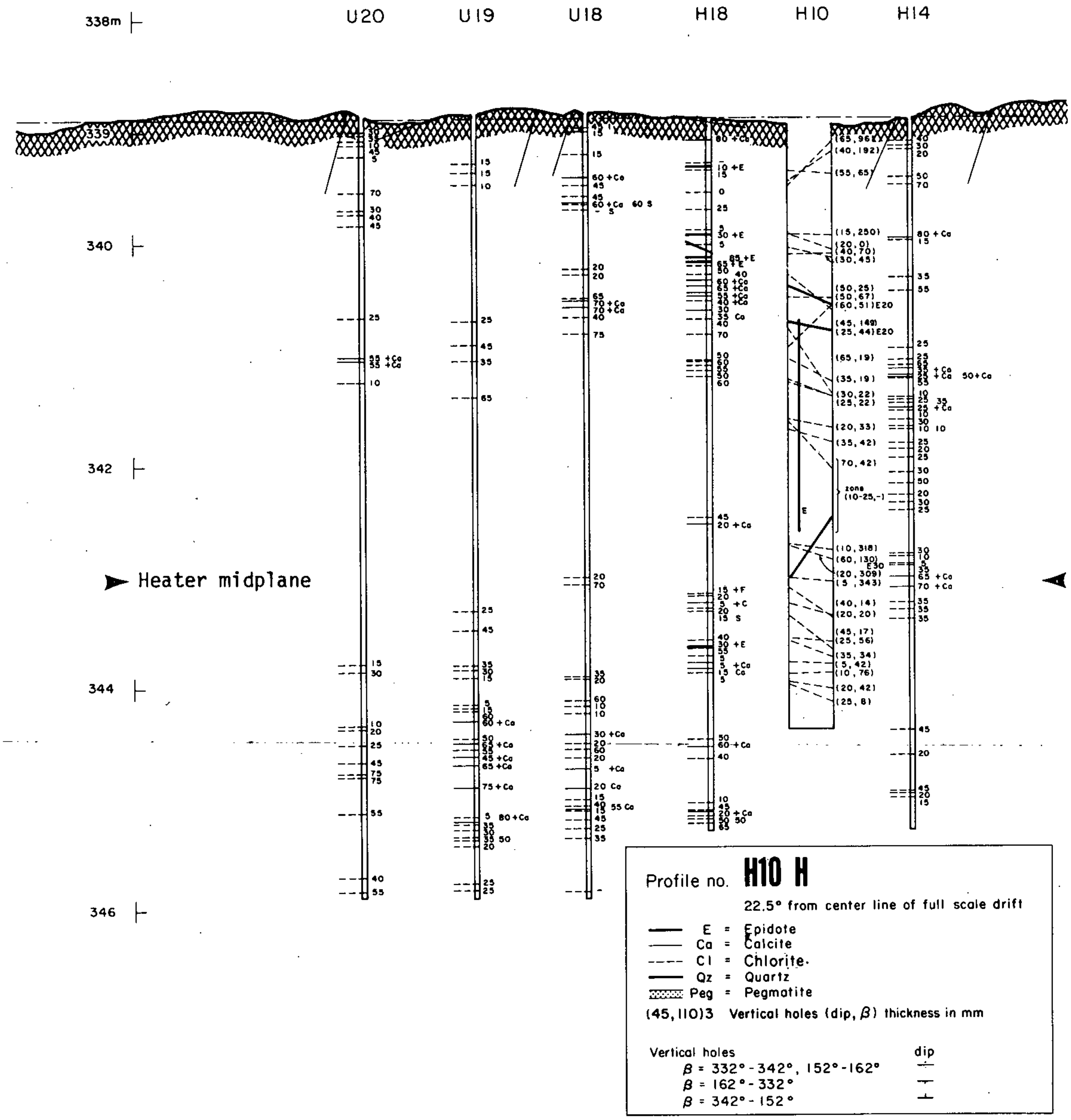

XBL 794-847

Fig. 4.5 H

Table 4.1. Orientation of fracture cross-sections. The H9 and H10 cross-sections have the same strike, so these angles apply for both experimental areas.

Section	Strike Direction	Angle from drift centerline, β_p
A	N51E	0.0
B	N73E	22.5
C	N84W	45.0
D	N61W	67.5
E	N39W	90.0
F	N16W	112.5
G	N06E	135.0
H	N29E	157.5

The results presented in this chapter are based mainly on graphical techniques such as cross sections and pole plots using all available fracture information. Alternatively, computer-aided mathematical methods could have been used to reconstruct the fracture network. However, a graphical method was judged to be faster and more effective in working with the complex fracture systems in the H9 and H10 areas. Most fractures are not continuous and are not traceable even between two closely spaced boreholes. To characterize a rock mass, a statistical approach is necessary to complement the graphical method. This approach is further discussed in Section 5.

4.1.2 Plexiglass model

As an additional tool for reconstructing the fracture system, a three-dimensional model was built using all the cross-sections from H9 and H10. Sections A-H, the mapped floor and walls of the FS drift, and the mapped walls of the EX drift were all reproduced at a scale of 1:20. The model, shown in Fig. 4.6, helps to synthesize all fracture information and gives an overall picture of the strike and dip of fractures and variations in fracture densities within the experiment area. It was, for instance, very helpful in lining up large features such as the pegmatite dikes and the epidote-coated faults. It showed that pegmatite A was faulted 6 meters between the full-scale and the extensometer drifts. Pegmatites E and B were also lined up with the help of the model.

4.2 Prominent Faults and Dikes

The pegmatite and quartz veins, readily identified by observation underground, provide excellent markers to define the offsets induced by the epidote-coated faults. Hence, all the prominent features that could be

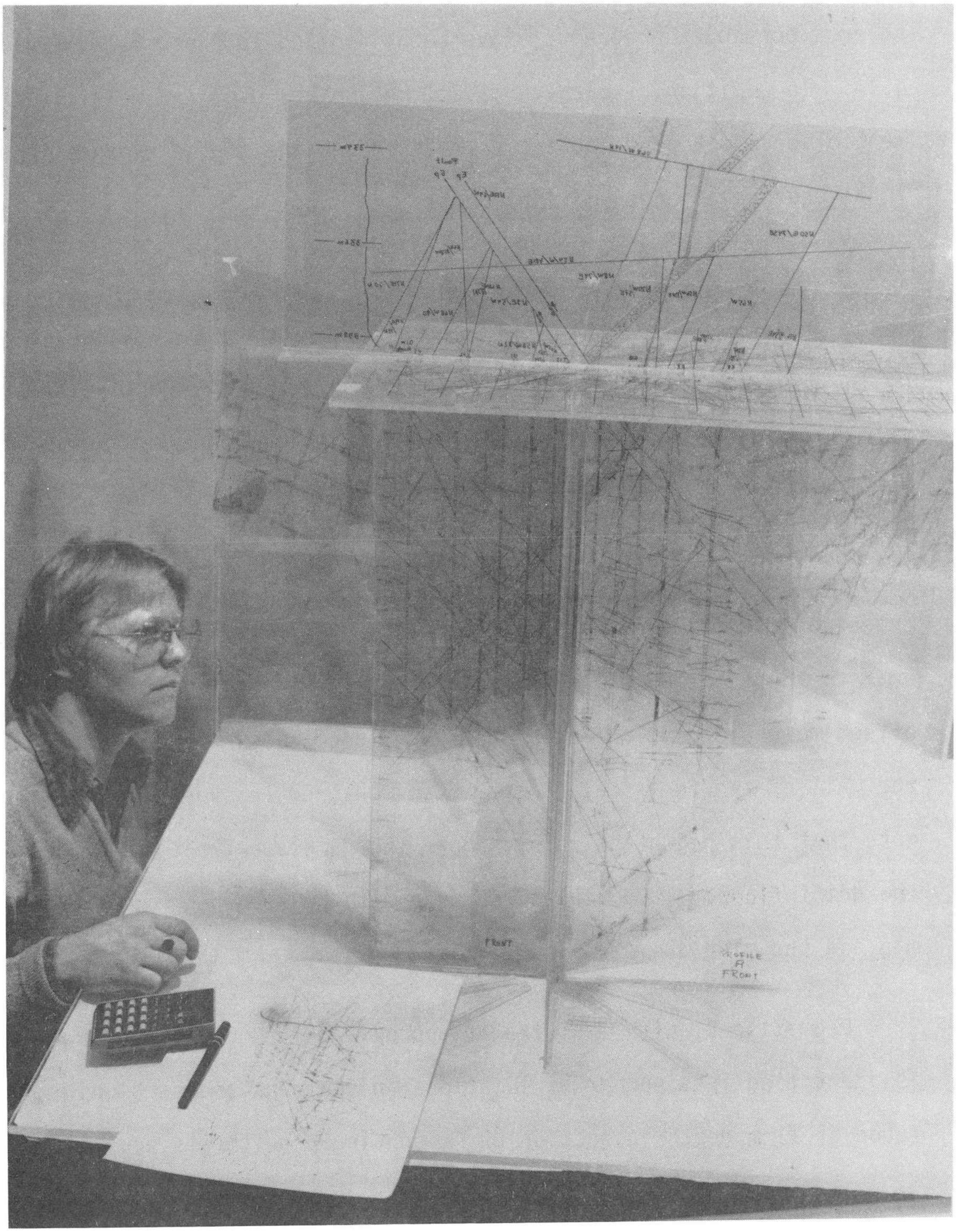

CBB 802-2342

Fig. 4.6. Plexiglass model (1:20 scale) for the fracture system in the H9 area. The H10 area is not shown here. Model is 0.7 m wide x 1.0 m high x 2.1 m long.

extrapolated successfully between drifts, or between a drift surface and several borehole intercepts, have been labelled in Figs. 4.1, 4.2, 4.3 and 4.4A. In addition, Table 4.2 gives the strike, dip, and relative displacement of each dike and fault * as measured on one of the exposed surfaces or in a sequence of borehole intercepts.

Some discontinuities appear as arcuate features on the floor and wall maps. This apparent lack of planarity is attributed to the irregular nature of the floor and wall surfaces, rather than to curvature of the fault planes. Examples are Qz C and H9-7 on both the detailed and simplified versions of the floor map (Fig. 4.1).

The key marker in the H9 area is pegmatite A. Its apparent truncated extent on the full-scale floor (Fig. 4.1) is due to the offset induced very near to the floor by the main fault labelled H9-1. Fig. 4.4A shows this offset more clearly, and also shows that pegmatite A is easily identified in the wall of the full-scale drift. Its measured thickness is about 20 cm. Note that this pegmatite cuts through the H9 heater hole about 2.5 m below the drift floor. Its displacement can also be seen by comparing the floor map and the midplane map.

Pegmatite B, with a strike of approximately N60W and a dip of about 50E, is identified in a number of locations in the maps and sections. It is first found at 11 m depth in section H9 A, continuous with its projection on the

---

*By "faults" we mean a fracture with a documented offset. By "epidote faults" we simply mean a fault with epidote mineralization. The faults we have been able to trace over the whole experiment volume we term "major faults". All faults are well healed, competent features with little or no water seepage.

Table 4.2. Strike/dip of dikes and faults in full-scale and extensometer drifts. Peg E is identified only in cross-section H9G. Dash indicates a feature is present but not measured.

Bore Hole Zone	Full Scale Floor Map	Extensometer Wall Map	Full Scale Wall (cross-sect. A)	Centerline Boreholes (cross-sect. A)	Vertical Component (normal or reverse)
Peg A	N20W/57E	N2W/52E			
Peg B	N67W/53E	N58W/52E		N50W/45E	
Qz C	N69W/65E		N65W/--	N69W/70E	
Peg D	N24E/86E	--			
Peg E					
H9-1	N7E/--	N-S/56W	N10E/64W	N11E/55W	R
H9-2	N7E/66W	--	N2E/54W	N11E/55W	R
H9-3				N9W/35W	R
H9-4				N1E/20W	R
H9-5			-- /48SE		
H9-6			-- /14N		
H9-7	N20W/67E	N24W/70E			N
H9-8	N89E/ ---	N86E/66W			R
H10-1		N7E/65W(?)			
H10-2	N8E/63W	N4E/66W	N-S/60W		R
H10-3	N9E/ --	N10E/64W	--		R
H10-4		N78E/76W			

midplane map (Fig. 4.3). Other segments, displaced by an E-W fault, are found on the extensometer drift wall, on the midplane map near the extensometer drift, and in the center of the FS drift floor map.

Pegmatite D is less useful as a marker because its near-vertical dip meant that it was rarely intercepted by the vertical boreholes. Its interpreted position can be seen in the midplane map (Fig. 4.3) and its interpreted intercept on the extensometer drift wall in Fig. 4.2.

The pair of parallel faults, H9-1 and H9-2, strike about N5E and dip 60W. Their apparent offset can be viewed on the various exposed surfaces which also reveal that these are oblique reverse, rather than normal faults. The sectional view in Fig. 4.4A shows a combined apparent offset of about 2 m for the two faults. Displacement in the horizontal plane (Fig. 4.1) is 1 m, although extrapolations in the midplane (Fig. 4.3) indicate that displacement is a fraction of a meter. Their true dip and relationship to the H9 heater hole is best viewed in vertical section H9C (Fig. 4.4C) which is almost perpendicular to the strike of H9-1 and H9-2.

Significant faulting must have occurred between the full-scale and extensometer drifts, because none of the pegmatites are found on the EX drift wall where simple projection would place them. The mid-plane map shows a plausible solution. An E-W fault labeled H9-8 is shown with 5 m of horizontal displacement and a likely vertical displacement component of several meters. The existence of H9-8 is in accord with faults mapped on the full scale floor and extensometer drift wall (see Figs. 4.1 and 4.2); however, it could also be shown as a series of en echelon faults of total equivalent displacement. Table 4.2 gives an approximate E-W strike and a dip of 66N to this major fault. The resulting interpretation of individual dikes and faults found on the extensometer drift wall appears satisfactory, as pegmatite A, fault H9-1, and pegmatite D are found there with similar strikes, dips, and relative separations as in the full-scale drift. Fault H9-2 has disappeared, however, and the exposure of pegmatite D is complicated by the convergence of pegmatite B and other faulting.

Other offsets in the H9 area are induced by faults H9-3 through H9-7, as well as by lesser, unnamed faults. Displacement magnitudes of these five faults appear to be on the order of 1 to 2 m. Fault H9-7, which is exposed on the extensometer drift wall (Fig. 4.2), is difficult to trace because of its near-vertical dip and its predicted intersection with only a few boreholes. Because its location has not been confirmed, its projected position has been omitted from the midplane map.

The offsets shown in the midplane map of Fig. 4.3 reveal the relative age of the faults. The E-W striking fault designated H9-8 must postdate the movement along the N-S faults (H9-1,2,3,4,7) and probably also postdates movement along the N60W faults (H9-5 and 6). It is noteworthy that both the N-S and E-W faults are reverse faults (Table 4.2).

In the H10 area, the most prominent features are the pair of parallel faults, H10-2 and H10-3 (see Fig. 4.1). The apparent offsets of pegmatite caused by faults H10-2 and -3 in the horizontal plane of the FS-drift floor is about 3 m. Direction of horizontal motion along the two faults could not be determined, but it is likely that the total offsets across the two parallel faults is 6 m or more. In vertical section (Fig. 4.5A), they are shown to be reverse faults. Both of these N-S striking planes project to, and have been identified in, the wall of the extensometer drift, as shown in Fig. 4.2. Thus there is no evidence for E-W faulting in the H10 area as there is in the H9 area.

The orientation of all major faults and dikes identified in the full-scale and extensometer drifts are summarized in the pole plot of Fig. 4.7. The quadrant labels such as W/E serve as a reminder that the poles in the southwest quadrant of the pole plot represent fault planes striking NW and dipping to the east. Note the lack of consistent grouping of the pegmatite dike and quartz vein orientations, and the consistent orientation of the N-S striking, 60W faults H9-1 and -2, and H10-1, -2, and -3. Their orientation is remarkably consistent with the four discontinuity planes determined in the time-scaled drift by Thorpe (1979).

4.3 The Fracture Cross Sections

The fracture cross sections presented in Fig. 4.4 (H9) and Fig. 4.5 (H10) are unusual in that they are drawn along radial planes with a common point of intersection at each central heater borehole. A good technique for becoming familiar with the cross sections is to view the H9 sections sequentially, keeping in mind the position of the key pegmatite A while moving from section to section. In so doing, the effect of changing perspective upon observed dip will become readily apparent. Beware of the left-right reversal of view in progressing from section H9 B to H9 C.

4.3.1. Calculation of apparent dip

The two measured angles α and β (see Section 3.3) describe the orientation of a fracture plane with respect to the borehole in which an oriented core was obtained. To extrapolate fracture planes in vertical cross sections,

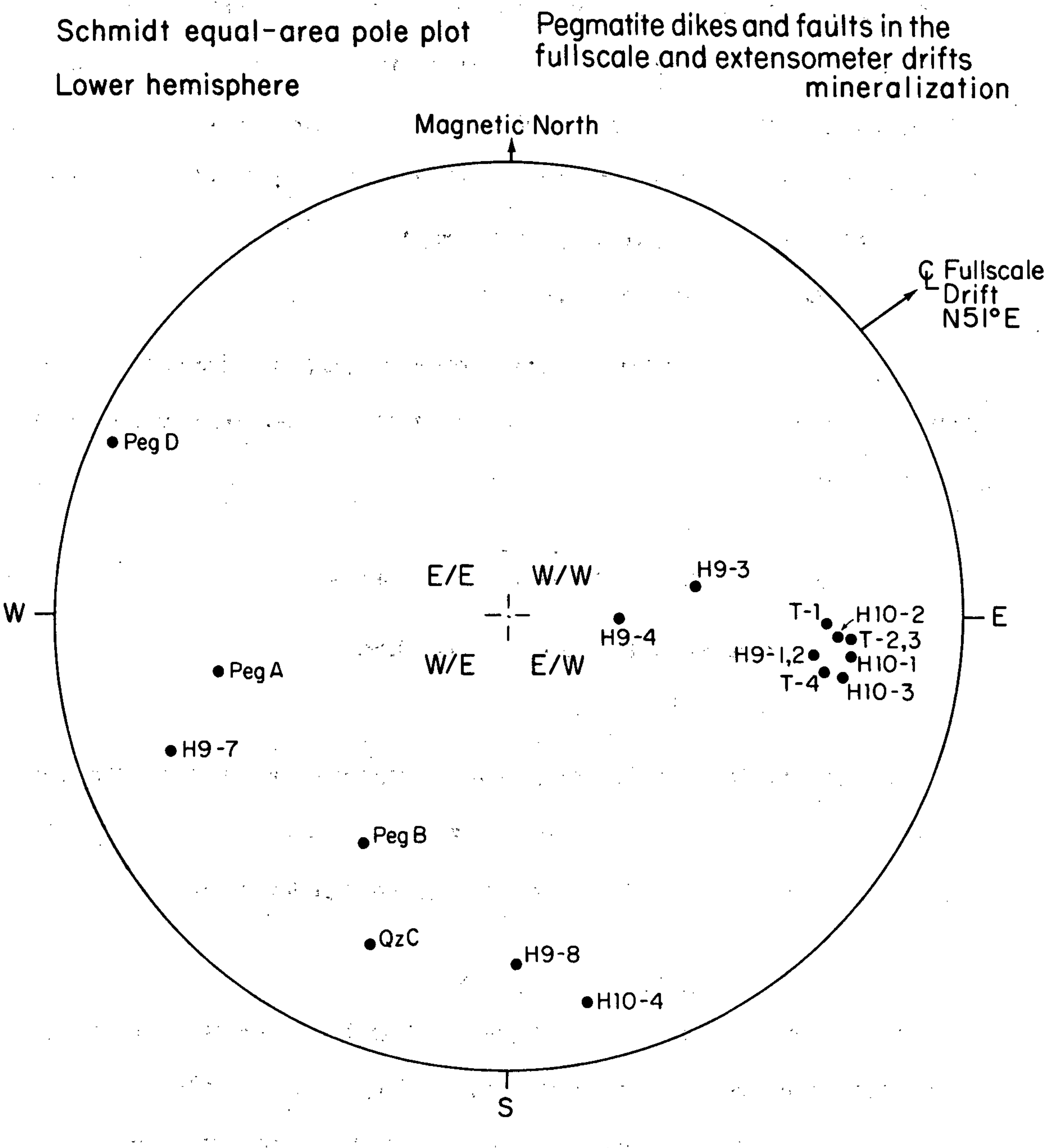

XBL 835-1838

Fig. 4.7. Pole plot of major dikes and faults in full scale and extensometer drifts, along with poles T-1 through T-4 identified in time scale drift by Thorpe (1979). Strike/dip directions are noted in each quadrant. For example pole H9-3 in quadrant W/W represents a plane with strike-dip of N09W/35W.

an apparent dip angle must be computed for each fracture intercept. The apparent dip θ is defined as the angle between a horizontal plane and a second line established by the intersection of the vertical cross-section and the fracture plane. For vertical boreholes the apparent dip is related to the measured angles α and β by using expression:

$$\tan \theta_V = \tan (90^\circ - \alpha) \cos(\beta - \beta_p) \quad ,$$

where β_p is the angle between the reference line and the vertical cross section (refer to Table 4.1). The corresponding expression for horizontal boreholes is:

$$\tan \theta_H = \sqrt{\tan^2\alpha + \tan^2\beta} \;\; \cos(\alpha \sin\beta) \quad .$$

It was later found that a simpler expression,

$$\cot \theta_H = \cot \alpha \cos\beta \quad ,$$

produces nearly identical results for horizontal boreholes. An additional correction of about 6 degrees was added or subtracted as appropriate to compensate for the upward incline of the horizontal boreholes.

4.3.2. Display of fracture data

The apparent dip of a fracture intercept is plotted with a short line segment on the vertical cross sections (Figs. 4.4 and 4.5). The orientation, thickness and dominant mineral type of each fracture intercept are also posted next to each line segment. Symbols were put on only for fractures filled with epidote or calcite mineralization. To minimize clutter, fractures filled with chlorite are plotted without any symbol, although many fractures filled with epidote or calcite have chlorite infilling as well.

4.3.2 Fracture Reconstruction

Because the fracture reconstruction for the H9 heater area is so detailed, the plots became quite cluttered when the interpreted fracture planes were overlain on the raw data. For this reason the raw data cross sections are relegated to Appendix B and the interpreted H9 area cross sections are shown in Fig. 4.4, without the subsidiary information. The reconstructed H10 heater area cross sections were far less complicated, however. Consequently, the interpreted fracture positions in the H10 area are shown overlain on orientation and mineralogical information in Fig. 4.5.

For each cross section, the boreholes with oriented core constitute the most important source of information for characterizing and mapping discontinuities in the H9 and H10 experimental areas. The unoriented core from the 46 and the 38 mm holes was used mainly to check the oriented core results. In a few cases it was apparent that the same fracture was sampled in neighboring 38 mm holes. The fractures were then connected on the cross section and assumed to exist between the boreholes, to verify that such fractures indeed belonged to the same discontinuity, the actual core and the fracture logs. In such comparisons, one must remember that even if the fractures are planar over a distance of tens of meters, the fracture surfaces undulate on a scale of decimeters and therefore strike and dip vary locally. Other uncertainties are the accuracy of the orientation mark, which is about ±5°, and the accuracy of the measured strike and dip, which is also estimated to be ±5°.

Fractures were extrapolated between boreholes based on the dip, strike, fracture infilling type and thickness, and proximity of fractures in adjacent boreholes. The most important criterion was the near-equality of the azimuth of fracture intercepts in adjacent boreholes. Intersecting pegmatite veins and highly fractured zones were also used. All distinctive discontinuities were then extrapolated along each cross section to a maximum depth of about 13 m below the drift floor and laterally from the northwestern wall of the extensometer drift to the downward projections of the northwestern and end walls of the full-scale drift.

4.3.2.1. Cross-section H9 A (Fig. 4.4A). The pegmatites and faults with epidote mineralization are the dominant features presented in Fig. 4.4A. Pegmatites A, B, and D, and quartz vein C are identified in the cross section, and four faults--H9-1, -2, -3, and -4, representing the major discontinuities--are identified in the boreholes. Since the orientation of these four faults is similar (see Table 4.2) they are assigned to the same fracture set. Faults H9-1 and H9-2 offset pegmatite A in the vertical plane by approximately 1 m for a total displacement of more than 2 m. The offset caused by the minor parallel or sub-parallel epidote-filled faults is generally less than 0.5 m. The horizontal displacement caused by faults H9-1 and H9-2 in the plane of the full-scale drift floor is only 1 m.

Pegmatite B, present at the bottom of boreholes E6, E7 and E8, is intersected by discontinuity H9-4 in boreholes E6 and E7. This discontinuity was extrapolated to the epidote-filled fracture in the bottom of borehole U3; the absence of pegmatite A in this borehole indicates that this pegmatite is also offset by H9-4.

The quartz vein C, prominent in the drift floor between boreholes E7 and E8, was found in three places in borehole E7. This has been interpreted as an "en echelon" faulting, which agrees well with interpretation of the offset of pegmatites A and B.

Although the small pegmatite D is clearly seen on the FS-drift floor (Fig. 4.1), where it is intersected and offset 1 m by discontinuities H9-1 and H9-2, it was difficult to locate it in boreholes because of its near-vertical dip. It is shown in Fig. 4.4A between boreholes E6 and E7 on the basis of the pegmatite intercepts in those two boreholes.

The epidote-filled fault H9-3, although present in this cross-section, is not well developed and therefore will be discussed in more detail in cross section H9 B.

To obtain the extent of subsurface discontinuites above the drift floor, both walls were mapped; the resulting fracture map was projected on the centerline of the drift. This projection shows clearly that pegmatites A and B, also present in both drift walls, are intersected by faults H9-5 and H9-6. These two discontinuities have orientations N54W/48E and N68W/14N respectively and belong to a different fracture set than discontinuities H9-1 through H9-4.

A number of calcite-filled fractures were found in both oriented and non-oriented boreholes in the cross section. Calcite-filled fractures present in oriented boreholes E6, E7, and E8 seem to correspond well with calcite-filled fractures extrapolated between non-oriented boreholes U1, U2, U3, T13, and T14. Several intersect the epidote-filled fault, thus providing the sequence of faulting which followed the intrusion of the pegmatite. An epidote-filled fracture being intersected by the calcite-filled fracture is shown in the thin-section photograph of Fig. 4.8. The first fault in the sequence was the intrusion of pegmatite, followed by the appearance of epidote-filled faults in the pegmatite. The last in this series was the development of calcite-filled fractures and faults.

4.3.2.2 Cross Section H9 B (Fig. 4.4B). The epidote-filled faults H9-1 and H9-2 are present in boreholes U4 and U5 at depths z = 342 m and z = 344 m respectively. Two additional discontinuities, H9-3 and H9-4, intersect boreholes C1 and M6, where this displacement was measured as 0.3 m for H9-3 and 0.4 m for H9-4. A number of minor epidote-filled faults in borehole M6 are interpreted to be parallel to the fracture set H9-1, -2, -3, -4, shown in cross section H9 A.

4.3.2.3 Cross Section H9 C (Fig. 4.4C). Five vertical and five horizontal boreholes, which are included in the H9 C cross section, provide a good data base for reconstructing the fracture system.

Pegmatite A is present in the middle of vertical boreholes H9 and T15 and at the bottom of horizontal boreholes U26 and E23. It is offset by the epidote-filled faults H9-1 and H9-2, which intersect boreholes T17, E9 and E10 at the depths of z = 340 m, Z = 341 m and z = 342 m respectively. Orientation of discontinuities H9-1 and H9-2 is N10E/60W. Another set of epidote-filled fractures parallel to faults H9-1 and H9-2 intersect horizontal boreholes from the extensometer drift. Faulting of pegmatite A in horizontal borehole E23 is associated with calcite mineralization in the fractures. This is most likely because the fault plane reopened and the

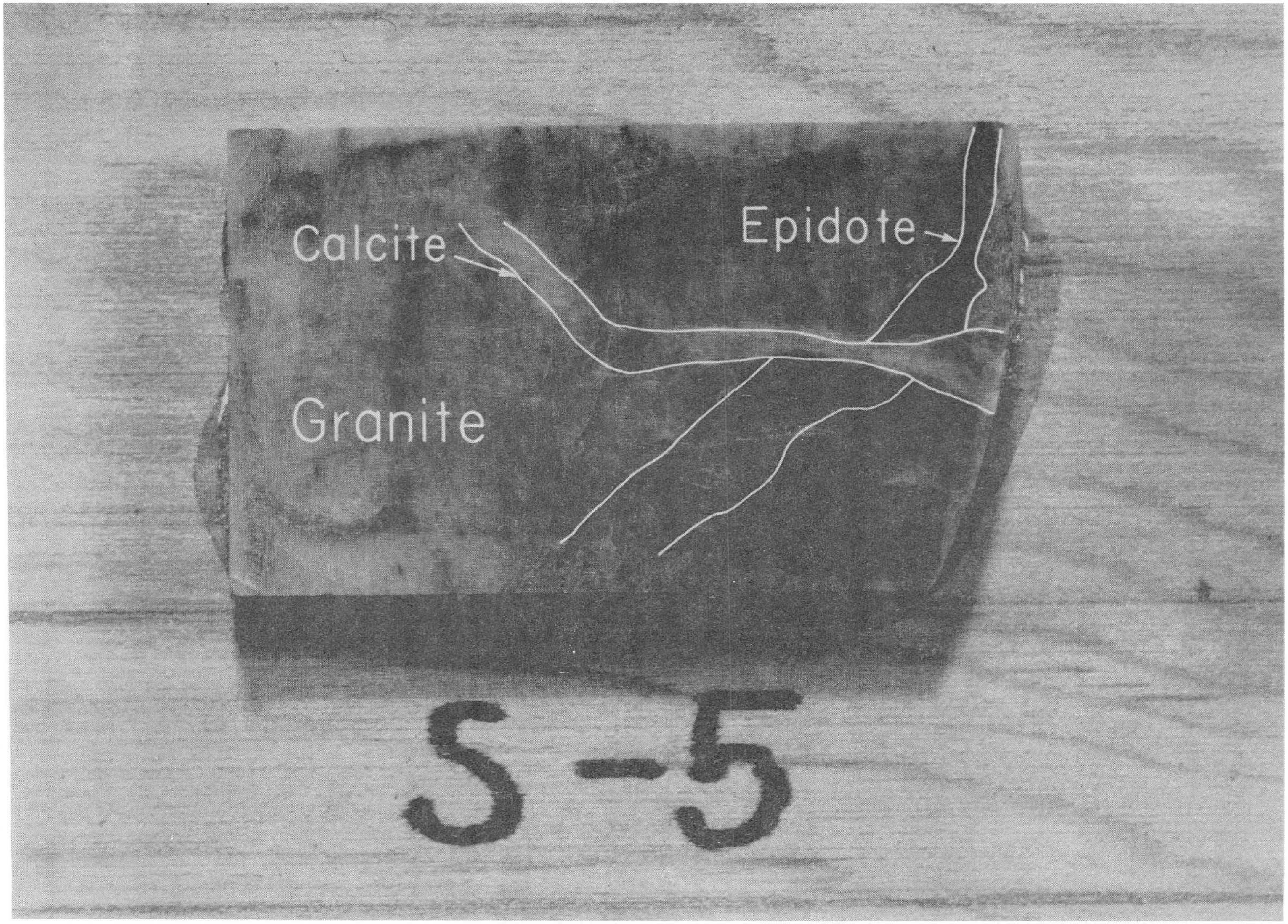

XBB 805-5923A

Fig. 4.8. Split core showing a fracture with epidote infilling which is offset by a calcite-filled fracture.

fracture was filled with calcite long after the actual faulting.

Some of the calcite-filled fractures can be extrapolated between three or four boreholes; the most prominent of these extends from borehole E21 through boreholes E22, E23, T15, E9 and E10. The location of other concentrations of calcite-filled fractures will be discussed in Sect. 4.4.

4.3.2.4 Cross Section H9 D (Fig. 4.4D). Lack of data, which is due to the small number of boreholes in the cross section, allows only pegmatite A to be extrapolated between boreholes H9 and C11.

4.3.2.5 Cross Section H9 E (Fig. 4.4E). Pegmatite A intersects vertical borehole H9 and horizontal boreholes E19, U27, and E20. Faults with offsets less than 1 m have been interpreted to account for hole-to-hole variations in apparent strike and dip. A major unresolved problem in the reconstruction of the pegmatite intercepts is the presence of a 3.2 m long intercept of pegmatite in horizontal borehole E20; it commences about 2.3 m from the collar. This could be a local widening of pegmatite A; however, its presence has been virtually ignored in the fault interpretation. Pegmatite A is again seen in section H9 E near the wall of the extensometer drift, where it is displaced by 6 m. The interpreted fault mechanism for this relatively large offset has already been discussed in connection with fault H9-8 in Fig.4.3.

Several epidote-filled fractures, found in horizontal boreholes E19, U27, and E20, can be traced to vertical borehole E11. This borehole is also intersected by epidote-filled discontinuities H9-1 and H9-2.

4.3.2.6 Cross Section H9F (Fig. 4.4F). Two distinct zones of epidote-filled fractures were found in borehole M7 at depths z = 339-341 m and 344-349 m. Borehole M7 also includes several calcite-filled fracture zones at depths z = 344 m, 345 m, 347 and 348 m. Except for the pegmatites A and D, no other major discontinuities were detected in any borehole of this cross section.

4.3.2.7 Cross Section H9 G (Fig. 4.4G). Pegmatite A intersects vertical boreholes U8, U7, U6, T18 and H9. Because this cross section is nearly parallel with the strike of Pegmatite A, the apparent dip is nearly horizontal. Although traces of pegmatite were also found a few meters from the end of borehole E24, it is uncertain whether this pegmatite is part of pegmatite A.

Two pegmatites, B and E, were found in horizontal boreholes E24, C8, E25, U18 and E26. Although the apparent dip of the dikes varies due to the different sectional orientations, pegmatite B in this cross section correlates well with pegmatite B in cross-section H9 A found in the lower end of the boreholes E6, E7, & E8. Pegmatite E in this cross section could not be successfully correlated with other pegmatite occurrences, but it may connect to one of the unidentified dikes located on the drift floor between the H9 and H10 heater (Fig. 4.1). Pegmatite B strikes perpendicular to cross section H9G and so if the pegmatite is extrapolated from its location in E24-E26 to the floor in the full scale drift it can be seen that the correlation, in fact, is quite good.

Four epidote-filled fractures intersect boreholes E24, C8, E25, U18, and E 26, and another three fractures can be traced between boreholes E24, C8 and

E25. Calcite-filled fractures are concentrated mainly in the horizontal holes (see Sect. 4.4).

4.3.2.8 Cross-section H9 H (Fig. 4.4H). Pegmatite A intersects boreholes U10, U9, H9 and C2 and is faulted in four places. While discontinuities H9-1 and H9-2 in boreholes H9 and C2 correlate well with other cross sections, the two in boreholes U10 and U9 cannot so be correlated with any degree of confidence.

4.2.3.9 The H10 Cross Sections (Fig. 4.5). Cross sections A-H from the H10 area, comparable in orientation and convention to those of the H9 area, are presented in Figs. 4.5A-4.5H. However, as discussed earlier, much less interpretive effort has been expended on results from the H10 area. The primary content of these cross sections is the apparent dip and strike data posted alongside the boreholes. These cross sections are therefore complementary to the H9 data cross sections presented in Appendix B.

Interpretation of the H10 area fractures and faults is inherently more difficult than it is for the H9 area because of the relative scarcity of pegmatite and quartz markers. More information could be interpreted from the available data if it appears to be warranted by the requirements for the thermomechanical analysis in the H10 heater area.

4.4 Zones of Intense Fracturing

Because of the potential importance of localized zones of intense fracturing to the displacements induced by the H9 and H10 heater experiments, some of the outstanding aspects of these zones in the heavily drilled areas are discussed here. Fracture intensity can be examined in the floor maps of

Figs. 4.1 and 4.3 and in the cross-sections of Figs. 4.4 and 4.5. However, in Fig. 4.4 the extended lines denoting the interpreted extent of the epidote fractures reduce the apparent significance of the chlorite and calcite fractures. For this reason the figures of Appendix B are better suited for examining zones of high fracture intensity in the H9 area.

In addition, fracture intensity is shown in a sequence of elevation plan maps encompassing 2-m intervals in Figs. 4.9 and 4.10. These were compiled from all fractures posted on the cross sections, and then contoured to give the general trend of fracture frequency. The H9 data of Fig. 4.9 are self-consistent in that both open and closed fractures are included; however, the H10 plots of Fig. 4.10 are from a mixed data base (Table 3.4). Some short core intervals were so intensely fractured that no count was made. In such cases a value of 1 fracture per cm was assigned to the fractured length. For example, in the 340-342 m interval, hole E6 contained 25 single fractures plus a 34-cm fractured zone; hence an entry 59* is posted in Fig. 4.9.

4.4.1 <u>H9 Area</u>.

The detailed floor map of Fig. 4.1 shows an area of high fracture intensity that seems to strike N-S and lies immediately adjacent to, and west of, heater hole H9. This crude trend is confirmed by the fracture intensity map in Fig. 4.9, which shows a roughly N-S striking zone of high fracture intensity. Five boreholes with fracture frequencies exceeding 40 per 2-m interval are within this trend.

It might be expected that this zone is controlled by the major epidote faults H9-1 and H9-2, which dip to the west. Such an association seems apparent in cross section H9A (Fig. B.1). Inspection of the three vertical

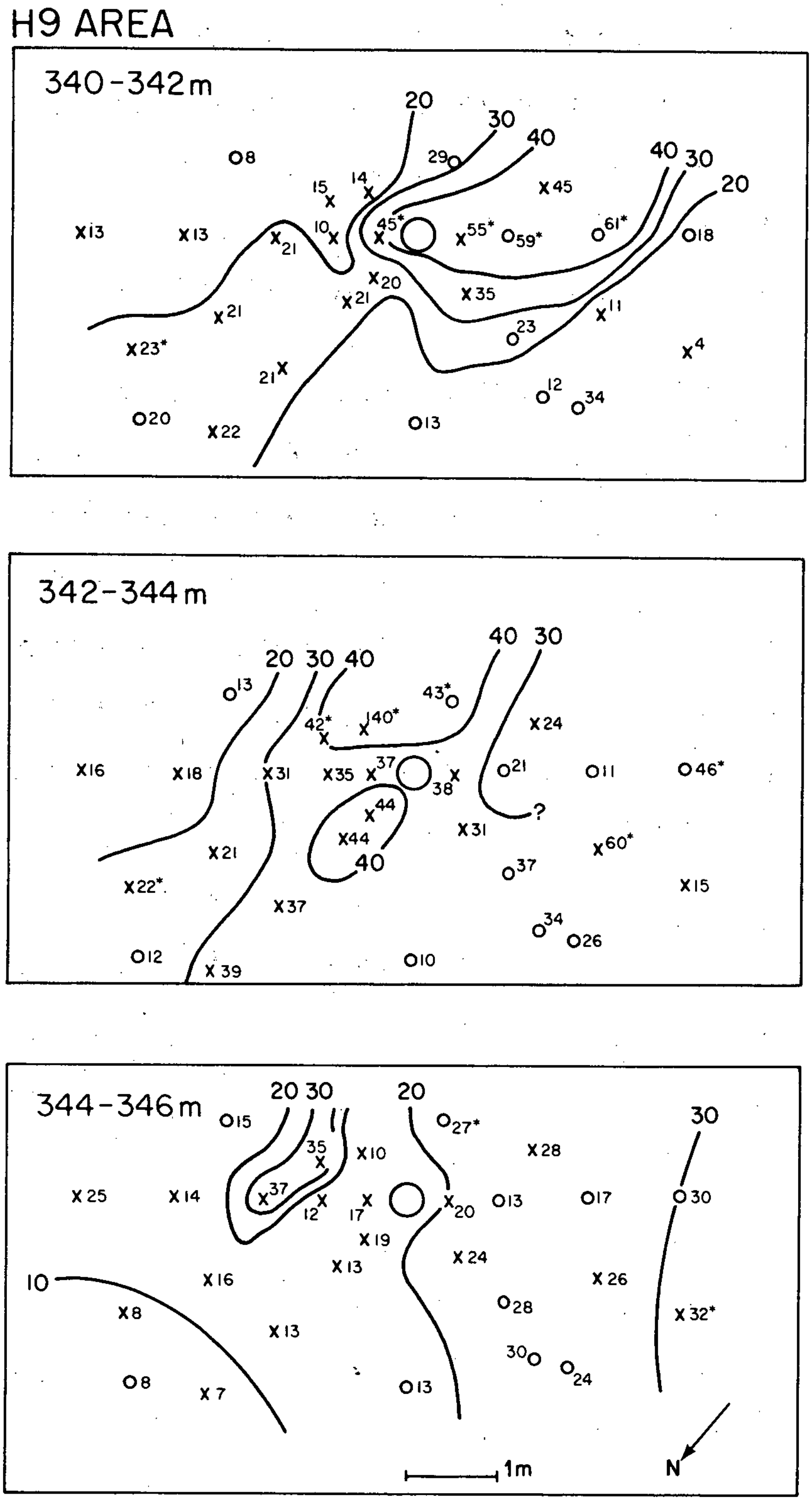

XBL 812-2615

Fig. 4.9. Fracture intensity as a function of elevation in vertical boreholes in H9 area. H9 heater midplane is at 343 m. Data and contours give number of open + closed fractures in 2 m interval. Asterisk indicates that a fractured zone is included, pro-rated at 1 fracture per cm. Isolated single data points are not accounted for in the contouring. View is toward extensometer drift.

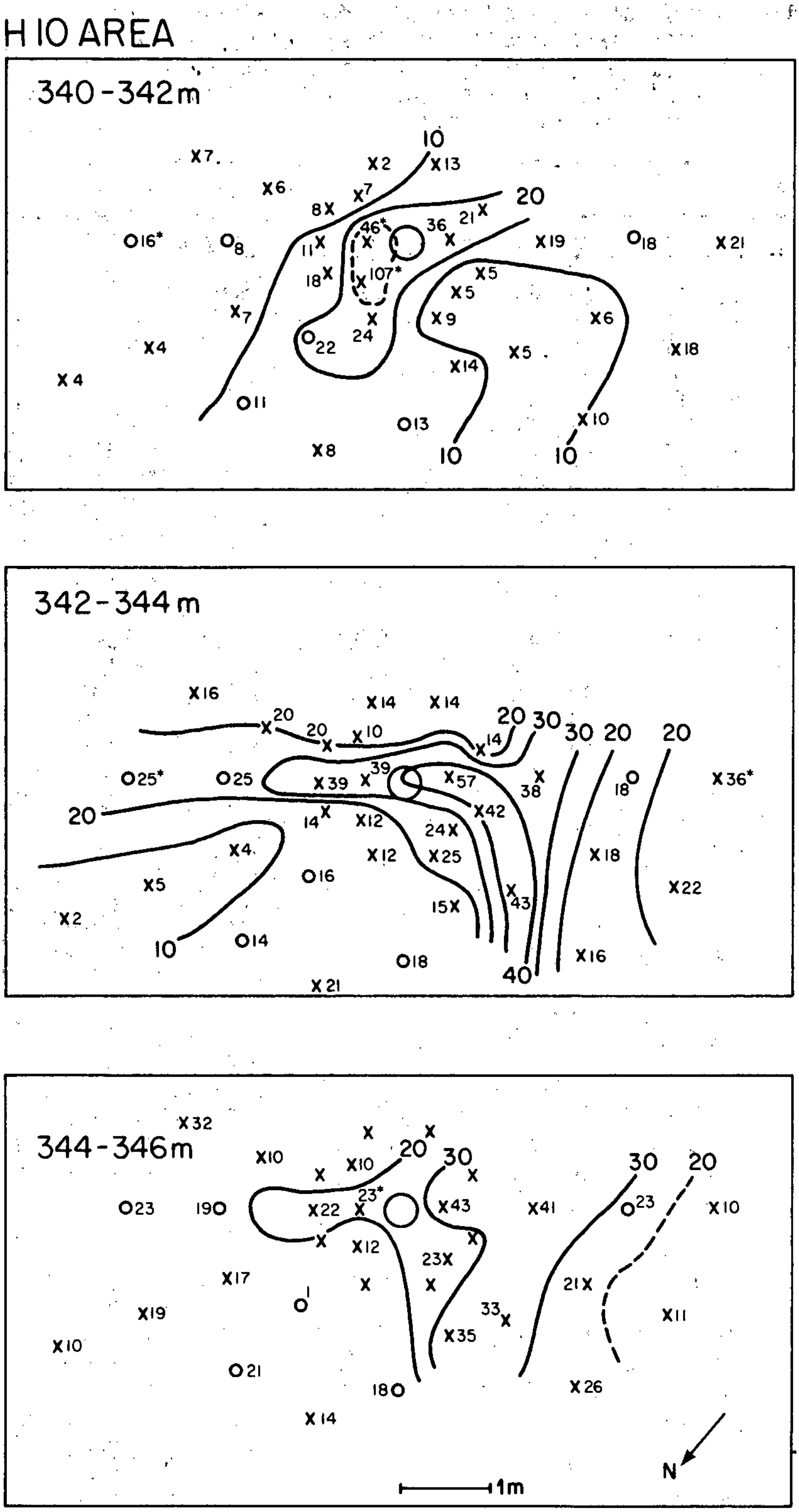

XBL 812-2616

Fig. 4.10. Fracture intensity in vertical boreholes in H10 area, given as number of fractures per 2 m interval. Data from 76 mm holes (small circles) are from open + closed fractures; data from 38 mm holes (small x) are open fractures only. For other details, refer to Fig. 4.9.

Table 4.3. Locations of calcite-coated borehole fractures (where there are 3 or more fractures per meter of borehole). Asterisk (*) denotes frequencies of six or more. Intervals (meters) are given in the mine z-coordinate for vertical holes; in distance from the collar for horizontal holes.

H 9 Area			H 10 Area		
Section	Hole	Interval (m)	Section	Hole	Interval (m)
H9A	U3	342-343	H10A	E13	343-346*
		344-345		E12	339-340
	U2	341-342			343-344*
		343-344*			347-348
	U1	343-345		T20	340-341
	T13	343-344			342-345*
	E6	349-350			346-347*
	E7	350-351*		T22	342-343
	E8	349-351*			344-347*
				U11	341-342
H9B	C1	339-340			344-345
		344-345		E14	349-350*
H9C	E10	340-341	H10B	C4	344-346
		347-348		C3	342-344
	M8	340-341		H11	340-341
		342-343			343-344
		347-348		H15	339-340
	E9	346-347			343-345*
		351-352		U14	340-341
	T15	344-345			
	E21	2-3	H10C	U16	341-342
		5-6			343-344*
	C6	0-1		T23	343-345
		3-4		T21	339-341*
		5-6*			345-347*
	E22	4-6		E30	0-5
		9-10			8-9
	U26	4-6			11-13*
	E23	0-3*		U23	1-2
		12-13			7-10
				E31	7-8
H9E	E11	340-341			10-11
		346-348		E32	3.5-4.5
	E20	6-10*			7-8
					12-13*
H9F	U22	2-3			
	C12	1-2	H10D	C5	340-341
				U29	4-5*
H9G	U7	343-345			
	T18	342-343	H10E	E15	344-345*
		344-345			346-348
	E24	0-2			350-351*
		4-5		E27	8-9
	C8	1-2		U24	1-2
	E25	4-5		C14	2-3
		9-10			7-8
	U18	10-12		E29	6-8
	E26	0-2*			10-11
		11-13			

Table 4.3. (continued)

H 9 Area			H 10 Area		
Section	Hole	Interval (m)	Section	Hole	Interval (m)
			H10F	H17	340-341*
				C10	2.5-3.5
				U30	4-5
			H10G	E17	339-341
					344-347*
				E16	341-342
					344-345
				U25	1-2
					5-6
				E34	1-2
					6-7
					10-12
				C15	1-4
				E35	2-5
					8-9
					11-13
			H10H	U19	344-346
				U18	344.5-345.5
				H18	340-341
				H14	341-342

extensometer holes E6, E7, and E8 shows fractures concentrated in the footwall of the H9-1/H9-2 fault system. Although this association probably persists, it does not dominate the overall picture, as can be seen in the 342-344 m (midplane) fracture intensity contour map of Fig. 4.9. Instead of migrating to the west, the contour pattern has broadened and even shifted to the east. The pattern seems to be complicated by the east-dipping pegmatite A or by an unidentified E-W striking feature.

The lowermost of the three fracture maps in Fig. 4.9 shows that fracturing has decreased below the heater H9 heater midplane.

4.4.2 H10 Area

Of the 15 extensometer holes in the H10 area, six have zones of high fracture frequency within reasonable proximity of the heater borehole. These zones can be distinguished by visual inspections of the cross sections. Vertical borehole E12, located 2 m from H10, has a zone of predominantly calcite fractures between the midplane and 1-m. Both E12 and its neighbor E13 have a high fracture density from the midplane to about 4 m below the midplane. Hole E14, also in cross section H10A, has a 1-m zone of chlorite fractures from 1 to 2 m below the midplane at a radial distance of 2.5 m. Likewise, borehole E15 at 2 m radial distance also contains a 1-m zone of calcite-filled fractures between -1 and -2 m. Fracturing in the vertical E-holes tends to be more concentrated immediately below the midplane rather than immediately above it.

The sonic waveform logs presented in Appendix D provide an independent visual indication of the degree of fracturing in the vertical E-holes. Four zones in holes E12, E13, and E14 are the most anomalous, based on perturbations of the shear-wave portion of the record. The waveform record of hole E15 appears to be the most generally disrupted throughout its length.

Figure 4.10 shows that progressive increase of fracturing with depth is a general feature of the H10 area, as observed in most of the vertical boreholes. In the 340-342 m interval, fracture density exceeding 20 per 2-m interval is present only in a limited area which includes the H10 heater holes. In the 342-344 and the 344-346 m intervals the area enclosed by the 20 per m fracture density contour broadens considerably and the overall fracture density increases.

During examination of the fracture density in the H10 horizontal holes, only 3 m of core from the ends of the horizontal holes were relogged to include the closed fractures (Sect. 3.3). This makes holes E27, E32, and E34 appear to be the most intensely fractured. Of these three, only E34 lies in the heater midplane. Its 2-m zone of more intense fracturing lies 2 to 4 m from H10.

4.4.3 Calcite Fractures

Discussion in Section 5.3 will show that the calcite-coated fractures are mechanically the weakest of the three mineralogical types present, as indicated by the open-versus-closed fracture statistics. Hence calcite fractures are highlighted by showing their projected locations on the H9 midplane map of Fig. 4.3, and by summarizing the 1-m core intervals with three or more calcite fractures in Table 4.3. The table was compiled by scanning the cross sections of Fig. 4.5 and Appendix B.

Occurrences of calcite fractures can be described as dispersed. However, the most concentrated zones occur at the bottom of holes E6 and E7

(Fig. B.1 and Table 4.3) in the H9 area. A number of intercepts are found close to pegmatite A in holes U3, U2, U1 and T13 (also in Fig. B.1). Calcite fractures seem to be almost completely absent in the first few meters on the hanging wall side of faults H9-1 and H9-2.

In the H10 area, calcite fractures are well distributed throughout the cross sections. Holes E12, at 343-344 m, and hole E15, at 344-345 m, show particularly well defined zones of calcite fractures. The cross sections show more calcite fractures occur in the H10 area than in the H9. This observation is confirmed by the statistical summary in Table 5.2, presented in the next section.

5. STATISTICAL ANALYSIS OF DISCONTINUITIES

5.1 Methodology

5.1.1 Introduction.

In the previous chapter, the vast majority of fractures were shown to be discontinuous and not traceable between two boreholes despite the high drilling density. To complete the picture of the fracture system, it was necessary to complement the mapping approach with a statistical analysis. The discussion in this chapter is based largely on stereonet pole plots compiled separately according to fracture mineralization, hole location, hole orientation, and whether the fracture was open or closed when core was retrieved. Although this approach has its limitations, it does allow examination of the influence of a variety of parameters on fracture character and comparison of observations between the experiment areas.

In addition to the stereographic plots, a Rock Quality Designation Index (RQD) was calculated and plotted for all vertical E and M boreholes in the full-scale drift. RQD is defined as the sum of the length of all core pieces 10 cm or larger over a given interval length. RQD is consequently between 0.0 and 1.0, with 1.0 meaning that all core pieces are larger than 10 cm. A further discussion of RQD is given by Deere (1963). A report by Olkiewicz, et al. (1979, Appendix D) presents the RQD results in log fashion alongside pictorial logs of fracture location. The RQD results for the E-holes also appear in Appendix D of this report, but for most purposes they have been superseded by the cross-sectional diagrams of Section 4 of this report. Although the RQD values may prove to be useful for engineering purposes, our analysis is based on stereonets only.

5.1.2 The Equal-Area Stereonet

Stereographic projections are commonly used to present the strike and dip of planar surfaces (Goodman, 1976). The example of Fig. 5.1 shows an epidote fault in the H9 area projected onto the lower hemisphere of an equatorial equal-area stereonet. The dashed line represents the intersection of the fault plane with the lower hemispherical surface, projected back to the equatorial plane. However, it is preferable to plot the stereographic projection of the normal to the plane rather than the plane itself. The pole projection in Fig. 5.1 includes arrows showing the area spanned by ± 5 degree variations in strike and dip.

The method of projection determines the properties of the stereogram. For statistical purposes, it is advantageous to use the equal-area projection, often called the Schmidt stereonet, which preserves solid-angle areas but distorts angles of intersection (Goodman, 1976). All stereograms in this report are equal-area projections.

The two angles α and β (see Section 3.3 for definitions) must be converted to true strike and dip before the data can be plotted on stereograms. For vertical boreholes, where the measured angle α is the complement of true dip, the procedure is straightforward, as Table 5.1 demonstrates. This conversion is more complicated for non-vertical boreholes. The conversions were done by University of Waterloo personnel using an existing computer code, following the procedure described by Lau and Gale (1976).

Fig. 5.2 demonstrates a good agreement between the data base and conversion algorithms. The poles of quartz veins encountered in horizontal

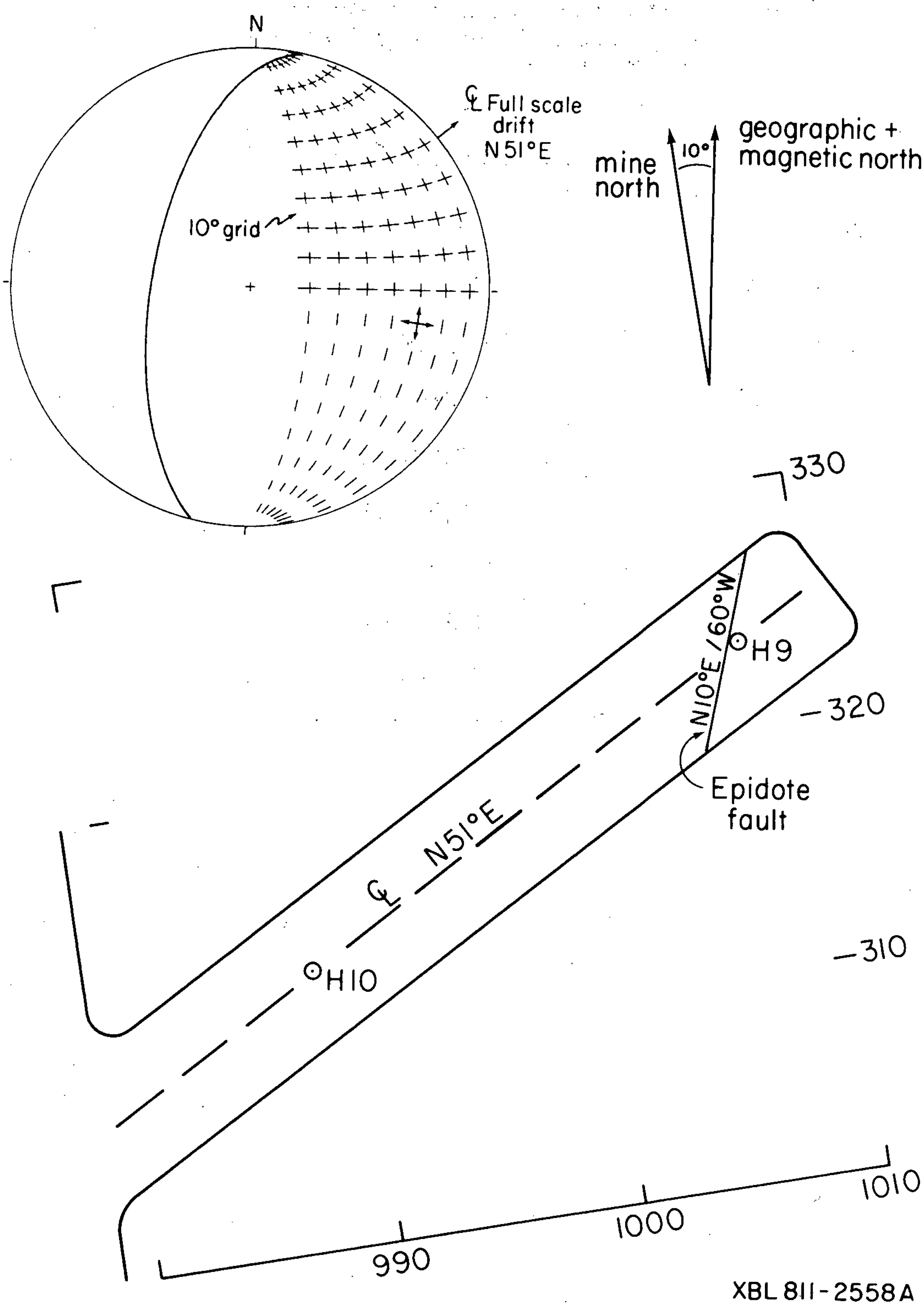

Fig. 5.1 An epidote fault plane and its normal projected onto the lower lower hemisphere of an equal area stereonet. The plan map of the fullscale drift shows the mine coordinates rotated 10 degrees to account for the offset with respect to true north.

Table 5.1. Sample conversions of measured orientation angles to geologic strike and dip.

α	β	Geologic strike and dip
30	0	N39W/60W
30	45	N 6E/60W
30	90	N51E/60W
30	135	N84W/60E
30	180	N39W/60E
30	225	N 6E/60E
30	270	N51E/60E
30	315	N84W/60W
30	360	N39W/60W

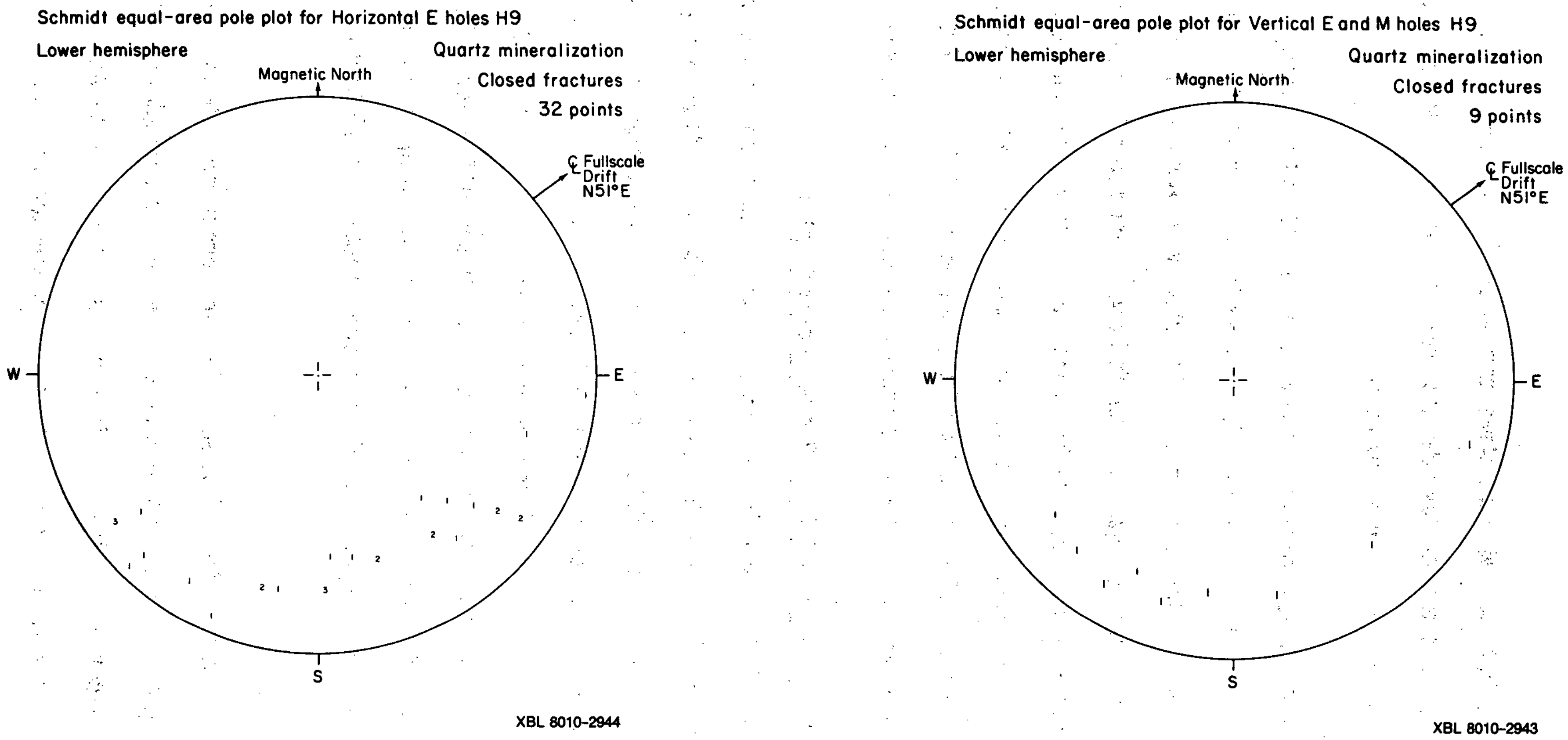

Fig. 5.2 Equal area pole plots of quartz veins intercepted in H9 area boreholes, plotted separately for vertical and horizontal boreholes.

and vertical holes fall within the same zones on the pole plots. The quartz veins furnish good control because they were limited in number and were relatively easy to distinguish in core.

All fractures from oriented core were hand-plotted, using a separate plot for each mineral in each hole. The holes were then divided into four groups corresponding to the horizontal and vertical holes in the H9 and H10 areas. Each of these groups was divided further into mineral subgroups for chlorite, calcite and epidote. The plotted poles in each subgroup were summed up over each 10 x 10 degrees area and the number was recorded in the middle of the area. After the data base was established, different subgroup categories were summed, or results were presented as a percentage of total.

5.1.3 Description of Pole Plots and Statistics

A total of 3,248 individual fracture intercepts are shown on the pole plots of Appendix C. Table 5.2 serves as an index to the pole plots and also summarizes the statistical data for each plot. As shown by Tables 5.2a and 5.2b, the four major groupings are vertical H9, vertical H10, horizontal H9 and horizontal H10. A third set of plots listed in Table 5.2c sums the vertical and horizontal statistics for the H9 and H10 holes. However, no pole plots exist for the H10 holes in this third category because of the more restricted sampling of the closed fractures from horizontal H10 holes (see Section 3.3).

The finer subdivisions in Table 5.2 are organized, first, by whether a fracture was open or closed when the core was retrieved and, second, by the dominant mineral coating the fracture surface. In Appendix C, corresponding plots from the two areas are placed side by side for easy

Table 5.2(a). Index of stereographic pole plots and summary of pole plot statistics for vertical holes.

		VERTICAL HOLES									
		H9 (E_v + M)					H 10 (E_v)				
Mineral	Closed/ Open	no. of frac	frac/ m	main pole	second pole	third pole	no of frac	frac/ m	main pole	second pole	third pole
Chlorite	C	456	3.93	N33E/30W (8.1)			329	4.40	N12E/23W (3.3)	N20W/16E (3.3)	N32W/30W (3.0)
Calcite	C	47	0.40	N 6E/65E (6.4)			39	0.52	N17W/16E (8)		
Epidote	C	316	2.72	N20E/27W (4.7)	N 6E/56W (4.1)	N21W/25E (2.2)	44	0.59	N12E/50W (7)		
All	C	819	7.05	N32E/29W (6.6)	N 6E/55W (2.0)	N12W/25E N62W/29E (1.4)	412	5.51	N21E/48W (2.9)	N14E/21W (2.7)	N 1W/15E (2.2)
Chlorite	0	174	1.50	N34E/ 8W (5.7)	N61W/81E (2.3)		248	3.31	N17W/16W (5.2)	N20W/16E (4.0)	N25E/38W (3.2) N80W/68E (2.0)
Calcite	0	67	0.58	N12E/25E (3/67)	N42E/ 7W (8/67)		127	1.70	N38W/16E (4.7)	N79W/68E (3.9)	N59E/43W (3.1) N 6E/12W (3.1)
Epidote	0	20	0.17	N44E/ 7W (10.0)	N10W/16E (10.0)	N 5W/86E (10.0)	6	0.08			
All	0	261	2.25	N47E/ 7W (5.7)	N10E/26E (2.3)	N61W/72E (1.9) N50E/62E (1.5)	381	5.09	N22W/10W (4.5) N50E/ 8W (4.5)	N20W/16E (4.2)	N46E/21E (2.9) N38W/70E (1.6)
Chlorite	C+0	630	5.43	N32E/30W (6.3)	N10E/26E (1.4)		577	7.71	N20W/16E (3.6)	N20E/16W (3.3)	N79W/68E (1.2)
Calcite	C+0	114	0.98	N43E/ 8W (3.5)	N38W/70W (2.6)	N 6E/75E (2.6) N12E/25E (2.6)	166	2.22	N20W/16E (5.4)	N78W/68E (3.0)	N59E/42W (2.4)
Epidote	C+0	336	2.90	N24E/27W (4.8)	N 7E/57W (4.2)	N60E/10W (3.0)	50	0.67	N12E/51W (6.0)		
All	C+0	1080	9.33	N34E/29W (5.3)	N 7E/55W (2.6)	N13E/25E (1.3)	793	10.60	N22W/16E (3.8)	N20E/16W (3.0)	N7W/68E (1.5)

Table 5.2(b). Index and summary of pole plots for horizontal holes.

		HORIZONTAL HOLES									
		H9 (E_h)					H 10 (E_h)				
Mineral	Closed/ Open	no. of frac	frac/ m	main pole	second pole	third pole	no of frac	frac/ m	main pole	second pole	third pole
Chlorite	C	260	2.41	N 6E/66W (5.8)	N16W/85E (3.5)	N73E/59W (2.3)	100	3.27	N25E/38W (5.0)	N10E/26W (3.0)	N51E/67E (3.0)
Calcite	C	29	0.27				20	0.65			
Epidote	C	138	1.28	N 5W/86W (6.5)	N54E/60W (2.2)	N87E/66W (2.2)	15	0.49			
All	C	417	3.86	N 5E/65W (4.8)	N15E/85W (2.9)	N81W/60E (1.5)	135	4.42	N24E/38W (4.4)	N52E/67W (3.7)	N12E/26E (3.3)
Chlorite	0	247	2.29	N16W/75E (3.2)	N36W/78E (2.4)	N72W/80E (1.6)	270	2.52	N25W/86E (3.3)	N 5E/66E (2.2)	N56E/60W (1.9)
Calcite	0	125	1.16	N54W/88W (3.2)			153	1.43	N25W/86E (3.3)	N16E/86W (2.6)	N88W/66E (2.0) N21E/47E (2.0)
Epidote	0	6	0.06				12	0.11			
All	0	378	3.50	N16W/75E (2.6)	N36W/78E (2.4)	N66W/84E (1.9)	435	4.05	N26W/86E (3.2)	N15E/86W (2.3)	N55E/60W (1.6)
Chlorite	C+0	507	4.69	N 6E/76W (3.7)	N16W/86E (3.4)	N55W/88W (2.0)	370	3.45	N25W/86E (2.4)	N55E/61W (1.9)	N15E/86W (1.9)
Calcite	C+0	154	1.43	N55W/88W (2.6)			173	1.61	N26W/86E (2.9)	N15E/86W (2.3)	N35E/86W (2.3)
Epidote	C+0	144	1.33	N 5W/86W (6.3)	N55E/61W (2.1)	N88E/66W (2.1)	27	0.25			
All	C+0	805	7.45	N6E/75W (3.1)	N55W/87W (1.7)	N74W/60W (1.1)	570	5.31			

Table 5.2(c). Index and summary of pole plots summed for vertical and horizontal holes.

		VERTICAL AND HORIZONTAL HOLES COMBINED						
		H9 (E_v, E_h, M)					H 10 (E_v, E_h)	
Mineral	Closed/ Open	no. of frac	frac/ m	main pole	second pole	third pole	no of frac	frac/ m
Chlorite	C	716	3.20	N33E/30W (5.6)	N 6E/65W (2.5)	N15W/85E (1.3)	439	4.17
Calcite	C	76	0.34	N55W/82W (3.9)	N48E/74W (3.9)	N 6E/65E (3.9)	59	0.56
Epidote	C	454	2.03	N21E/26W (3.7)	N 7E/56W (3.5)	N 5W/86W (2.4)	59	0.56
All	C	1246	5.57	N34E/29W (4.7)	N 7E/55W (2.5)	N26W/38E (1.0)	547	5.19
Chlorite	0	421	1.88	N50E/ 8W (2.6)	N16W/76E (1.9)		518	2.84
Calcite	0	192	0.86	N55W/88W (2.1)	N48E/ 8W (1.6)	N66E/84E (1.6)	280	1.54
Epidote	0	26	0.12				18	0.10
All	0	639	2.86	N48E/ 7W (2.5)	N16W/76E (1.6)	N61W/72E (1.4)	816	4.48
Chlorite	C+0	1137	5.07	N34E/30W (3.8)	N 5E/70W (1.9)	N16W/85E (1.3)	947	7.01
Calcite	C+0	268	1.20	N48W/72W (1.9)	N48E/35W (1.9)	N74E/46W (1.5)	339	2.10
Epidote	C+0	480	2.14	N24E/27W (3.8)	N 6E/56W (3.5)	N 4W/86W (2.3)	77	0.66
All	C+0	1885	8.41	N33E/29W (3.5)	N 7E/55W (2.1)	N16W/86E (1.2)	1363	9.67

comparison.

Table 3.4 shows the relationship between the core inventory and data used in the pole plots. Only the oriented core retrieved from the 56 mm and 76 mm diameter holes could be used to construct the pole plots. The core from 406 mm heater holes is not included. The headings in Table 5.2 also designate the prefix of the hole type incorporated into the data base: E_V designates the vertical 76 mm extensometer holes, E_H the horizontal 76 mm extensometer holes, and M the 56 mm monitor holes.

The pole plots in Appendix C are presented in two formats, determined by the number of fractures counted in a given sub-group. If more than 100 fractures occur on a given pole plot, the number in each 10 x 10 degree area is entered as a percentage of the total for that plot, and the result is contoured. If less than 100 fractures were counted, then the number of fractures in a 10 x 10 degree area is given, and no contours are drawn.

The core length, number of fractures, and the average fracture frequency are listed on each pole plot. The latter two data entries are repeated in the Table 5.2 summary. Table 5.2 also includes the strike and dip of fracture planes with the most prominent poles, accompanied by the percentage of fractures comprising that pole. Usually the three most prominent poles are listed, although it was sometimes difficult or impossible to find more than one well-defined cluster.

Bar graph summaries of the statistical data are shown in Figs. 5.3 and 5.4. Fig. 5.3, showing the open fractures as a percentage of total fractures, contains data from Table 5.2 with the addition of statistics for the

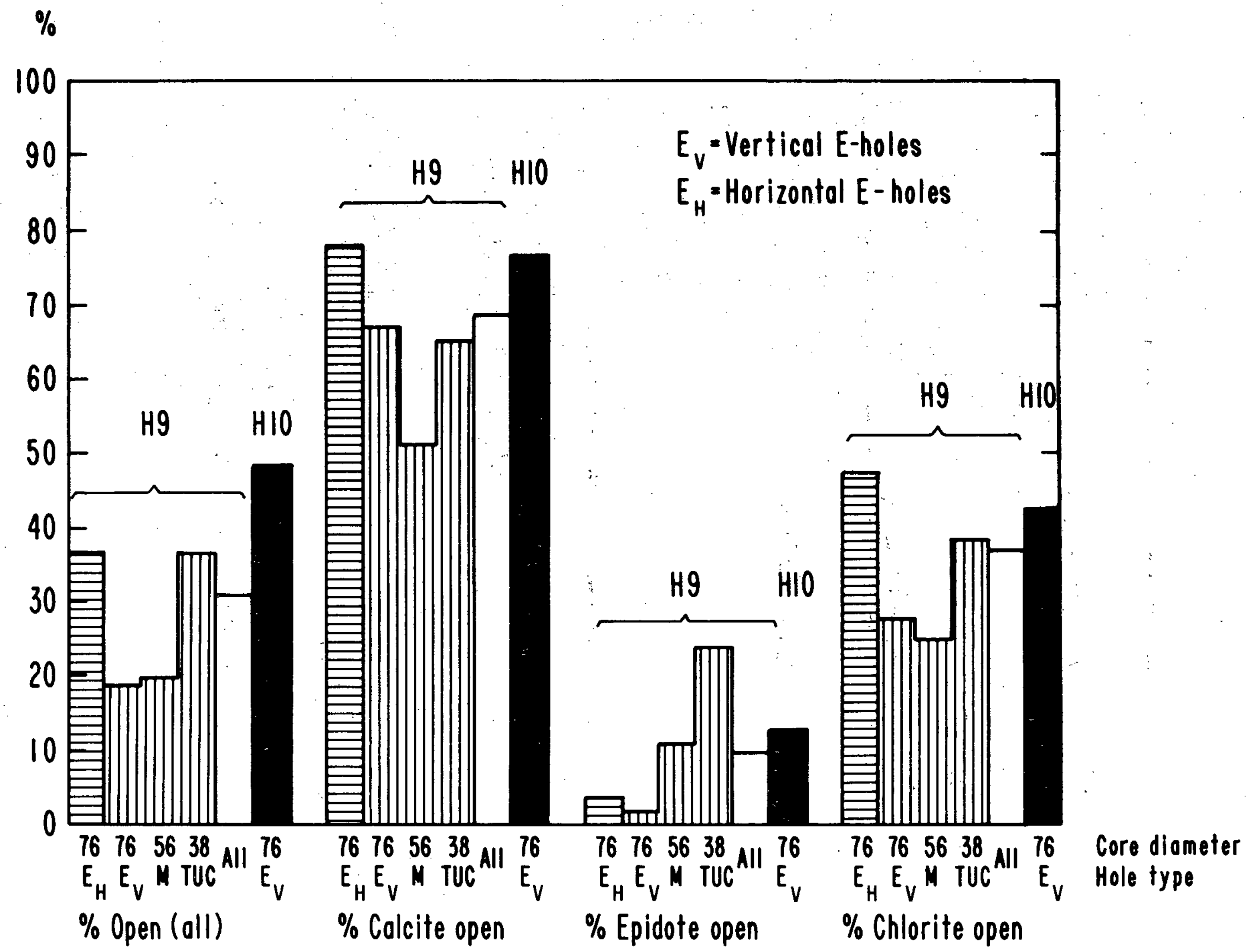

XBL 7912-13475

Fig. 5.3. Percentage of open fractures in core as removed from core barrel, categorized by borehole location, diameter, and dominant mineral on fracture surface.

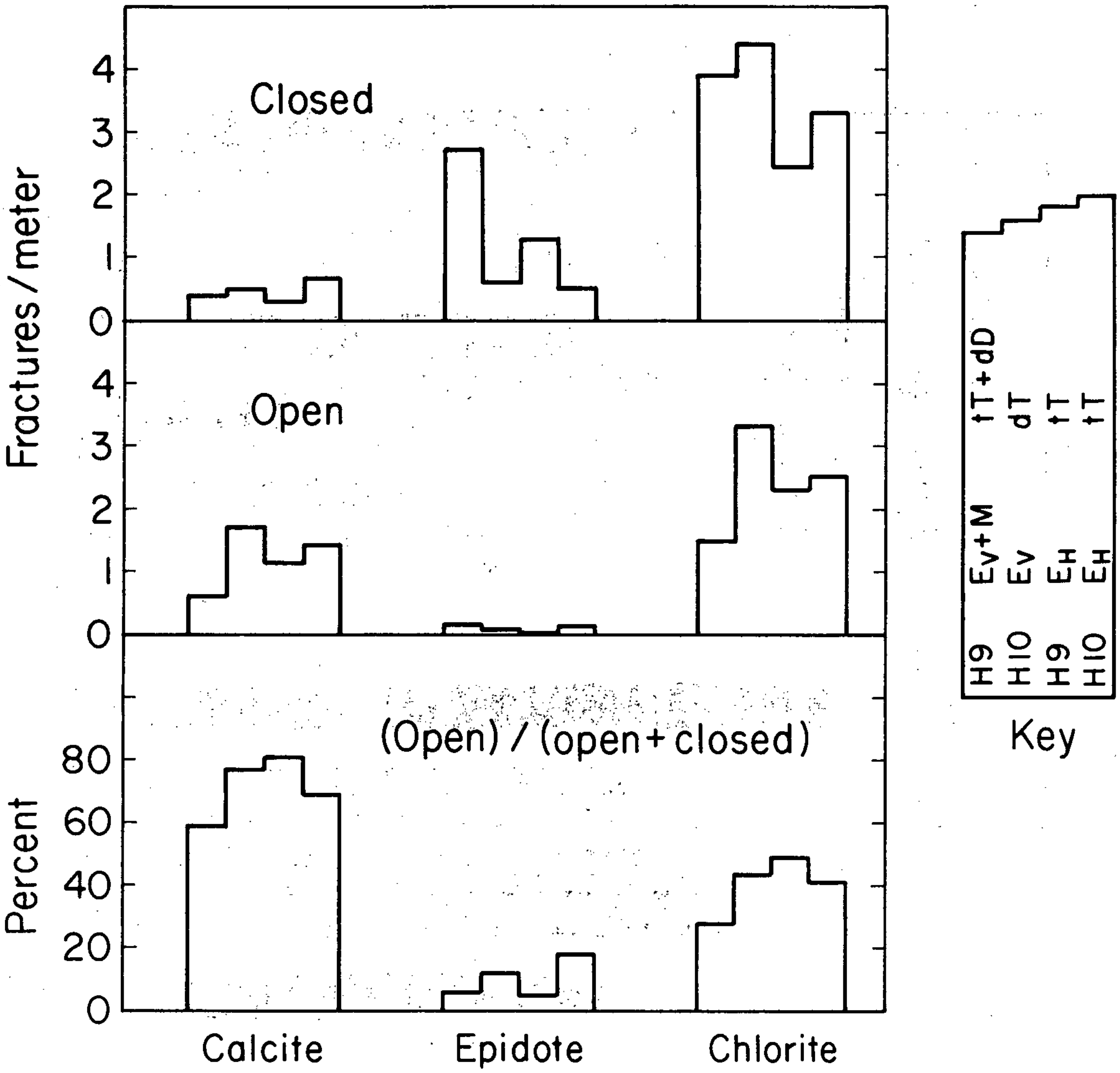

XBL 811-2557

Fig. 5.4 Fracture frequency for open and closed fractures, and percentage of open to all fractures. In the key, d, t designate double, triple-tube core barrels; D, T designate Diamec, Toram drill rigs.

38 mm holes. Statistics of the vertical boreholes in the H9 area are graphed separately for E_V and M boreholes, whereas in the pole plots and in Table 5.2 these data are combined. The second set of bar graphs given in Fig. 5.4, which are taken directly from Table 5.1, display the fracture density, mineral, and core condition classifications for each borehole. Both Figs. 5.3 and 5.4 and Table 5.2, as well as selected pole plots will be referred to in the following discussion.

5.2 Limitations of the Pole Plots

5.2.1 Sampling Bias Due to Drilling Direction

A true representation of the joint frequency is obtained only when the drilling is perpendicular to a particular joint set. Fractures intersected at less than normal incidence tend to be underrepresented. Goodman (1976) and Terzaghi (1965) state that the correction factor is given by the cosine of the angle of intersection. If N_α is the number of joints observed at an angle α, with α being the angle between the drill axis and the normal to the fracture surface, then the correct number of joints N_C is given by expression

$$N_C = N_\alpha / \cos\alpha \quad .$$

To correct the observations a weighting factor of $\cos\alpha$ would have to be applied to data collected from single, isolated boreholes. No such correction has been applied to the data in this report.

Figure 5.5 demonstrates clearly that the resulting directional bias is readily observable in many of the pole plots. The calcite-coated fractures from the H10 area were about equally sampled by the vertical and the horizontal boreholes. The tendency of the vertical holes to intersect a greater

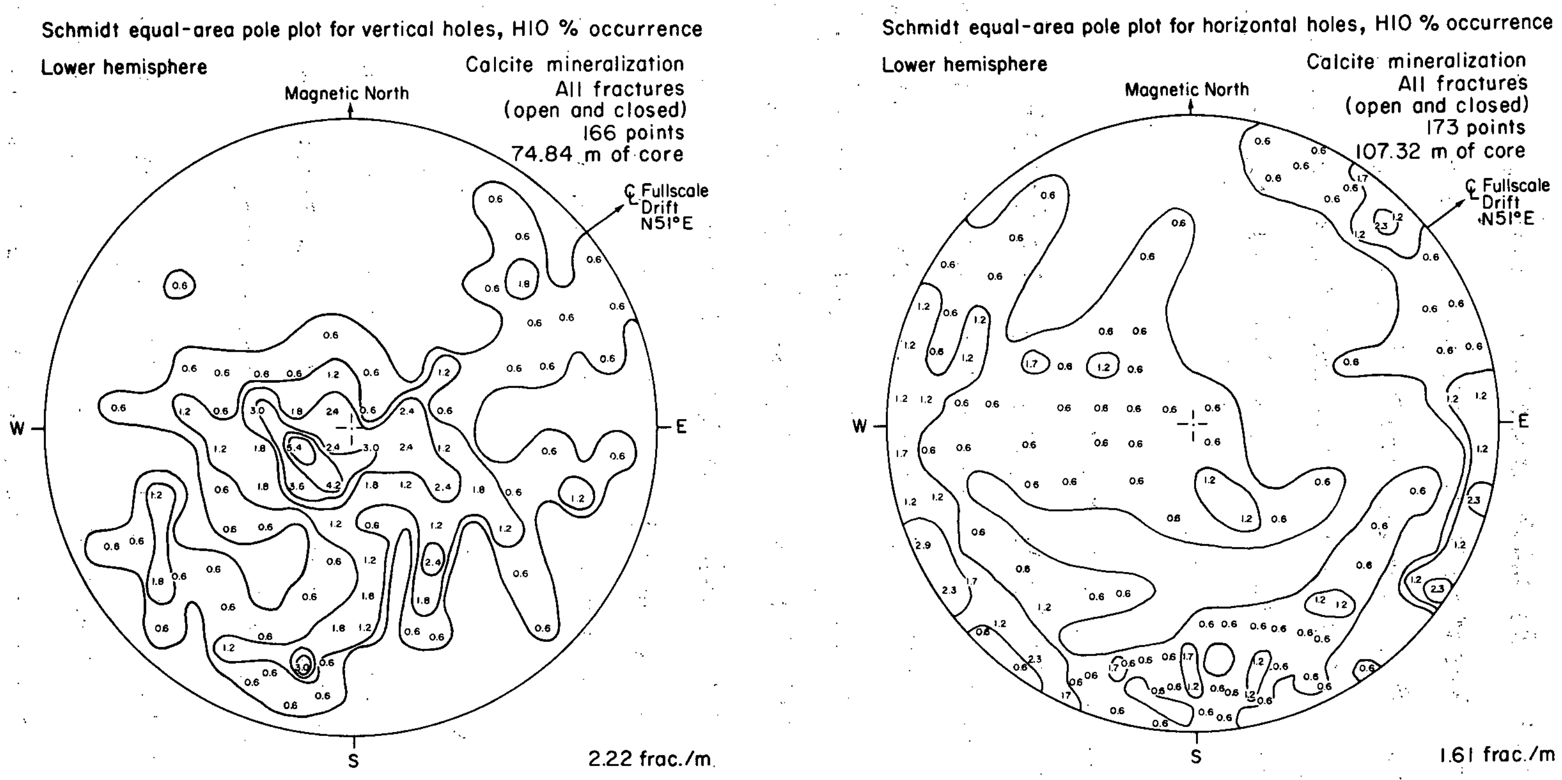

XBL 8010-2939 B

Fig. 5.5 Pole plots of fractures with calcite mineralization from H10 area, from vertical (left) and horizontal boreholes (right). Poles from the vertical boreholes, which intercept a greater number of horizontal fractures, group toward the center of plot, while poles from the horizontal holes tend to group around the perimeter.

number of horizontal fractures is shown clearly by the grouping of the fracture poles towards the center of the pole plot. Likewise, horizontal holes produce a plot with the fracture poles clustered around the perimeter. Although the sample data have not been weighted to reduce this bias, when the two pole plots are summed, the bias is greatly reduced. The tight clustering of the boreholes of several orientations in the sample volume (as opposed to a single borehole sample) also tends to reduce the directional bias. Because the sample geometry is complex the directional bias thereby introduced has not been analyzed. This problem is not as severe as it might seem because the drilling geometries in the H9 and H10 areas are almost identical, and hence comparisons between the two areas are valid.

5.2.2 Overrepresentation of Continuous Fractures

Because of the dense concentration of boreholes used in the H9 and H10 areas, different holes will indeed sample a fracture more than once if its length much exceeds the mean borehole spacing. Moreover, because the horizontal holes converge toward the central heater holes, multiple sampling will depend on absolute fracture location. A continuous fracture near the heater hole will intersect more holes one several meters farther away.

A pole plot of the epidote-filled closed fractures from the H9 area (Fig. 5.6) shows overrepresentation of the dominant epidote faults. Profile H9A (Fig 4.4) shows a sectional view of the continuous epidote features. The prominent contoured highs in Fig. 5.6 and the high incidence of epidote fractures (2.78/meter in H9 area compared with 0.59/ meter in H10 area) are largely attributed to oversampling of continuous features in the H9 area.

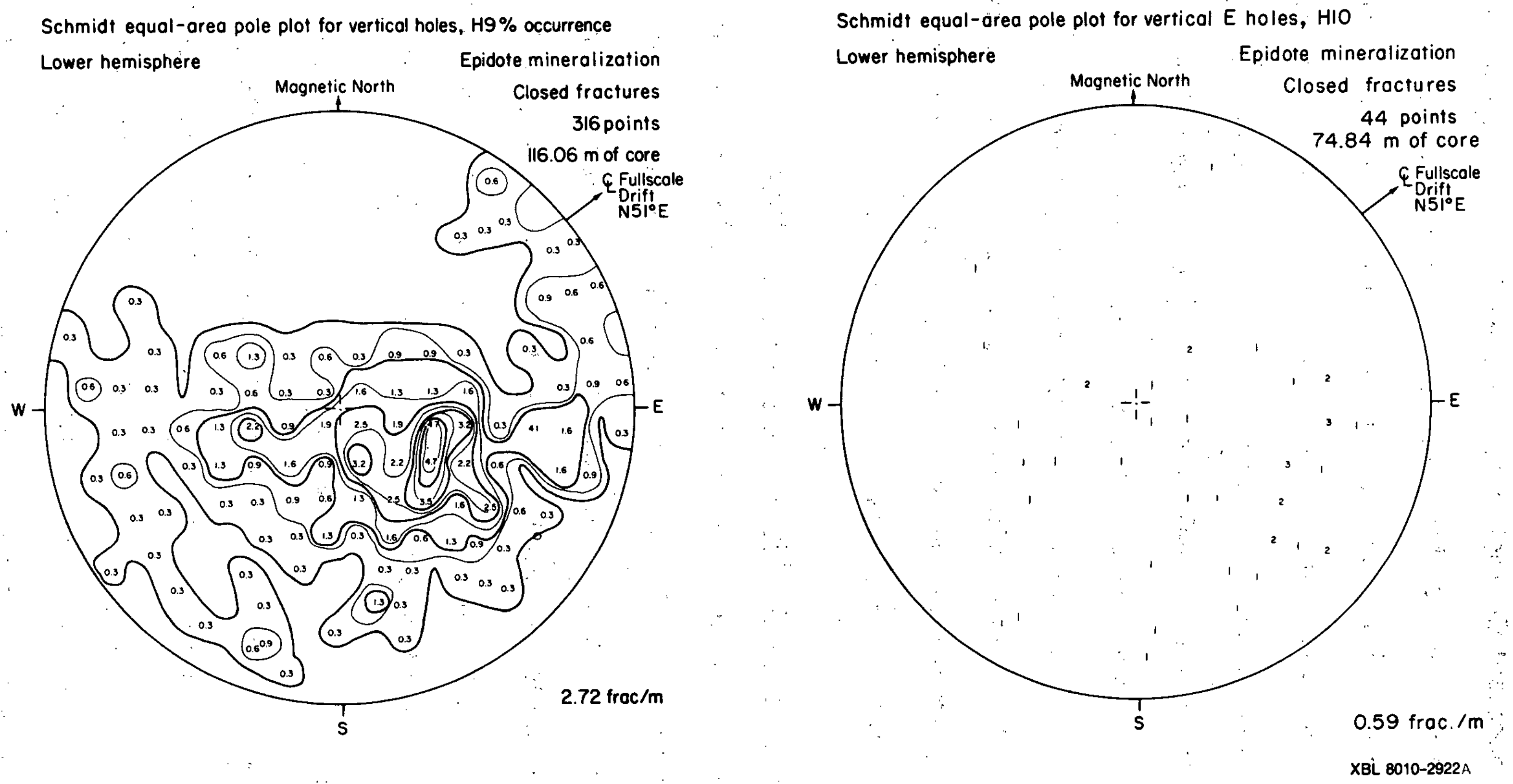

Fig. 5.6 Epidote-coated fractures from H9 (left) and H10 heater areas (right). The prominent contour peak in the H9 area pole plot is largely attributed to over-sampling caused by the intersection of a few continuous epidote fractures in several boreholes.

Such "overrepresentation" would be misleading only if each data point were considered as an individual fracture. For representing overall fracture density, it is probably quite equitable.

5.2.3 Effects of Coring and Drilling Procedures

In considering the effects of hole diameter, it was found that the percentage of open fractures in the 38 mm vertical boreholes was the highest, both for fractures with each type of mineral-infilling material and for all fractures combined (Fig. 5.3). This result is caused by the small diameter of the retrieved core, and by the use of the double-tube core barrel. The percentages of open fractures from the 56 and 76 mm vertical boreholes did not differ much, despite the different coring techniques and drilling machines used. This is attributed primarily to the special care exercised in the recovery of the 56 mm (M-hole) core.

Cores from the vertical 76 mm holes in the H9 and H10 areas do show a substantial difference in the number of open fractures. Table 5.2 shows that 48% of fractures from the H10 vertical E-holes were opened by drilling, while only 20% were opened in the H9 area. When the open/closed fracture data are examined by mineral type, as in Figs. 5.3 and 5.4, the same results are obtained: in the H10 area, open fracture percentages are significantly higher than in the H9 area, regardless of infilling. The difference is explained by the different coring techniques used for the vertical E-holes in the H9 and H10 areas. In the H9 area, a triple-tube barrel retrieved core; in the H10 area, a conventional thin-walled, double-tube core barrel was used. The double tube produced larger core than the triple-tube barrel, and thus it should be less susceptible to breakage. In fact, there are approximately

2.5 times more fractures opened during drilling with the double tube (H10 area) than with the triple (H9). The reduced handling and vibration achieved with triple-tube core recovery produced the better results.

Also noteworthy is the higher number of open fractures in the H9 and H10 76-mm horizontal boreholes. These boreholes yielded higher percentages than the 76-mm vertical boreholes in the H9 area (see Table 5.2 or Fig. 5.4), even though the coring and drilling techniques were the same in all three cases (triple-tube core barrel and Toram drill rig). For example, consider the chlorite fractures in Fig. 5.4: 49% of fractures in core from the H9 and 41% from the H10 horizontal boreholes were opened, while only 28% of fractures from the H9 vertical holes were opened. While this result could be an effect of orientation--perhaps due to horizontal boreholes intersecting weaker fracture sets than vertical ones, or to different angles of incidence between borehole and fracture plane--it seems more likely that some mechanical effect associated with drilling horizontal holes is the cause. Our data thus suggests that the quality of the core retrieved from a borehole is a function of drilling angle. As borehole inclination increases, the quality of the core samples decreases.

5.3 Discussion of Pole Plots and Statistics

5.3.1 Relative Mineral Abundances

Chlorite is found coating the majority of fracture surfaces, while epidote and calcite are present on less than half the fracture surfaces. In the H9 heater area, a total of 3,385 open and closed fractures were logged, including core from the 38 mm boreholes. In this large sampling, chlorite was noted on 72%, epidote on 21%, and calcite on 12% of the fracture surfaces.

This total exceeds 100% because more than one mineral was counted on fracture surfaces. Table 5.2 gives the number of fractures coated with the three minerals in both horizontal and vertical boreholes. In the H9 area, chlorite, calcite and epidote are the dominant mineral on 60%, 14%, and 26% of the fractures, respectively. In the H10 area, the respective percentages are 70%, 25% and 5%. This shift in relative abundances is attributed in large part to the abundance of epidote-coated faults in the H9 area, as discussed below.

5.3.2 Relative Strength of Fracture Coatings

The type of fracture infilling mineral is reflected in the percentage of fractures opened during the drilling process. To eliminate any bias due to variation in core size and borehole orientation, the percentages of epidote, chlorite, and calcite-filled open fractures were calculated separately for horizontal and vertical boreholes and for various borehole diameters. The results are plotted in the bar graph shown in Fig. 5.3.

When compiling Fig. 5.3 it was realized that the H10 area data base was less complete than for the H9 area, due to the double-tube core recovery and the smaller amount of horizontal core relogged. For these reasons, Fig. 5.3 emphasizes H9 data and includes data from the vertical boreholes in the H10 area for reference. The conclusions are therefore based mainly on the H9 results. Figure. 5.3 shows that 90% of the epidote-filled fractures, 63% of the chlorite-filled fractures, and 31% of calcite-filled fractures are closed. The drilling-induced breakage clearly indicates that the calcite-coated fractures are considerably weaker and the epidote-coated fractures considerably stronger than average. It is concluded that these significant differences in fracture strength are caused by the type of mineral filling.

5.3.3 Relationship of Chlorite and Epidote Fractures to Faulting

The most important feature in the H9 area is the prominent cluster of poles in the south-east quadrant of most H9 pole plots, as shown in Fig. 5.7. The floor map (Fig. 4.1) shows that the drilling for the H9 experiment intersected one of the major fault zones found throughout the experimental drifts (also shown in the extensometer drift wall map, Fig. 4.2). When a fault zone is intersected by drilling, as in the H9 area, a large cluster of poles oriented normal to the fault occurs.

Only a few epidote-coated fractures are found in the H10 area, as can be seen in the pole plots or in the numerical summary (Table 5.2c). The floor map (Fig. 4.1) confirms that there are fewer faults with epidote mineralization in the H10 area than in the H9 area.

5.3.4 Mineralization Type and Orientation (H9 area)

The effects of different mineralization types show up most clearly when comparing open with closed fractures, or when discussing differences between the H9 and H10 areas. However, there is also some dependence of fracture orientation upon mineralization type. This is best examined in the H9 pole plots, which have an adequate population of epidote-filled fractures. The pole plots for the vertical boreholes in the H9 heater area are reproduced in Fig. 5.7. Similar observations were made in the horizontal holes (Figs. C41, C43, and C45) and in the summaries of borehole orientations (Figs. C57, C58, C59 of Appendix C).

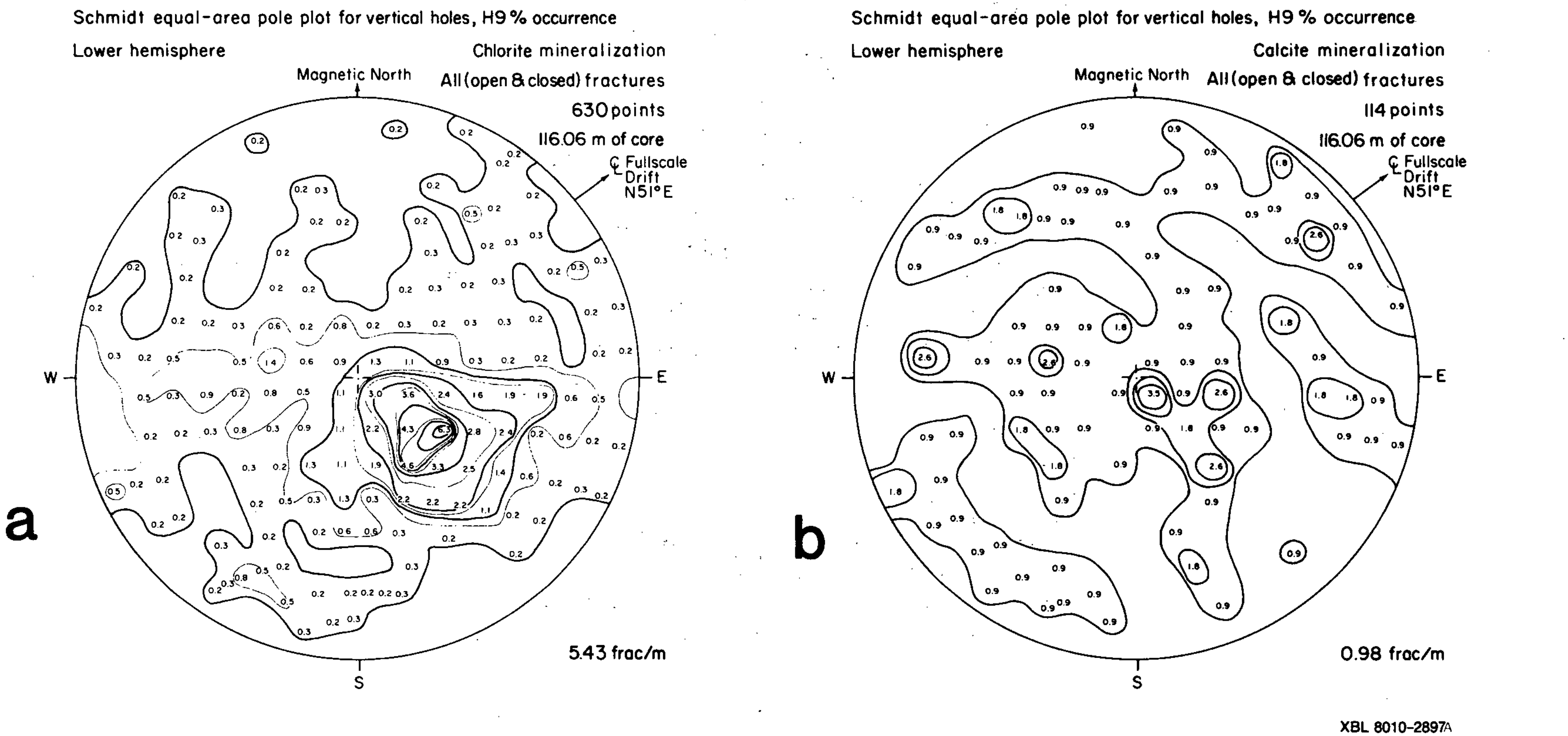

Fig. 5.7 Pole plots from the H9 area vertical holes for open and closed fractures, plotted separately for chlorite, calcite, and epidote.

Schmidt equal-area pole plot for vertical holes, H9 % occurrence

Lower hemisphere

Epidote mineralization

All (open & closed) fractures

336 points

116.06 m of core

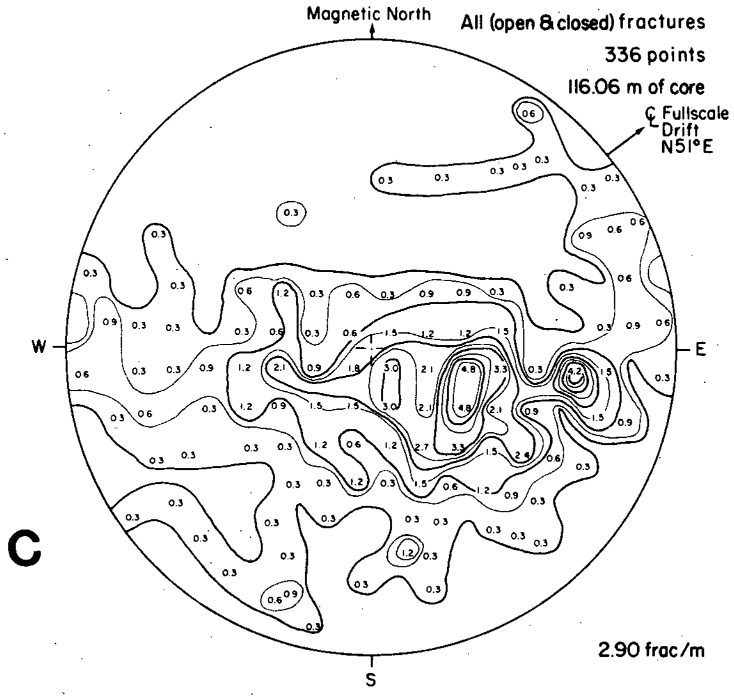

C

2.90 frac/m

XBL 8010-2898

Figure 5.7 shows that the dominant poles of epidote and chlorite fractures coincide, indicating fracture planes with strikes of N30E (±8) and with dips of about 30W. The contour patterns of epidote and chlorite are fairly concordant throughout the pole plot, showing the general coincidence of the two fracture types. The calcite population is more widely distributed, although many calcite fractures have the same dip and strike as the dominant chlorite and epidote fractures. In general, the calcite fracture orientations are more dispersed than the epidote and chlorite fractures.

5.3.5 Comparisons Between H9 and H10 Areas

It is instructive to compare the pole plots from the two heater arrays. Although only 22 m apart and situated in the same drift, they have marked differences in fracture orientation and, as discussed elsewhere, in fracture infilling minerals.

Because the number of chlorite fractures logged in the H9 and H10 areas are comparable, the chlorite fracture pole plots (Fig. 5.8) are used to discuss the differences in fracture orientation between the two areas. In Fig. 5.8 we retain the separate presentations for vertical and horizontal holes. Differences between the distributions for H9 and H10 are not too obvious at first inspection. However, when considering the vertical boreholes (upper portion of Fig. 5.8), it can be seen that the H10 area does not display a cluster of poles at the same orientation (N32E/30W) for the plane as the dominant H9 pole cluster; this is attributed to the through-going epidote faults. The two clusters of poles in the H10 area indicate that the fractures are more nearly horizontal and closer to the north-south strike. Table 5.2 gives the fracture plane orientations as N20W/16E and N20E/16W.

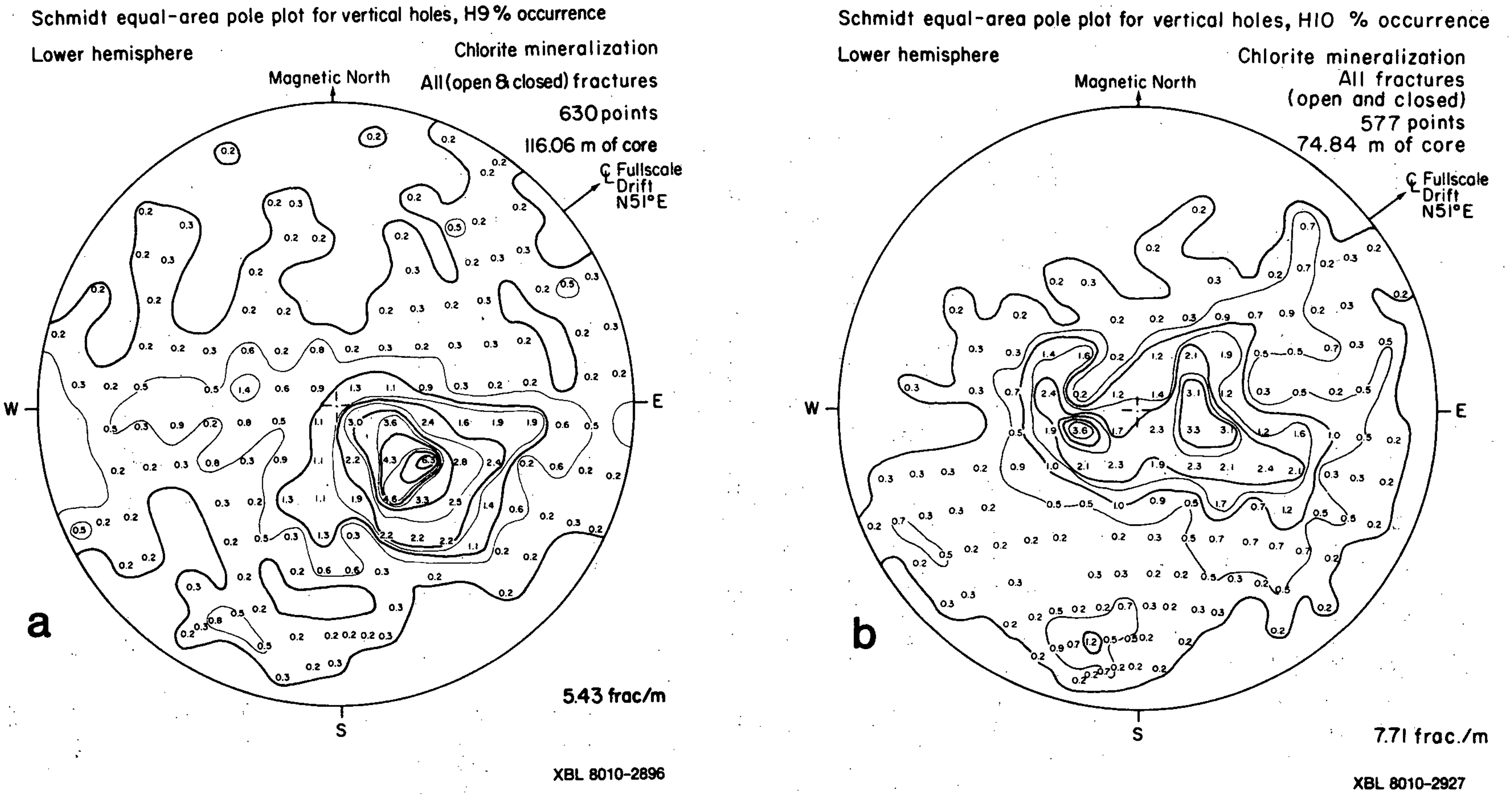

Fig. 5.8 Vertical and horizontal chlorite fractures for H9 and H10 heater areas showing differences in fracture plane orientations.

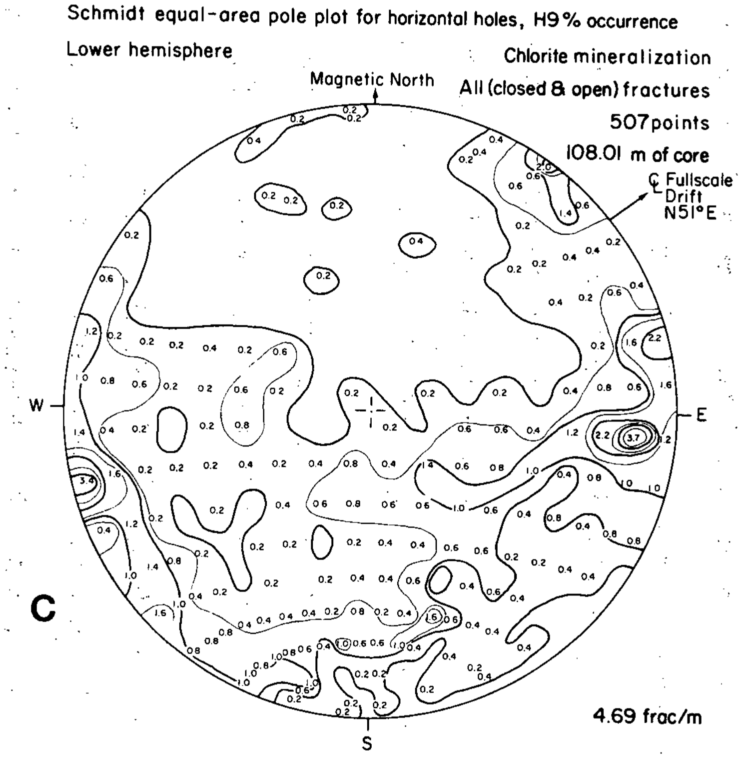

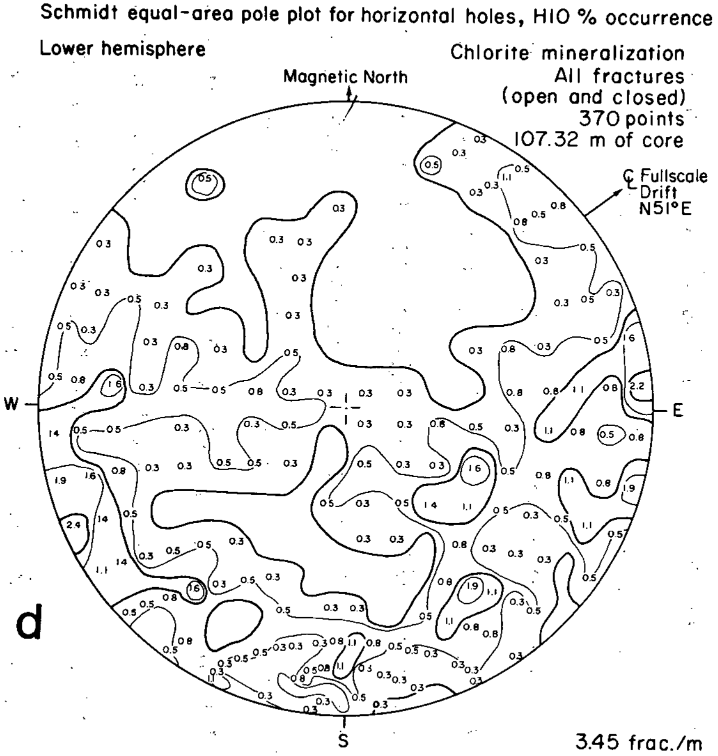

XBL 8010-2938A

The drift floor map (Fig. 4.1) confirms that fractures in the H10 area are more nearly horizontal than in the H9 area. Since the two areas are only 22 m apart, this change is rather remarkable.

Comparative statements about the horizontal holes are more difficult to make (see lower half of Fig. 5.8). A cluster of fracture planes in the H9 plot oriented N06E/76W does not reappear in the H10 pole plot. Other contour maxima, which designate near-vertical planes striking N55W and N20W, appear in both H9 and H10 pole plots. None of the contour maxima of the vertical holes reappear in the horizontal holes. The fractures in the H10 heater area are probably too nearly horizontal to be sampled by horizontal holes. In the H9 area the epidote faults and their associated chlorite fractures are not intersected by any of the horizontal holes (see Fig. 4.1 and Fig. 4.3).

The fracture density statistics (Fig. 5.8), showing 7.7 fractures per meter in H10 area compared with 5.43 fractures per meter in H9 area, reflect the differences in orientation to some extent. When considered with the fracture density values from the horizontal boreholes (Table 5.2c), the respective values are 9.67 and 8.41 fractures per meter, showing the fracture density in the H10 area to be 15% greater than in the H9 area.

Besides the fact that the H10 area is somewhat more fractured, the fractures in this area are less continuous than in H9.

5.3.6 Comparison with Time-Scaled Pole Plot

Figure 5.8 includes a summary pole plot adapted from Fig. 14 of Thorpe's (1979) fracture study in the time-scaled drift. Since Thorpe used the mine coordinate system rather than geographic north, his pole plot has been rotated 10 degrees to coincide with the geographic north convention used in this report. At Stripa, geographic north and magnetic north coincide within ±0.2 degrees, with mine coordinate north oriented 10 degrees west of geographic north. (Some of the pole plots in the report by Thorpe erroneously indicate "Mag.N." at the top, rather than "Mine N"--these are Fig. 23, Fig. 24, and the pole plots of Appendix C.)

To assure that the data sets are compatible, Fig. 5.9 includes only open fractures for all mineralization types. Of the four fracture sets identified in the contour diagram by Thorpe, only sets 1 and 4 are consistent with the full-scale (FS) fracture plots. Set 3 of the time-scaled drift is not reflected in the H9 and H10 pole plots. Set 2 is only weakly found in the H9 and the H10 area pole plots. However, examination of FS plots in which horizontal sampling is included, such as Fig. C56, does not demonstrate the presence of this fracture set in the FS drift. Evidence for set 3 is completely lacking in the FS plots. Thorpe comments that set 3, although the dominant cluster in the time-scaled drift in terms of fracture frequency, is comprised largely of short joints with trace lengths less than 0.5 m, and is poorly represented in the time-scaled floor map.

The side lobe in the contour pattern of fracture set 1 from the time-scaled drift corresponds to the direction of the four major fracture planes identified in the floor map of the FS drift. The corresponding lobe in the H9 area pole plot includes the major through-going epidote-coated faults identified on the wall and floor of the H9 area. The lobe is less developed in the H10 area plot, but is still identifiable. The continuity in strike

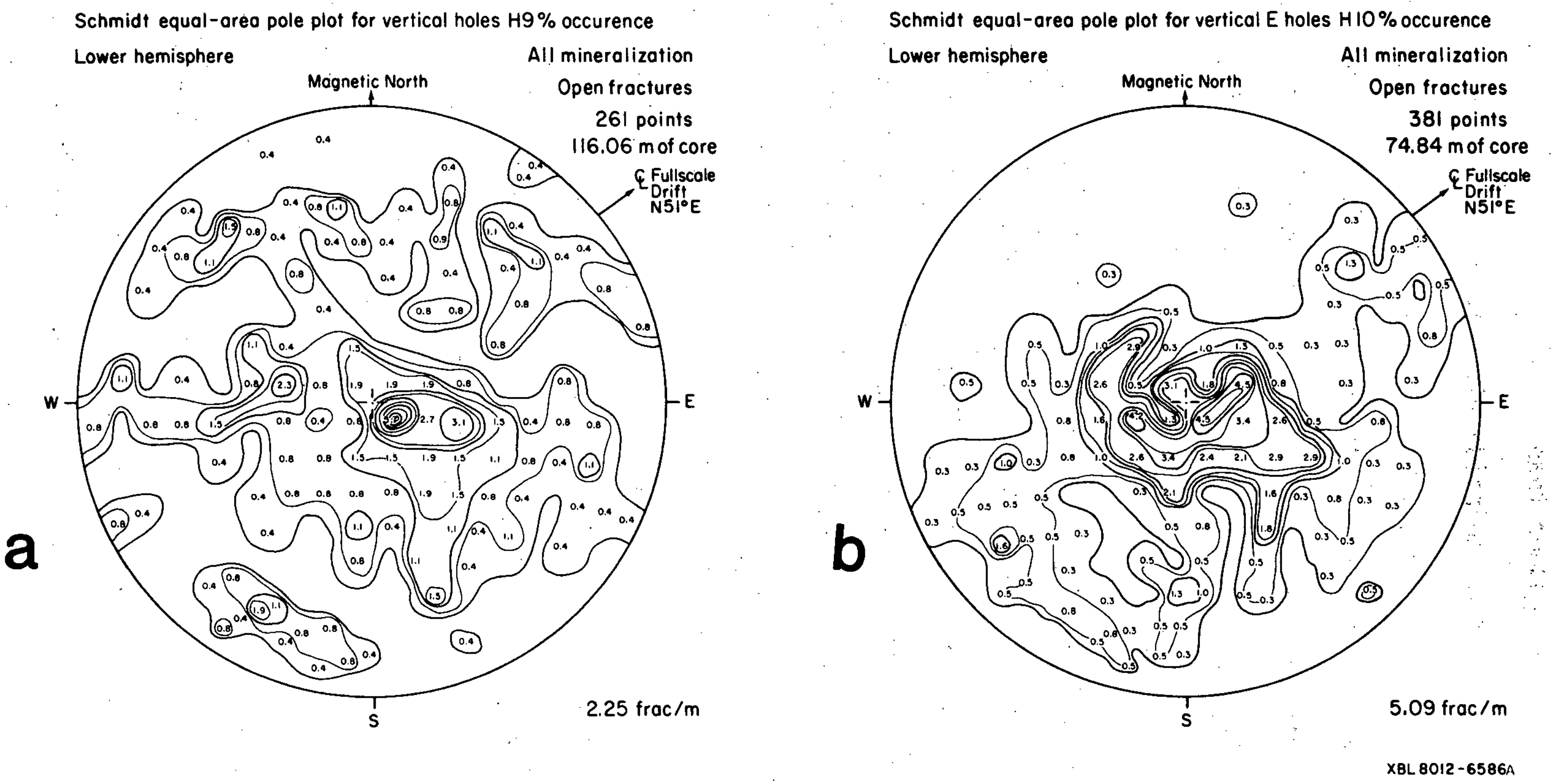

Fig. 5.9 Open fractures, with all mineralization types, for H9, H10 heater areas and from time scale from Thorpe (1979).

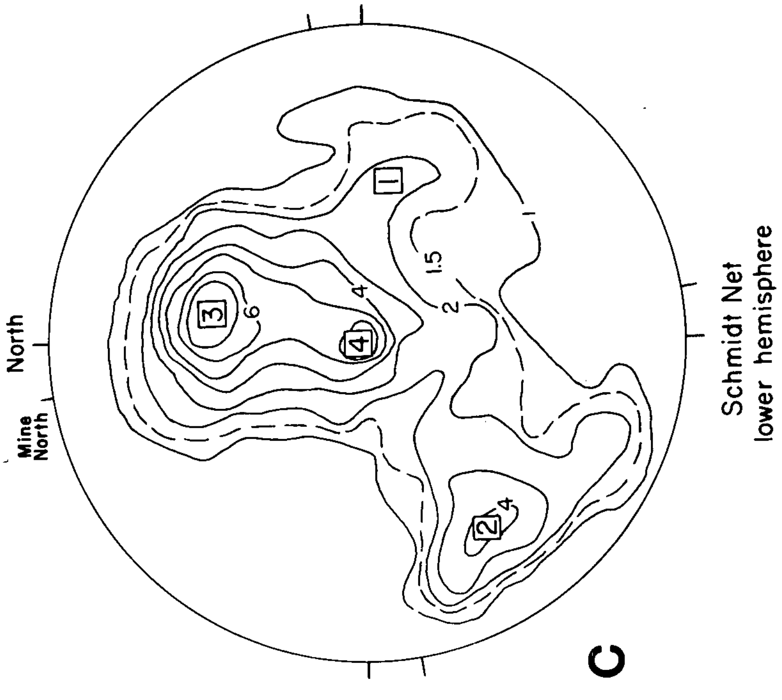

XBL 799-11320

and dip of this set of epidote faults (Fig. 4.7) has already been discussed in section 4.2.

Fracture set 4 identifies horizontal fractures in the time-scaled drift. Horizontal and sub-horizontal fractures comprise the dominant population sampled by vertical holes in the FS drift, where the strike skews about a N-S direction to considerable extent. In the time-scaled drift, the strike of sub-horizontal features is obscured by the fracture set 3 population.

6. SUMMARY

(1) Fractures have been mapped on drift surfaces and in core to characterize the rock mass surrounding the two full scale heater experiments at Stripa. Mapping of the drift floor was carried out at an unusual level of detail, with discontinuities only a fraction of a meter in length recorded. The drift walls were mapped in less detail, only prominent features with exposed lengths of a meter or more being recorded. Compared with interpretation of core data, mapping is quicker and produces a superior product for visualizing the spatial character of the fracture network.

Virtually all discontinuities occurring in core were logged for orientation, thickness, and mineral type, first by recording open fractures at the time of core recovery, and second by relogging the core to record all closed fractures. Reconstruction of the subsurface fracture system from this data was time-consuming, tedious, and subject to interpretive judgment despite the high intensity of drilling coverage and the excellent quality of core recovery and logging. The certainty with which major discontinuities could be located depended on their intersection with exposed surfaces and with offset pegmatite dikes. Only a small fraction of the total number of fractures observed in core could be interpolated between boreholes. However, the core data were invaluable for locating fractures, defining their orientation, examining effects of mineral infilling, and comparing drill and core recovery techniques. The resulting data base will be useful in interpreting results from experiments carried out in and near the full-scale drift, such as the cross-hole ultrasonic measurements, borehole determinations of the state-of-stress, and thermomechanical results from the heater experiments.

(2) Several prominent pegmatite dikes and quartz veins were found on drift surfaces and in boreholes; their presence made it possible to define the extent and magnitude of several major faults. The dominant set of through-going faults, striking N-S and dipping about 60W, is consistent with the four prominent discontinuities present in the time-scaled drift (Fig. 4.7). Epidote is the dominant mineral coating the fault surfaces. Offsets determined by the positions of dikes range between 1 and 6 m. All faults appear to have reverse vertical components of displacement.

A second prominent fault, striking E-W and dipping 60W, has been inferred on the basis of the observed offset of dikes on the extensometer drift wall relative to the full-scale drift. This fault post-dates the N-S faulting, its inferred offset is about 6 m, and it also is a reverse fault.

Pegmatites and N-S faults cut through many of the boreholes in the H9 area, including the H9 heater hole itself. In the H10 area, however, there is no evidence that either dikes or major faults cut through the vertical holes.

(3) Chlorite, epidote, and calcite were identified as the three most common minerals coating fracture surfaces; statistics on their relative abundances are summarized in Table 5.2 and Figs. 5.3 and 5.4. Chlorite is ubiquitous and is the dominant mineral on 60 to 70% of the fracture surfaces. Calcite is rarest, being found on 15 to 25% of the fractures. In the major faults, epidote is the dominant mineral, but it is less common where faults are not present. Stereoplots show that the orientations of chlorite and epidote fractures are concordant, with a single prominent concentration of fracture planes oriented N30E/30W. Calcite fracture orientations are more

diffuse, lacking even the single prominent pole of the chlorite and epidote fractures.

The separate recording of closed and open fractures provides a crude ranking of relative fracture strength (Fig. 5.3). Few (~10%) epidote fractures are open in retrieved core, while most calcite fractures (~70%) are found to be open. About 30 to 40% of the chlorite-coated fractures were open in the retrieved core. Hence the core data rank the relative strength of the three fracture types as follows: epidote > chlorite > calcite. There is no evidence, however, that this ranking actually depends on mineral type. Calcite fractures are the youngest of the three types.

(4) Our observations in the full-scale drift agree with those of others who report that the degree of fracturing at the Stripa experimental drifts is intense. This can be seen by a cursory inspection of the detailed floor map (Fig. 4.1). Several zones with intense fracturing where individual features could not be mapped are indicated by hatching in the FS-drift floor and the extensometer drift wall maps. The fracture statistics compiled from the core data confirm these observations: the bottom line of Table 5.2c shows that the average fracture density for all fracture types is 9.1 fractures per meter, for a typical spacing of 11 cm. This value of fracture frequency is comparable to an estimate made by Thorpe (1979) from a somewhat different data base compiled in the time-scaled drift.

In the H10 area boreholes, local concentrations of intense fracturing of about 1 m extent could be located in the cross sections, but no patterns indicative of structural control were evident. In the H9 area, on the other hand, fracturing is more intense in some boreholes immediately west of the H9 heater hole, and may be related to the major N-S faults located there.

(5) Despite the high intensity of fracturing, the Stripa quartz monzonite is generally quite competent, as reflected by the quality of core recovery. The generally intact nature of recovered core is reflected in the RQD values (Olkiewicz et al., 1978, and Appendix D of this report), which only occasionally drop below 100%.

Other evidence that the fractures in the underground drifts are well sealed comes from a series of sonic borehole logs acquired in the vertical extensometer holes (Appendix D). Compressional travel time and sonic waveform logs yielded very few anomalies in the full-scale and time-scaled drifts, even though all discernible deviations were picked. In the 17 vertical E holes, only 17 cases were found in which both compressional and shear arrival times were perturbed; an additional 23 cases were distinguished in which only shear wave arrival times varied. This yielded an average spacing between waveform anomalies of about 4.3 m. In contrast, core data (Table 5.2a) show that the spacings between fractures are 10 to 11 cm for all fractures and 20 to 50 cm for open fractures. Only a small percentage of the fractures, therefore, registers on the sonic waveform logs.

(6) The data base resulting from fracture mapping and core logging in the full-scale and extensometer drifts is available as follows:

- A computer-based listing of individual fractures, both open and closed, taken from the original field logging forms (Sect. 3.3).

- Detailed and simplified floor maps of the full-scale drift (Fig. 4.1), a map of the full-scale wall (upper portions of Figs. 4.4A and 4.5A), and a map of the extensometer drift wall (Fig. 4.2).

- Eight vertical radial sections spaced 22.5 degrees apart, through the H9 area (Fig. 4.4 and Appendix B) and through the H10 area (Fig. 4.5).

- Pictorial logs of open and closed fractures, RQD, and stereoplots for the vertical E and M holes in the full-scale drift (Appendix D of Olkiewicz et al. 1979).

- Stereoplots of fracture plane poles, categorized by hole orientation, hole location, mineral type, and whether the fracture was open or closed (Appendix C of this report).

- A three-dimensional plexiglass model at 1:20 scale, 0.7 m x 1.0 m x 2.1 m, showing prominent dikes, faults, and all borehole locations (Fig. 4.6).

ACKNOWLEDGMENTS

The authors wish to acknowledge the major contribution to this report by Mr. T. Daugaard, University of Luleå, Sweden, who spent many hours mapping drift walls, reeducing fracture data, and preparing cross sections.

Individuals who participated in the fracture logging included: S. Abrahamson, K-E. Almen, L. Andersson, T. Daugaard, L. Jacobsson, and U. Jacobsson. R. Thorpe did most of the fracture mapping of the full-scale drift floor.

A special note of appreciation is directed to Margot Harding who not only did most of the fine illustrations but also advised in their design. A special note of thanks is given to Dr. J.E. Gale for his support and help with reducing the fracture orientation data.

REFERENCES

Deere, D.U., 1963. "Technical Description of Rock Cores for Engineering Purposes," Felsmechanik und Ingenieurgeologie, 1, 16-22.

Geijer, P., 1938. Stripa Odalfaeltsgeologie (Stripa Mine District Mapping). Stripa Mine File. Stora, S-71050, Sweden.

Geijer, P and E. Magnusson, 1943. (Geological Description of Lundesburg SW). SGU Ser. Ca. No. 35. Stockholm, Sweden.

Goodman, R.E., 1976. Methods of Geological Engineering in Discontinuous Rocks, West Publishing Company, Minneapolis.

Kendorski, F.S. and M.A. Mahtab, 1976. "Fracture Patterns and Anisotropy of San Manuel Quartz Monzonite," Bulletin of Association of Engineering Geologists, Vol. XIII, No.1.

Knill, J. and K. Jones, 1965. "The Recording and Interpretation of Geological Conditions in the Foundations of the Roseires, Kariba, and Latiyan Dams," Geotechnique, Vol. 15.

Koark, and I. Lundstrom, 1979. Geological Description of Lindesberg SW. SGU Ser. Af. 126. Stockholm, SW.

Kurfurst, P.J., T. Hugo-Persson, and G. Rudolf, 1978. Borehole Drilling and Related Activities at the Stripa Mine. Lawrence Berkeley Laboratory report LBL-7080, SAC-05, Berkeley, California.

Lau, J.S.O.and J.E. Gale, 1976. "The determination of Attitudes of Planar Structures by Stereographic Projection and Special Trigonometry," from Report on Activities, Part C, Geological Survey of Canada, Paper 76-1C.

Ljung, S., 1966. Gruffaltkarteringar (Mine Field Mapping). Stripa Mine File. Stora S-71050, Sweden.

Nelson, P. et al., 1979. Preliminary Report on Geophysical and Mechanical Borehole Measurements. Lawrence Berkeley Laboratory report LBL-8280, SAC-16, Berkeley, California.

Olkiewicz, A., J. Gale, R. Thorpe, and B. Paulsson, 1979. Geology and Fracture System at Stripa, Lawrence Berkeley Laboratory report LBL-8907, SAC-21, Berkeley, California.

Olkiewicz, A., K. Hansson, K-E. Almen, and G. Gidlund, 1978. Geological and Hydrogeological Documentation of the Stripa Test Station, KBS Technical Report 63, Stockholm, Sweden.

Paulsson, B.N.P. and M.S. King, 1980. A Cross Hole Acoustic Investigation of a Rock Mass Subjected to Heating. Lawrence Berkeley Laboratory report LBL-10975, SAC-32, Berkeley, California.

Swan, G., 1978. The Mechanical Properties of the Stripa Granite, Lawrence Berkeley Laboratory report LBL-7074, SAC-03, Berkeley, California.

Terzaghi, R.D., 1965. "Sources of Error in Joint Surveys," Geotechnique, Vol. 15.

Thorpe, R., 1979. Characterization of Discontinuites in the Stripa Granite--Time-Scale Heater Experiment. Lawrence Berkeley Laboratory report LBL-7083, SAC-20, Berkeley, California.

Wesslen, A., 1956. Gruvfaeltkarteringar (Mine Field Mapping). Stripa Mine File. Stora S-71050, Sweden.

Witherspoon, P.A., N.G.W. Cook, and J.E. Gale, 1980. Progress with Field Investigations at Stripa. Lawrence Berkeley Laboratory report LBL-10559, SAC-27, Berkeley, California.

Wollenberg, H., S. Flexser, and L. Andersson, 1980. Petrology and Radiogeology of the Stripa Pluton. Lawrence Berkeley Laboratory report LBL-11654, SAC-36, Berkeley, California.

APPENDIX A: FORMAT FOR FRACTURE LOGS

The following explanation of fracture logs is modified from Appendix A of Thorpe (1979). The headings apply to the sample fracture logs of Fig. A.1.

Depth - Length from collar to midpoint of fracture surface (nearest cm).

Description of Strata - The term "granite" is a general descriptor here, referring more correctly to quartz monzonite. Variations in color and texture are also noted.

Structures and Discontinuities

Natural - Naturally occurring fracture; usually open in situ and containing some mineralization.

Induced - Break caused by drilling.

Uncertain - May be a natural fracture; however, its openness in situ is very questionable.

Open/Closed - Refers to condition of fracture in core and, by inference, to its condition in situ.

Other - Refers to a discontinuity other than a fracture.

Roughness - Amplitude of small-scale irregularities with wavelengths < 1-2 cm. Larger scale roughness is denoted as "irregular."

Amount of Mineralization - Amount of coating of wall rock:

HW - A lot of mineralization

MW - Moderate mineralization

SW - Slight mineralization

NW - No mineralization

Gouge

Type - Coded by occurrence, not predominance. Main types are chlorite, calcite, epidote and pyrite.

Color

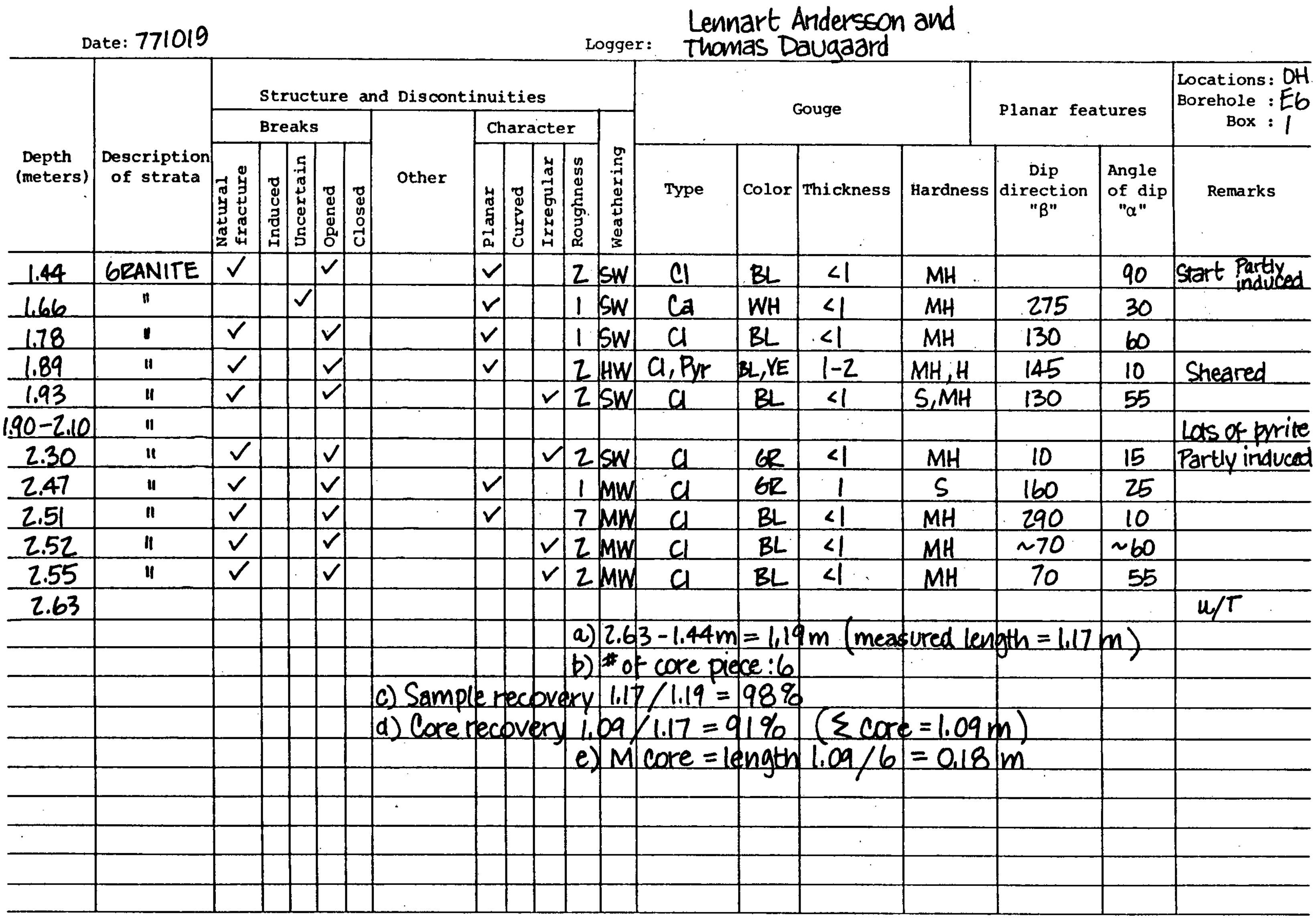

Date: 771019

Logger: Lennart Andersson and Thomas Daugaard

Locations: DH
Borehole : E6
Box : 1

Depth (meters)	Description of strata	Structure and Discontinuities											Gouge				Planar features		Remarks
		Breaks					Other	Character				Weathering							
		Natural fracture	Induced	Uncertain	Opened	Closed		Planar	Curved	Irregular	Roughness		Type	Color	Thickness	Hardness	Dip direction "β"	Angle of dip "α"	
1.44	GRANITE	✓			✓			✓			2	SW	Cl	BL	<1	MH		90	Start Partly induced
1.66	"			✓				✓			1	SW	Ca	WH	<1	MH	275	30	
1.78	"	✓			✓			✓			1	SW	Cl	BL	<1	MH	130	60	
1.89	"	✓			✓			✓			2	HW	Cl, Pyr	BL, YE	1-2	MH, H	145	10	Sheared
1.93	"	✓			✓					✓	2	SW	Cl	BL	<1	S, MH	130	55	
1.90-2.10	"																		Lots of pyrite
2.30	"	✓			✓					✓	2	SW	Cl	GR	<1	MH	10	15	Partly induced
2.47	"	✓			✓			✓			1	MW	Cl	GR	1	S	160	25	
2.51	"	✓			✓			✓			7	MW	Cl	BL	<1	MH	290	10	
2.52	"	✓			✓					✓	2	MW	Cl	BL	<1	MH	~70	~60	
2.55	"	✓			✓					✓	2	MW	Cl	BL	<1	MH	70	55	
2.63																			u/T

a) 2.63 - 1.44 m = 1.19 m (measured length = 1.17 m)
b) # of core piece : 6
c) Sample recovery 1.17/1.19 = 98%
d) Core recovery 1.09/1.17 = 91% (Σ core = 1.09 m)
e) M core = length 1.09/6 = 0.18 m

Fig. A.1. Facsimile of field fracture log for borehole E6.

Thickness - Approximate thickness in mm; "hairline" fractures are about 1/2 mm thick.

Hardness - Soft(S) - scratch with thumbnail.

Moderately hard (MH) - scratch with steel.

Hard (H) - cannot scratch with steel.

Planar Features

Dip Direction - Azimuth of apparent dip, looking down hole.

Angle of dip - Acute angle between fracture plane and core axis.

Remarks - As required.

APPENDIX B: COMPILATION OF H9 FRACTURE DATA ON VERTICAL CROSS SECTIONS

Orientation and dip measurements based on the original fracture logs are posted in the vertical cross sections of Figs. B1-B8. On each cross section the apparent dip of a given fracture plane is plotted with short line segments. If the core was not oriented, then the line segment is horizontal. Both open and closed fractures are posted.

If the core was oriented, then both dip and beta angle are given in parentheses; for unoriented core only the dip angle is given. Note that the dip angle is the angle between the horizontal and the fracture plane rather than the alpha angle originally recorded in the core logs. In vertical boreholes, the dip is 90-α. The key on each figure indicates the beta ranges which distinguish between fracture planes projecting downwards towards the front and rear of a given cross section.

The key also indicates the dominant mineral type on a fracture surface. In addition, a letter designating mineral type is posted next to the line segments if the dominant mineral is other than chlorite. Occasionally an "s" appears to designate the presence of slickensides. The estimate of fracture thickness is also posted.

There are a few peculiarities in the cross sections. Sections H9A (Fig. C1) and H9H (Fig C8) include projections of through-going features; the other cross sections do not. These sections were compiled before it was realized that the clutter was too great to display both the raw data and the reconstruction on a single fracture. A second peculiarity is the reversal of view between cross sections B and C. An imaginary viewer walking counterclockwise

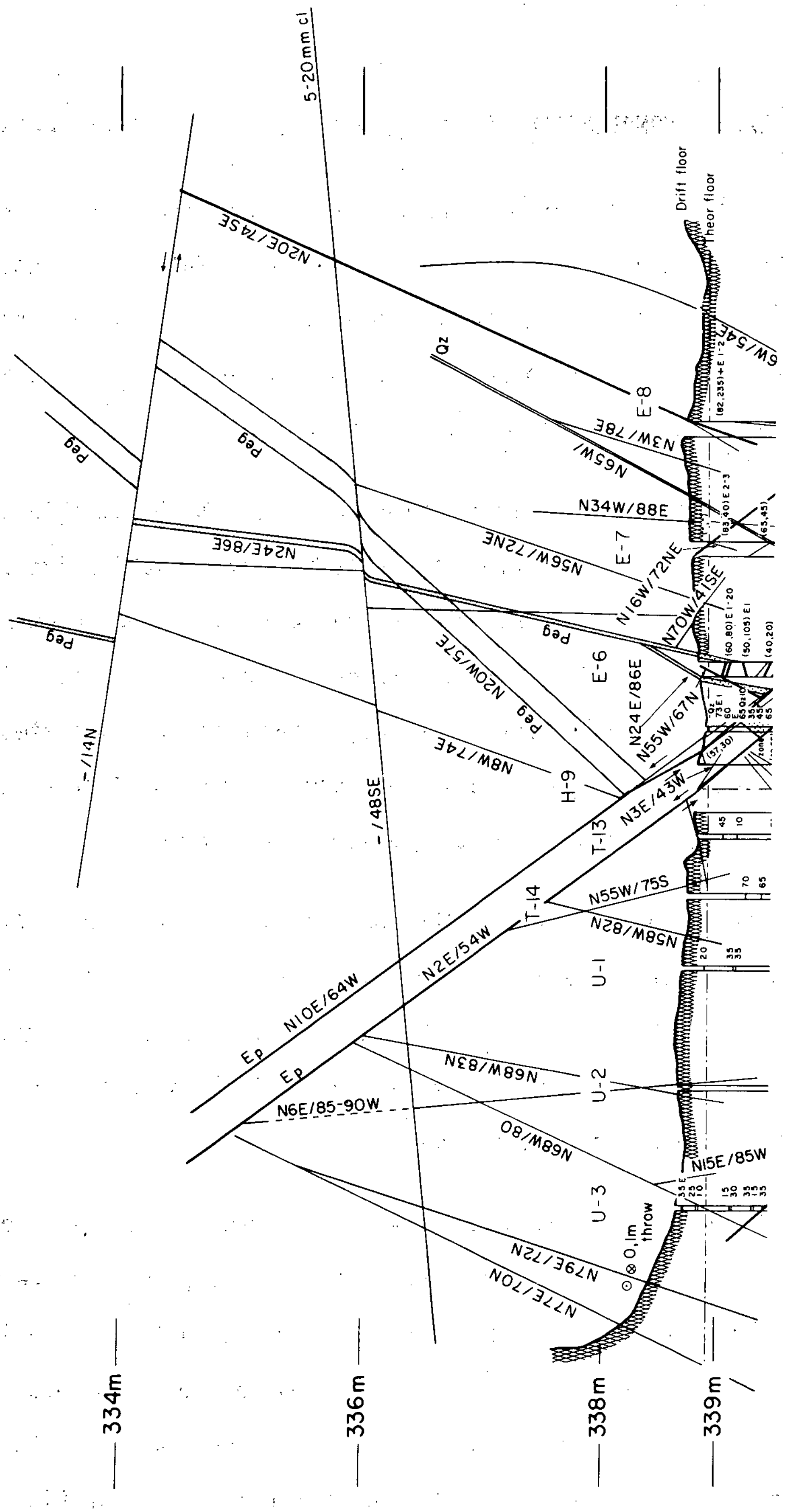
5-20mm cl
Drift floor
Theor floor
N20E/74SE
6W/54E
Qz
E-8
(82,235)+E 1-2
N3W/78E
N65W/
N34W/88E
(83,40) E 2-3
(65,45)
Peg
Peg
N24E/86E
N56W/72NE
E-7
N16W/72NE
N70W/41SE
(60,80) E 1-20
(50,105) E1
(40,20)
Peg
Peg
E-6
N24E/86E
N20W/57E
Peg
Qz
73E
60
60
E
65Qz10
35
65
N55W/67N
(57,30)
-/14N
N8W/74E
H-9
-/48SE
N3E/43W
T-13
45
10
N55W/75S
70
65
T-14
N58W/82N
20
35
35
N2E/54W
U-1
N10E/64W
Ep
Ep
N68W/83N
U-2
N6E/85-90W
N68W/80
N15E/85W
35E
75
70
15
30
35
15
35
U-3
0.1m throw
N79E/72N
N77E/70N
334m
336m
338m
339m

Fig. B-1 (top)

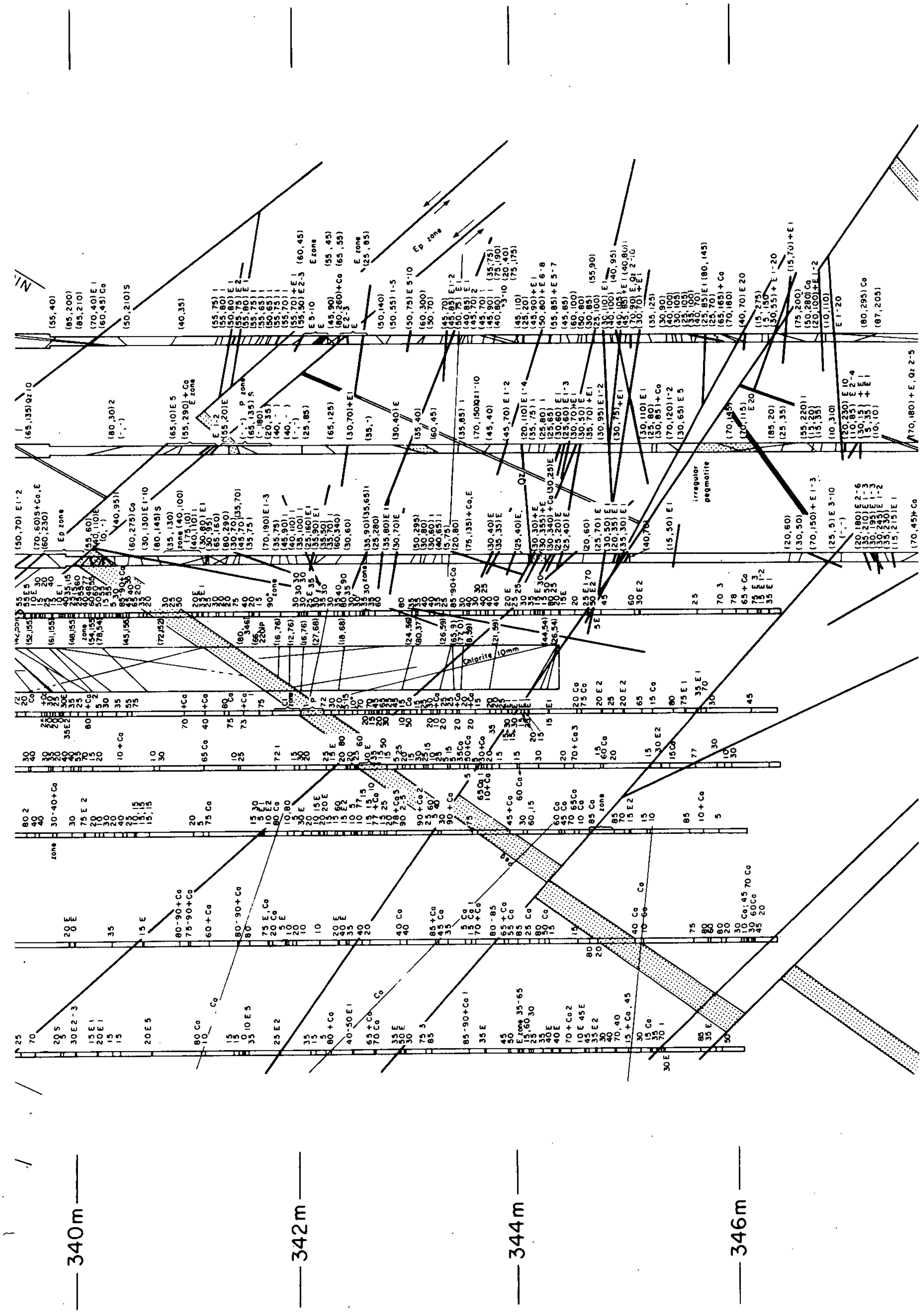

Fig. B-1 (middle)

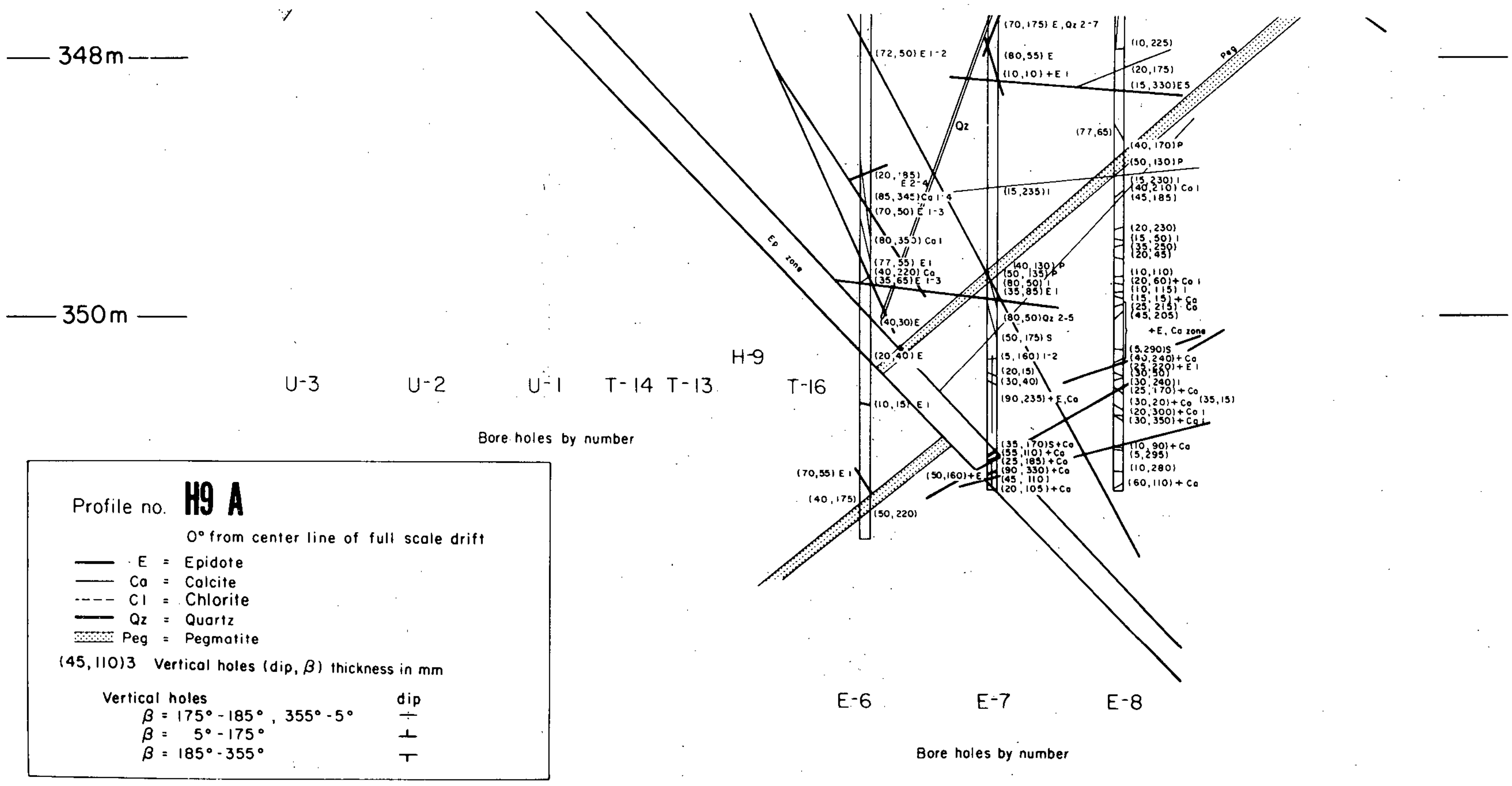

XBL 791-253

Fig. B-1 (bottom)

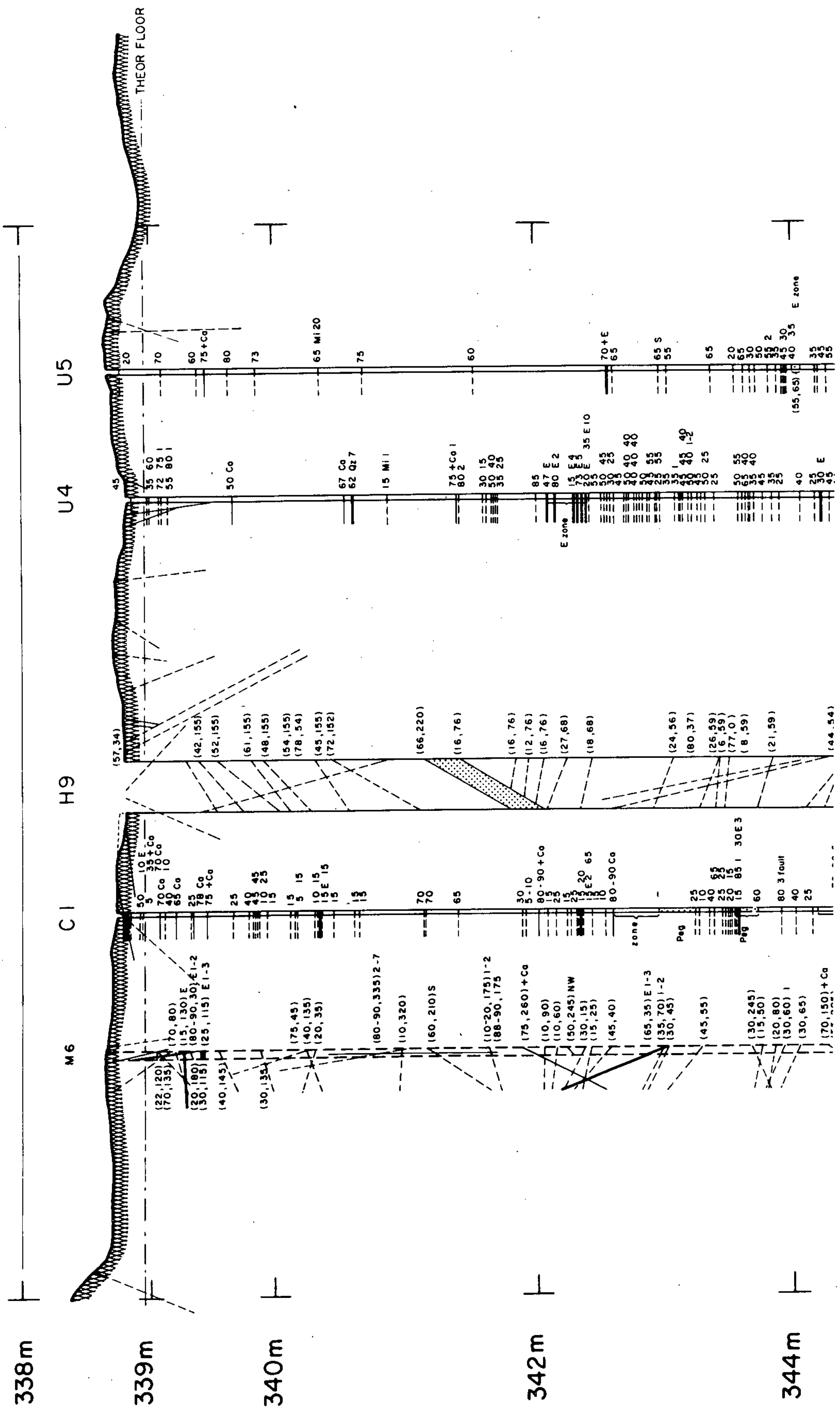

Fig. B-2 (top)

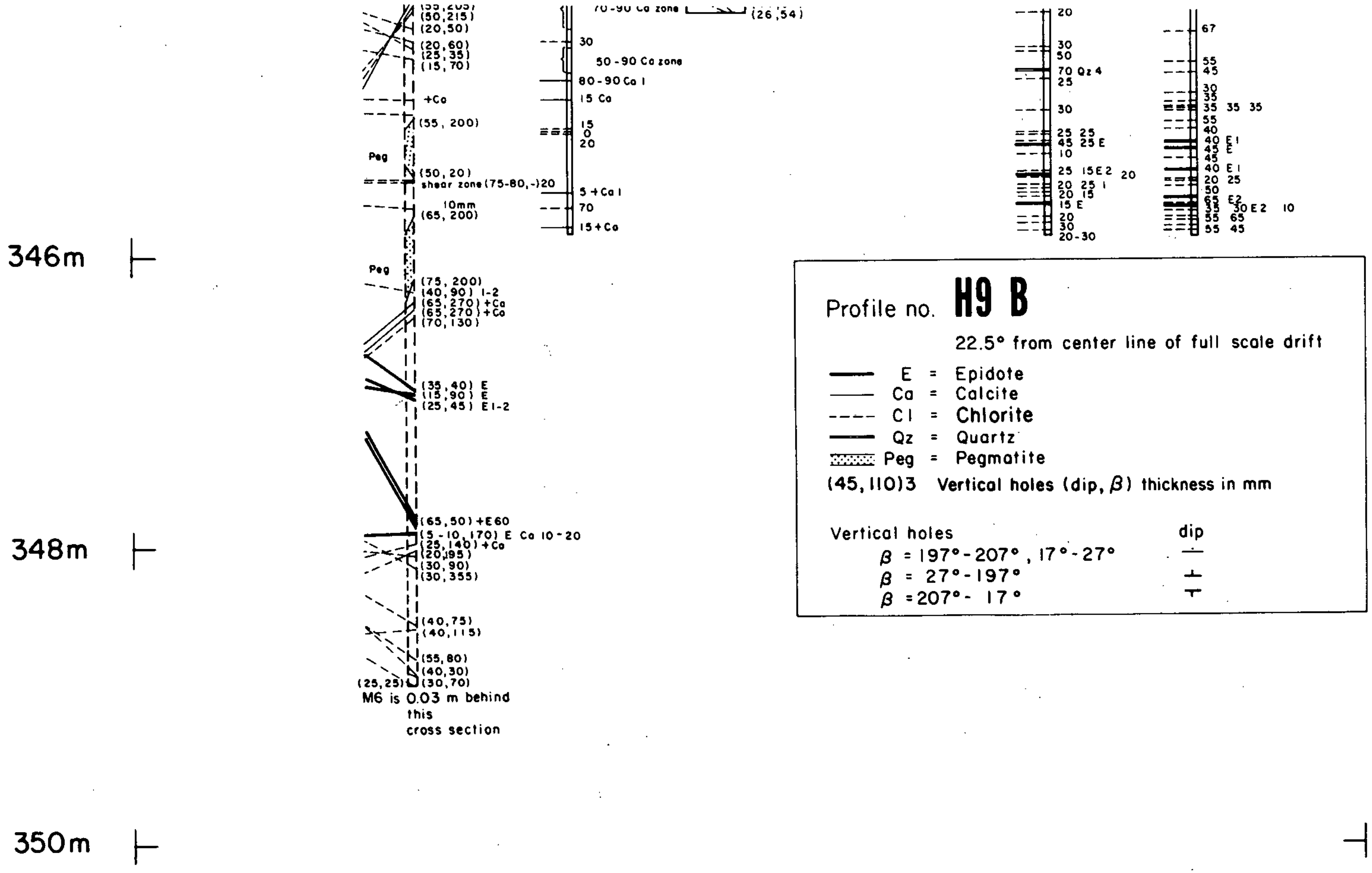

XBL 793-655

Fig. B-2 (bottom)

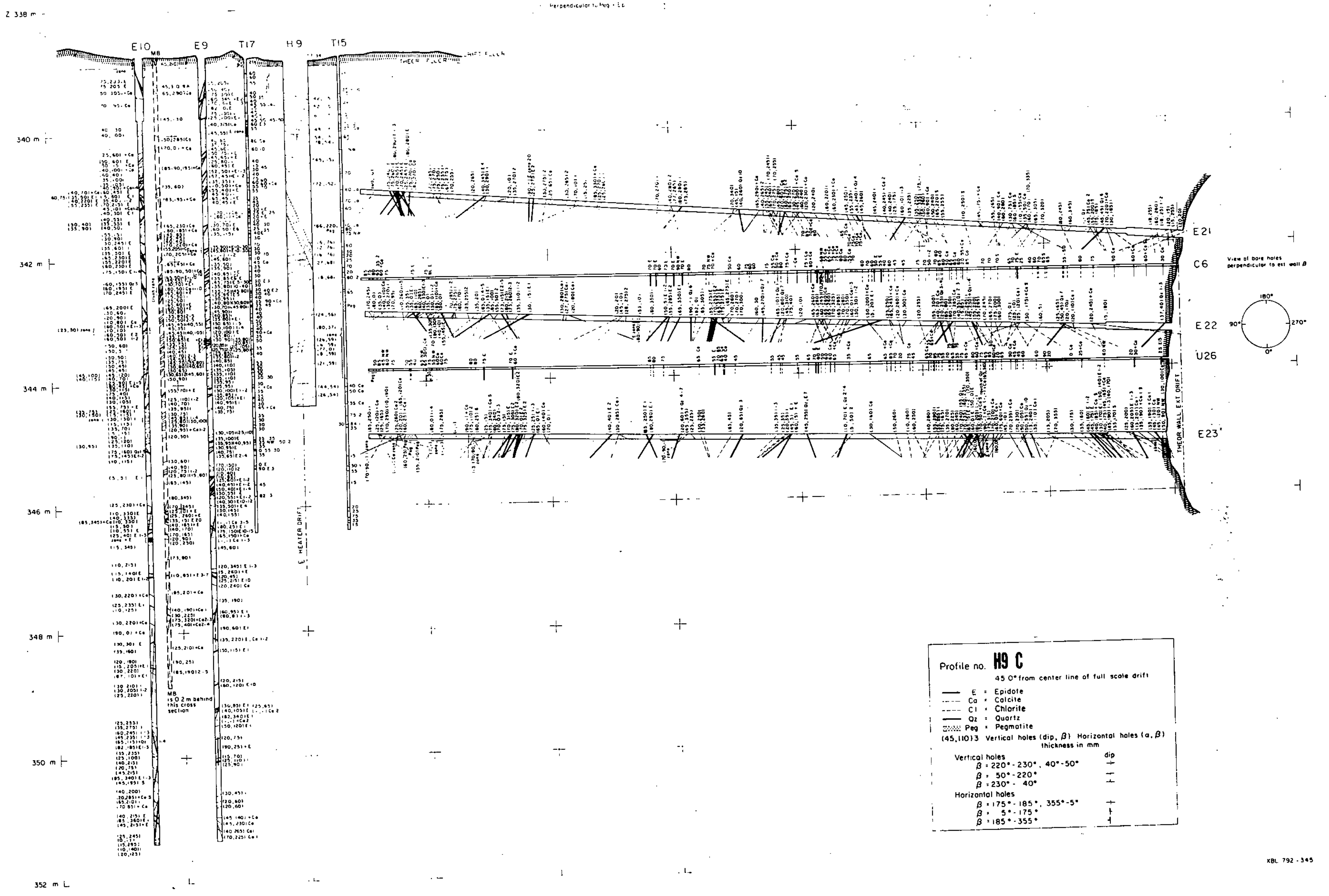
Z 338 m
340 m
342 m
344 m
346 m
348 m
350 m
352 m
E10
E9
T17
H9
T15
MB
MB is 0.2 m behind this cross section
THEOR FLOOR
DRIFT FLOOR
Perpendicular to Peg + Ep
HEATER DRIFT
E21
C6
E22
U26
E23'
THEOR WALL EXT DRIFT
View of bore holes perpendicular to ext wall β
180°
90°
270°
0°
Profile no. H9 C
45.0° from center line of full scale drift
E = Epidote
Ca = Calcite
Cl = Chlorite
Qz = Quartz
Peg = Pegmatite
(45,110)3 Vertical holes (dip, β) Horizontal holes (α, β) thickness in mm
Vertical holes
dip
β = 220° - 230°, 40° - 50°
β = 50° - 220°
β = 230° - 40°
Horizontal holes
β = 175° - 185°, 355° - 5°
β = 5° - 175°
β = 185° - 355°
XBL 792-345

Fig. B-3

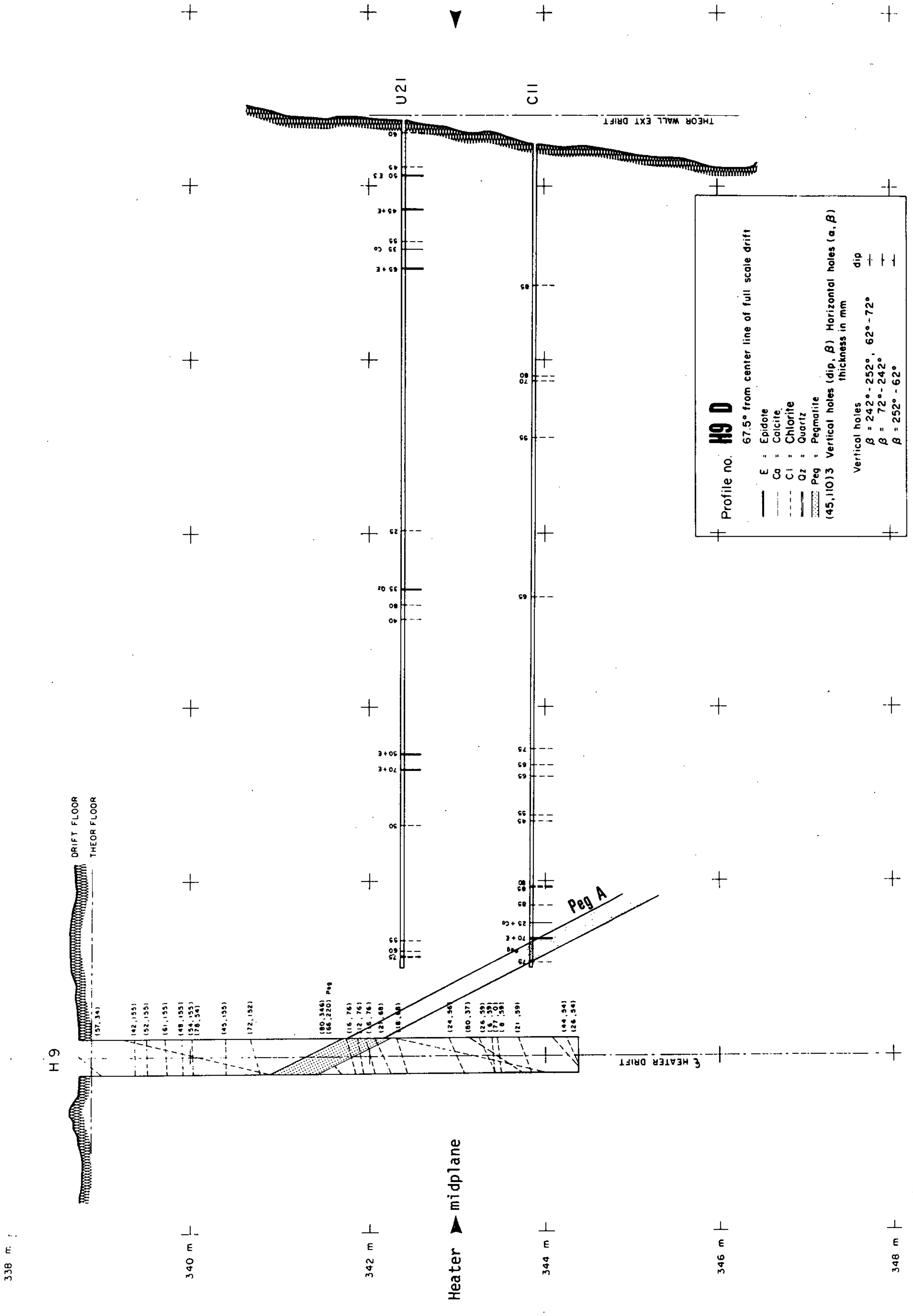

XBL 796-10326

Fig. B-4

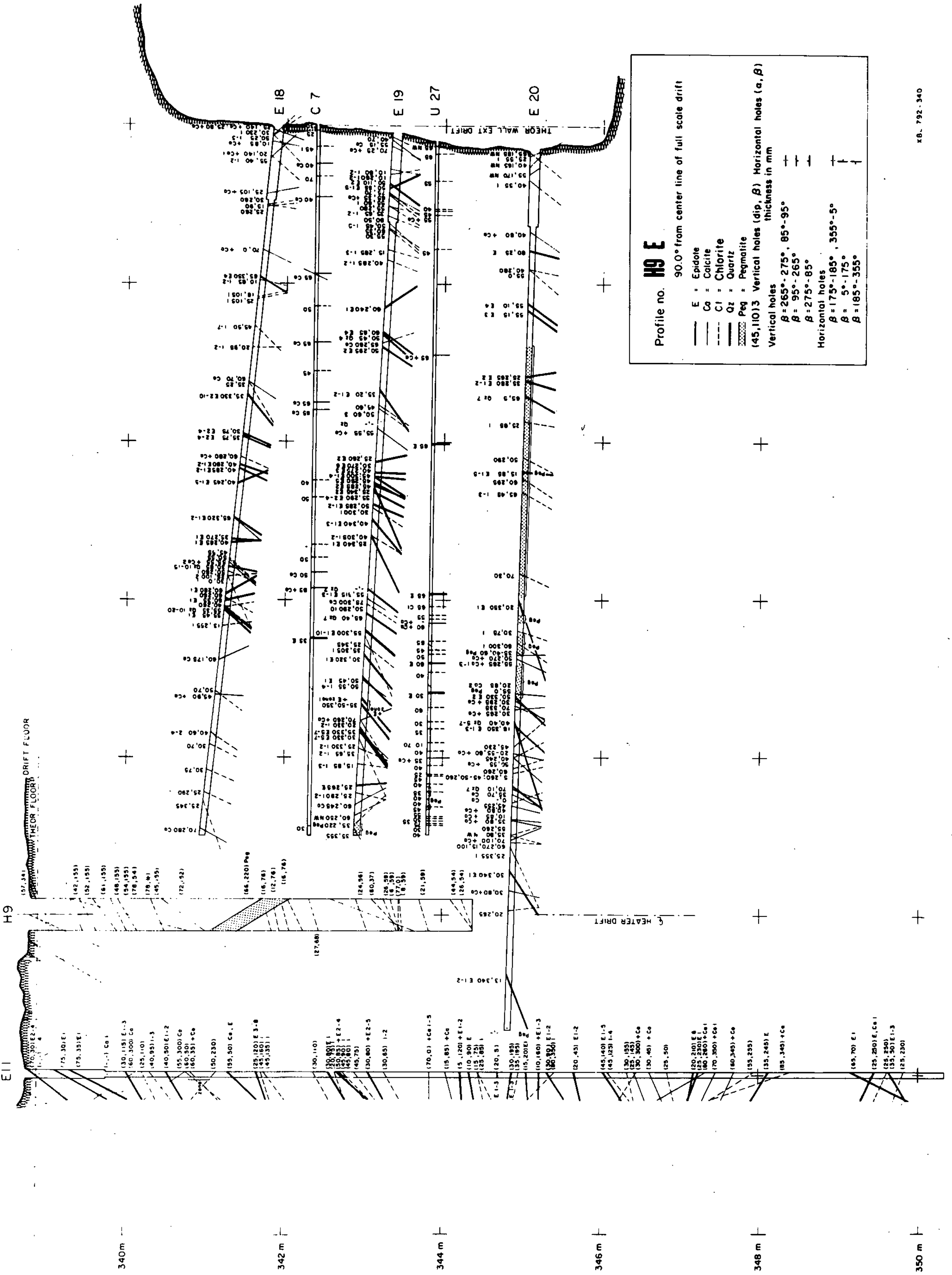
Profile no. H9 E
90.0° from center line of full scale drift
E = Epidote
Ca = Calcite
Cl = Chlorite
Qz = Quartz
Peg = Pegmatite
(45,110)13 Vertical holes (dip, β) Horizontal holes (α, β) thickness in mm
Vertical holes
β = 265°-275°, 85°-95°
β = 95°-265°
β = 275°-85°
Horizontal holes
β = 175°-185°, 355°-5°
β = 5°-175°
β = 185°-355°
E 18
C 7
E 19
U 27
E 20
THEOR WALL EXT DRIFT
H9
E11
DRIFT FLOOR
THEOR FLOOR
℄ HEATER DRIFT
340m
342 m
344 m
346 m
348 m
350 m
XBL 792-340

Fig. B-5

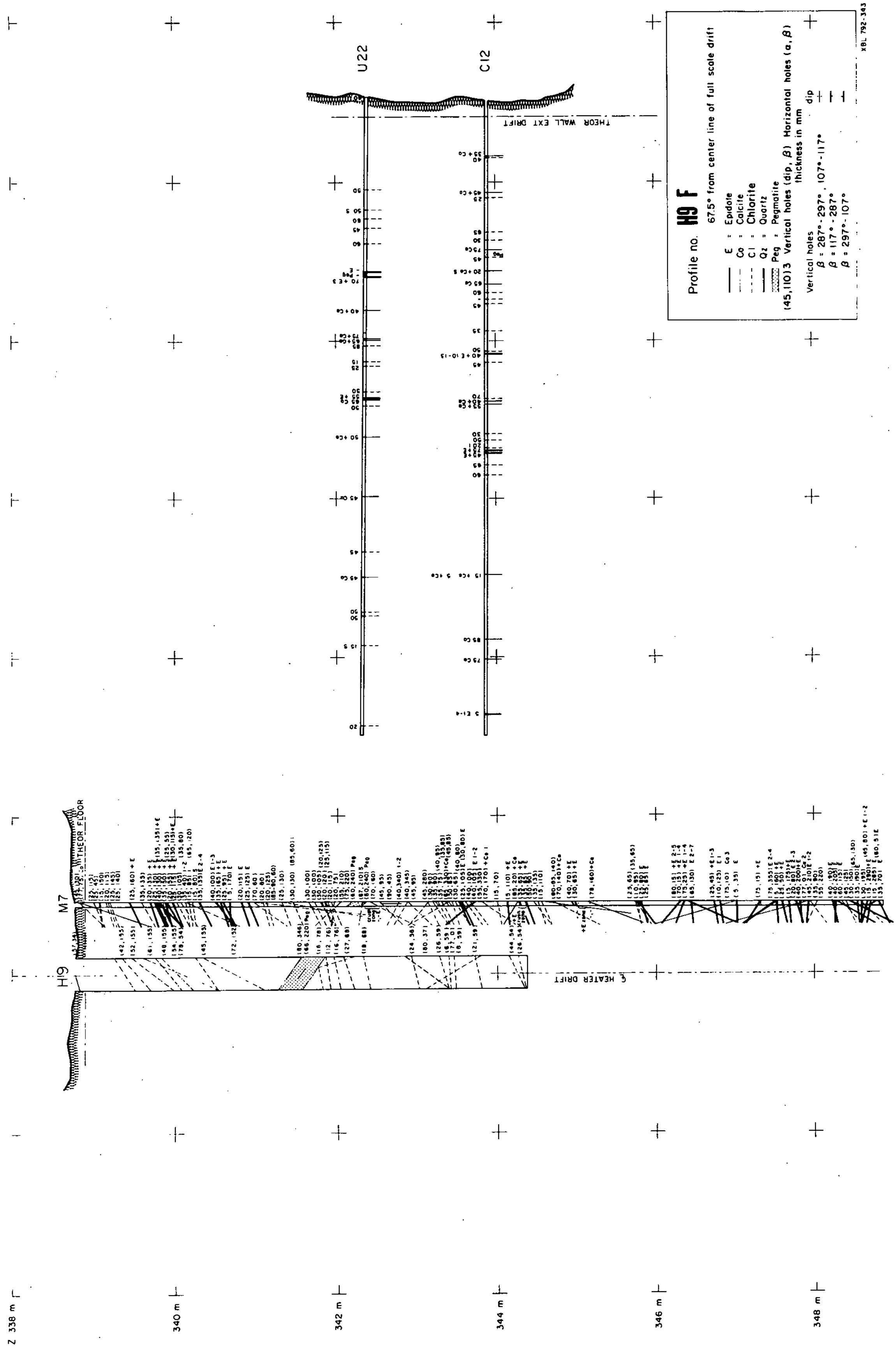
Profile no. H9 F
67.5° from center line of full scale drift
E = Epidote
Ca = Calcite
Cl = Chlorite
Qz = Quartz
Peg = Pegmatite
(45,110)3 Vertical holes (dip, β) Horizontal holes (a, β) thickness in mm
Vertical holes
dip
β = 287° - 297°, 107° - 117°
β = 117° - 287°
β = 297° - 107°
XBL 792-343
U22
C12
THEOR WALL EXT DRIFT
M7
H9
THEOR FLOOR
℄ HEATER DRIFT
Z 338 m
340 m
342 m
344 m
346 m
348 m

Fig. B-6

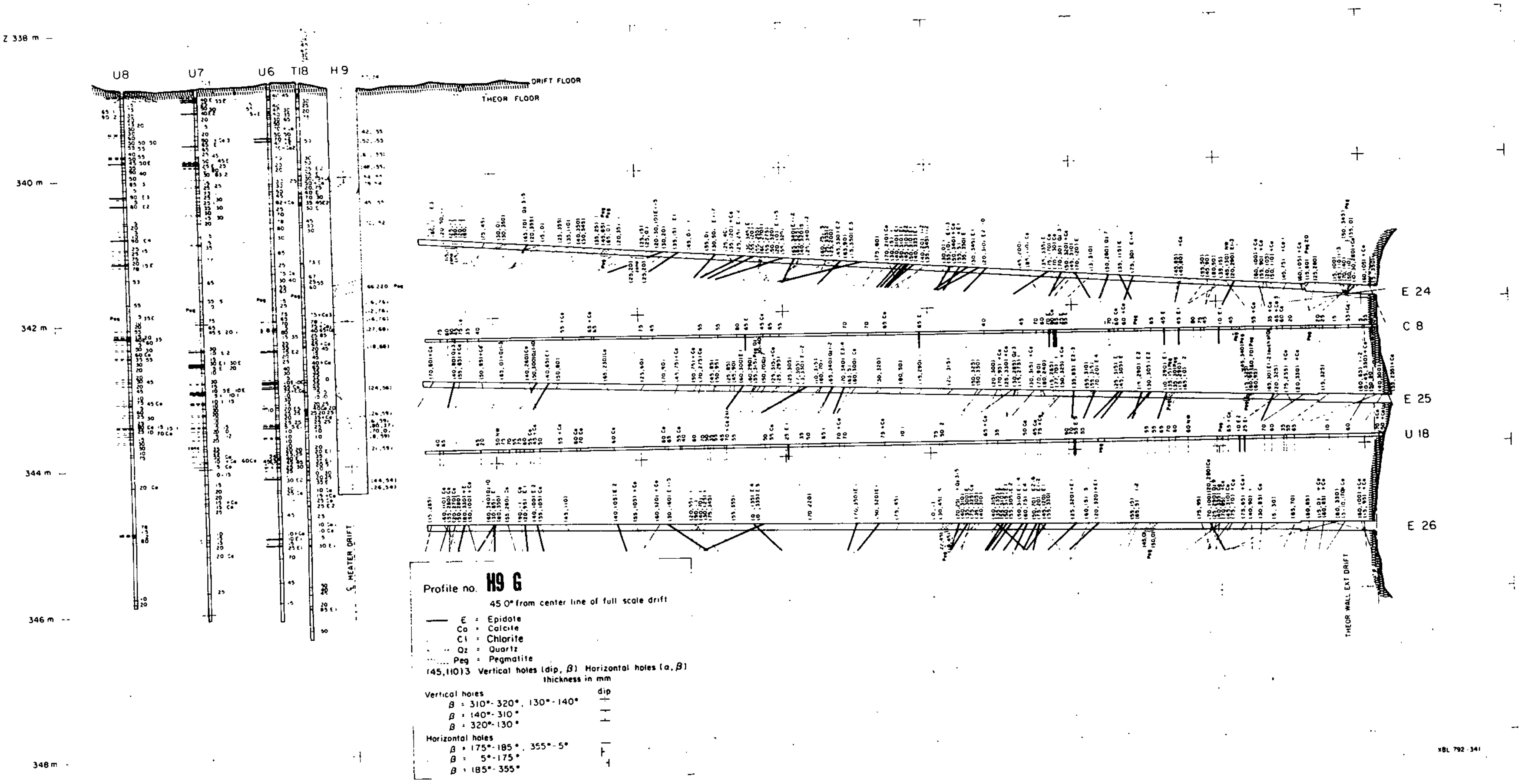
Z 338 m
340 m
342 m
344 m
346 m
348 m
U8
U7
U6
T18
H9
DRIFT FLOOR
THEOR FLOOR
℄ HEATER DRIFT
E 24
C 8
E 25
U 18
E 26
THEOR WALL EXT DRIFT
Profile no. H9 G
45.0° from center line of full scale drift
E = Epidote
Ca = Calcite
Cl = Chlorite
Qz = Quartz
Peg = Pegmatite
(45,110)3 Vertical holes (dip, β) Horizontal holes (α, β)
thickness in mm
Vertical holes
dip
β = 310°-320°, 130°-140°
β = 140°-310°
β = 320°-130°
Horizontal holes
β = 175°-185°, 355°-5°
β = 5°-175°
β = 185°-355°
XBL 792-341

Fig. B-7

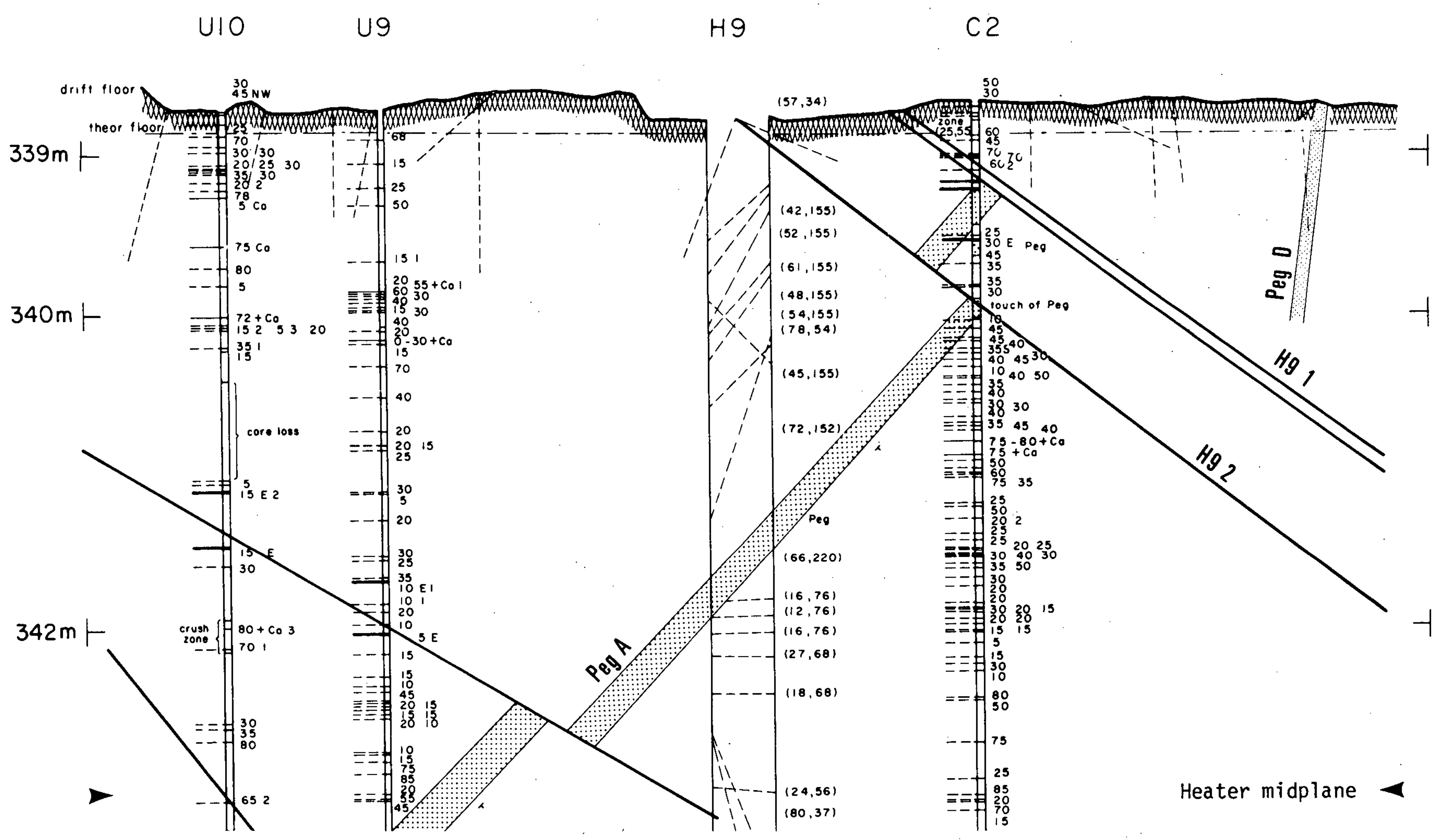
U10
U9
H9
C2
drift floor
theor floor
339m
340m
342m
core loss
crush zone
touch of Peg
Peg
Peg A
Peg D
H9 1
H9 2
Heater midplane

Fig. B-8 (top)

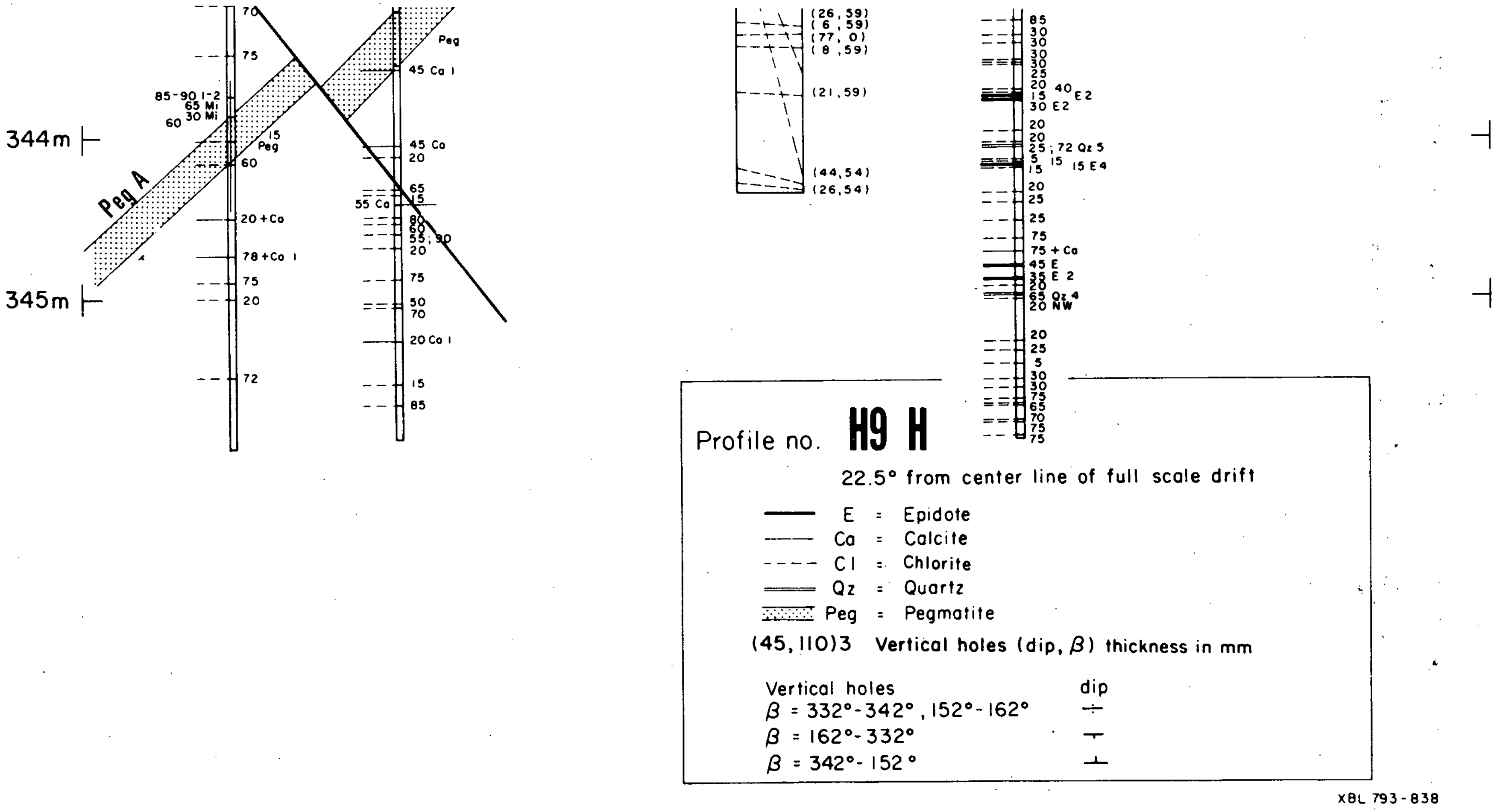

Fig. B-8 (bottom)

around H9 will see cross sections H9H through H9C in a consistent orientation, but must reverse his direction of travel to view H9A and H9B in the same orientation.

APPENDIX C: FRACTURE POLE PLOTS

This appendix contains 59 fracture pole plots from the H9 and H10 heater experiment areas in the Stripa full-scale drift. Comparable plots from the H9 and H10 areas appear side by side. If the number of fractures in a given category is less than 100, then the number of fractures in a 10 x 10 degree area is given explicitly; if there are more than 100, then each entry indicates the percentage of the total and contours have been drawn. Subsidiary information on each plot is self-explanatory. Table C.1 serves as an index for the plots.

Table C.1. Index of fracture pole plots grouped by location, mineralization, and whether open or closed.

Fracture Type		Vertical Boreholes H9 Area	Vertical Boreholes H10 Area	Horizontal Boreholes H9 Area	Horizontal Boreholes H10 Area	Vertical and Horizontal H9 Area
Closed	Chlorite	C1	C2	C25	C26	C49
	Calcite	C3	C4	C27	C28	C50
	Epidote	C5	C6	C29	C30	C51
	All	C7	C8	C31	C32	C52
Open	Chlorite	C9	C10	C33	C34	C53
	Calcite	C11	C12	C35	C36	C54
	Epidote	C13	C14	C37	C38	C55
	All	C15	C16	C39	C40	C56
Closed plus Open	Chlorite	C17	C18	C41	C42	C57
	Calcite	C19	C20	C43	C44	C58
	Epidote	C21	C22	C45	C46	C59
	All	C23	C24	C47	---[a]	C60

[a] Figure C48 was not drawn due to insufficient core length in this category.

Schmidt equal-area pole plot for vertical holes, H9 % occurrence
Lower hemisphere

Chlorite mineralization
Closed fractures
456 points
116.06 m of core

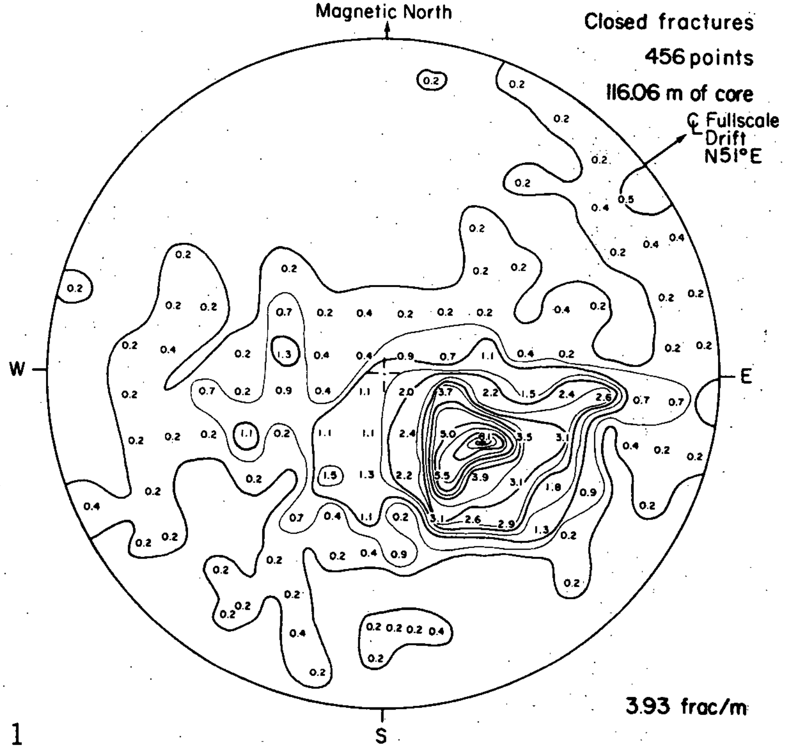

3.93 frac/m

C 1

XBL 8010-2890

Schmidt equal-area pole plot for vertical holes, H10 % occurrence
Lower hemisphere

Chlorite mineralization
Closed fractures
329 points
74.84 m of core

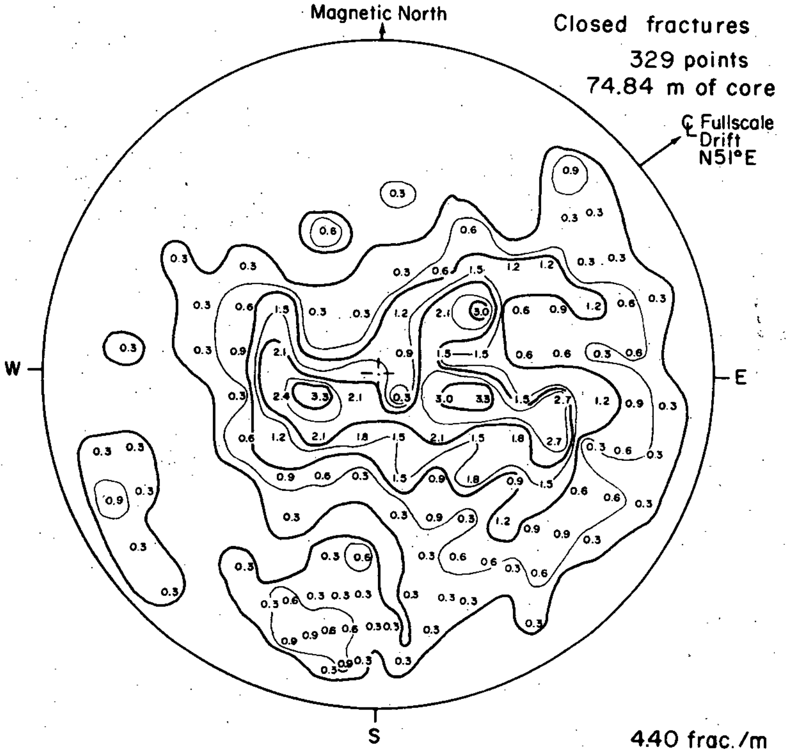

4.40 frac./m

C 2

XBL 8010-2920

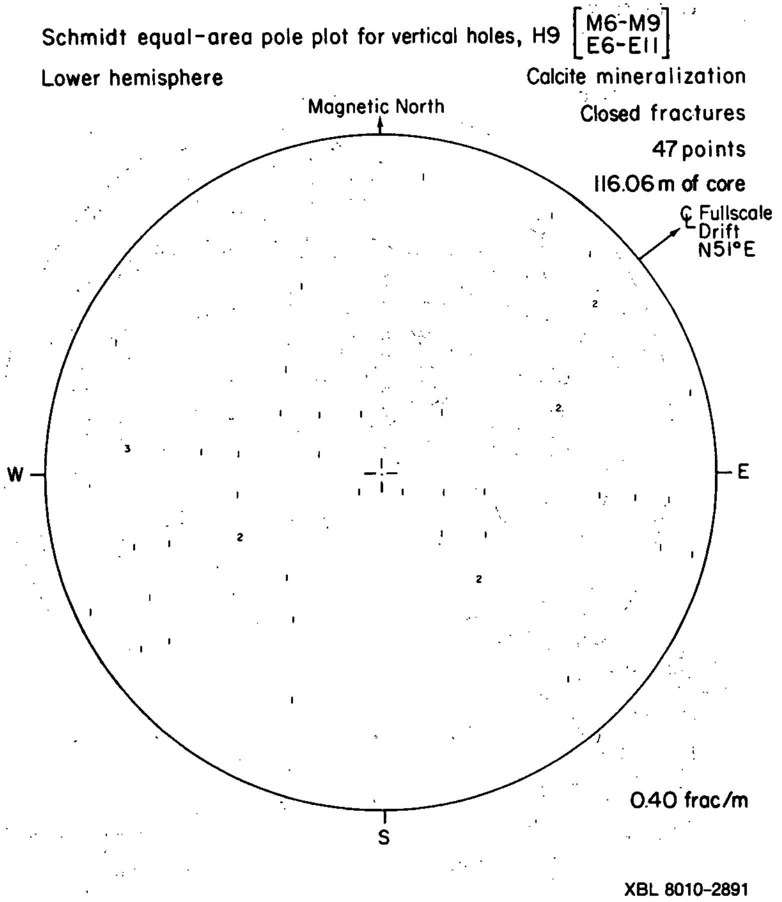

Schmidt equal-area pole plot for vertical holes, H9 [M6-M9 E6-E11]

C 3

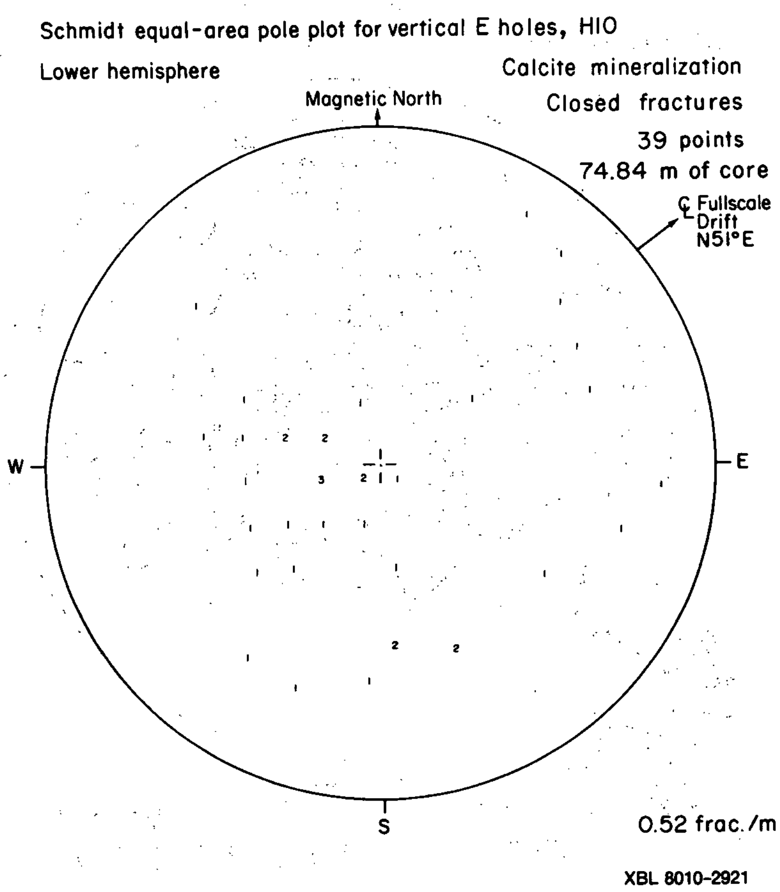

Schmidt equal-area pole plot for vertical E holes, H10

C 4

Schmidt equal-area pole plot for vertical holes, H9% occurrence

Lower hemisphere

Epidote mineralization

Closed fractures

316 points

116.06 m of core

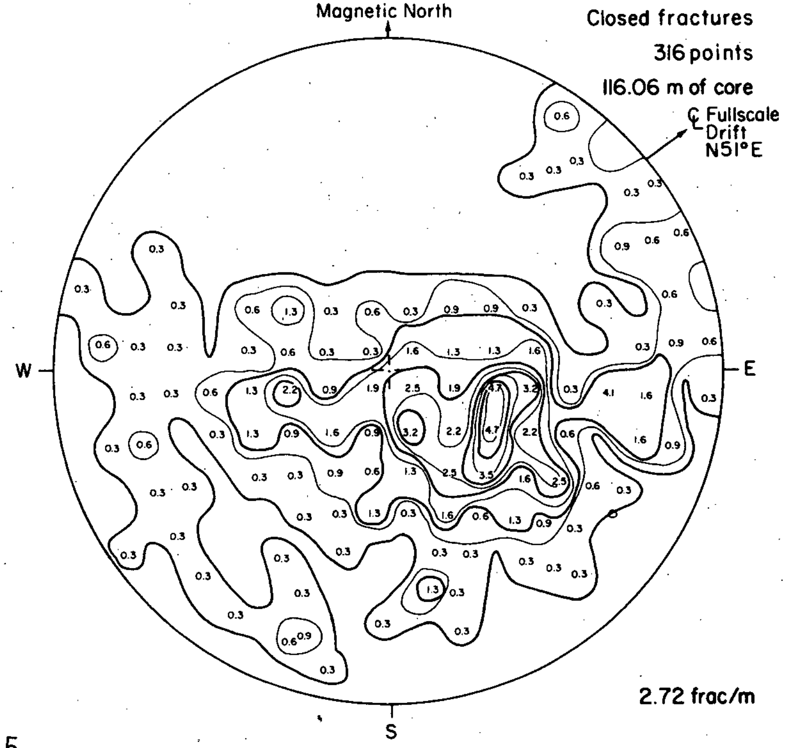

2.72 frac/m

C 5

XBL 8010-2892

Schmidt equal-area pole plot for vertical E holes, H10

Lower hemisphere

Epidote mineralization

Closed fractures

44 points

74.84 m of core

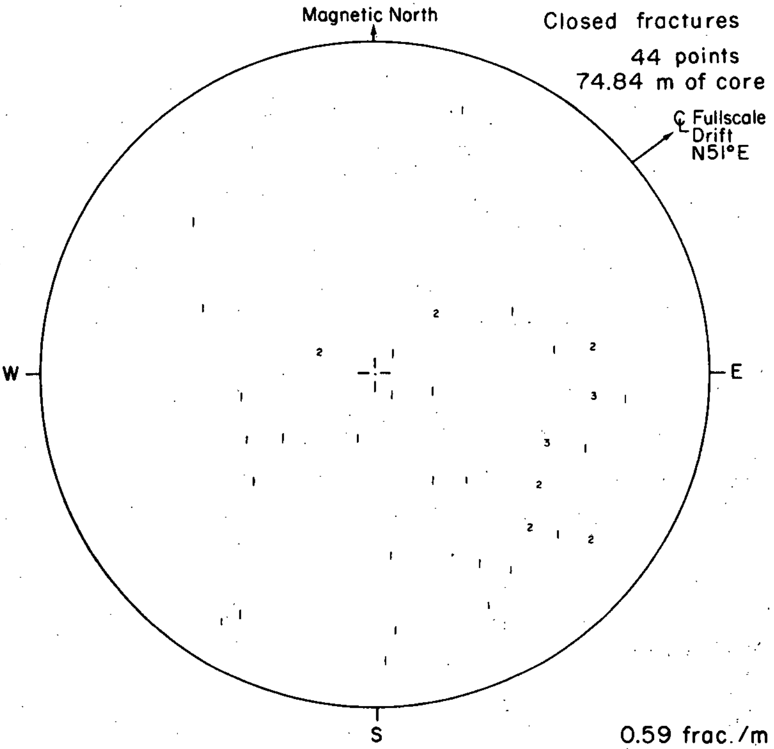

0.59 frac./m

C 6

XBL 8010-2922

Schmidt equal-area pole plot for vertical E and M holes, H9 % occurrence

Lower hemisphere

All mineralizations

Closed fractures

100% = 819 points

116.06 m of core

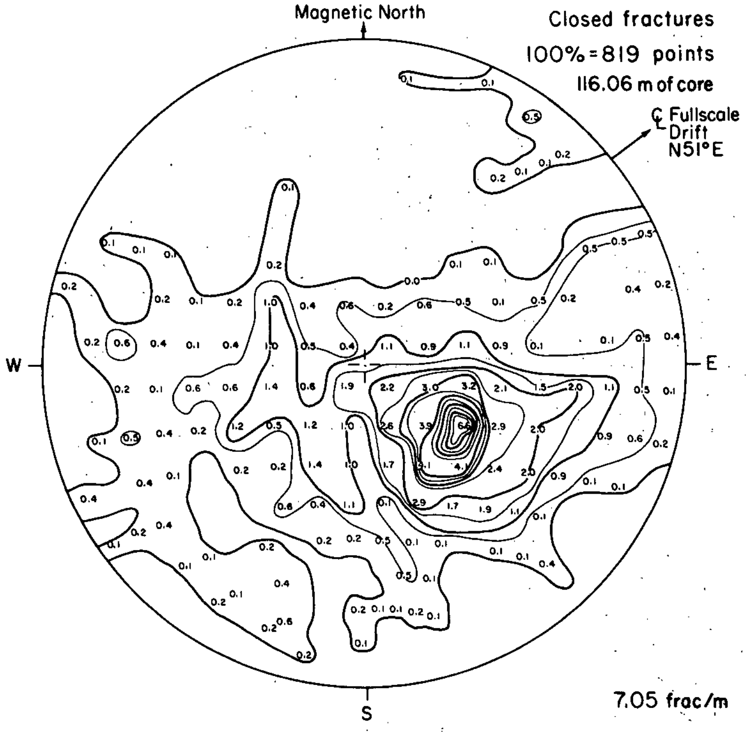

7.05 frac/m

XBL 8010-2945

C 7

Schmidt equal-area pole plot for vertical E holes, H10 % occurrence

Lower hemisphere

All mineralizations

Closed fractures

100% = 412 points

74.84 m of core

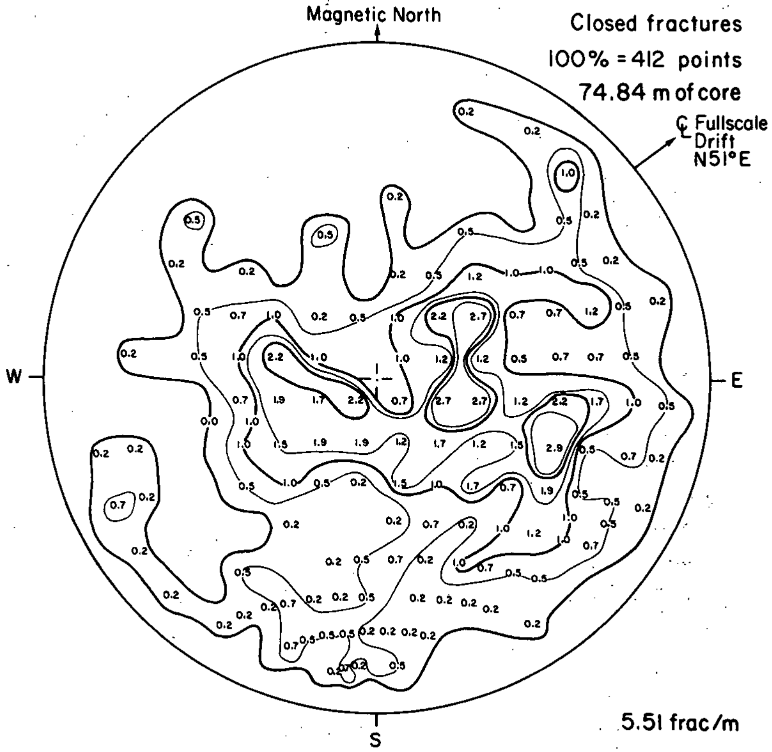

5.51 frac/m

XBL 8010-2923

C 8

Schmidt equal-area pole plot for vertical holes, H9% occurrence

Lower hemisphere

Chlorite mineralization
Open fractures
174 points
116.06 m of core

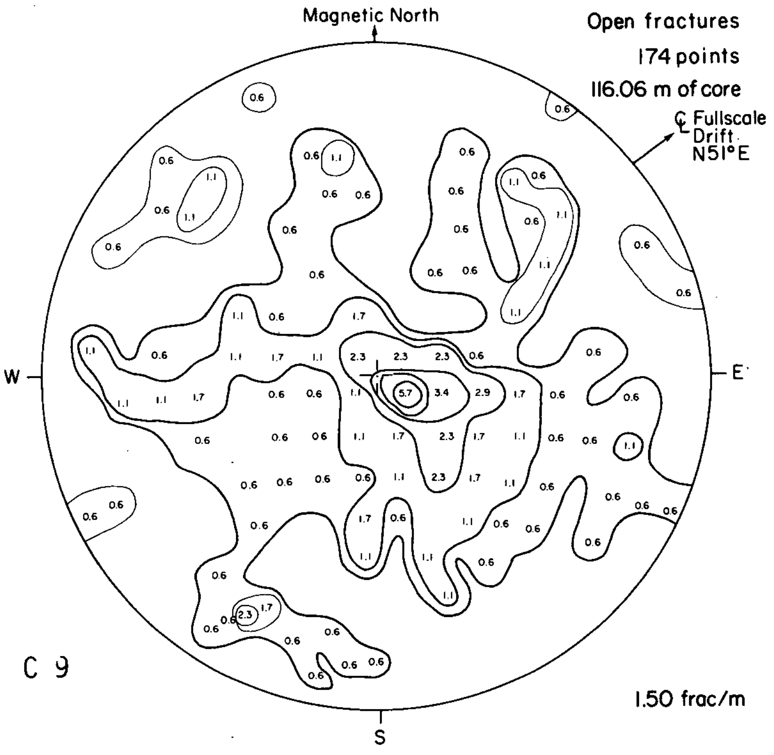

C 9

1.50 frac/m

XBL 8010-2893

Schmidt equal-area pole plot for vertical holes, H10 % occurrence

Lower hemisphere

Chlorite mineralization
Open fractures
248 points
74.84 m of core

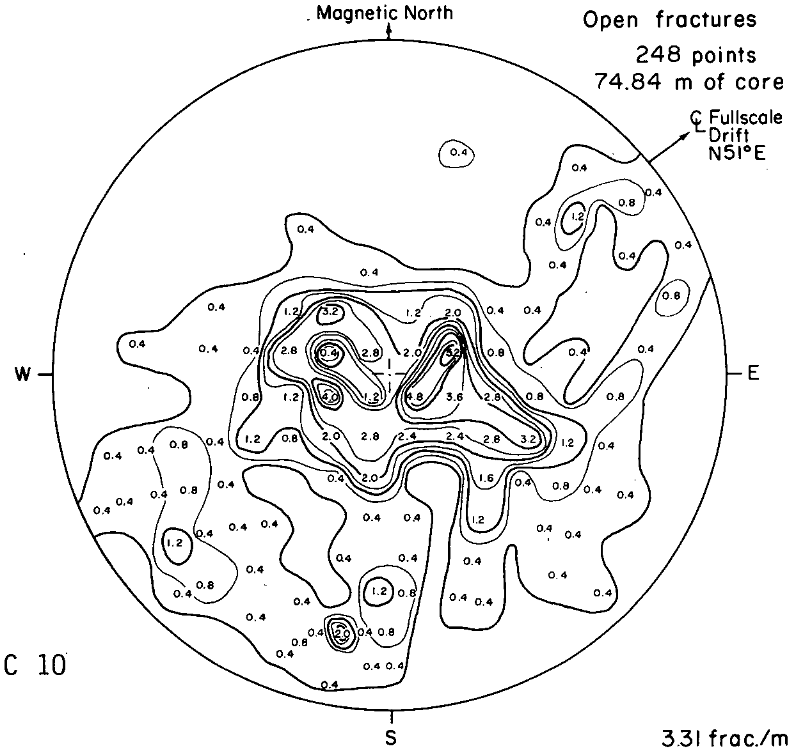

C 10

3.31 frac./m

XBL 8010-2924

Schmidt equal-area pole plot for vertical holes, H9

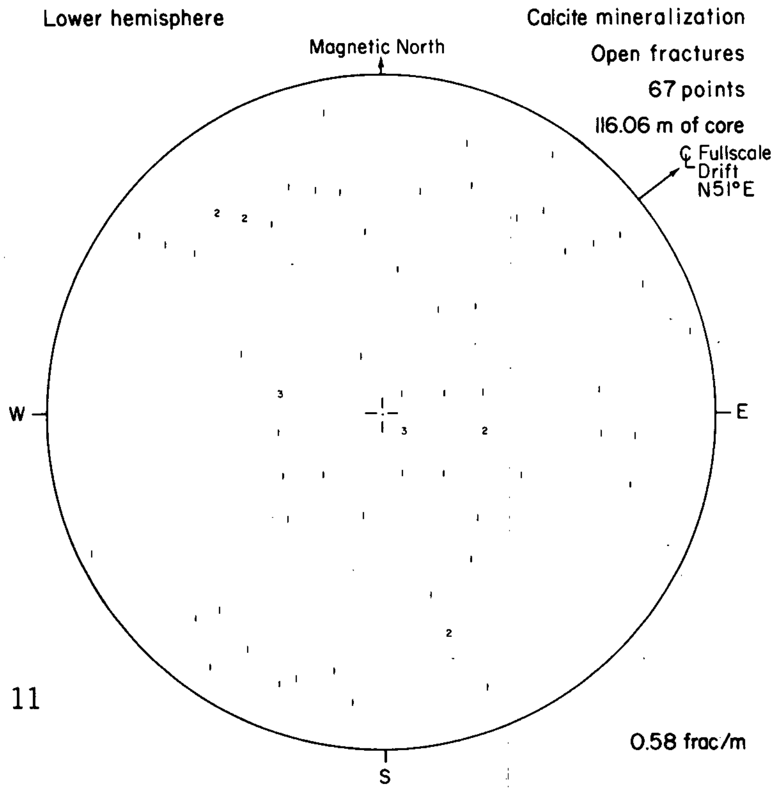

C 11

XBL 8010-2894

Schmidt equal-area pole plot for vertical holes, H10 % occurrence

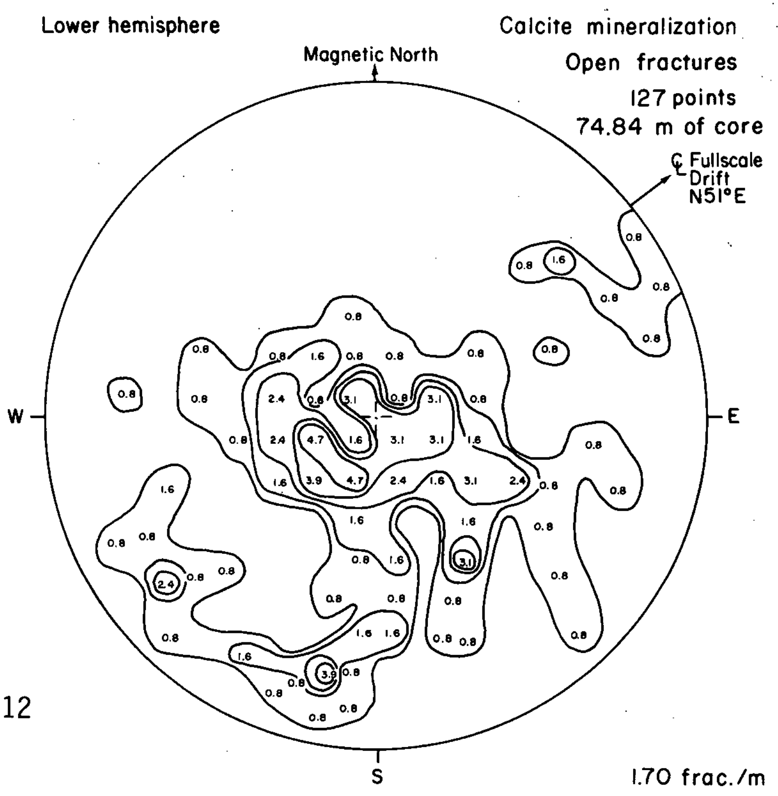

C 12

XBL 8010-2925

Schmidt equal-area pole plot for vertical holes, H9

Lower hemisphere

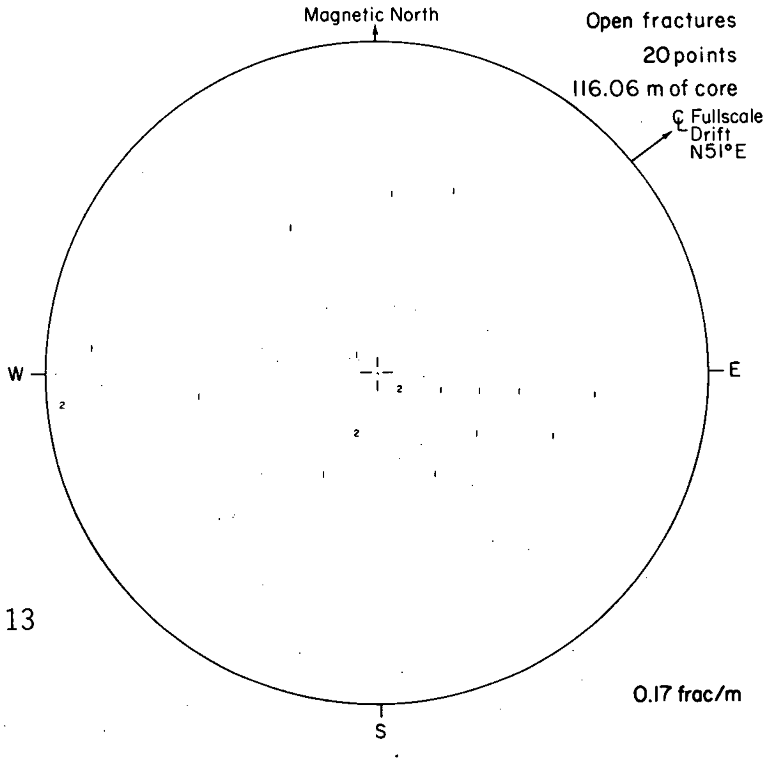

C 13

XBL 8010-2895

Schmidt equal-area pole plot for vertical E holes, H10

Lower hemisphere

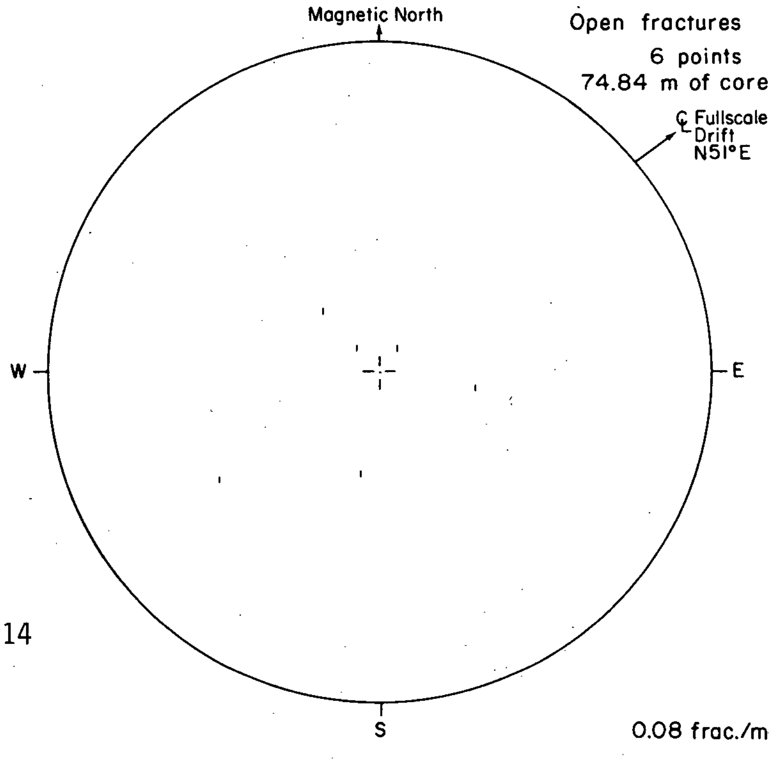

C 14

XBL 8010-2926

Schmidt equal-area pole plot for vertical holes H9% occurence

Lower hemisphere

All mineralization

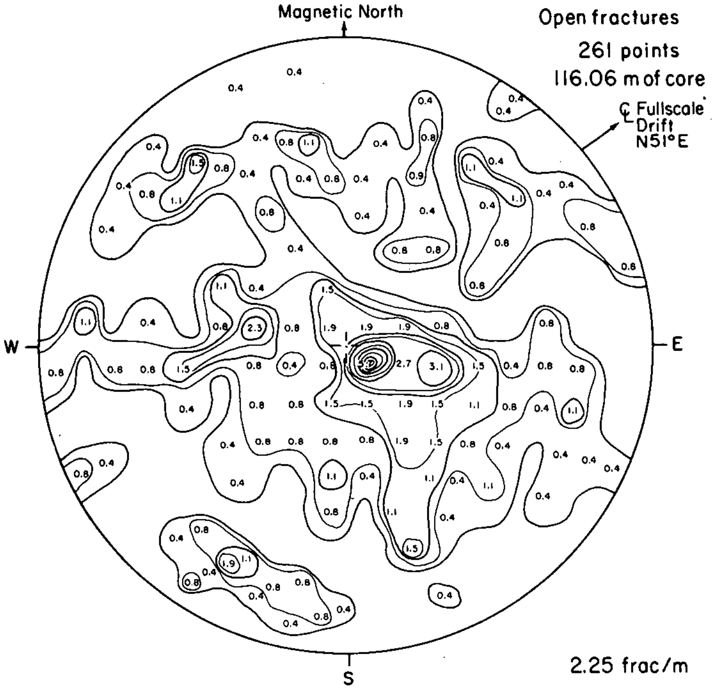

C 15

Schmidt equal-area pole plot for vertical E holes H10% occurence

Lower hemisphere

All mineralization

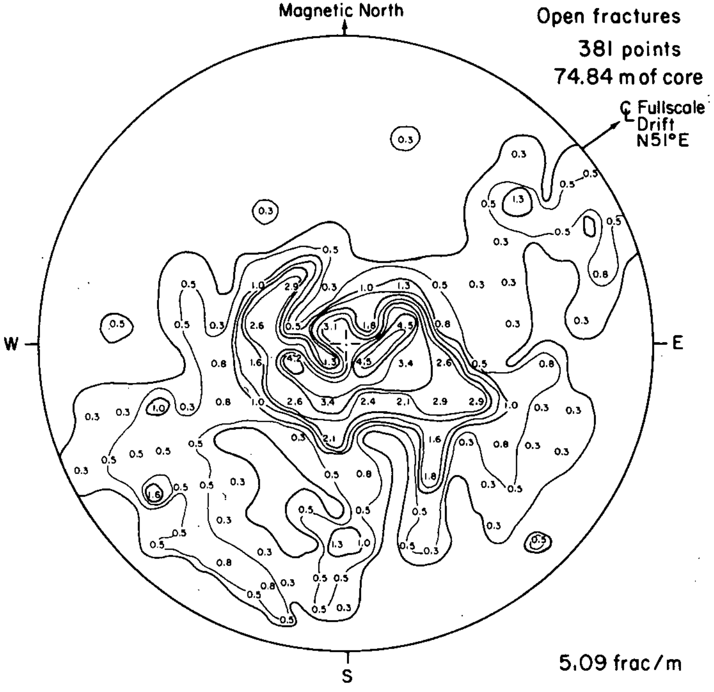

C 16

XBL 8012-6586A

Schmidt equal-area pole plot for vertical holes, H9 % occurrence

Lower hemisphere

Chlorite mineralization
All (open & closed) fractures
630 points
116.06 m of core

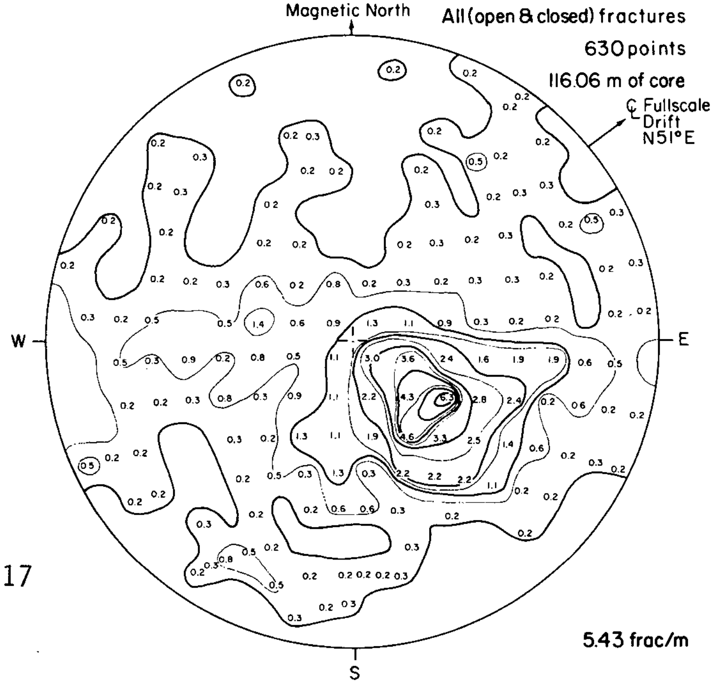

5.43 frac/m

C 17

Schmidt equal-area pole plot for vertical holes, H10 % occurrence

Lower hemisphere

Chlorite mineralization
All fractures
(open and closed)
577 points
74.84 m of core

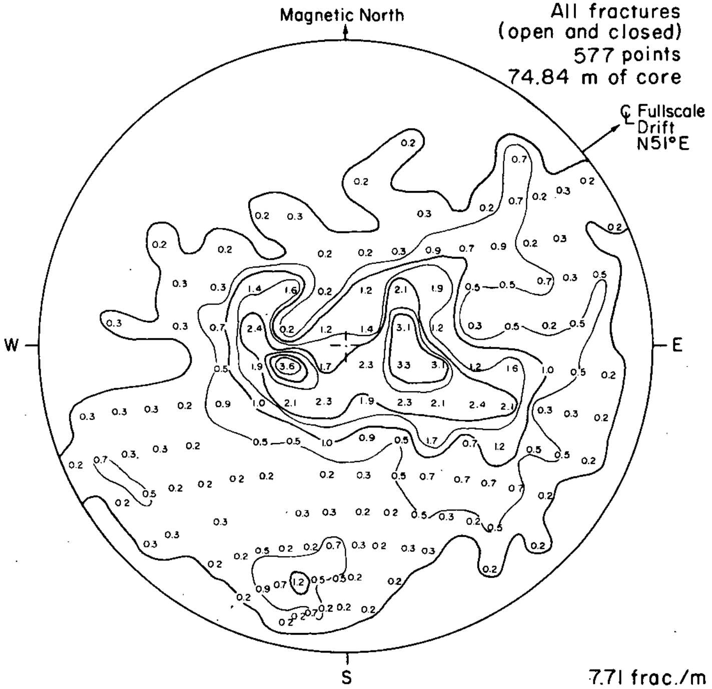

7.71 frac./m

C 18

XBL 8010-2927 B

Schmidt equal-area pole plot for vertical holes, H9 % occurrence

Lower hemisphere

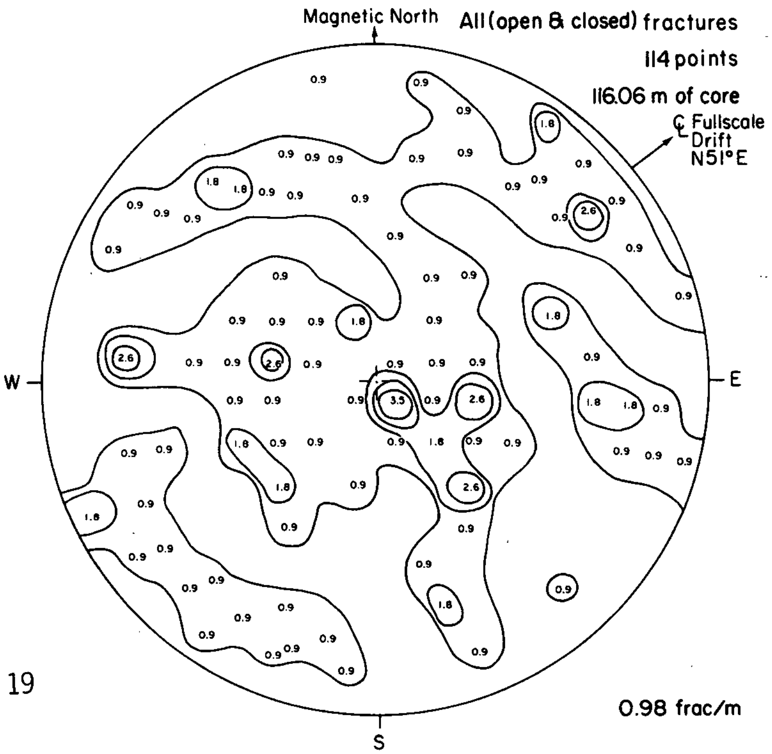

Calcite mineralization
All (open & closed) fractures
114 points
116.06 m of core

C 19

0.98 frac/m

XBL 8010-2897

Schmidt equal-area pole plot for vertical holes, H10 % occurrence

Lower hemisphere

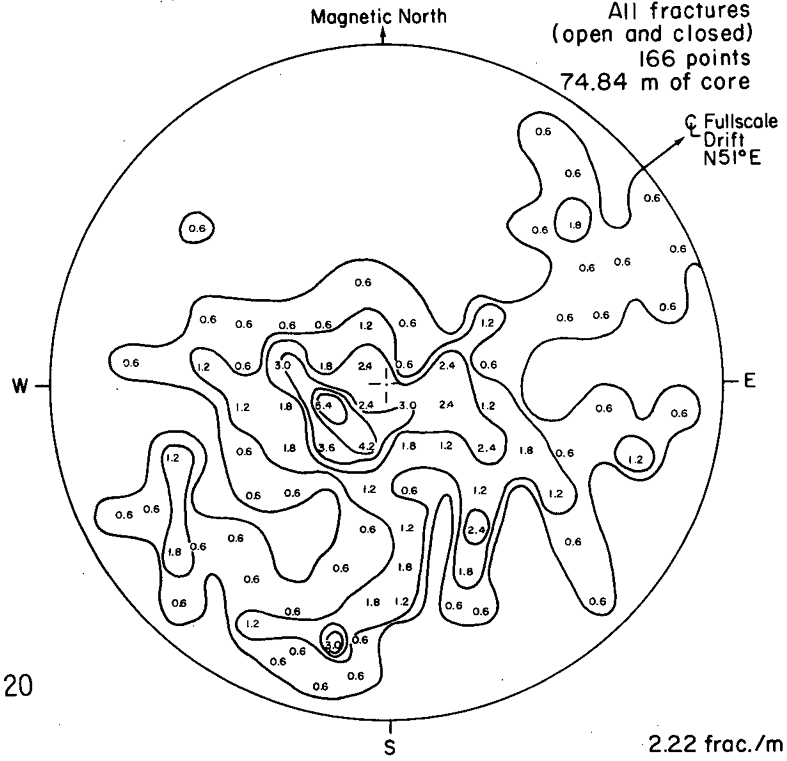

Calcite mineralization
All fractures
(open and closed)
166 points
74.84 m of core

C 20

2.22 frac./m

XBL 8010-2928

Schmidt equal-area pole plot for vertical holes, H9 % occurrence

Lower hemisphere

Epidote mineralization

All (open & closed) fractures

336 points

116.06 m of core

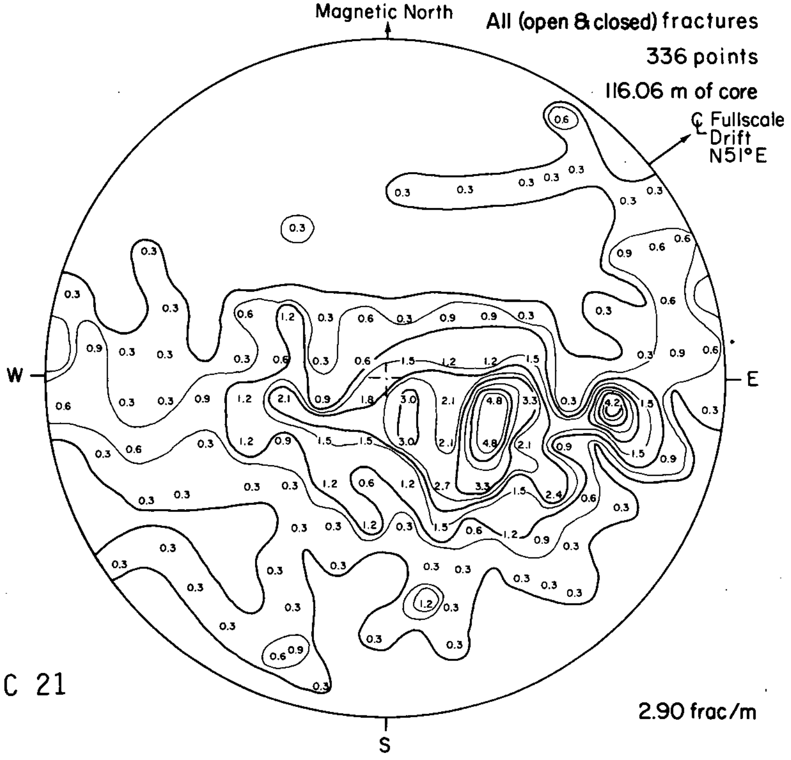

C 21

2.90 frac/m

XBL 8010-2898

Schmidt equal-area pole plot for vertical E holes, H10

Lower hemisphere

Epidote mineralization

All fractures

(open and closed)

50 points

74.84 m of core

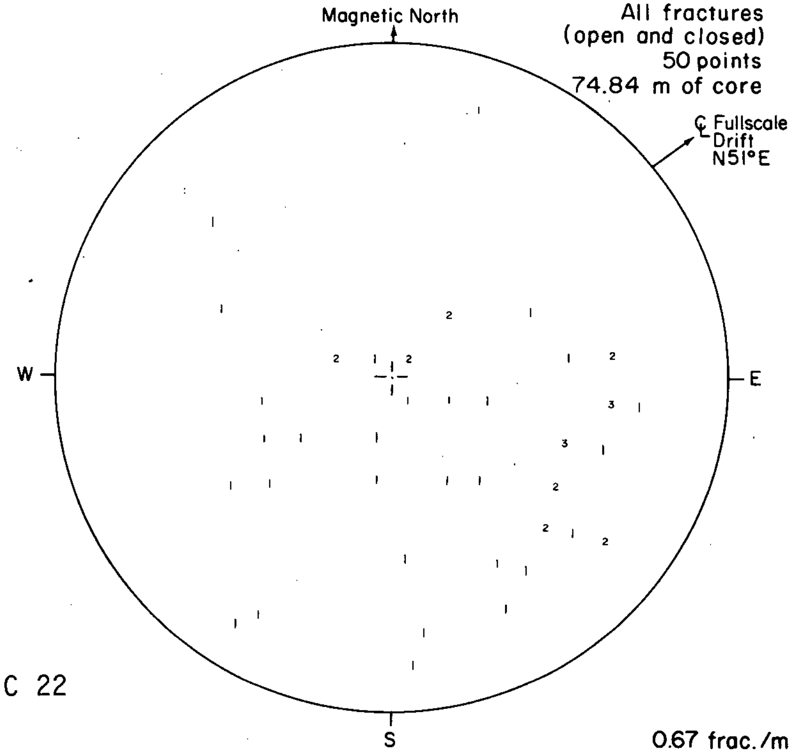

C 22

0.67 frac./m

XBL 8010-2929

Schmidt equal-area pole plot for vertical holes, H9 % occurrence

Lower hemisphere

All mineralization

All (closed & open) fractures

1080 points

116.06 m of core

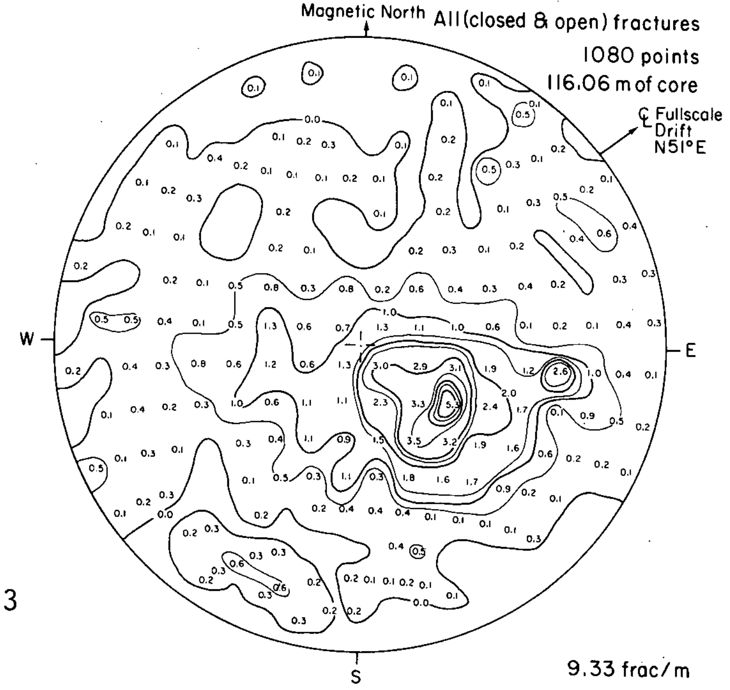

C 23

Schmidt equal-area pole plot for vertical E holes, H10 % occurence

Lower hemisphere

All mineralization

All (open & closed) fractures

793 points

74.84 m of core

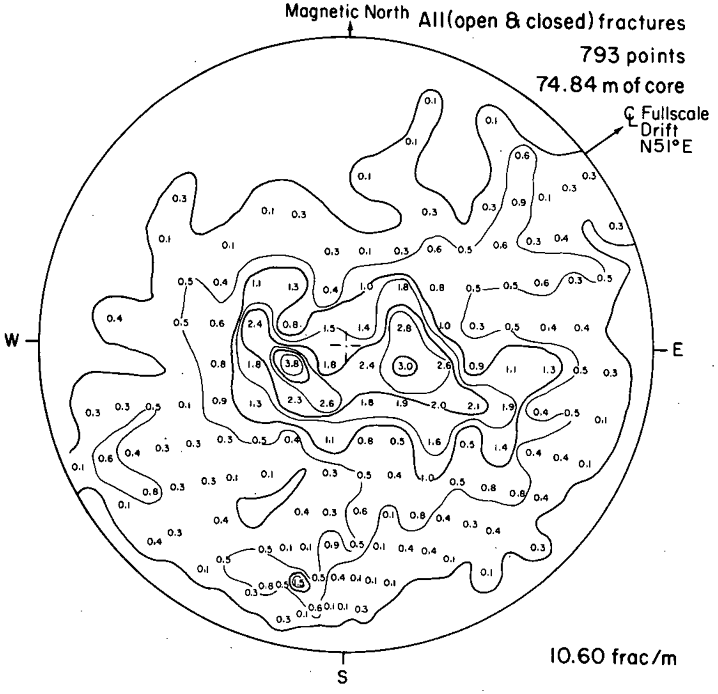

C 24

XBL 8010-2930 B

Schmidt equal-area pole plot for horizontal holes, H9 % occurrence

Lower hemisphere

Chlorite mineralization

Closed fractures

260 points

108.08 m of core

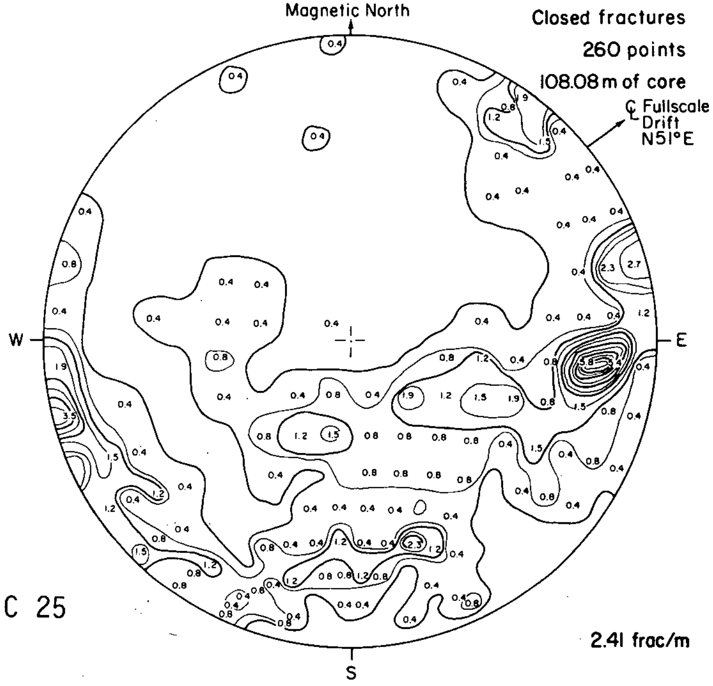

C 25

2.41 frac/m

Schmidt equal-area pole plot for horizontal holes, H10 % occurrence

Lower hemisphere

Chlorite mineralization

Closed fractures

100 points

30.54 m of core

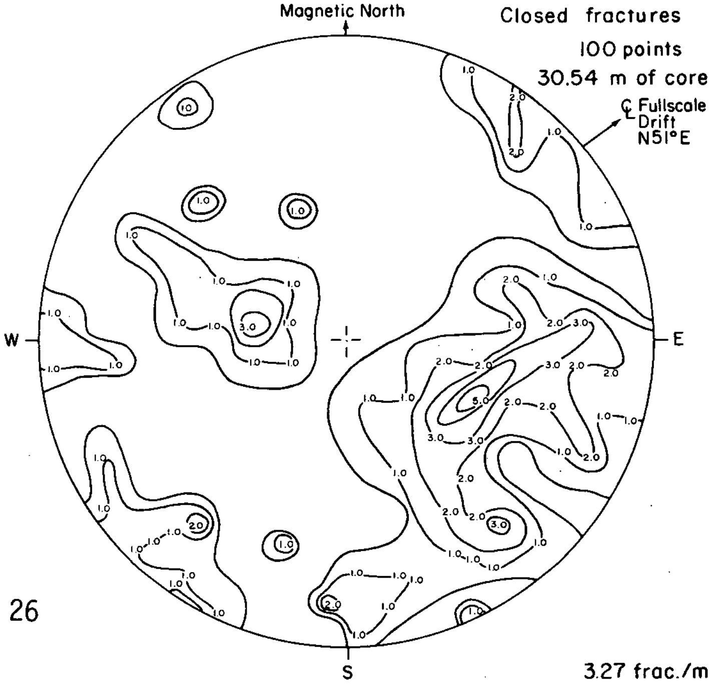

C 26

3.27 frac./m

XBL 8010-2931A

Schmidt equal-area pole plot for horizontal E holes, H9

Lower hemisphere

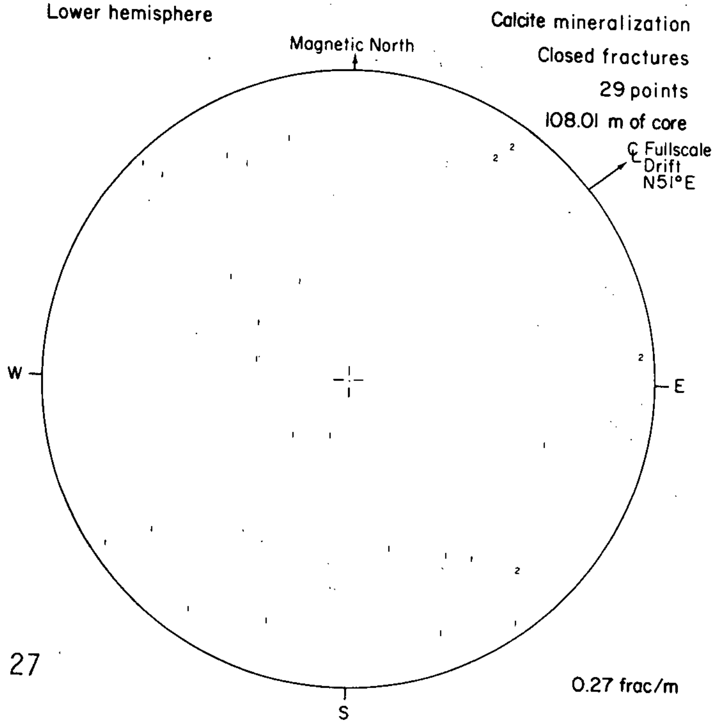

C 27

Schmidt equal-area pole plot for horizontal E holes, H10

Lower hemisphere

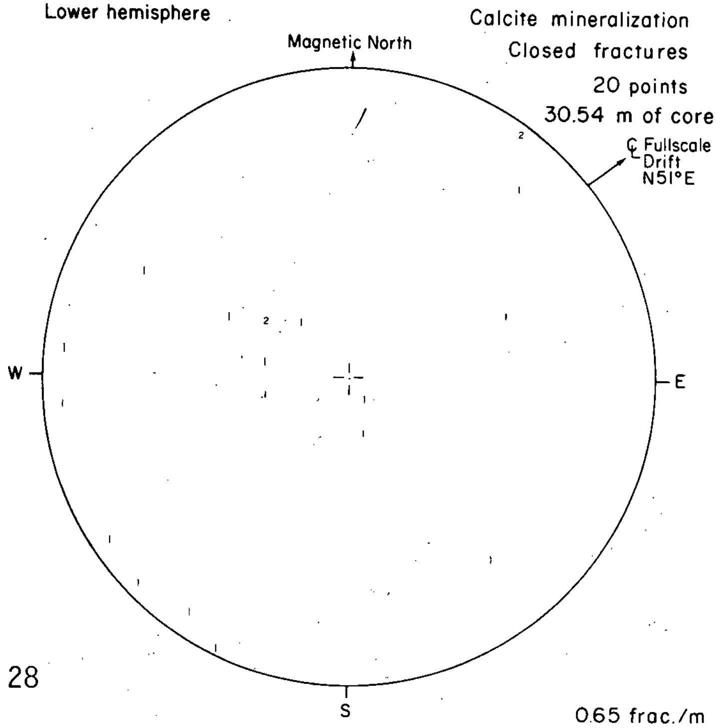

C 28

XBL 8010-2932 A

Schmidt equal-area pole plot for horizontal holes, H9% occurrence

Lower hemisphere

Epidote mineralization

Closed fractures

138 points

108.01 m of core

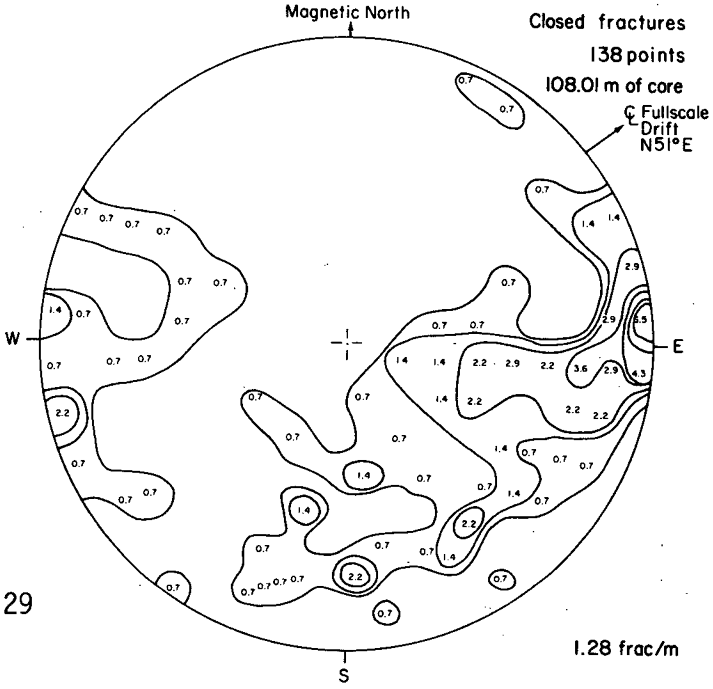

C 29

1.28 frac/m

Schmidt equal-area pole plot for horizontal E holes, H10

Lower hemisphere

Epidote mineralization

Closed fractures

15 points

30.54 m of core

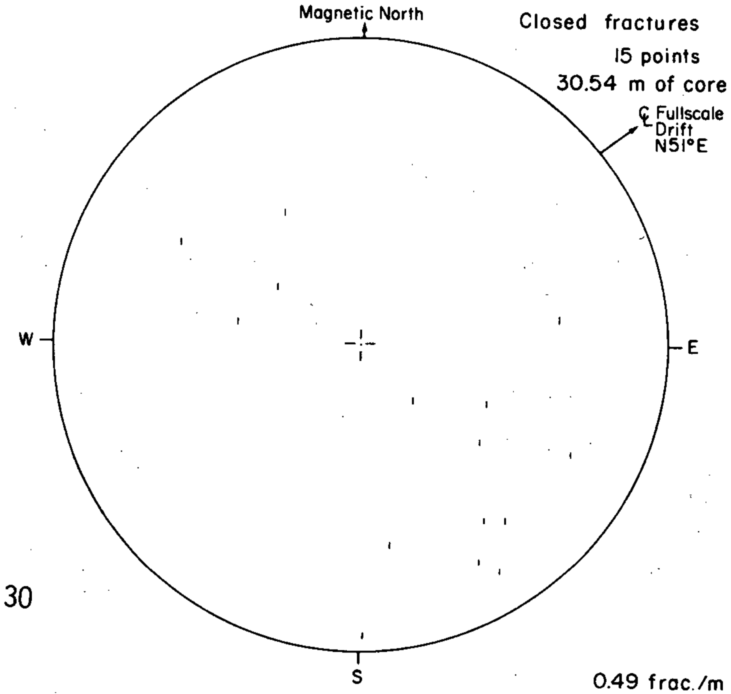

C 30

0.49 frac./m

XBL 8010-2933A

Schmidt equal-area pole plot for horizontal E holes, H9 %occurrence

Lower hemisphere

All mineralizations
Closed fractures
100% = 417 points
108.01 m of core

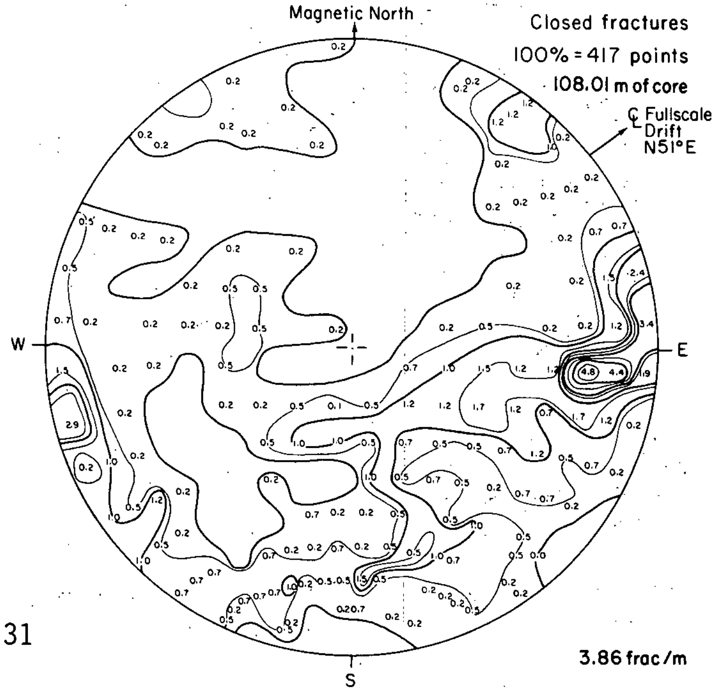

C 31

3.86 frac/m

Schmidt equal-area pole plot for horizontal E holes, H10 %occurrence

Lower hemisphere

All mineralizations
Closed fractures
100% = 135 points
30.54 m of core

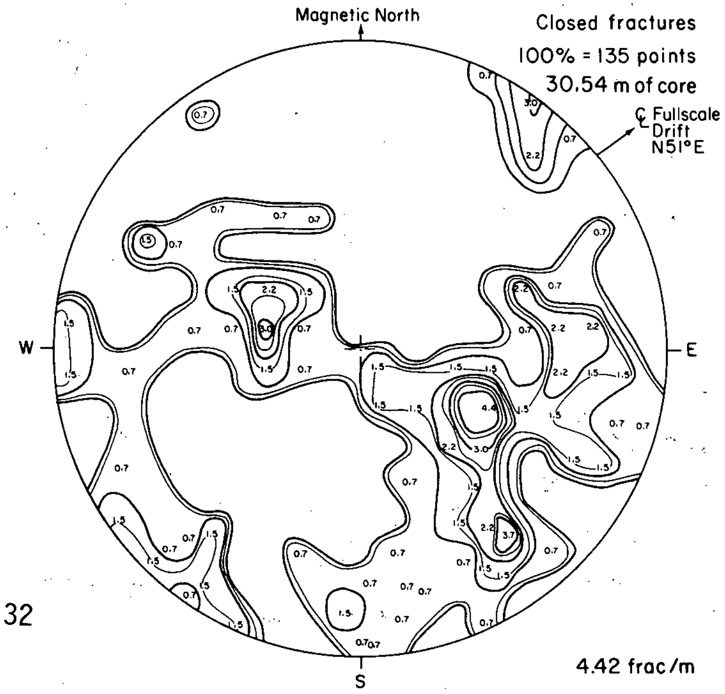

C 32

4.42 frac/m

XBL 8010-2934A

Schmidt equal-area pole plot for horizontal E holes, H9% occurrence
Lower hemisphere
Chlorite mineralization
Open fractures
247 points
108.01 m of core

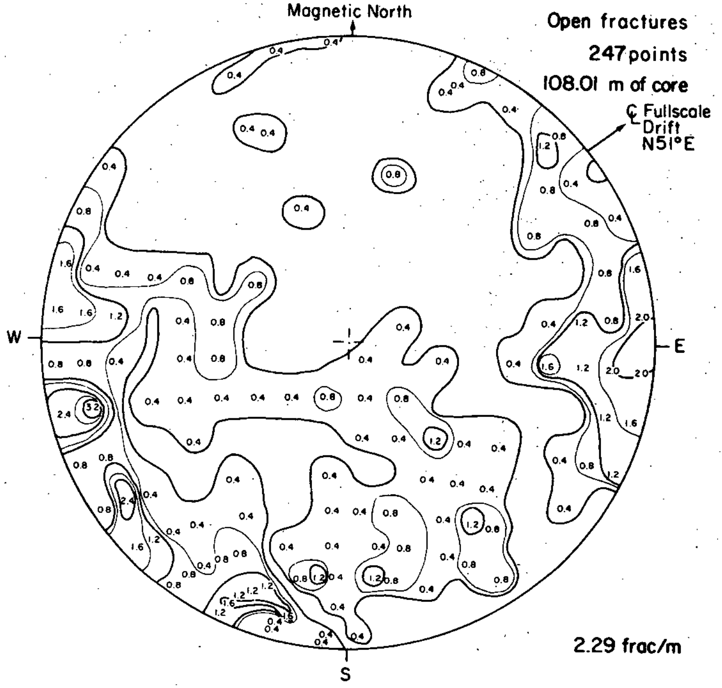

2.29 frac/m

C 33

Schmidt equal-area pole plot for horizontal holes, H10 % occurrence
Lower hemisphere
Chlorite mineralization
Open fractures
270 points
107.32 m of core

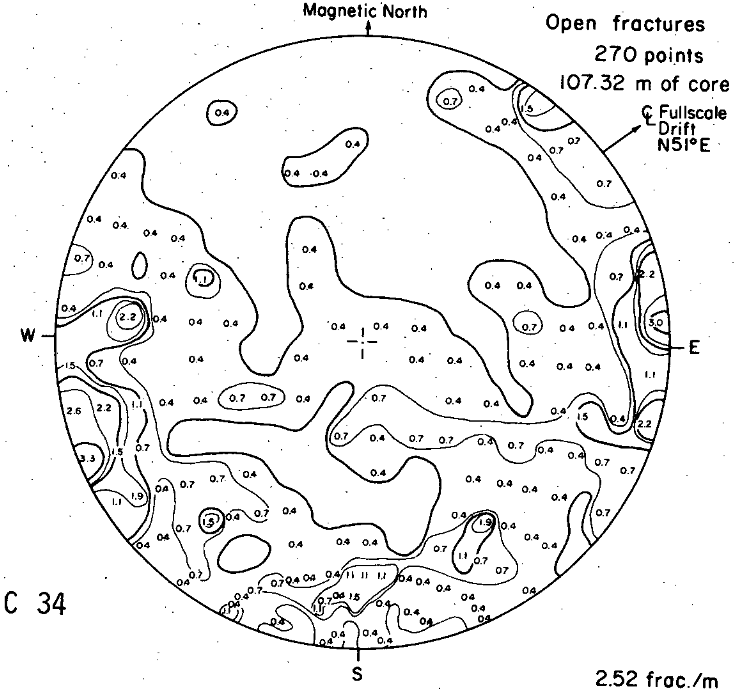

2.52 frac./m

C 34

XBL 8010-2935A

Schmidt equal-area pole plot for horizontal E holes, H9 % occurrence

Lower hemisphere

Calcite mineralization

Open fractures

125 points

108.01 m of core

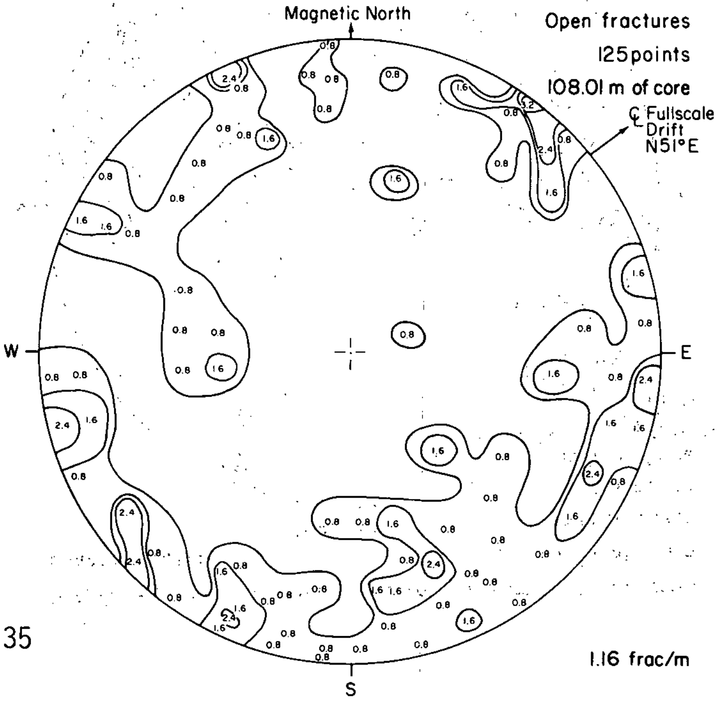

C 35

1.16 frac/m

Schmidt equal-area pole plot for horizontal holes, H10 % occurrence

Lower hemisphere

Calcite mineralization

Open fractures

153 points

107.32 m of core

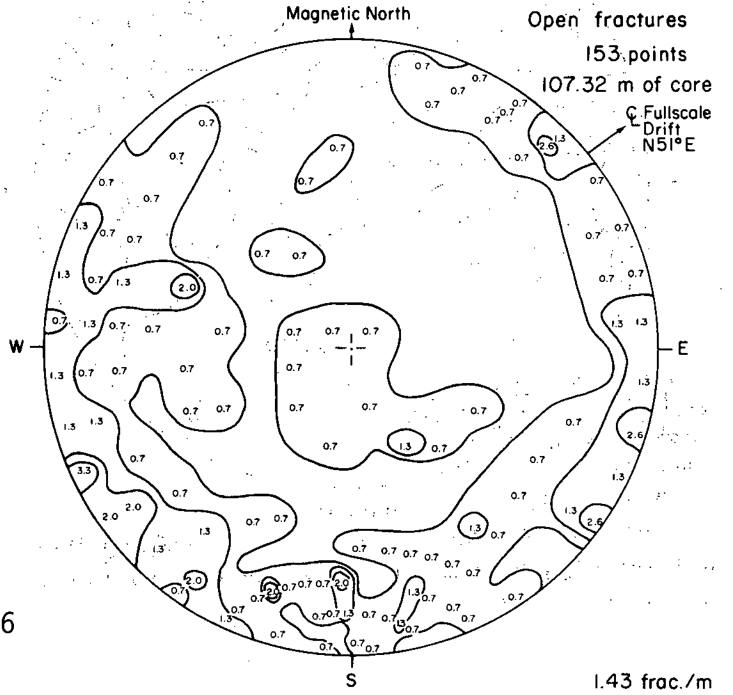

C 36

1.43 frac./m

XBL 8010-2936A

Schmidt equal-area pole plot for horizontal E holes, H9

Lower hemisphere

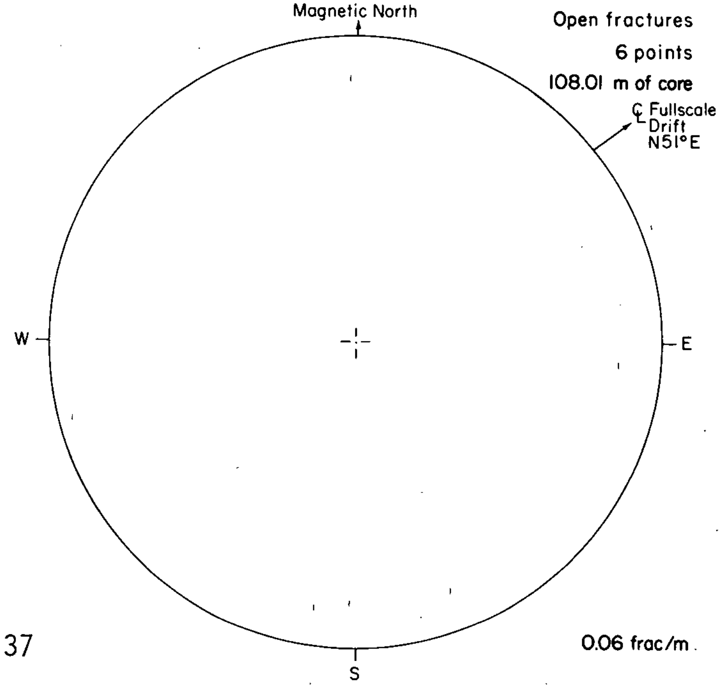

C 37

Schmidt equal-area pole plot for horizontal E holes, H10

Lower hemisphere

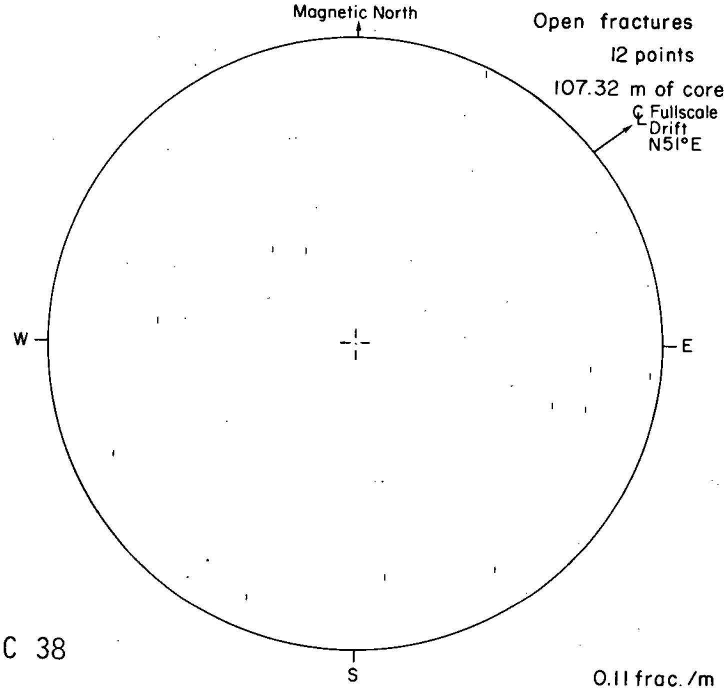

C 38

XBL 8010-2937A

Schmidt equal-area pole plot for horizontal holes, H9 % occurence

Lower hemisphere

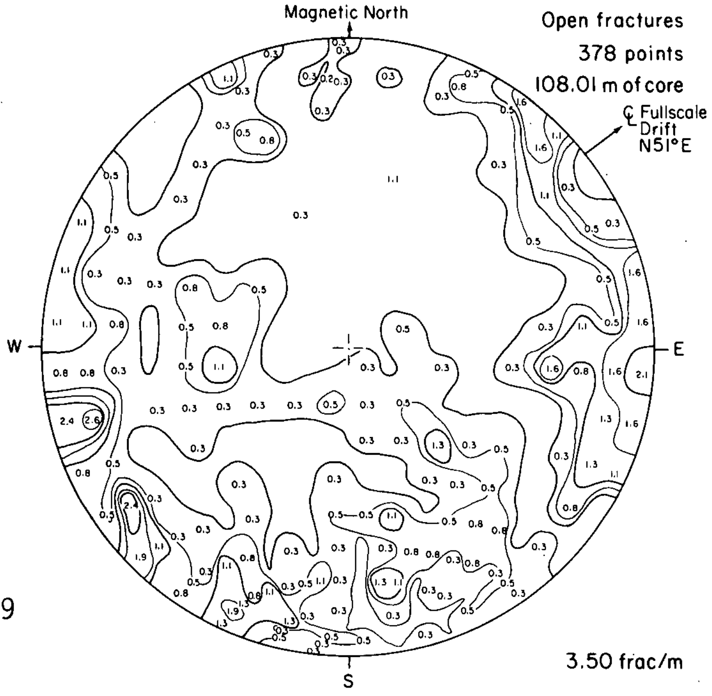

All mineralization

Open fractures

378 points

108.01 m of core

3.50 frac/m

C 39

Schmidt equal-area pole plot for horizontal holes, H10% occurrence

Lower hemisphere

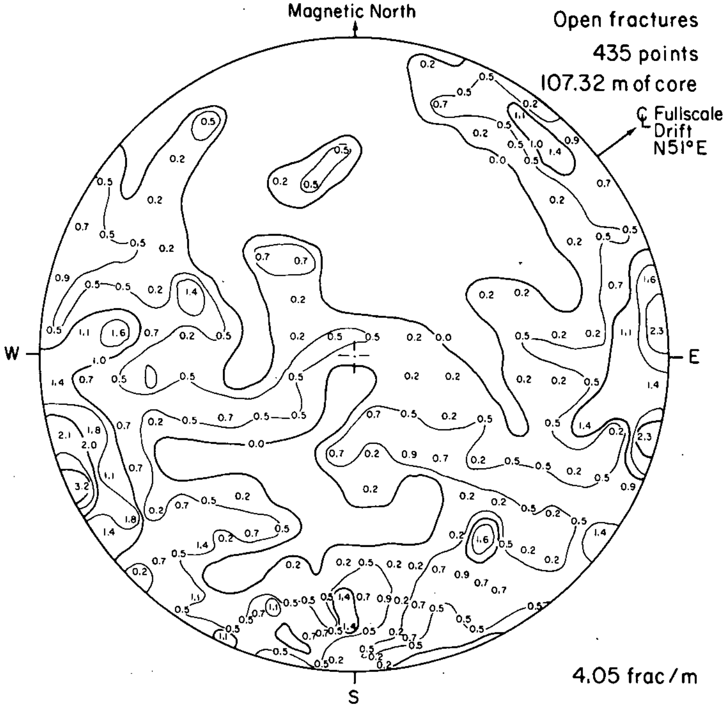

All mineralization

Open fractures

435 points

107.32 m of core

4.05 frac/m

C 40

XBL 8011-6400A

Schmidt equal-area pole plot for horizontal holes, H9 % occurrence

Lower hemisphere

Chlorite mineralization
All (closed & open) fractures
507 points
108.01 m of core

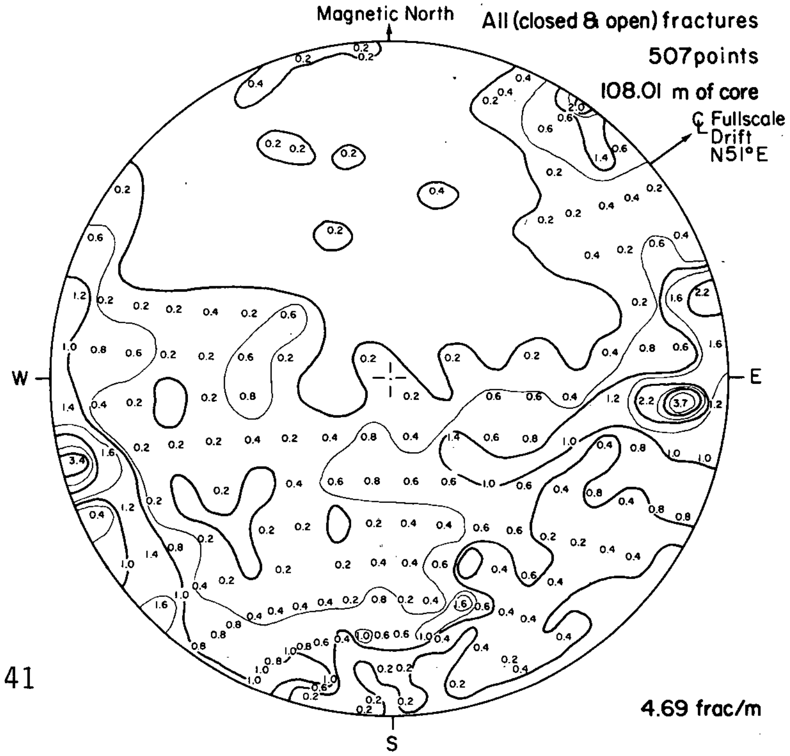

4.69 frac/m

XBL 8010-2907

C 41

Schmidt equal-area pole plot for horizontal holes, H10 % occurrence

Lower hemisphere

Chlorite mineralization
All fractures
(open and closed)
370 points
107.32 m of core

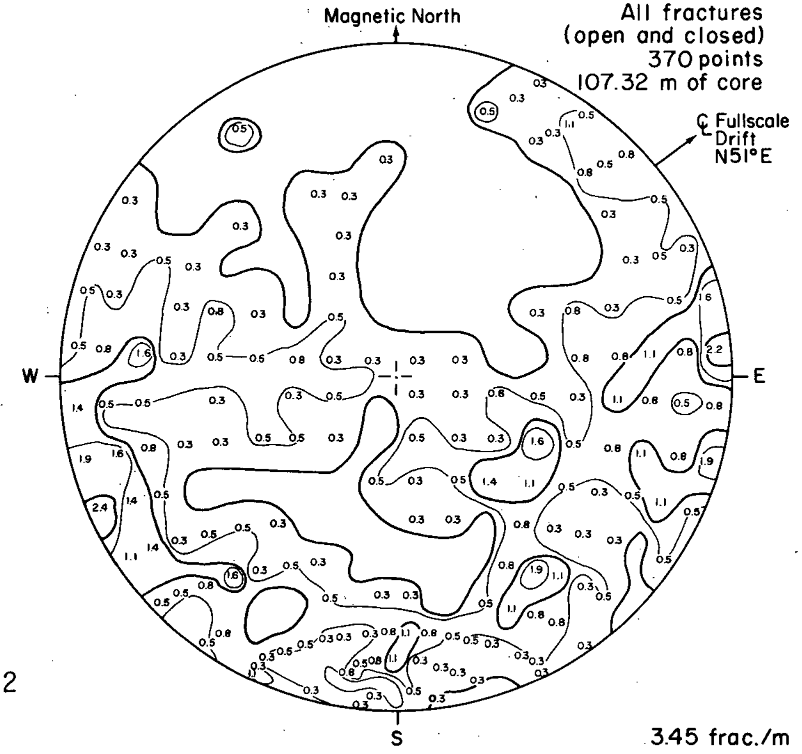

3.45 frac./m

XBL 8010-2938

C 42

Schmidt equal-area pole plot for horizontal holes, H9% occurrence

Lower hemisphere

Calcite mineralization

All (open & closed) fractures

154 points

108.01 m of core

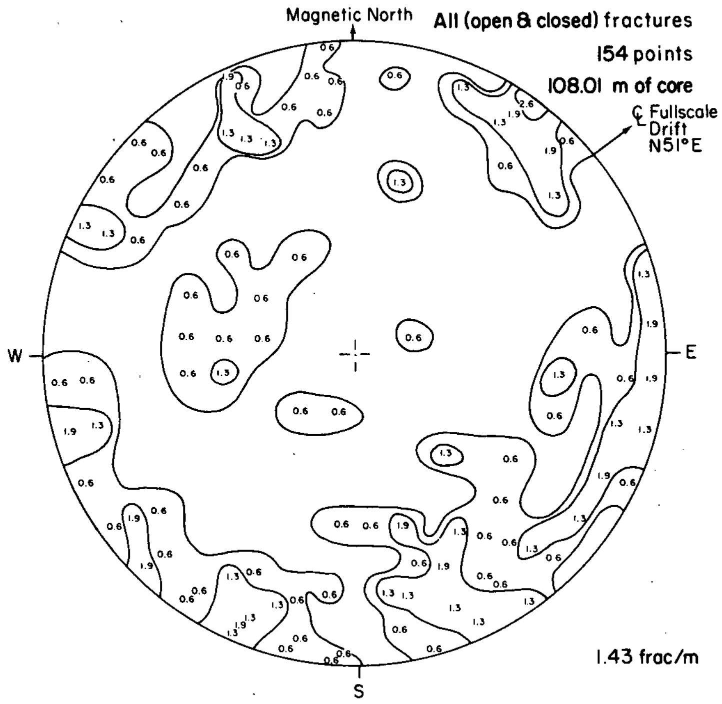

1.43 frac/m

C 43

Schmidt equal-area pole plot for horizontal holes, H10 % occurrence

Lower hemisphere

Calcite mineralization

All fractures

(open and closed)

173 points

107.32 m of core

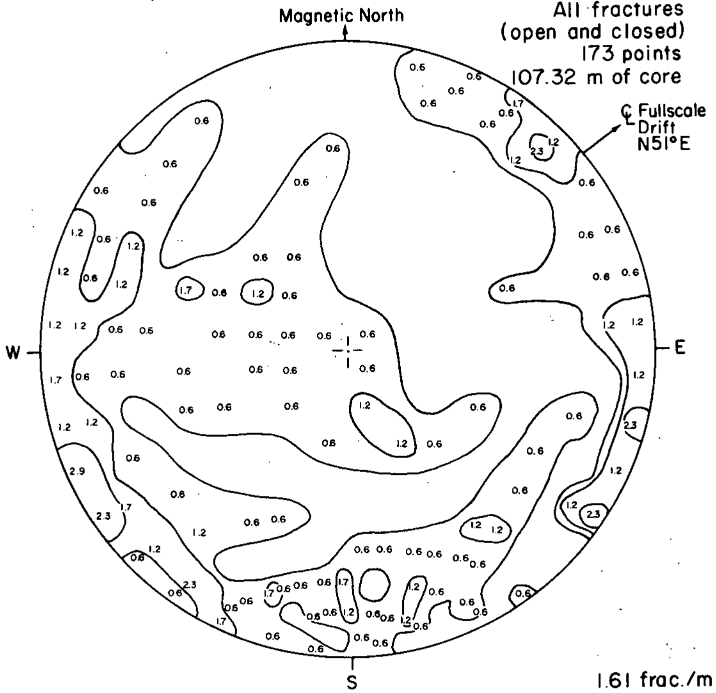

1.61 frac./m

XBL 8010-2939A

C 44

Schmidt equal-area pole plot for horizontal holes, H9% occurrence

Lower hemisphere

Epidote mineralization

All (open & closed) fractures

144 points

108.01 m of core

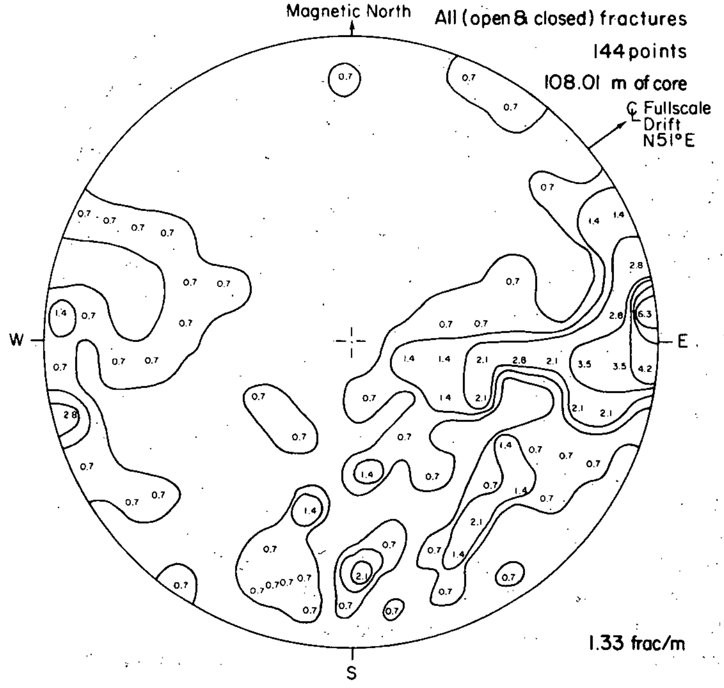

1.33 frac/m

C 45

Schmidt equal-area pole plot for horizontal E holes, H10

Lower hemisphere

Epidote mineralization

All fractures

(open and closed)

27 points

107.32 m of core

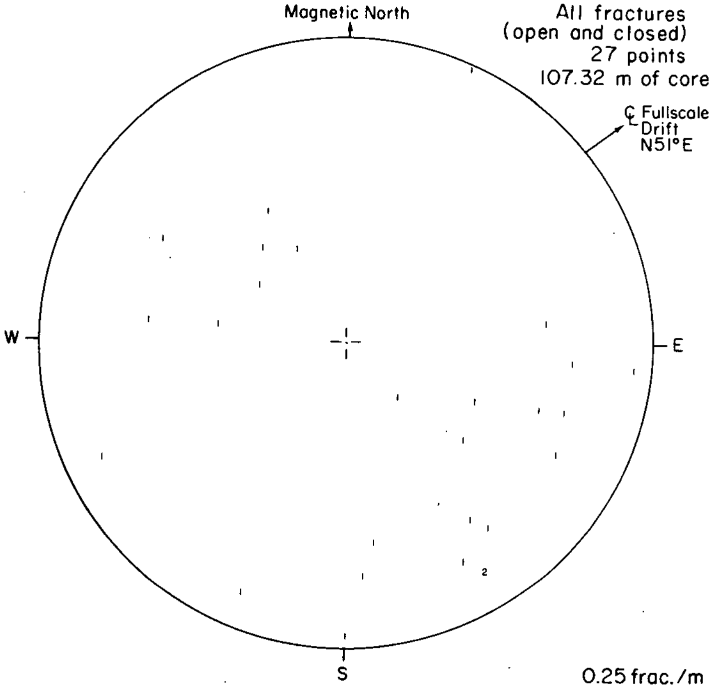

0.25 frac./m

C 46

XBL 8010-2940A

Schmidt equal-area pole plot for horizontal E holes H9% occurence

Lower hemisphere

All mineralization

All fractures

805 points

108.01 m of core

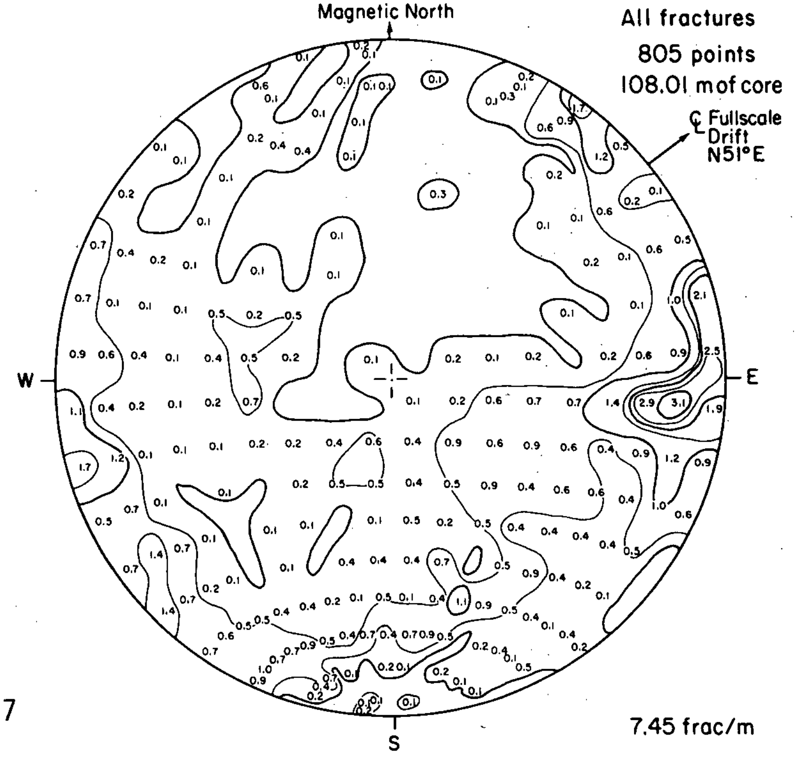

C 47

7.45 frac/m

XBL 8012-6588

Schmidt equal-area pole plot for vert. and horiz. holes, H9 % occurrence

Lower hemisphere

Chlorite mineralization

Closed fractures

716 points

224.07 m of core

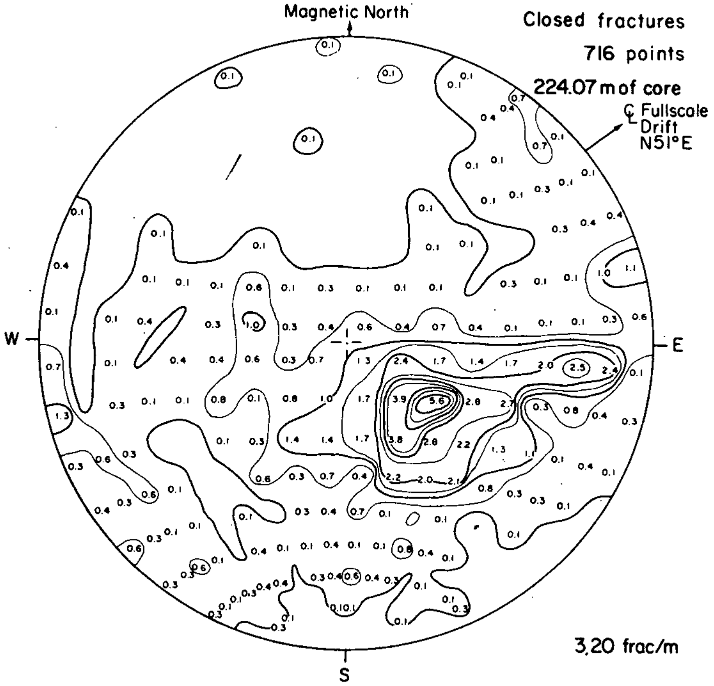

C 49

Schmidt equal-area pole plot for vert. and horiz. holes, H9 % occurrence

Lower hemisphere

Calcite mineralization

Closed fractures

76 points

224.07 m of core

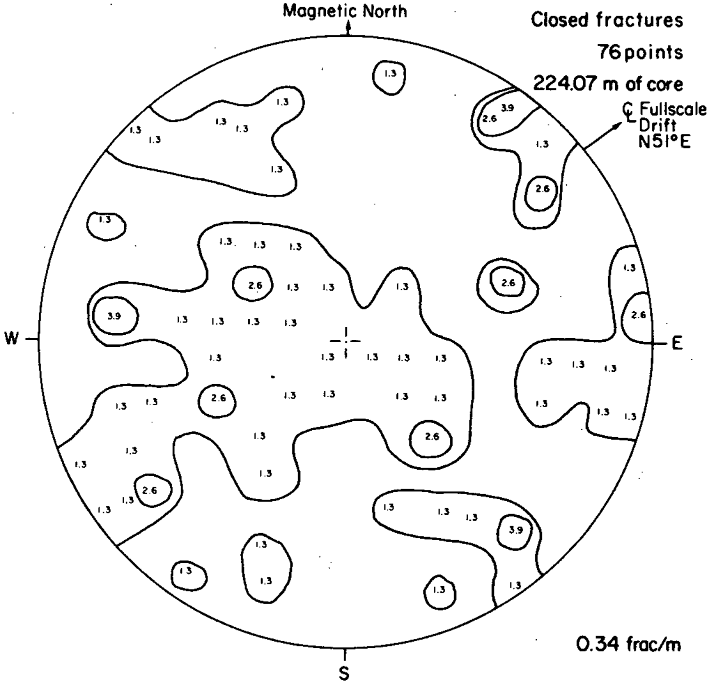

C 50

XBL 8010-2911A

Schmidt equal-area pole plot for vert. and horiz. holes, H9 % occurrence

Lower hemisphere

Epidote mineralization
Closed fractures
454 points
224.07 m of core

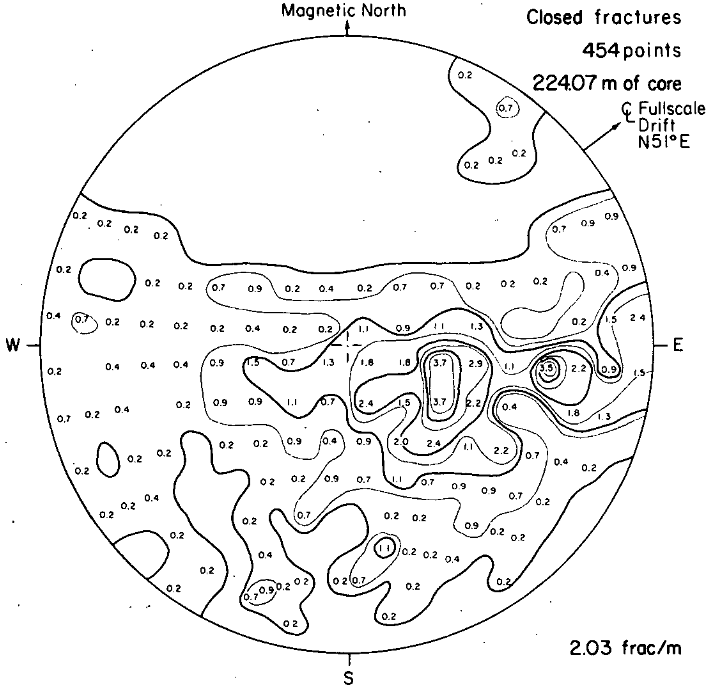

2.03 frac/m

C 51

Schmidt equal-area pole plot for vertical and horizontal holes H9 % occurence

Lower hemisphere

All mineralization
Closed fractures
1246 points
224.07 m of core

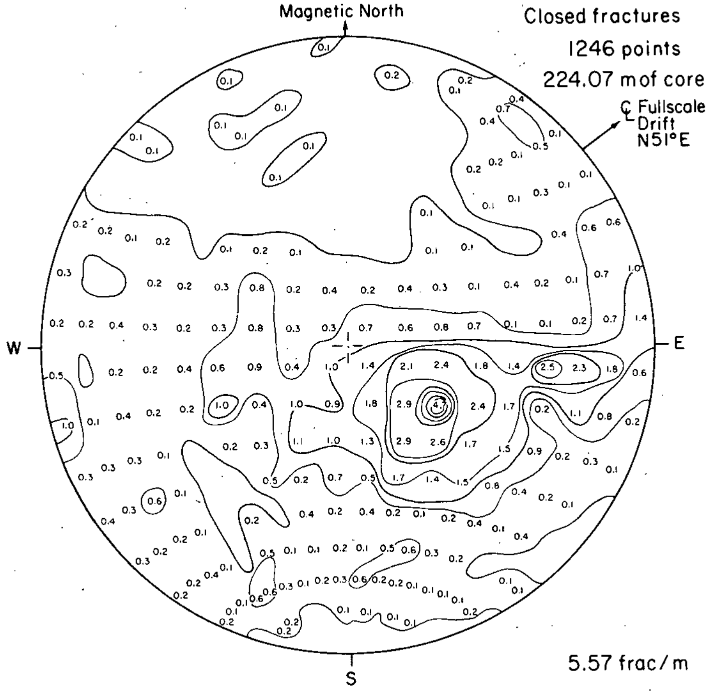

5.57 frac/m

C 52

XBL 8012-6590A

Schmidt equal-area pole plot for vert. and horiz. holes, H9 % occurrence

Lower hemisphere

Chlorite mineralization

Open fractures

421 points

224.07 m of core

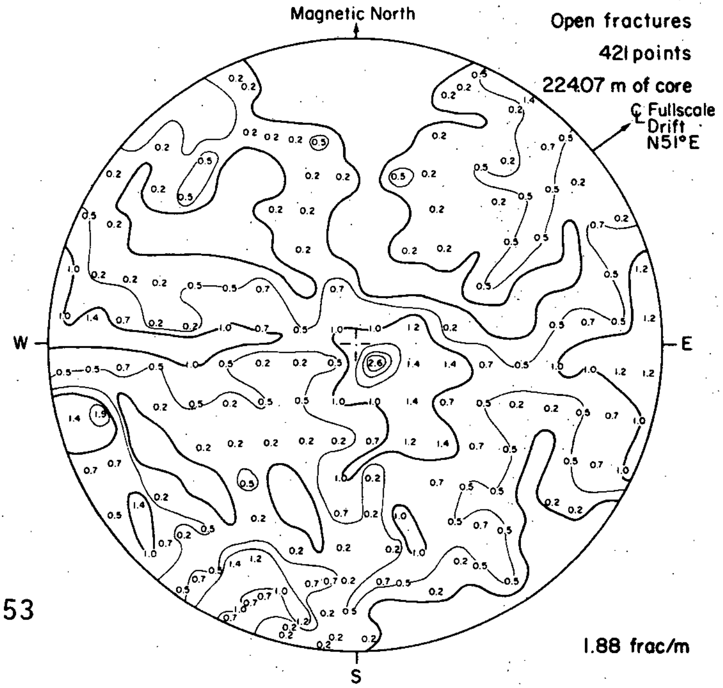

C 53

1.88 frac/m

Schmidt equal-area pole plot for vert. and horiz. holes, H9 % occurrence

Lower hemisphere

Calcite mineralization

Open fractures

192 points

224.07 m of core

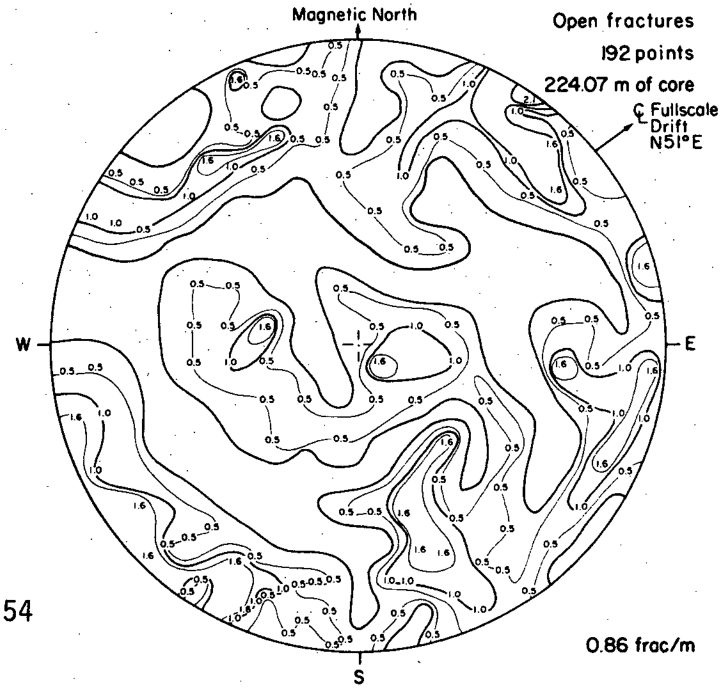

C 54

0.86 frac/m

XBL 8010-2914A

Schmidt equal-area pole plot for vert. and horiz. holes, H9

Lower hemisphere

Epidote mineralization

Open fractures

26 points

224.07 m of core

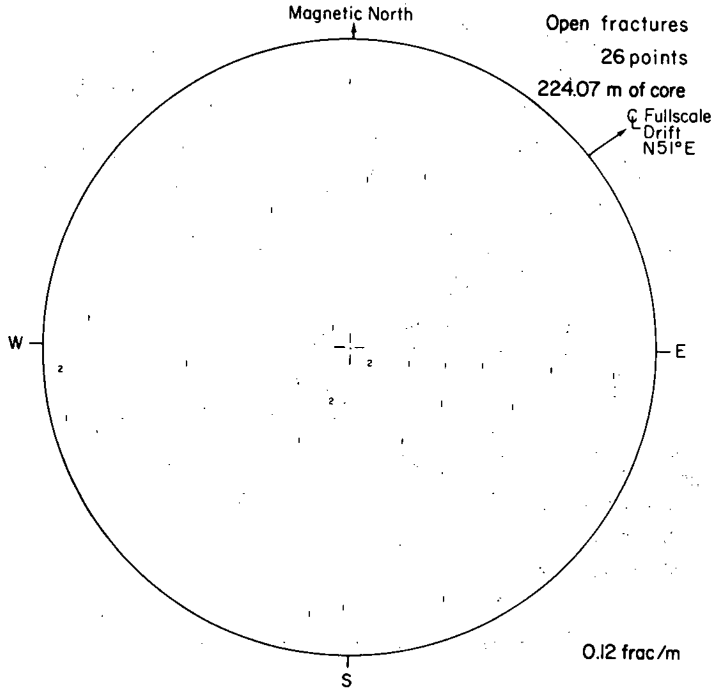

C 55

Schmidt equal-area pole plot for all holes, H9 % occurrence

Lower hemisphere

All mineralization

Open fractures

100% = 639 points

224.07 m of core

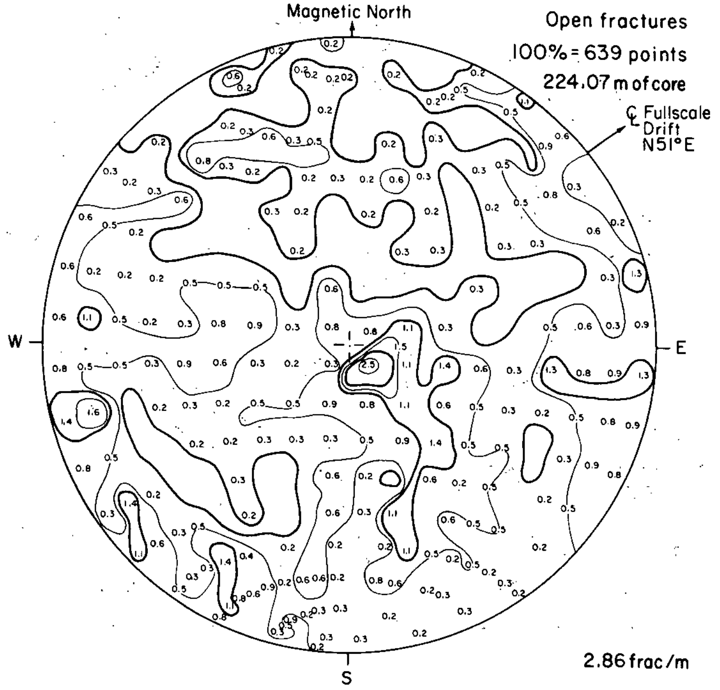

C 56

XBL 8010-2916A

Schmidt equal-area pole plot for vertical and horizontal holes,
H9 % occurrence
Lower hemisphere

Chlorite mineralization
All fractures
(open and closed)
1137 points
224.07 m of core

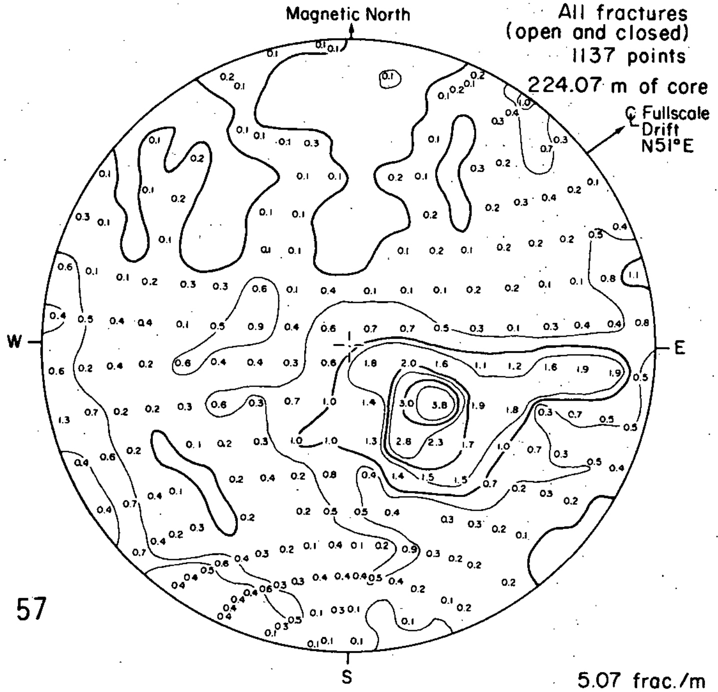

C 57

5.07 frac./m

Schmidt equal-area pole plot for all holes with oriented core, H9 %occurrence
Lower hemisphere

Calcite mineralization
Open and closed fractures
100% = 268 points

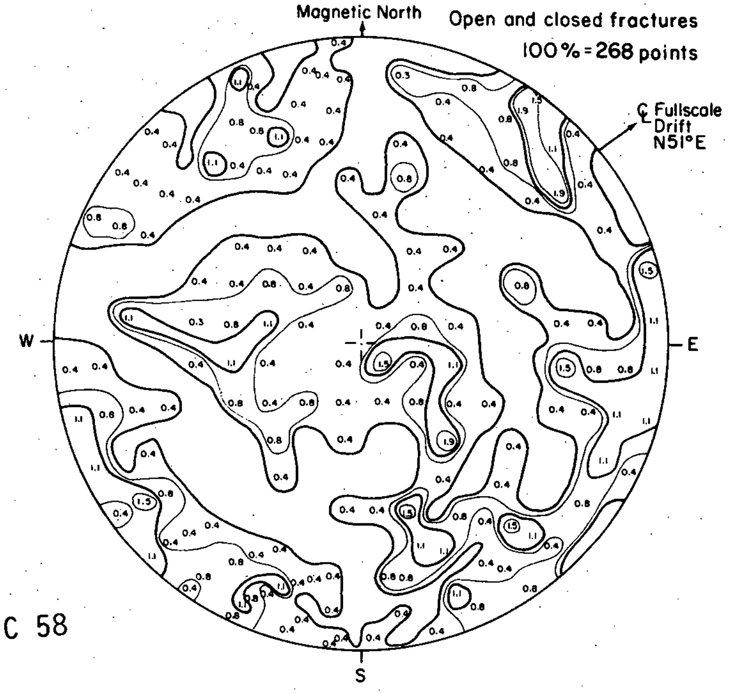

C 58

XBL 8010-2918A

Schmidt equal-area pole plot for vertical and horizontal holes, H9 % occurrence
Lower hemisphere

Epidote mineralization
All fractures
(open and closed)
480 points
224.07 m of core

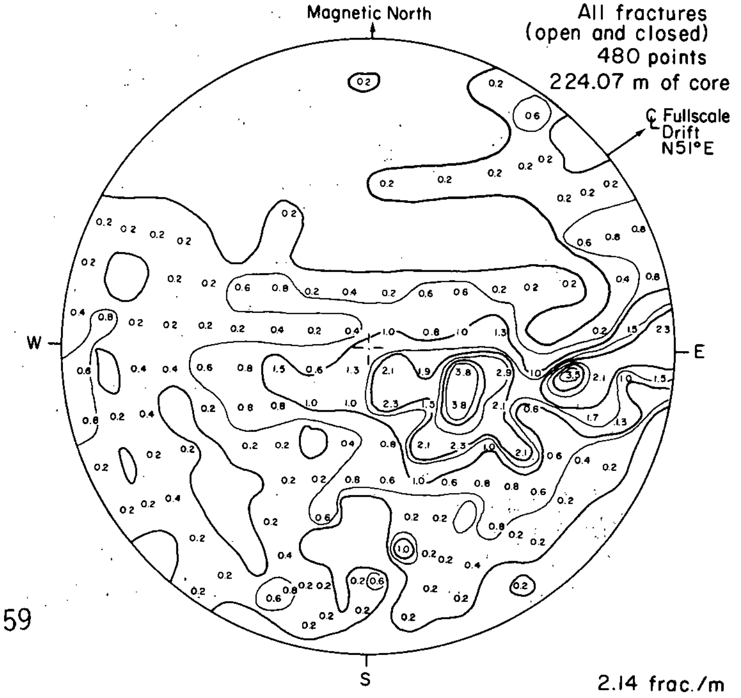

C 59

Schmidt equal-area pole plot for vertical and horizontal holes. H9% occurence
Lower hemisphere

All mineralization
All fractures
1885 points
224.07 m of core

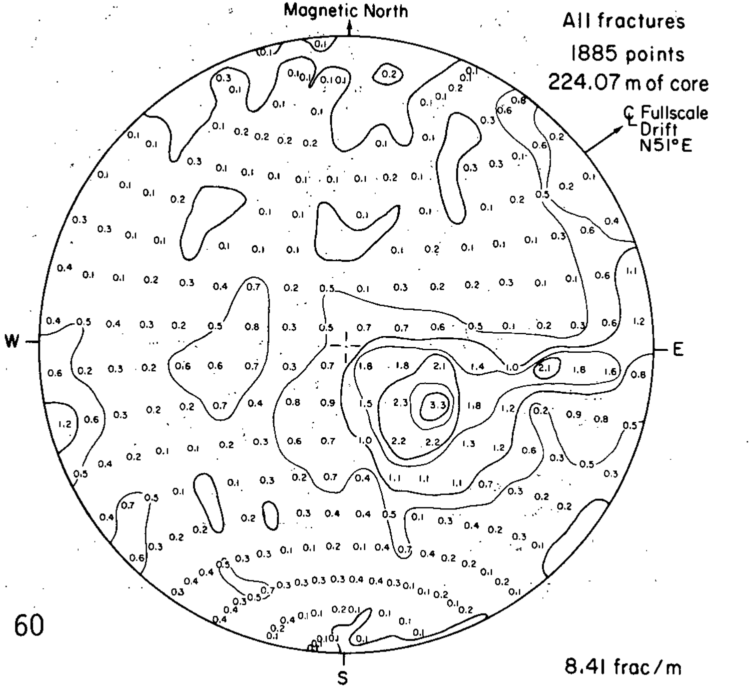

C 60

XBL 8012-6589A

APPENDIX D: SONIC WAVEFORM AND OTHER BOREHOLE LOGS IN VERTICAL EXTENSOMETER HOLES

Introduction

During January-February, 1978, six months before heater experiments began, a suite of geophysical borehole logs was acquired from the underground holes at Stripa. Nelson et al. (1979) list these logs and their results, although much of the discussion is preliminary and incomplete.

For example, the sonic waveform logs required further inspection to see if the cause of waveform features could be found by examining the cores. This appendix documents our efforts at correlating the sonic waveform logs with the cores taken from the extensometer boreholes.

The figures contain all borehole logs run in each extensometer hole, E-1 - E-17, as well as the sonic records. Also shown are the installed instrument locations, pictorial fracture logs, TV fracture logs, and RQD (rock quality designation) plots.

Sonic Data Acquisition

The sonic probe consists of a single transmitter and a single receiver one foot apart, operating at a frequency of about 30 kHz (see Nelson et al., 1979, for further detail). The probe diameter is 60 mm and could be operated only in the 76 mm extensometer holes and the larger heater holes. Waveforms were recorded on film at an oscilloscope time scale of 20 microseconds per centimeter, as displayed in the accompanying figures. In addition, the time of the first compressional wave arrival was recorded as an analog trace and is also included in the figures. The other logs, although included in the figures, are not discussed here.

The sonic waveforms were recorded in the following manner. To record the alternating dark and light bands shown in the figures, the amplifier gain is increased and the conventional "wiggle-trace" becomes a square wave which is used to modulate the z-axis intensity on the oscilloscope. The oscilloscope display is then photographed by stepping the film along at a rate controlled by the motion of the probe. This results in the black bands representing the negative-going and the white bands the positive-going portions of the wavetrain. The first three black bands are comprised of acoustic energy traveling along the borehole wall in a compressional mode; the fourth and fifth bands are a mix of the decaying compressional mode plus shear and surface modes. These later bands are often called "shear."

Since the transmitter-receiver spacing is about 30 cm, the delineation of anomalies is about ± 15 cm. The only exceptions occurred where the film failed to step properly near the bottom of the boreholes, resulting in a broken series of dashes (record from borehole E12). In these cases, accurate depth control was lost for the waveform recordings and alignment relied on the upper depth reading and upon correlation with the travel time log acquired on a separate run.

Anomalous zones were selected visually from the distortions which had some consistency on two or more adjacent bands. The first column in Tables D1-D3 gives the depth of those zones where a discernable offset is present in the first band, usually accompanied by smaller offsets in bands two and three. Similarly, the second column in the tables records the depth for anomalous shear wave arrivals based upon bands four and five. In cases where the distortion pattern is greater than the tool spacing, the center of the distortion pattern is given.

Column 4 of Tables D1-D3 gives the number of open fractures in core, as tabulated in the original core logs, which lie within a 20-cm length centered on the anomaly. In addition, after the waveform anomalies were selected, the core in the immediate vicinity of each anomaly location was carefully inspected. Column 5 in the tables lists the total fracture density per 10 cm length of core, determined by visual observation of a length of core equivalent to the transmitter-receiver separation. The last column contains a brief description of the core within ±10 cm of the anomaly. Where no description is given, the rock was intact, usually with a few chlorite-filled fractures intersecting the interval.

Comments - H9 Area

Twelve sonic waveform anomalies were picked as discernable features from the extensometer borehole logs in the H9 area, as listed in Table D1. Of these twelve:

- eight anomalies correspond to an open (and mineralized) fracture as noted in the original core logs. Four others occur where unbroken core was recovered.

- two anomalies in borehole E8 are the most difficult to explain -- there is neither an open fracture nor any unusual feature visible in the core.

- only three of the twelve waveform anomalies occur below 6 m, in the lower parts of the boreholes. Seven anomalies occur within four meters of the drift floor.

- two distinct differential electrical resistance peaks occurred close to pyrite veins logged in core.
- three boreholes along the centerline of the drift (E6, E7, and E8) produce all but one of the twelve waveform anomalies. The log from borehole E10 is especially free of anomalies.

Comments -- H10 Area

In the H10 area, 19 sonic waveform anomalies were selected and the corresponding core examined (Table D2.) Of these 19:

- sixteen occur near an open (and mineralized) fracture as noted in the original core logs. Three other anomalies occur where unbroken core was recovered.
- of these latter three, two (boreholes E12, 2.4 m and E13, 2.4 m) occur near a pyritic fracture and the third (borehole E12, 10.6 m) is unexplained.
- there are fewer waveform anomalies in the lower part of the boreholes than in the upper; however, the depth dependence is not as convincing as it is in the H9 area.
- three boreholes along the drift centerline (E12, E13, and E14) produce 13 of the 19 anomalies.
- although only one sonic anomaly was recorded in borehole E15, the later time portions of the waveform are more consistently disrupted

than in any of the other E-holes. The resulting impression that borehole E15 contains more sealed fractures is supported by (1) inspection of the core, which appears to be fractured throughout more of its length than core for other holes, especially below 4.0 m and (2) inspection of the fracture plots based on logs of all fractures, both open and closed. It is also apparent that borehole E15 is more consistently fractured along its length than any other E-holes.

- in these 6 holes, four zones produce shear wave disturbance over a length of about one meter:

  E12, 4.0-4.9 m -- high angle calcite fractures with about 12 open breaks
  E12, 8.0-8.8 m -- high density of chlorite fractures, 4 open breaks
  E13, 5.4-5.9 m -- six open, calcite-coated breaks
  E14, 5.2-5.5 and 6.2-7.0 m -- few open breaks, but core over 4.0-7.4 m is highly fractured, both chlorite and some epidote

  In terms of the sonic waveform data, these four zones are the most anomalous.

<u>Comments -- Time Scale Area</u>

Nine waveform anomalies (Table D-3) were recorded in 5 extensometer boreholes in the time scale drift.

- although there are fewer anomalies recorded in the time scale drift holes (9 vs. 12 and 19 in H9 and H10 heater areas), there was also less meterage drilled (5 holes vs. 6 and 6). Neither the number nor the character of the waveform anomalies differ much between the two experimental areas.

- five of the nine anomalous zones occur where a high density of chlorite fractures occur in the core. Of the remaining four anomalies, two occur near open, calcite-coated fractures and two (borehole E3, 8.0m and E4, 2.9-3.5 m) have no obvious associated features.

Summary

(1) Despite the high incidence of fractures observed in core, the sonic waveform logs indicate that the rock in the experimental drifts is quite competent. The visual threshold for anomaly selection was low in order to include the largest possible number of waveform disruptions. Even so, in the 17 vertical extensometer boreholes, only 40 anomalies could be picked with confidence. Of these, 17 disrupted both compressional and shear wave arrivals while the remainder were apparent only in the shear wave records. The average incidence of anomalies is only one for every 10 m for compressional plus shear disruptions, and one every 4.3 m for all waveform anomalies. This indication of general rock competence in the experimental drifts is in accord with the sonic waveform data from borehole SBH-1, which indicated a decline in fracture population below 225 m vertical depth (Nelson et al., 1979).

(2) Our success in "explaining" individual waveform anomalies by visual inspection is mixed:

(a) With only a few exceptions, the waveform anomalies could be attributed to some feature in the rock; that is, only three or four of the anomalies occurred in sections of boreholes free of fracturing.

(b) Thirty of the 41 waveform anomalies occurred close to fractures found to be open in the core; however, open fractures are relatively common, so the correlation is not very convincing. Moreover, most of the observed open fractures did not produce waveform anomalies.

(c) All well-defined waveform anomalies occurred at zones of pronounced geological features, such as calcite-coated fractures, a sequence of open breaks, or a high density of chlorite-coated fractures. However, none of these types of geological features consistently produced sonic anomalies; such features were also present where the sonic waveform was quite uniform.

(3) The later time arrivals of the waveform records, referred to as "shear," exhibit considerably more character than the first, or compressional, energy. This can easily be seen in a quick examination of the records. All compressional wave distortions produced shear wave distortions, but the converse is obviously not true. Sensitivity of shear wave arrivals to fracturing has been known for some time; such results furnish motivation for continuing developmental work with shear wave propagation in borehole probes.

Acknowledgments

The sonic probe was made available through the cooperation of H. Harrel, and was operated by D. Scott, both of the Tennessee Valley Authority. R. Rachiele compiled the logs and associated data.

Table D-1: Sonic waveform anomalies observed in the H9 area extensometer holes, along with observations of the core.

	P-wave (1st band)	S-wave (4th band)	Open fractures in core ± 10 cm	Fracture density /10 cm	Visual observations
E6					
	1.8	1.8	3	2-3	One-cm band of fractures at 1.78m; pyrite in blebs and along veins.
	--	2.5	4	4	Fine fracturing present with ~1 cm spacing.
	--	2.9	1	3	--
	3.7	3.7	2	1	--
	4.4	4.4	1	2	--
	--	5.6	1	3	A high-angle (75°) calcite fracture extends from 5.60 to 5.77 m.
E7					
	2.2	2.1	1	2-3	Several high-angle epidote fractures; unusually high density of fine fractures with lengths <1 cm. Pyrite vein at 2.05 m.
	3.1	3.1	4	1-2	--
	--	7.3	0	1	Pegmatite 0.5 m in length aligned vertically in core; core is 50% granite and 50% pegmatite.
E8					
	4.7	4.7	0	2-3	No unusual features.
	--	8.9	0	<1	Two nearly vertical, sealed fractures; core is intact.
E9					
			NA		No sonic waveform anomalies in E9.
E10					
			NA		No sonic waveform anomalies in E19.
E11					
	11.2	11.2	0	1	One calcite fracture at 11.05 m, rock is intact, almost no fractures.

Table D-2: Sonic waveform anomalies and core observations in the H10 area extensometer holes.

Bore-hole	P-wave (1st band)	S-wave (4th band)	Open fractures in core $\pm$ 10 cm	Fracture density /10 cm	Visual observations
E12					
	2.4	2.4	0	1	Single sealed pyritic fracture at 2.6 m.
	--	4.2	3	3-5	Sonic waveform disrupted over 4.0-4.9 m; fine calcite fractures from 3.8 to 5.0 m, intercepting core at of 45° & more.
	--	3.4	3	5	Sonic waveform disrupted over 8.0-8.8m; high density of both fine discontinuous and through-going fractures over 8.1 to 9.0 m.
	--	10.6	0	0	Core intact, no fractures.
	--	11.6	1	--	Core destroyed by drilling.
E13					
	2.4	2.4	0	1	One high-angle sealed pyritic fracture and one high-angle sealed epidote fracture.
	--	4.0	2	3	Calcite features.
	--	4.8	2	2	One, 1-cm, sealed chlorite fracture.
	--	5.7	4	4	Calcite on all four open fractures at 5.67, 5.74, 5.78, 5.84 m.
	--	9.1	2	3	A 7-cm band of epidote adjacent to a 5-cm band of chlorite fractures.
E14					
	5.5	5.5	2	--	Sonic waveform distorted over 5.2-5.5m (4th and 5th bands).
	--	6.5	1	--	Sonic waveform distorted over 6.2-7.0 m (4th and 5th bands).
					The entire 4.0-7.4 m section of core is highly fractured, both chloritic and many epidote fractures. There is no obvious reason why the shear arrivals are distorted over only these two limited portions of this 3-4 m interval, rather than over all of it.

Table D2 (continued)

Bore-hole	P-wave (1st band)	S-wave (4th band)	Open fractures in core ± 10 cm	Fracture density /10 cm	Visual observations
	--	11.0	2	3	discontinuous fine fractures as well as through-going fractures.
E15	--	7.1	3	2	Three, high-angle, open fractures centered at 7.05, 7.17 , and 7.26 m (see further comments on E15 in the text).
E16	2.1	2.0	3	2	Few fractures other than the 3 open ones which have calcite on surfaces.
	3.4	3.4	3	2	Few fractures other than the 3 open ones which have calcite on surfaces.
	--	5.6	3	2	Mica, pyrite on fractures.
	7.3	7.3	3	4	Fine, discontinuous fractures as well as through-going fractures.
E17	--	7.8	2	5	Zone 7.3-7.6 m is highly fractured with both epidote and chlorite. Six open breaks lie in this 30-cm zone. From 7.6 to 8.0 m the rock is intact, hence a 30 cm depth error is assumed.

Table D-3: Sonic waveform anomalies and core observations in the time scale extensometer holes.

Bore-holes	P-wave (1st band)	S-wave (4th band)	Open fractures in core ± 10 cm	Fracture density /10 cm	Visual observations
E1	--	7.1-7.5	0	4	Very dense network of fine chloritic fractures from 7.0-7.7 m.
E2	--	7.1	2	3-4	Slickensides on the chloritic coating of one of the two open fractures.
	12.5	12.5	5	5	20 cm. interval of parallel chloritic fractures, including the open ones, which intersect the core at ~45°.
E3	12.3	12.3	4	--	The core from 12.25 to 12.32 m is in small pieces due to a number of intersecting chloritic fractures, some of which contain calcite.
	--	8.0	0	2	No unusual features.
	--	8.8	4	5	Very dense network of fine discontinuities and through-going chloritic fractures from 8.70 to 8.90 m.
E4	2.9-3.5	2.9-3.5	--	--	Core broken by the drilling from 2.7 to 3.4 in, does not apear to contain many fractures.
	4.6	4.6	0	2	Two open calcite fractures at 4.77 m.
E5	--	4.0-6.0	--	--	The 4.0-6.0 m interval appears to have a higher-than-average density of chloritic fractures, quite often 4 to 5 per 10 cm. However, it is not much different in overall appearance than the 2-m interval from 2.0 to 4.0 m.

E1

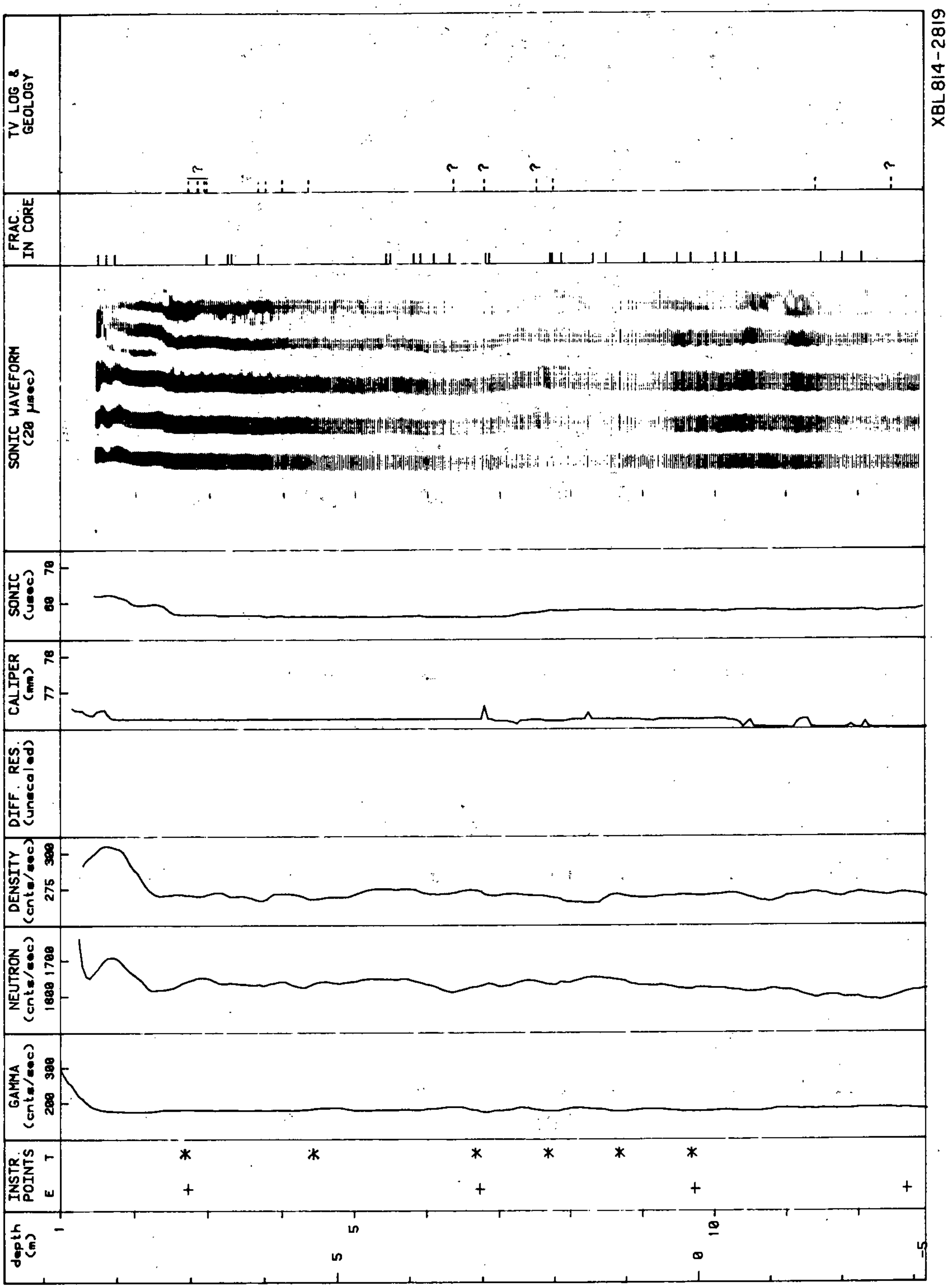

XBL 814-2819

E2

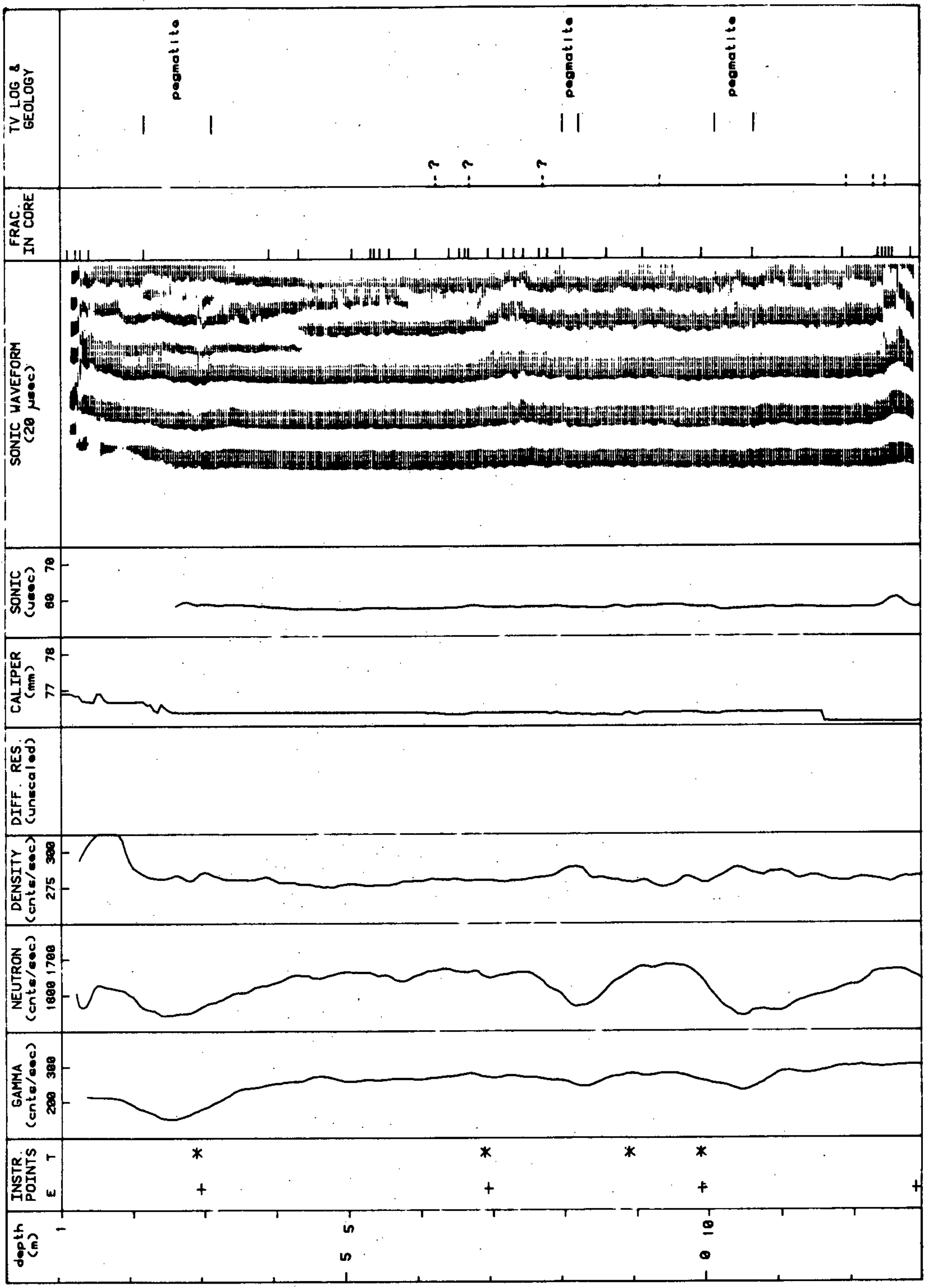

XBL 814-2820

E3

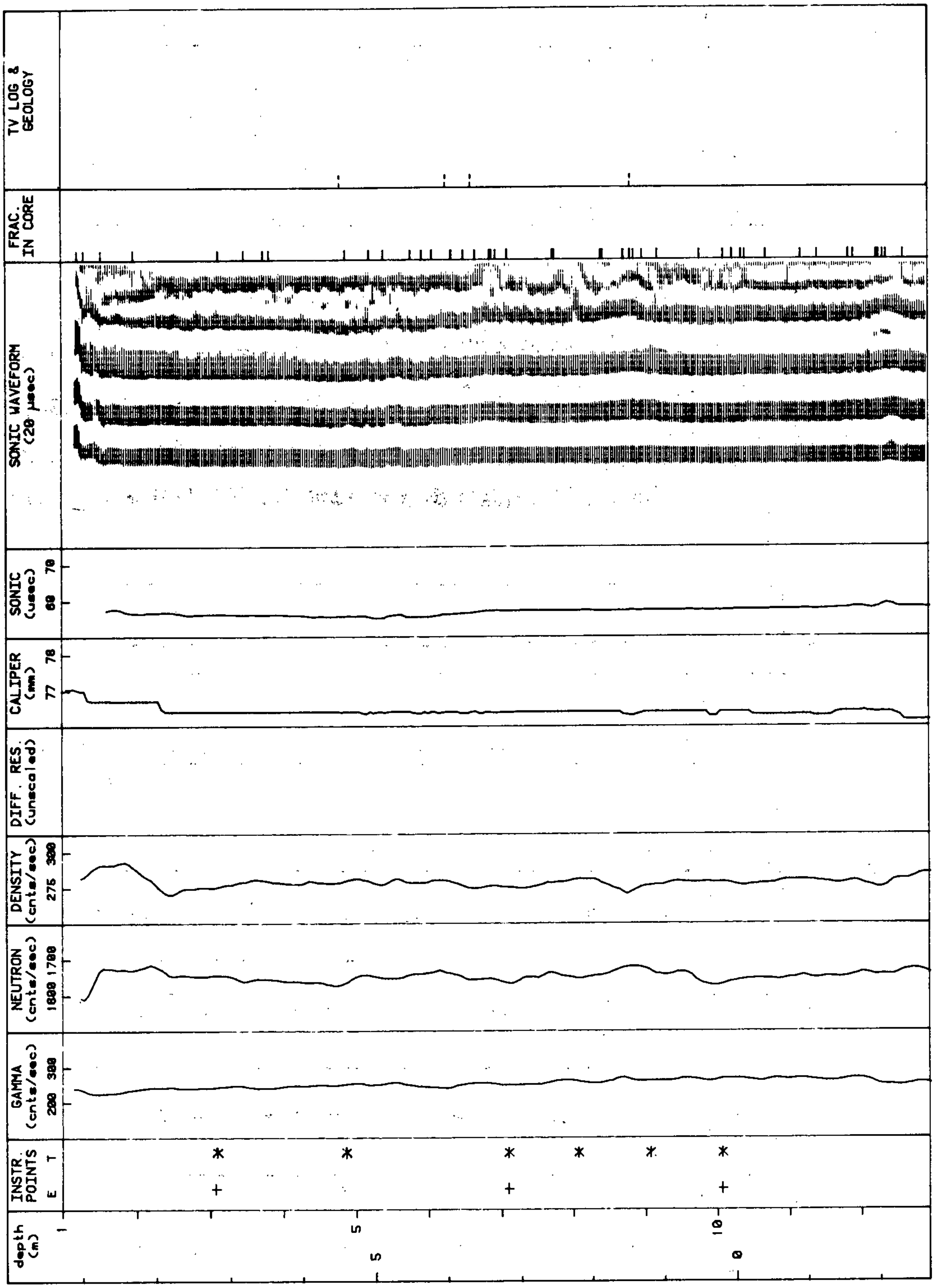

XBL 814-2821

E 4

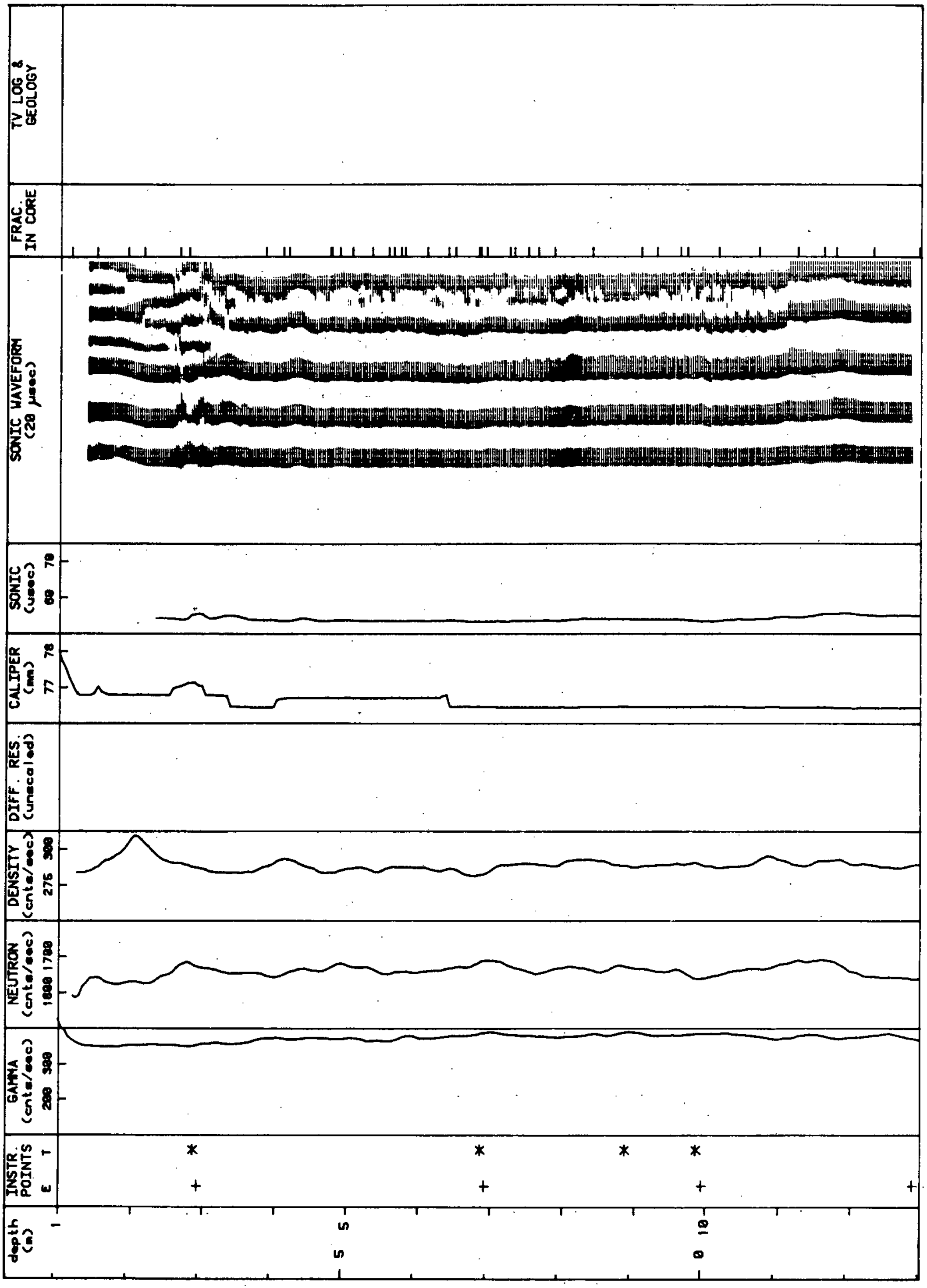

XBL 814-2822

E5

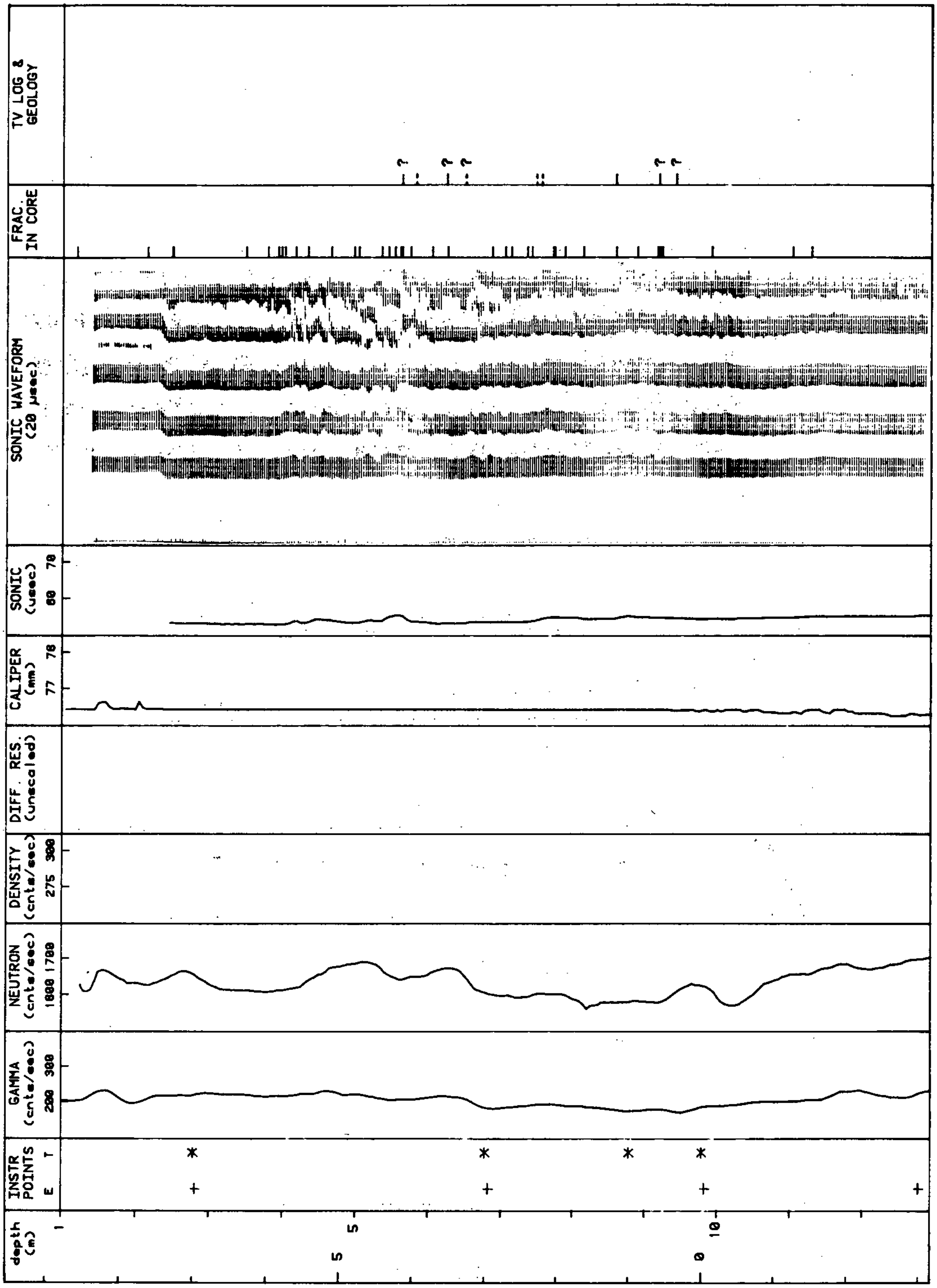

XBL 814-2823

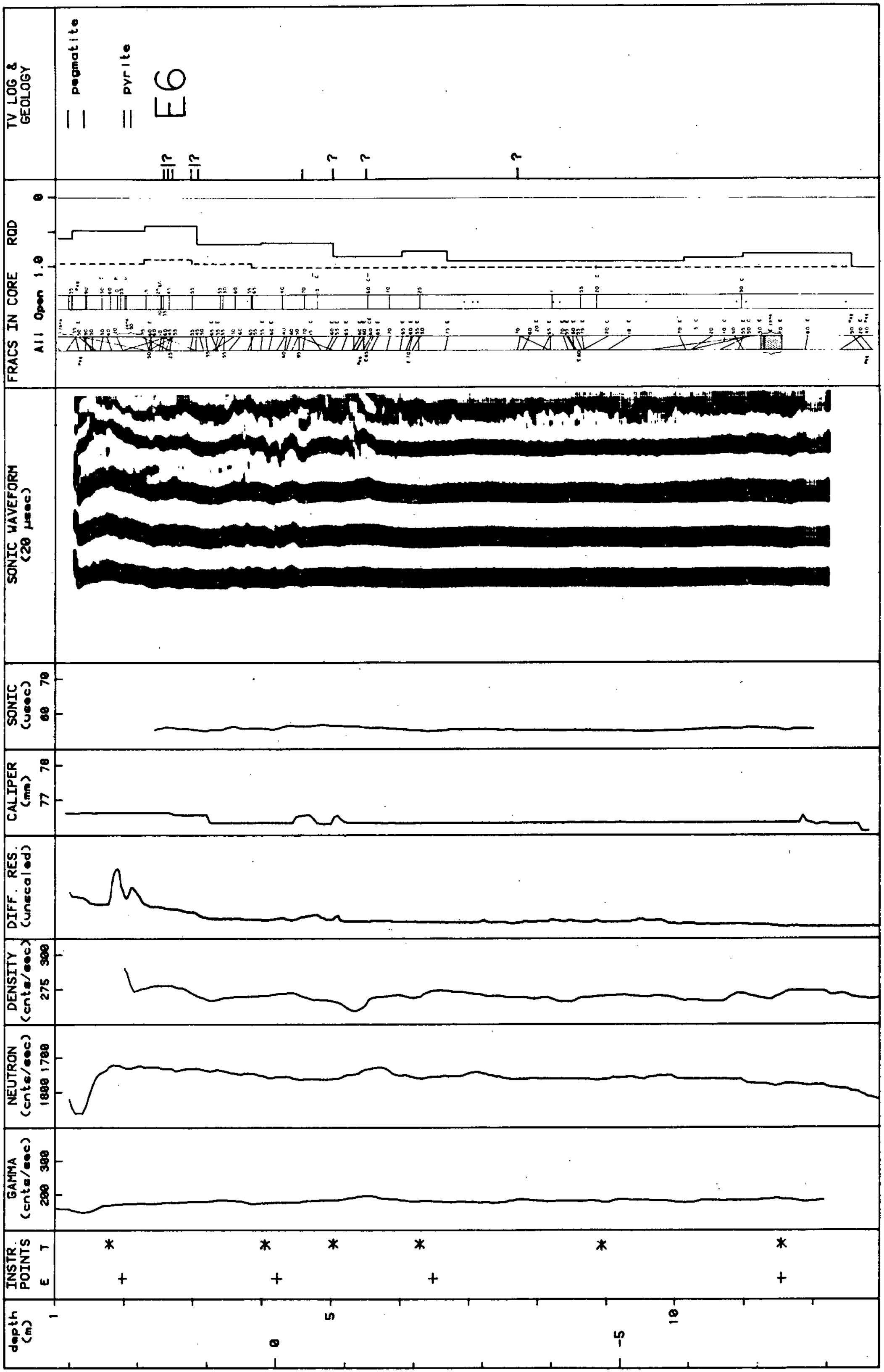
TV LOG & GEOLOGY
pegmatite
pyrite
E6
?
FRACS IN CORE
All
Open
RQD
0
1.0
SONIC WAVEFORM (20 µsec)
SONIC (usec)
60
70
CALIPER (mm)
77
78
DIFF. RES. (unscaled)
DENSITY (cnts/sec)
275
300
NEUTRON (cnts/sec)
1600
1700
GAMMA (cnts/sec)
200
300
INSTR. POINTS
T
E
depth (m)
1
5
10
0
-5

XBL814-2824

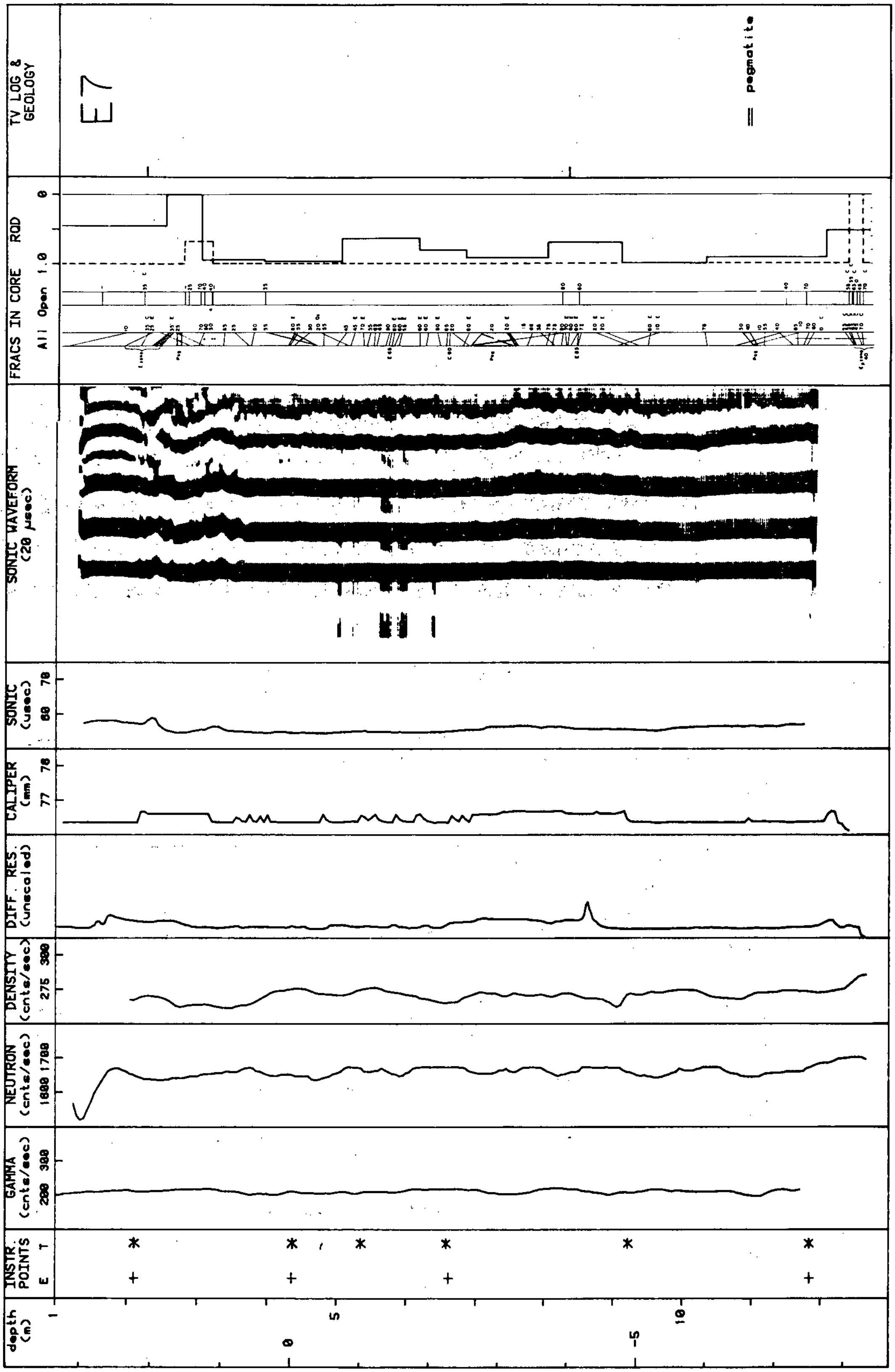
TV LOG & GEOLOGY
E7
pegmatite
FRACS IN CORE
All
Open
RQD
0
1.0
SONIC WAVEFORM (20 μsec)
SONIC (usec)
60
70
CALIPER (mm)
77
78
DIFF. RES. (unscaled)
DENSITY (cnts/sec)
275
300
NEUTRON (cnts/sec)
1600
1700
GAMMA (cnts/sec)
200
300
INSTR. POINTS
T
E
depth (m)
1
5
10
0
-5

XBL 814-2825

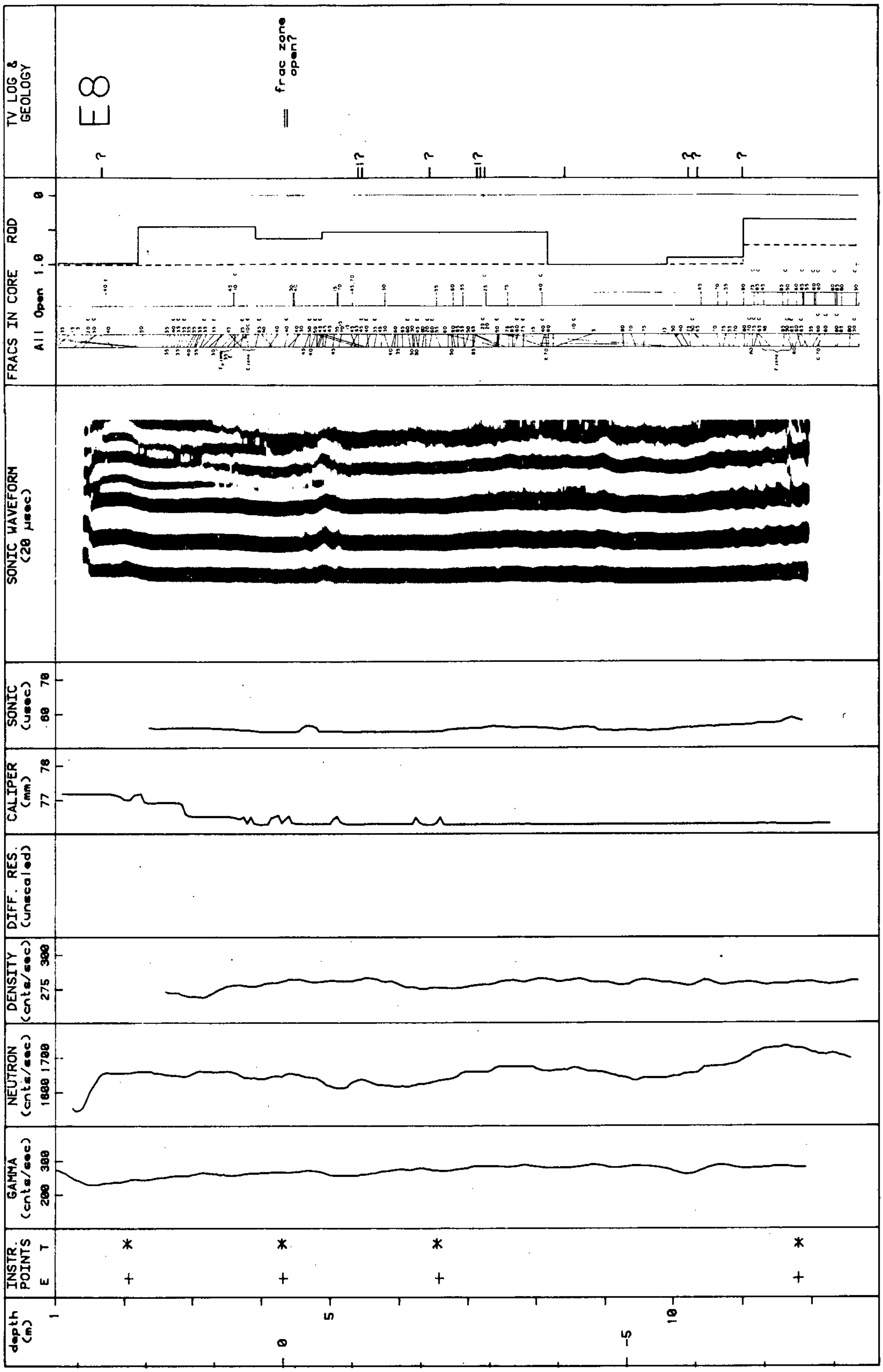
TV LOG & GEOLOGY
E8
frac zone open?
?
FRACS IN CORE
All
Open
1.0
RQD
0
SONIC WAVEFORM (20 μsec)
SONIC (usec)
60
70
CALIPER (mm)
77
78
DIFF. RES. (unscaled)
DENSITY (cnts/sec)
275
300
NEUTRON (cnts/sec)
1600
1700
GAMMA (cnts/sec)
200
300
INSTR. POINTS
T
E
depth (m)
1
5
10
0
-5

XBL 814-2826

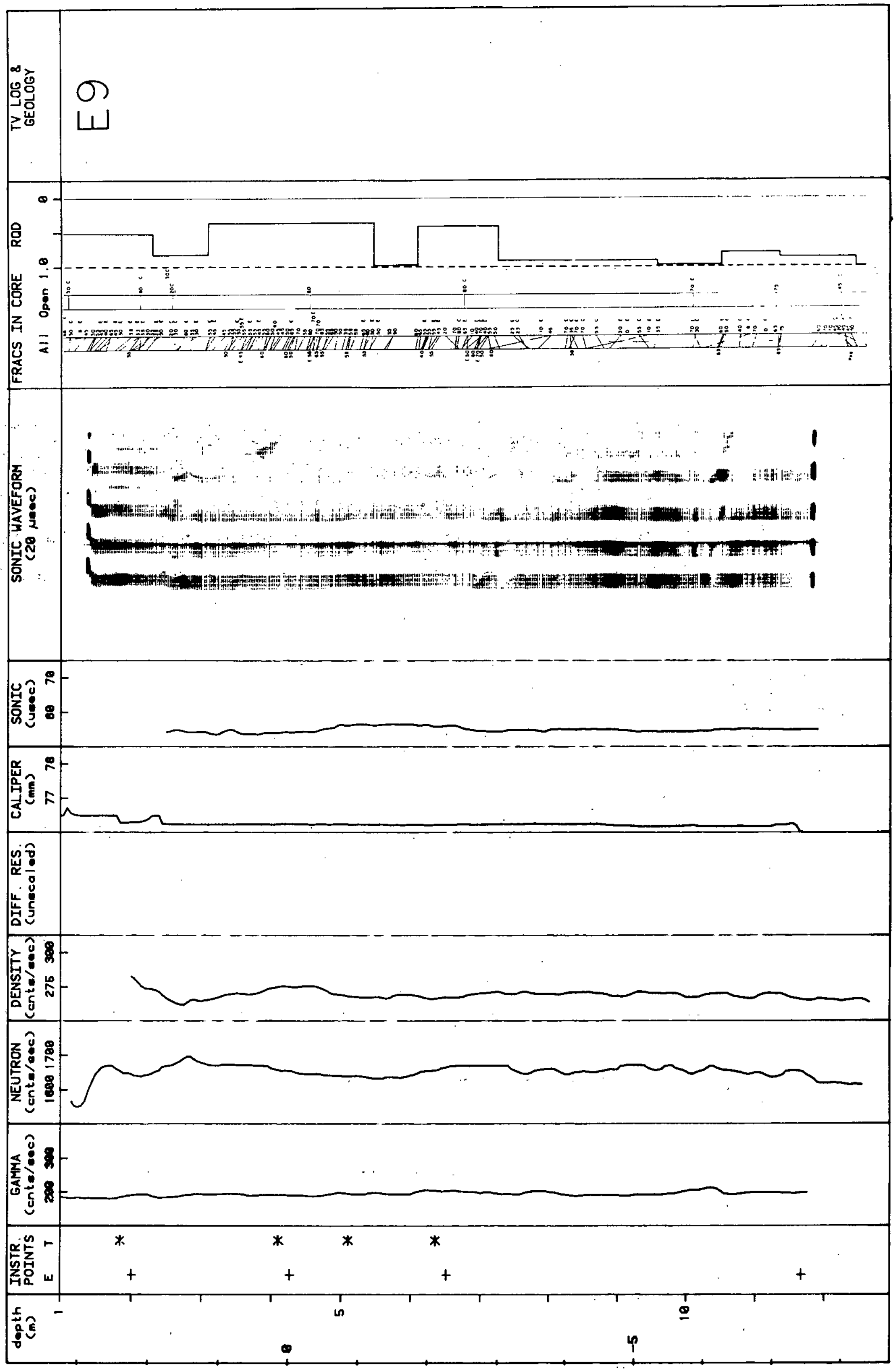
TV LOG & GEOLOGY
E9
FRACS IN CORE
All
Open
1.0
RQD
0
SONIC WAVEFORM (20 μsec)
SONIC (μsec)
60
70
CALIPER (mm)
77
78
DIFF. RES. (unscaled)
DENSITY (cnts/sec)
275
300
NEUTRON (cnts/sec)
1600
1700
GAMMA (cnts/sec)
200
300
INSTR. POINTS
T
E
depth (m)
1
5
10
0
-5

XBL 814-2827

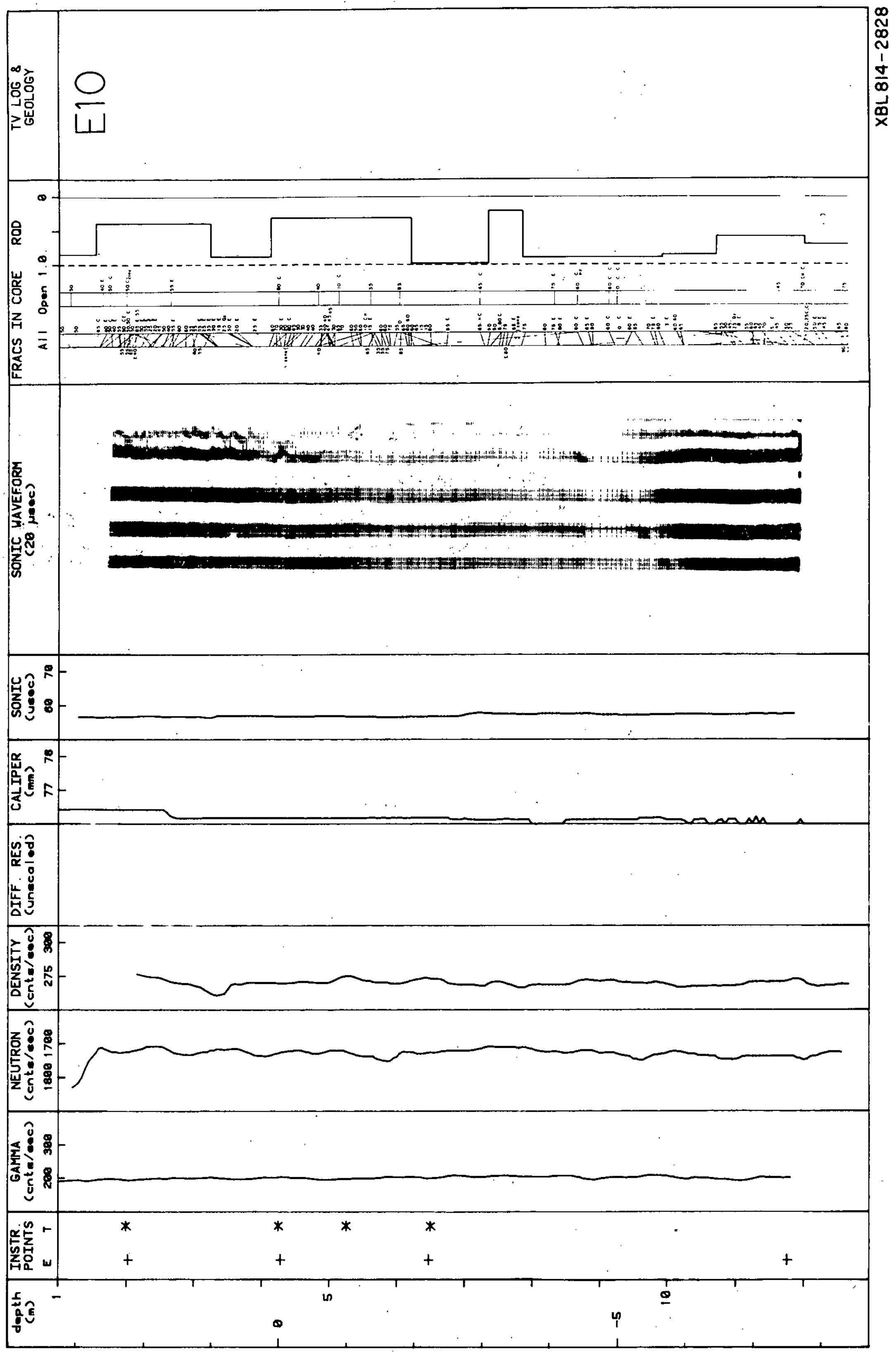
TV LOG & GEOLOGY
E10
FRACS IN CORE
All
Open
1.0
RQD
0
SONIC WAVEFORM (20 µsec)
SONIC (usec)
60
70
CALIPER (mm)
77
78
DIFF. RES. (unscaled)
DENSITY (cnts/sec)
275
300
NEUTRON (cnts/sec)
1600
1700
GAMMA (cnts/sec)
200
300
INSTR. POINTS
T
E
depth (m)
1
5
10
0
-5

XBL 814-2828

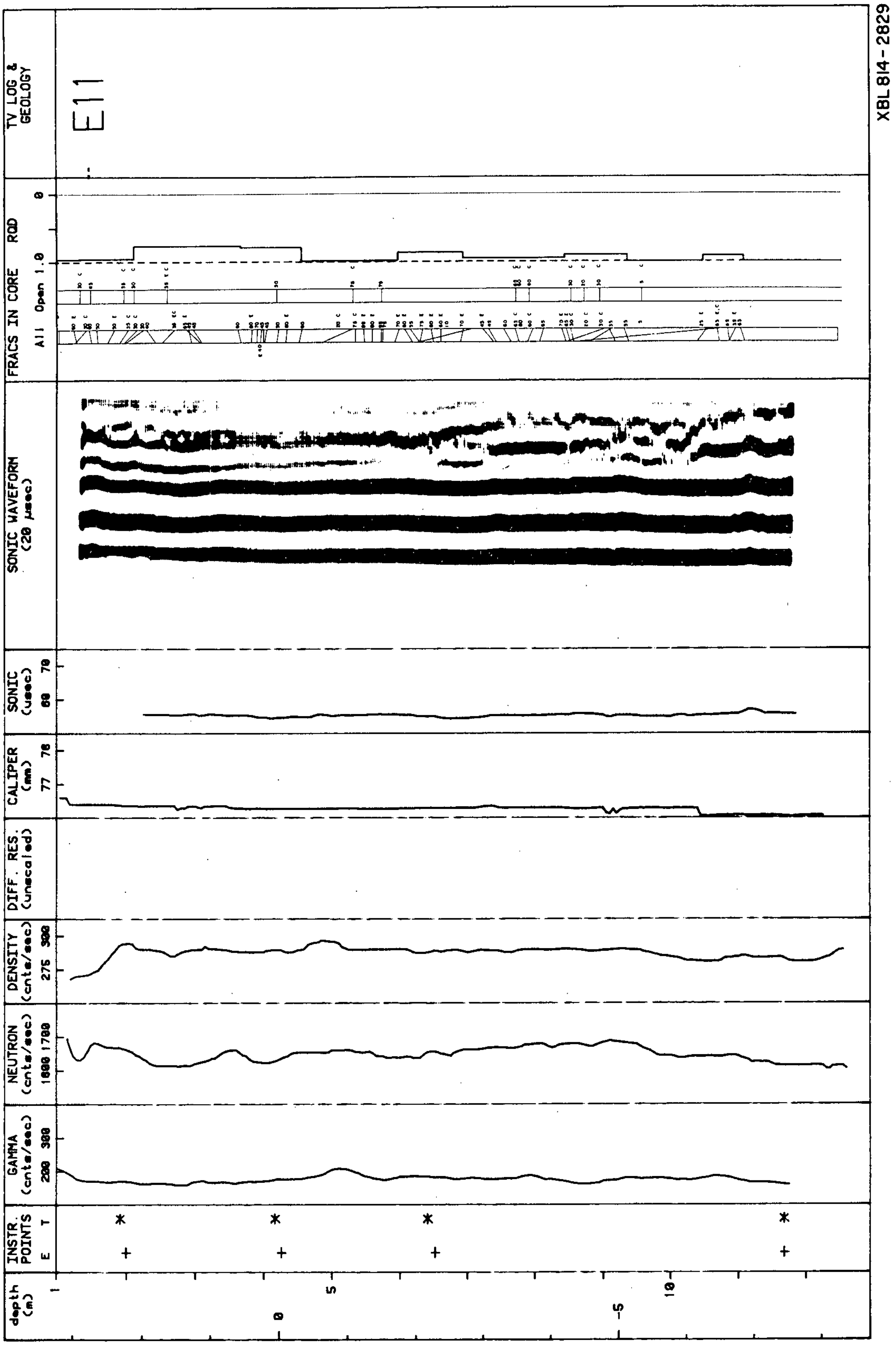
TV LOG & GEOLOGY
E11
FRACS IN CORE
All
Open
1.0
RQD
0
SONIC WAVEFORM (20 µsec)
SONIC (usec)
60
70
CALIPER (mm)
77
78
DIFF. RES. (unscaled)
DENSITY (cnts/sec)
275
300
NEUTRON (cnts/sec)
1600
1700
GAMMA (cnts/sec)
200
300
INSTR. POINTS
E
T
depth (m)
1
5
10
0
-5
XBL 814-2829

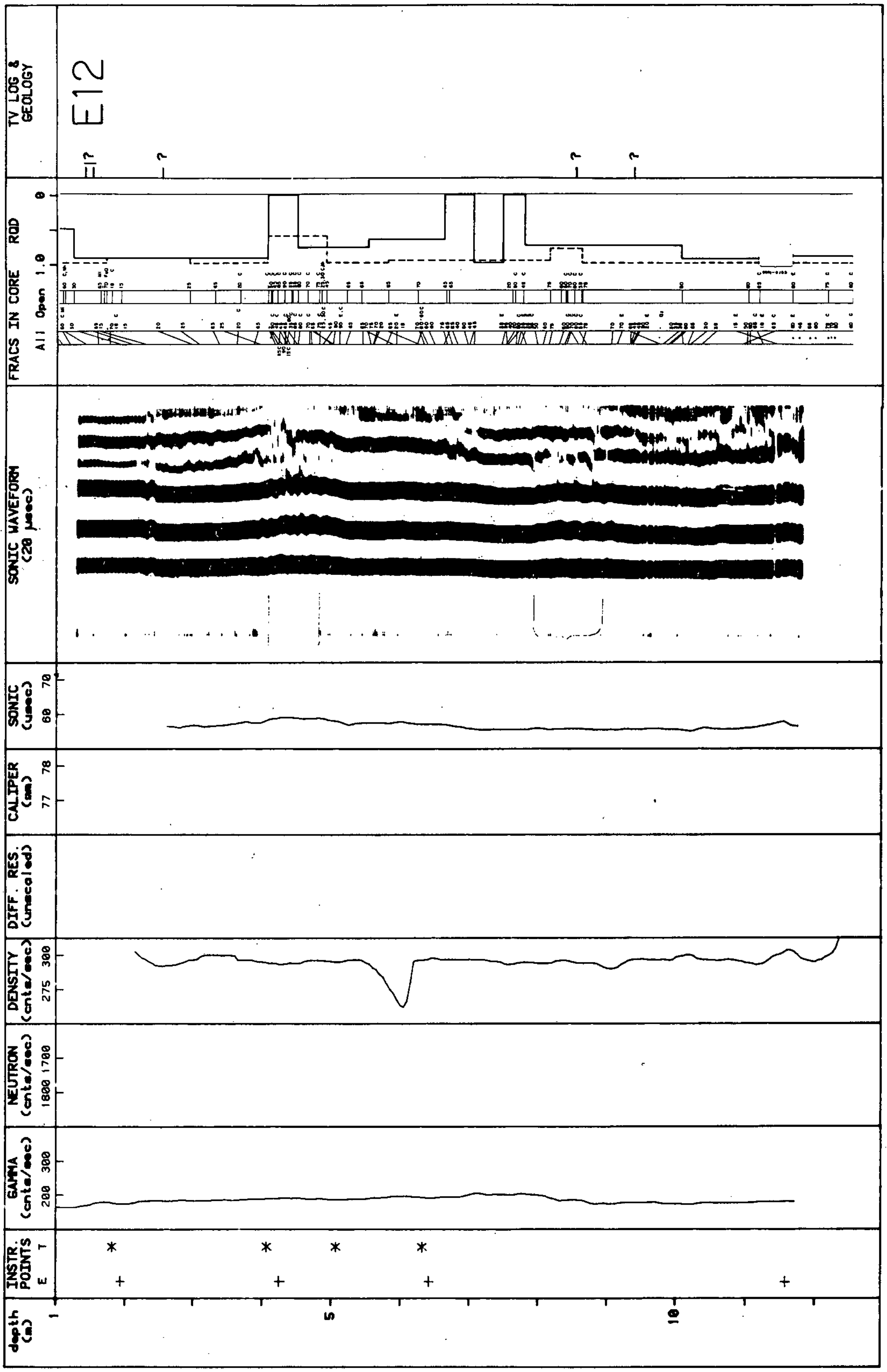
TV LOG & GEOLOGY
E12
?
?
?
RQD
0
1.0
FRACS IN CORE
All
Open
SONIC WAVEFORM (20 μsec)
SONIC (μsec)
60
70
CALIPER (mm)
77
78
DIFF. RES. (unscaled)
DENSITY (cnts/sec)
275
300
NEUTRON (cnts/sec)
1800
1700
GAMMA (cnts/sec)
200
300
INSTR. POINTS
T
E
depth (m)
1
5
10

XBL 814-2830

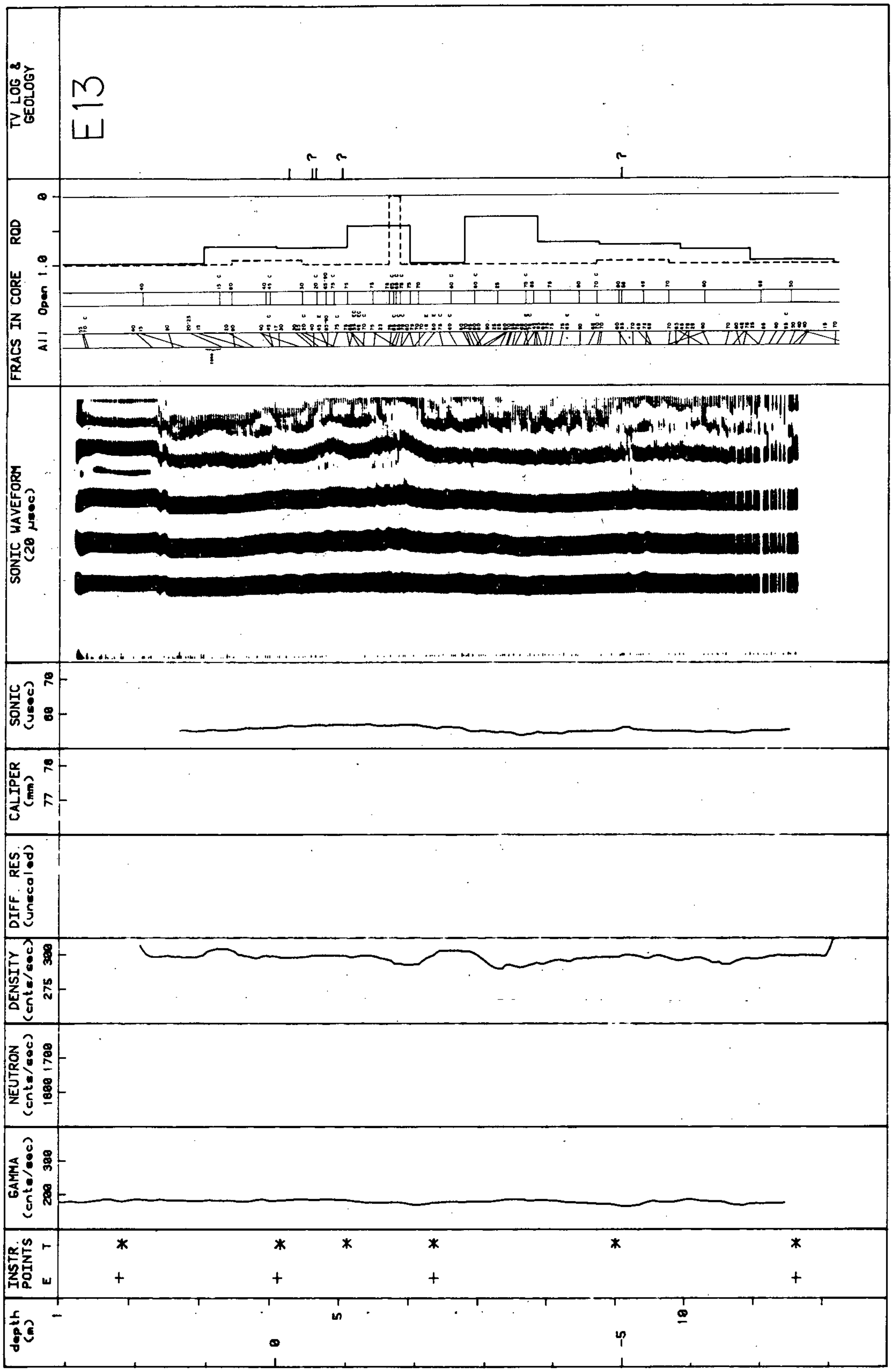
TV LOG & GEOLOGY
E13
?
?
?
FRACS IN CORE
All
Open
RQD
0
1.0
SONIC WAVEFORM (20 μsec)
SONIC (μsec)
60
70
CALIPER (mm)
77
78
DIFF. RES. (unscaled)
DENSITY (cnts/sec)
275
300
NEUTRON (cnts/sec)
1600
1700
GAMMA (cnts/sec)
200
300
INSTR. POINTS
T
E
depth (m)
1
5
10
0
-5

XBL814-2831

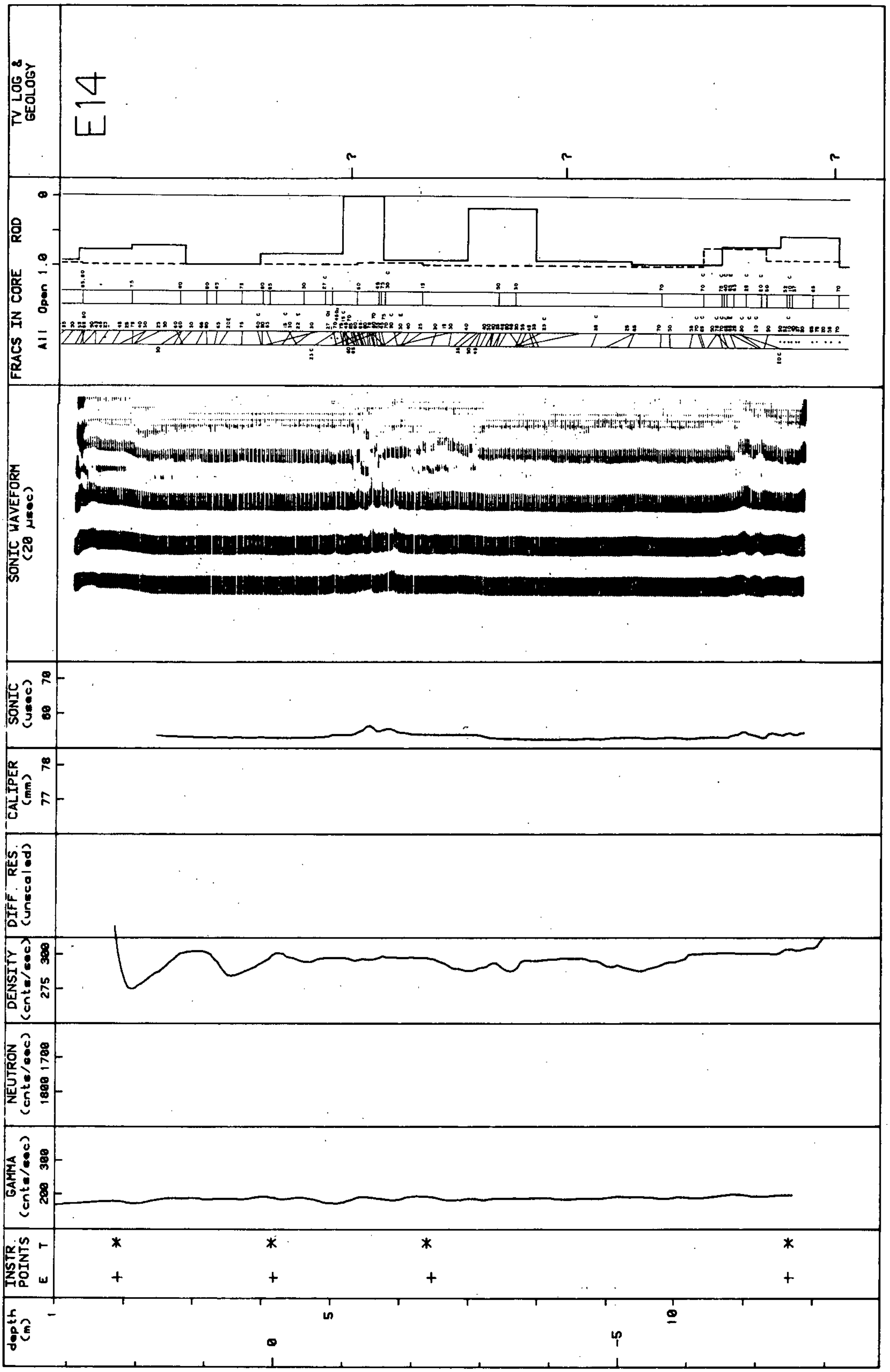
TV LOG & GEOLOGY
E14
?
?
?
FRACS IN CORE
All
Open
RQD
0
1.0
SONIC WAVEFORM (20 µsec)
SONIC (usec)
60
70
CALIPER (mm)
77
78
DIFF. RES. (unscaled)
DENSITY (cnts/sec)
275
300
NEUTRON (cnts/sec)
1600
1700
GAMMA (cnts/sec)
200
300
INSTR. POINTS
T
E
depth (m)
5
10
0
-5

XBL 814-2832

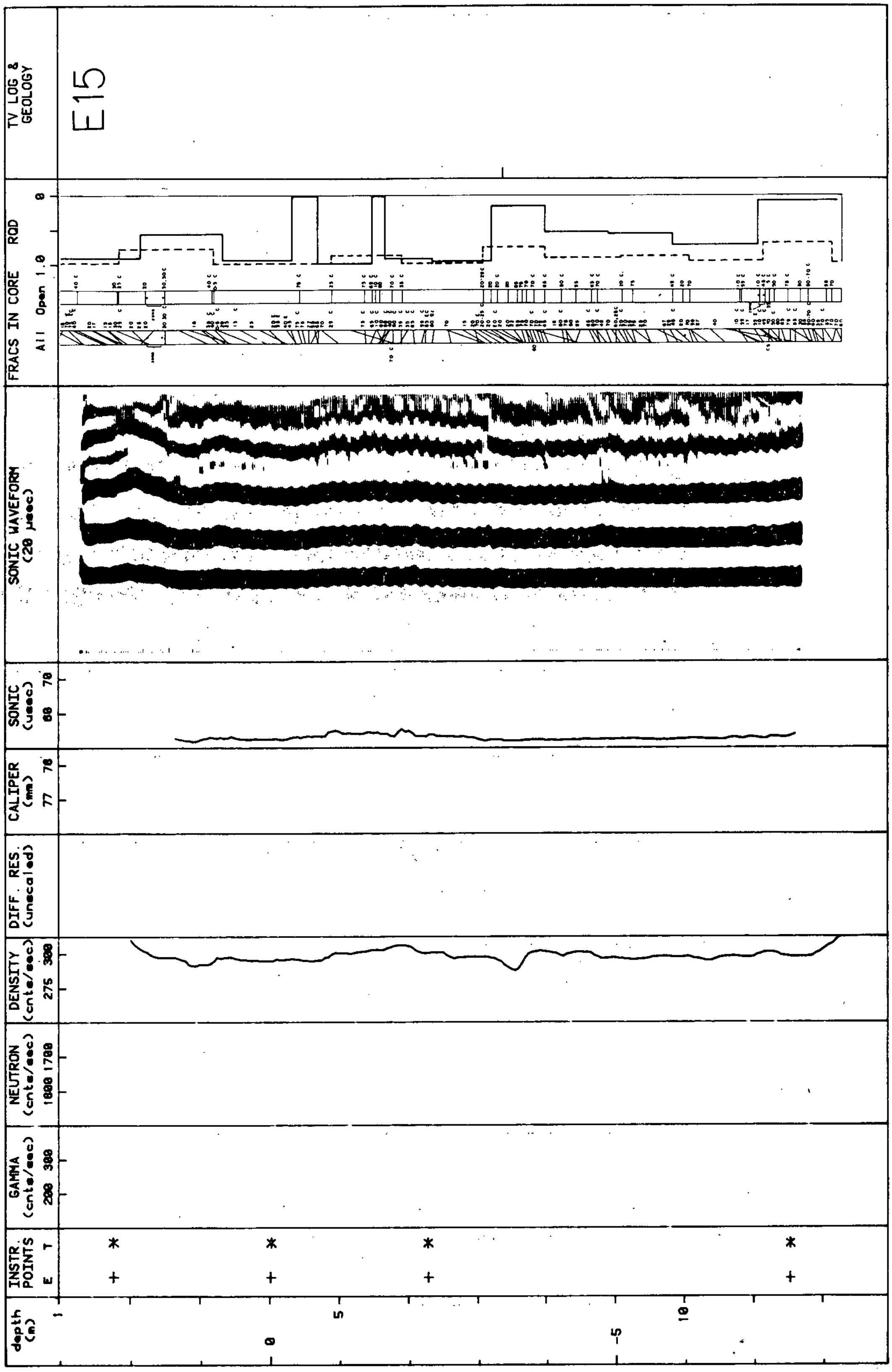
TV LOG & GEOLOGY
E15
FRACS IN CORE
RQD
0
1.0
All
Open
SONIC WAVEFORM
(20 μsec)
SONIC
(μsec)
60
70
CALIPER
(mm)
77
78
DIFF. RES.
(unscaled)
DENSITY
(cnts/sec)
275
300
NEUTRON
(cnts/sec)
1600
1700
GAMMA
(cnts/sec)
200
300
INSTR. POINTS
T
E
depth
(m)
1
5
10
0
-5

XBL 814-2833

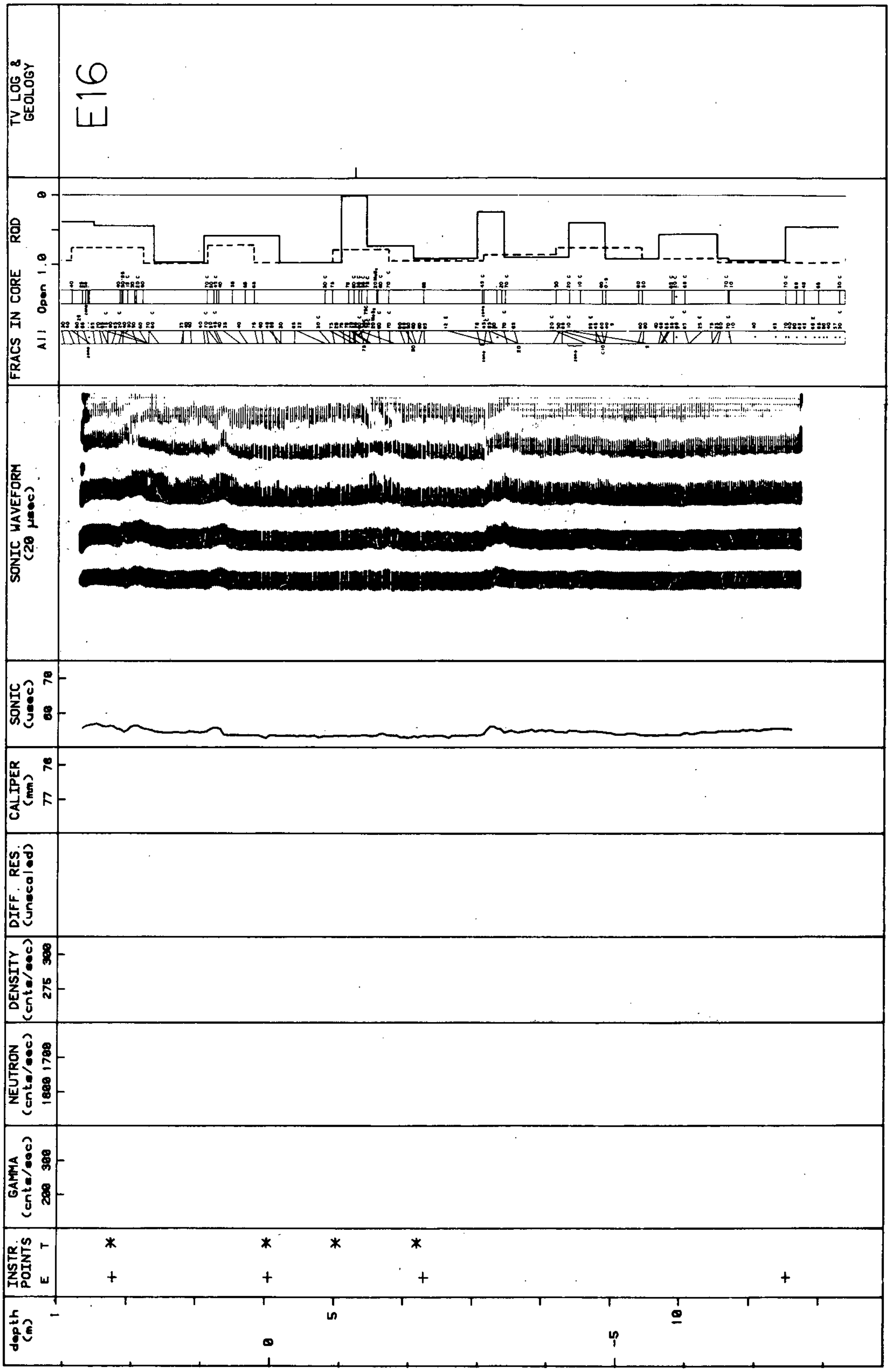
TV LOG & GEOLOGY
E16
FRACS IN CORE
All
Open
RQD
0
1.0
SONIC WAVEFORM (20 µsec)
SONIC (usec)
60
70
CALIPER (mm)
77
78
DIFF. RES. (unscaled)
DENSITY (cnts/sec)
275
300
NEUTRON (cnts/sec)
1600
1700
GAMMA (cnts/sec)
200
300
INSTR. POINTS
T
E
depth (m)
1
5
10
0
-5

XBL 814-2834

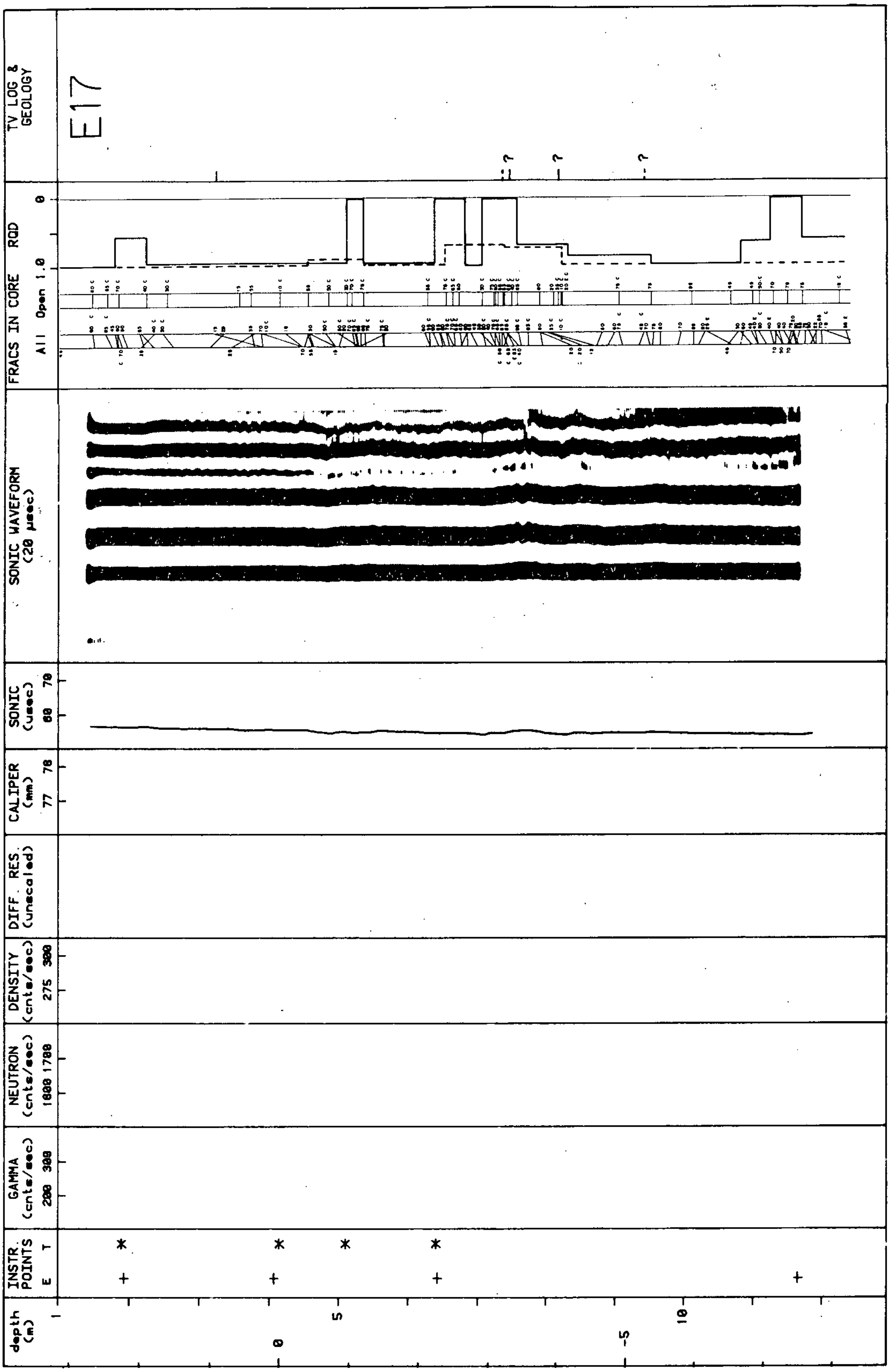
TV LOG & GEOLOGY
E17
?
?
?
FRACS IN CORE
All
Open
RQD
1.0
0
SONIC WAVEFORM (20 μsec)
SONIC (usec)
60
70
CALIPER (mm)
77
78
DIFF. RES. (unscaled)
DENSITY (cnts/sec)
275
300
NEUTRON (cnts/sec)
1600
1700
GAMMA (cnts/sec)
200
300
INSTR. POINTS
T
E
depth (m)
5
10
0
-5

XBL 814-2835

TECHNICAL INFORMATION DEPARTMENT
LAWRENCE BERKELEY LABORATORY
UNIVERSITY OF CALIFORNIA
BERKELEY, CALIFORNIA 94720